Two-dimensional Materials and their Charge Transfer Properties

A Thesis submitted for the degree of

Doctor of Philosophy

by

Manaswee Barua

JNCASR

New Chemistry Unit
Jawaharlal Nehru Centre for Advanced Scientific Research
(A Deemed University)
Bangalore, India

May 2022

Dedicated to my parents and teachers

DECLARATION

I hereby declare that the matter embodied in this thesis entitled "**Two-dimensional Materials and their Charge Transfer Properties**" is the result of investigations carried out by me under the supervision of Prof. C.N.R. Rao, FRS at the New Chemistry Unit, Jawaharlal Nehru Centre for Advanced Scientific Research, Bangalore, India and that it has not been submitted elsewhere for the award of any degree or diploma.

In keeping with the general practice in reporting scientific observations, due acknowledgment has been made whenever the work described is based on the findings of other investigators. Any oversight due to error of judgment is regretted.

Manaswee Barua

Manaswee Barua

CERTIFICATE

I hereby certify that the matter embodied in this thesis entitled “**Two-dimensional Materials and their Charge Transfer Properties”** has been carried out by Ms. Manaswee Barua at the New Chemistry Unit, Jawaharlal Nehru Centre for Advanced Scientific Research, Bangalore, India under my supervision and it has not been submitted elsewhere for the award of any degree or diploma.

Prof. C.N.R. Rao
(Research Supervisor)

ACKNOWLEDGEMENTS

First and foremost, I express my deepest gratitude to my research supervisor, Prof. C. N. R. Rao, FRS, for guiding me throughout my Ph.D. I consider myself privileged to have worked under his supervision, guidance, and mentorship. The values he has instilled in me, helped me become more informed and positive toward science and life in general. His unending source of motivation has encouraged me to value the importance of hard work. His "no substitute for hard work" philosophy will remain ingrained in me and will be followed throughout my life. His unique methodology to manage his students and bring out the best in them has indeed helped me in my Ph.D. work to learn more and stay motivated. He has always encouraged me to pursue good science, to have an innovative outlook while solving challenging problems, and be able to think unique. I am grateful to him for introducing me to the fascinating and vast field of materials chemistry. Not only has he been a great teacher, but also valuable moral support on the personal front. It has been a fulfilling experience, a lifetime opportunity for me to work under his full-spirited guidance. He has not only been instrumental in shaping my research, my career but my entire personality and my outlook on life as a whole.

I express my sincere gratitude to Prof. Subi J George, Chairman NCU, for his immense help and support in various aspects throughout my Ph.D.

I thank Prof. U. Ramamurthy (IISc) and Prof. Swapan K. Pati for successful collaborations and insightful discussions. I thank Prof. Sridhar Rajaram for many fruitful scientific discussions. I thank Dr. C.P.Vinod for his immense help in XPS measurements.

I would like to thank all my Integrated Ph.D. course instructors Prof. H. Ila, Prof. S**.** Balasubramanian**,** Prof. A. Sundaresan, Prof. Eswaramoorthy, Prof. Sridhar Rajaram, Prof. Shobhana Narasimhan, Prof. T. K. Maji, Prof. S. J. George, Prof. R. Viswanatha, Prof. Jayanta Haldar, Prof. Kanishka Biswas, Dr. Meher Prakash, Prof. Sebastian C. Peter, and Dr. Sarit Agasti for the courses they provided and stimulating scientific discussions.

I am thankful to the chairmen of NCU, CPMU, MBGU, and ICMS for allowing me to use the various departmental facilities.

I am indebted to Dr. Sreedhara M.B. for his mentorship during my initial days of research.

The contributions from my co-workers have been indispensable and without them most of the works would have been incomplete. I thank Dr. Sreedhara, Dr. Pramoda, Dr. Vishnoi, Mr. Rajesh, Dr. S. Manjunath, Dr. Fatahi, Dr. Arkamita Bandyopadhyay, Dr. Abhishek Chaturvedi (IISc), Ms. Madhulika Mazumdar, Mr. Mohd. Monis Ayyub, Dr. Shashidhara Acharya, and Ms. Aditi Saraswat for their immense contribution towards completing my Ph.D. work.

It has been a wonderful experience working with all my past and present labmates. I thank Dr. R. Saha, Dr. Gopalakrishnan, Dr. R. Kumar, Dr. S. Dey, Dr. P. Vishnoi, Dr. D. Narang, Dr. K. Manjunath, Dr. M. Jaiswal, Dr. Lingampalli, Dr. Pramoda, Dr. Jana, Dr. Sreedhara, Dr. Gupta, Dr. Roy, Dr. Chhetri, Dr. S. Manjunatha, Dr. Kaur, Rajesh, Monis, Amit, Navin, Rohit, Reetendra, Swaraj, Devesh, and Aditi for providing a healthy atmosphere in lab and for their help on various occasions.

I acknowledge the assistance of technical staff at JNCASR especially Dr. J. Ghatak, Mr. Mahesh, Ms. N. R. Selvi, Mrs. T. Usha, Mr. A. Srinivas, Mr. Vasu, Ms. Meenakshi, Mr. Sachin, Mr. Nandakishore, Mr. Kannan, Mr. Shivakumar, Mr. Rajakumar, Mr. Arun, and Mr. Anil. I thank, Mrs. Sudha, Mrs. Shashi, Mr. Gowda, and Mr. Victor for their help in various ways. I also thank NCU and ICMS office staff Melissa, Ramya, Naveen, and Nandesh.

I thank JNCASR and DST for research fellowship and facilities. The hostel, Admin staff, Academic staff, Library staff, Complab staff, and Dhanvantari for all their help during my stay at JNCASR.

My deepest thanks to Mrs. Indumati Rao for her love, affection, and warm hospitality extended to me during the last six years. Her enthusiasm age notwithstanding has been a source of inspiration for me. I take this opportunity to thank Mr. Sanjay Rao for his hospitality.

In addition to those who had a scientific impact on my graduate school career, I am forever grateful for the presence of all the people who have supported me and inspired me on a personal level throughout my Ph.D. Thanks to all my Int. Ph.D. batch mates with whom I started my life at this centre and whose cheerful company made these years so memorable. I thank all my friends Janaky, Bornika, Monis, Ashutosh, Momin, Divya, Sreyan, Niloy, Jia da, Anindita, Satyajit, Santu, Reetendra, Shashank, Pradeep, Anjana, Manisha di, Naba di and many more. I especially thank my friends from B.Sc.; Akansha, Dipshi, Pallavi, Kritika, and Sulbha for the enriching experiences I had with them which motivated me to pursue Ph.D.

I express my deep gratitude to all my teachers from Don Bosco High school, Kendriya Vidyalaya, and Miranda House. Their contributions to the completion of my

Ph.D. have been enormous. Special thanks to Stormy Teacher, Pujari Sir, Bipul Bora Sir, Pathak Sir, and Sheikh Ma’am for always believing in me.

I would love to extend my deepest gratitude to my parents for their unending inspiration and support and for always believing in me. I thank my brother and my sister for all their love. I thank my entire extended family for their understanding and support throughout my life.

Above all, I thank the Almighty for everything.

Manaswee Barua

Prologue

Two-dimensional materials constitute an important class of atomically thin materials with exceptional electronic, magnetic, spintronic, and mechanical properties. Despite their short synthetic history, they have introduced a cornucopia of new physics and potential applications. The restriction in a spatial dimension introduces fundamental changes in the material properties. In the last two decades, two-dimensional materials have come out as promising candidates for multiple electronic and optoelectronic applications due to easy tailoring of charge carrier types and concentrations; strong light-matter interactions; and dimension dependent band structure tunability and these are fundamentally dependent on effective charge transfer in this class of materials. This thesis focuses on the synthesis of different classes of two-dimensional materials and tries to understand different aspects of their charge transfer behavior. This thesis is divided into six chapters.

Chapter 1 gives a brief overview of two-dimensional materials and introduces different material classes and discusses the commonly used synthetic techniques. Further, it gives a concise introduction to the importance of charge transfer in two-dimensional systems.

Chapter 2 focuses on understanding the role of surface functional groups in tuning material properties. These surface groups define various properties of a material like chemical reactivity, wettability, adhesion, conduction or insulation, optical transmission, hardness, biocompatibility, and the interaction of the material with its surroundings in general. In **Part A** of this chapter, we try to estimate the number of different surface functional groups on graphene, boron nitride, and borocarbonitrides by selectively covalently linking them with different dye molecules and using fluorescence spectroscopy to quantify the groups using a technique known as fluorescence labeling of surface species (FLOSS). This quantitative estimate of surface functional groups will be useful in understanding molecular-level interactions of these materials with their surroundings. In **Part B** of this chapter, we made polymer nanocomposites of polyvinyl alcohol with 0.2 wt% graphene, boron nitride, and borocarbonitrides as nanofillers and observed an improvement of 105% in hardness (*H*) and 69% in elastic modulus (*E*) along with significant improvement in thermal properties. This improvement in mechanical properties could be correlated with the increase in crystallinity and effective stress transfer between the filler and polymer backbone owing to strong molecular-level interactions.

In **Chapter 3**, we introduce a new synthetic technique for large-scale synthesis of pristine γ-graphyne, an artificial carbon allotrope, using Sonogashira cross-linking reaction. Graphynes are an interesting family of artificial carbon allotropes that are layered in nature and incorporate both sp and sp^2 hybridized carbon in the lattice. Theoretically, graphynes are predicted to show excellent electronic properties, however, an effective synthesis strategy is a primary deterrent for its experimental exploration. The as-synthesized γ-graphyne showed an sp C: sp^2 C ratio of 1:1, a bandgap of ~2.3eV, and mesoporous behavior with a BET surface area of ~ 473 m^2g^{-1}. We were able to understand the mechanism of product formation in detail. Charge transfer studies were carried out with donor and acceptor molecules to understand the electron transfer behavior and defect density of γ-graphyne wherein it showed a similar / better charge transfer behavior with electron acceptors compared to few-layered graphene.

In **Chapter 4**, we have tried to understand the photocatalytic hydrogen evolution behavior (HER) of 2D metal phosphochalcogenides. Metal phosphochalcogenides (MPX_3) are an interesting and relatively less explored class of two-dimensional materials whose band edges are predicted to be suitable for HER. In this work, we have synthesized eight monometallic ($NiPS_3$, $FePS_3$, $MnPS_3$, $CdPS_3$, $ZnPS_3$, $NiPSe_3$, $FePSe_3$, and $MnPSe_3$) and two bimetallic phosphochalcogenide compounds ($Ag_{0.5}In_{0.5}PS_3$ and $Ag_{0.5}In_{0.5}PSe_3$) by high-temperature synthesis method and studied their photocatalytic HER activity. Among the ternary MPS_3, the Nickel compound exhibits the highest HER activity (2.6 mmol $h^{-1}g^{-1}$), while $MnPS_3$, $CdPS_3$, and $ZnPS_3$ exhibit low activity, due to their large band gaps and presence of long P-P and M-S bonds. Amongst phosphoselenides, $FePSe_3$ shows higher HER activity of 1.7 mmol $h^{-1}g^{-1}$ than the Mn and Cd compounds. The quaternary phosphochalcogenide, $Ag_{0.5}In_{0.5}PS_3$, shows high photochemical HER activity of 1.9 mmol $h^{-1}g^{-1}$. We were able to correlate the trend observed in H_2 yields with the crystal field stabilization energy (CFSE), P-P bond lengths, and M-S bond lengths.

In **Chapter 5**, we try to understand the charge transfer behavior in phosphorene and phosphorene quantum dots. In **Part A** we synthesize few-layered phosphorene, a group 15, 2D pnictogen by liquid exfoliation in N-methyl pyrrolidone. The reactivity of phosphorene is due to the presence of lone pairs on each atom, and we were able to study its charge transfer behavior with different donor and acceptor molecules using Raman spectroscopy and we establish that both hole and electron can be doped into phosphorene by molecular charge transfer. Moreover, charge transfer of phosphorene with acceptor molecules showed surface passivation signatures. Optoelectronic applications of phosphorene are still limited by its narrow bandgap. In **Part B** were able to prepare blue-fluorescent phosphorene quantum dots of diameters ~5nm, 3nm, and 1nm by liquid exfoliation, which showed excitation-dependent emission characteristics. These materials showed appreciable fluorescence quantum yields. We have also studied the charge transfer behavior of these quantum dots with donor and acceptor molecules.

Chapter 6, studies the charge transfer interactions in few-layered bismuthene. We were able to synthesize emissive few-layered bismuthene sheets by liquid exfoliation in N-methyl pyrrolidone. The reactivity of 2D pnictogens is due to the presence of lone pair on each atom which can be effectively utilized to tune material properties via different functionalization strategies. In **Part A**, we have covalently functionalized these bismuthene sheets with p-Nitrobenzenediazonium tetrafluoroborate salt. Spontaneous covalent functionalization of bismuthene nanosheets with diazonium salt leads to the formation of quaternary Bi species with the preferential attachment of organic moieties via Bi-C linkage along with simultaneous rehybridization of bismuthene band structure leading to a redshift in the emission spectra. In **Part B**, we have functionalized these bismuthene sheets with group 12 and 13 Lewis acids ($ZnCl_2$, $CdCl_2$, BCl_3, $GaCl_3$, $AlCl_3$, and $InCl_3$). Interaction of these Lewis acids with the lone pairs on Bi leads to the formation of Lewis acid-base adduct with corresponding changes in bonding environment along with lattice distortion and rehybridization of the band structure. Interestingly, Lewis acid-base adduct formation leads to a blue shift in the bismuthene emission. This work demonstrates the easy tunability of bismuthene emission by different functionalization strategies leading to the rehybridization of the band structure and opens a path for tuning the properties of bismuthene for integration in electronic and optoelectronic devices.

In the **Appendix**, we study the covalent functionalization of ZnS, ZnSe, and CdS nanoparticles using iodobenzene in the presence of Pd(0) catalyst. Covalent functionalization introduces a charge-transfer band in the absorption spectra of these materials. Moreover, this work also demonstrates the possibility of attaching donor-acceptor molecules into similar systems to study Förster resonance energy transfer (FRET).

Table of Contents

References

Chapter 5: Charge transfer studies in phosphorene and phosphorene quantum dots 129

References

Chapter 6: Covalent functionalization and Lewis acid-base adduct formation in Bismuthene nanosheets 163

Chapter-1

A brief introduction to two-dimensional materials

SUMMARY

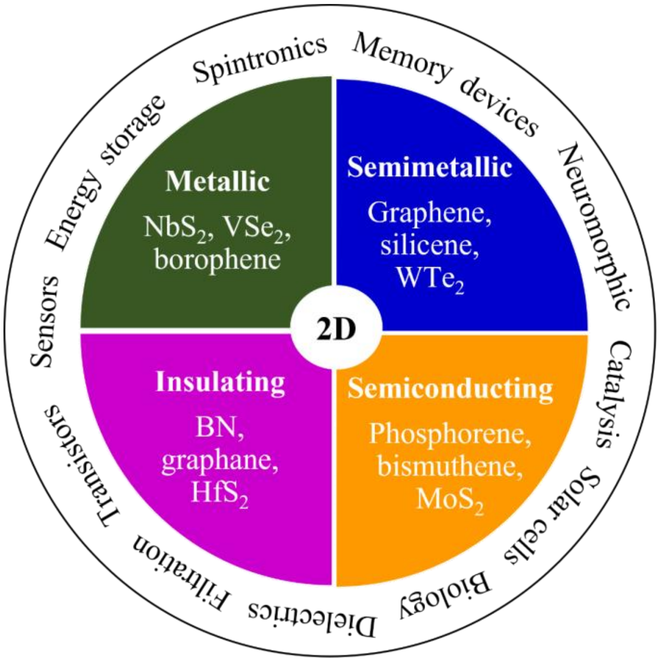

Two-dimensional materials constitute an important class of materials with exceptional electronic, magnetic, spintronic, and mechanical properties. Despite their short synthetic history, they have introduced a cornucopia of new physics and potential applications. Graphene, the flag-bearer of this group, represents a conceptually new material class that offers newer inroads into low-dimensional physics and provides a fertile ground for potential applications. The family of 2D materials is very widespread and encompasses most of the elements of the periodic table.

1.1 Preface

In Richard Feynman's prophetic lecture in 1959 termed "*There is plenty of room in the bottom: an invitation to enter a new field of Physics*" he talked about the possibility of manipulating and controlling properties on the atomic scale, and this could be regarded as a significant event in the development of the field of nanoscience.[1] Nanoscale materials are defined as materials where at least one dimension is in the nanometer scale ~ 1-100 nm. The reduction in the spatial dimension, in one or more crystallographic directions within the structure, leads to changes in the fundamental properties of the material. Two-dimensional material is an important class of nanomaterials that are atomically thin and confined in one dimension. This criterion offers new in-roads into low-dimensional physics, which never cease to inspire scientists and provides a fertile ground for interesting applications. Two-dimensional materials are a widespread family of materials encompassing almost all elements of the periodic table with the possibility of large variations in their properties.[2] These materials present the possibility to play a fundamental role in the future of nanoelectronics, spintronics, optoelectronics, mechanical fillers, in the assembly of novel ultra-thin flexible devices, etc. The flag-bearer of this material class is graphene, the father of all 2D materials.[3] Although pure graphene was experimentally synthesized only in 2004, this field has been of interest to scientists for more than seven decades. [4]

1.2 Introduction

Graphene

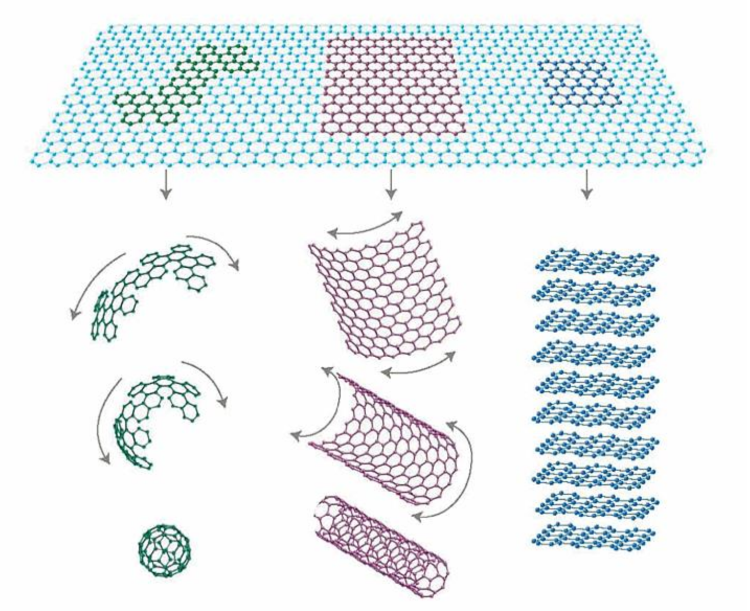

Figure 1: Graphene, mother of graphitic materials of all dimensions. Reprinted by permission from Nature ref 4 , Copyright 2009

The fascination with graphene was fueled by a constant search for new non-traditional materials with the semiconductor industry approaching its limits with Silicon-based technologies. Graphene is a two-dimensional hexagonal lattice of sp^2 hybridized carbon atoms and is the building block of graphitic materials of different dimensions like fullerenes (0D), nanotubes (1D), and graphite (3D). [3,4] Although theoretical calculations of all these graphitic materials were carried out using graphene as the starting material; the stability of 2D graphene was considered doubtful both theoretically and experimentally until 2004 when scientists were able to isolate monolayer graphene sheets. [3,5,6]

Theoretically, it was predicted that according to standard harmonic approximation, thermal fluctuations will destroy long-range order, thus no 2D lattice can be stable at finite temperature and this was also backed by experimental results wherein thin films become

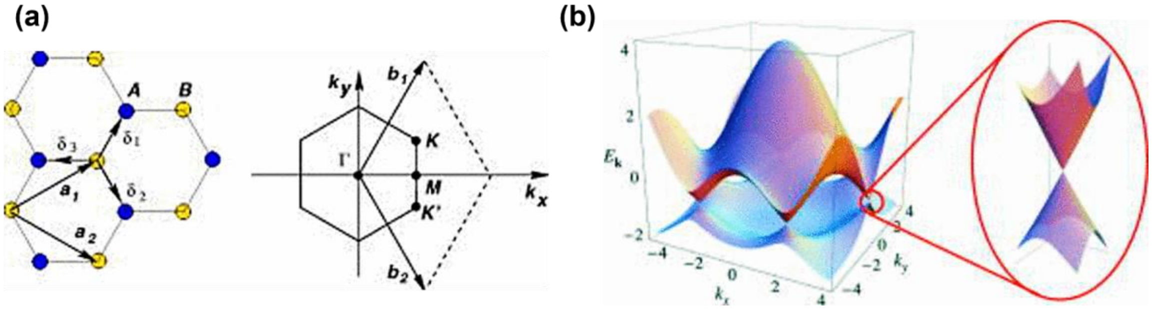

Figure 2: (a) Honeycomb lattice of graphene and corresponding Brillouin zone. The Dirac cones are located at the K and K′ points, (b) Electronic dispersion in the honeycomb lattice with a zoomed in image of the energy bands close to one of the Dirac points. Reprinted with permission from ref 9, Copyright (2009) by American Physical Society

thermodynamically unstable and segregate out or decompose below typically a dozen atomic layers.[5,7,8] But there was a catch, theoretical calculations did not forbid the existence of nearly-perfect 2D crystals in 3D space and indeed it was found that the interaction between stretching and bending long-wavelength phonons could in principle stabilize a 2D lattice through their deformations in the third dimension. Hence, surface roughness/ corrugations are essential for structural stability of 2D materials, and these out-of-plane deformations lead to significant elastic strain in the lattice which in turn leads to interesting results like high carrier mobility, transport characteristics, etc.[5,9] Graphene exhibited extraordinary properties like ultra-high carrier mobility (200,000 cm^2/V^{-1} s^{-1}), micron-scale mean free path, electron-hole symmetry, and quantum Hall effect, the elastic modulus of 1TPa with an outstanding fracture strength, high thermal conductivity, extremely low surface energy and permeability, and optical transparency.[4] Single-layer graphene has two atoms per unit cell and this gives rise to two conical points K and K' per Brillouin zone where band crossing occurs. Near these crossing points, electron energy is linearly dependent on the wave vector.[10] The charge carriers in graphene mimic relativistic particles and are more easily and naturally described by the Dirac equation rather than the Schrödinger equation.[4,6] The interaction of electrons with the periodic potential of graphene's honeycomb lattice gives rise to quasiparticles called massless Dirac fermions; and these can be described by (2+1)-dimensional Dirac equation. At present, applications of graphene are limited by its zero-bandgap leading to low on/off ratios and although many methods for bandgap widening have been suggested, most of these affect the excellent properties of the material.[11] But this has been instrumental towards the discovery of other classes of 2D materials.

1.3 2D materials beyond graphene

The synthesis/stabilization of graphene renewed interest in 2D materials and led to the discovery of different classes of materials exhibiting a plethora of interesting properties.[2,12–14] At present, there are many broad classes of materials that have been brought under this umbrella, some of these will be discussed below:

a. **Hexagonal boron nitride (h-BN)**

   It is a wide indirect band-gap semiconductor (5.9eV) with an sp^2 hybridized honeycomb lattice, belonging to $P6_3/mmc$ space group. It is isoelectronic with carbon and is referred to as white graphite. h-BN is an excellent ceramic material with low dielectric constant, low dielectric loss, low electrical and high thermal conductivity, and low coefficient of thermal expansion. h-BN is also chemically inert to a wide range of acids, solvents, and oxidizers. In recent years, h-BN is being regarded as an excellent dielectric substrate material for the fabrication of 2D material devices for electronic and optoelectronic applications because of its atomically flat surface and absence of dangling bonds and charge traps on the surface.[15–19] h-BN has already been shown to be a superior substrate for graphene-based devices with more than an order of improvement in mobility values compared to SiO_2/Si substrate.[20]

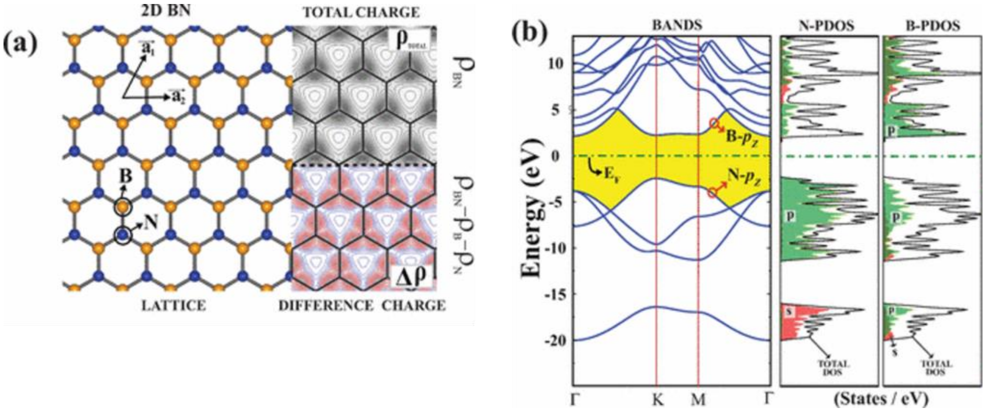

Figure 3: (a) Primitive unit cell of the honeycomb structure of 2D h-BN with calculated total charge density ρ_{BN} and difference charge density $\Delta\rho$ are also shown in the same panel. (b) Calculated electronic structure of 2D BN honeycomb crystal together with total, TDOS, and partial density of states, PDOS, on B and N atoms. Reprinted with permission from ref 18, Copyright (2009) by American Physical Society

b. Transition metal dichalcogenides (TMD)

This is a broad class of more than 60 materials denoted by MX_2 wherein M is a transition metal from group 4-10 and X is a chalcogen as S, Se, Te, and exhibit versatile chemistry. Bulk TMDs are mainly layered materials and have been under study for decades. 2D TMDs consists of three atomic layers in which a hexagonally packed transition metal layer is sandwiched between two chalcogen layers. In monolayer TMDs, the metal atom can be bonded either as trigonal prismatic or octahedrally. TMDs find applications in a variety of fields including catalysis, energy storage, sensing, electronic devices such as FETs and logic circuits, lubrication, photovoltaics, supercapacitors, and rechargeable battery systems. The electronic structure of these materials depends on the metal coordination and its d-electron count and leads to a wide variety of electronic and magnetic properties. Members of this group show diverse properties including insulators such as HfS_2, semiconductors such as MoS_2 and WS_2, semimetals as $TiSe_2$, WTe_2, and metals as NbS_2 and VSe_2. $NbSe_2$ and TaS_2 exhibit low-temperature superconductivity and Mott transition.[21–24] Members of this group like MoS_2 and $MoSe_2$ are considered forerunners in the field of hydrogen evolution by water splitting with efficiencies nearing that of Pt.[25]

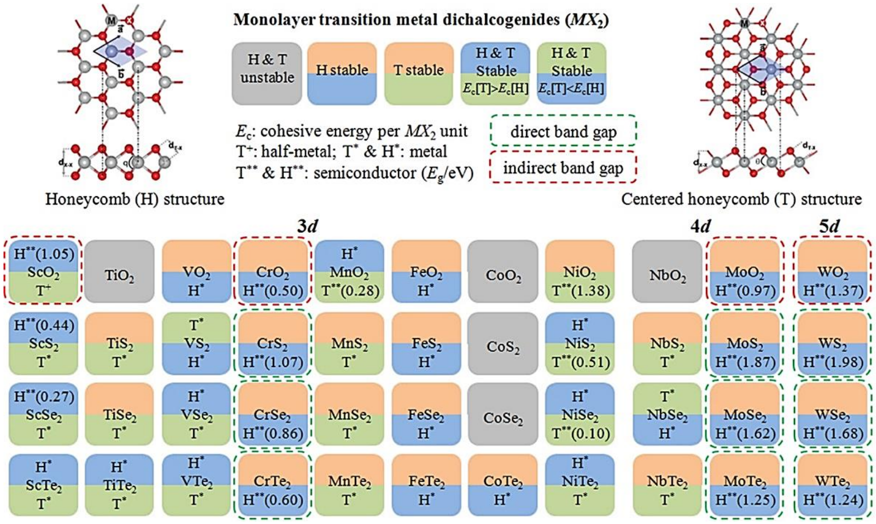

3d								4d	4d	5d
H^{**}(1.05) ScO_2 T^+	TiO_2	VO_2 H^*	CrO_2 H^{**}(0.50)	H^* MnO_2 T^{**}(0.28)	FeO_2 H^*	CoO_2	NiO_2 T^{**}(1.38)	NbO_2	MoO_2 H^{**}(0.97)	WO_2 H^{**}(1.37)
H^{**}(0.44) ScS_2 T^*	TiS_2 T^*	T^* VS_2 H^*	CrS_2 H^{**}(1.07)	MnS_2 T^*	FeS_2 H^*	CoS_2	H^* NiS_2 T^{**}(0.51)	NbS_2 T^*	MoS_2 H^{**}(1.87)	WS_2 H^{**}(1.98)
H^{**}(0.27) $ScSe_2$ T^*	$TiSe_2$ T^*	H^* VSe_2 T^*	$CrSe_2$ H^{**}(0.86)	$MnSe_2$ T^*	$FeSe_2$ H^*	$CoSe_2$	H^* $NiSe_2$ T^{**}(0.10)	T^* $NbSe_2$ H^*	$MoSe_2$ H^{**}(1.62)	WSe_2 H^{**}(1.68)
H^* $ScTe_2$ T^*	H^* $TiTe_2$ T^*	H^* VTe_2 T^*	$CrTe_2$ H^{**}(0.60)	$MnTe_2$ T^*	$FeTe_2$ H^*	$CoTe_2$ H^*	H^* $NiTe_2$ T^*	$NbTe_2$ T^*	$MoTe_2$ H^{**}(1.25)	WTe_2 H^{**}(1.24)

Figure 4: Family of 2D transition metal chalcogenides. Reprinted with permission from ref 22, Copyright (2013) American Chemical Society

c. Functionalized and doped graphenes

The members of this group are quite diverse and cannot be represented by a single molecular formula. Important members of this group include hydrogenated graphene or graphane, fluorographene, graphene oxide, doped graphenes like N-doped graphene or B, N-codoped graphene or borocarbonitrides, etc. and each of these has its unique properties. Chemical functionalization and doping are interesting methods to tune the physical and chemical properties of materials. Graphane and flurographene are produced by partial to complete hydrogenation or fluorination respectively. These consist of sp^3 hybridized puckered lattice and in principle, its electronic properties are tunable between metallic to insulating and magnetic properties from non-magnetic to magnetic with the degree of reaction. These materials have been considered for a wide range of applications such as hydrogen storage, electrochemical storage, and sensing applications for graphene and large negative magnetoresistance, high optical transparency, good thermal stability, extreme hydrophobicity, and even shows the potential of being a potential cathode material with long-term stability for flurographene.[26,27] Graphene oxide (GO) is obtained by treating graphite with strong oxidizing agents like potassium permanganate, sulfuric acid, and hydrogen peroxide. In GO the previously continuous lattice of graphene is interrupted by alcohols, epoxides, carbonyls, and carboxylic acid groups and hence is highly hydrophilic. Although GO shows appreciable mechanical properties, it has low electronic conductivity, is impermeable to most gases, and is a promising material for water treatment, etc. The synthesis of GO is an important step in the large-scale synthesis of graphene.[26,28,29] Nitrogen doping of graphene is an interesting approach to tune the performance of graphene in electrocatalysis, supercapacitors, sensors, magnetic properties, and thermal stability.[30–32] Borocarbonitrides are a class of layered 2D materials wherein both boron and nitrogen are doped into the graphene lattice and contain domains corresponding to both graphene and h-BN along with B-C-N domains.[33,34] In principle, the electronic properties of this material can be tuned from metallic to insulating by changing the ratios of dopants. Borocarbonitrides will be discussed in further detail in Chapter 2.

d. Elemental 2D materials

Interest in mono-elemental layered materials has been rejuvenated with the discovery of graphene. Unlike planar graphene, most of these materials have buckled/puckered hexagonal lattices and this buckling provides enormous flexibility in tuning the material's properties and chemical reactivity. The electronic properties of this group can range from metallic behavior in group III monolayers

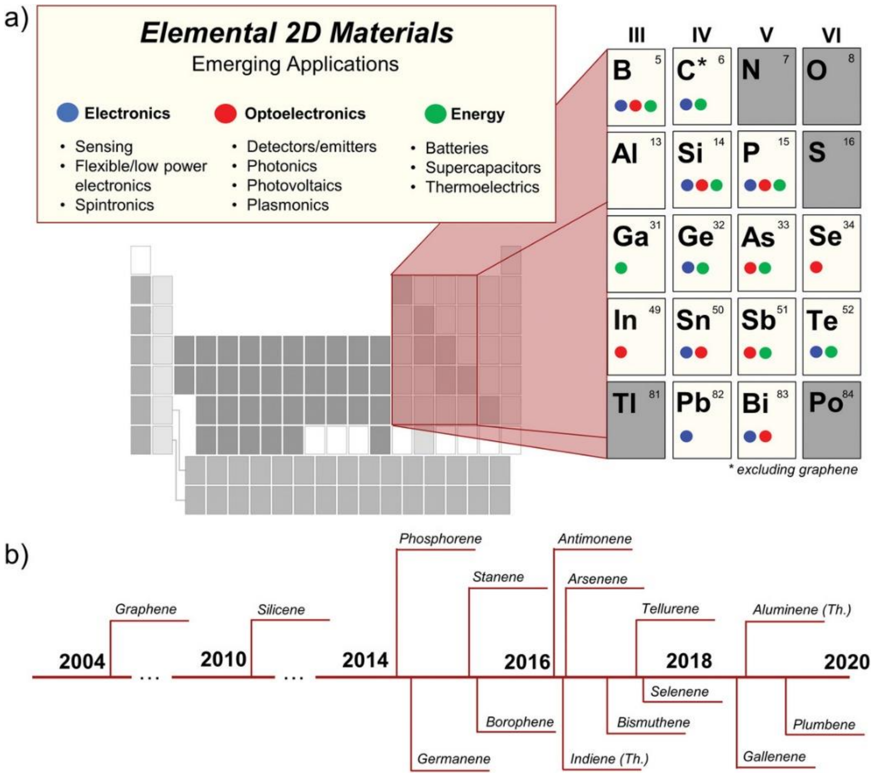

Figure 5: Family of elemental 2D materials and timeline for the synthetic discover of different materials. Reprinted with permission from ref 110, Copyright 2020 John Wiley and Sons

like borophene and heavier group IV monolayer stanene; to semi-metallic behavior in group IV graphene, silicene, and germanene; to semiconducting behavior in group V pnictogens as phosphorene, arsenene, antimonene, and bismuthene, group IV plumbene and group VI telluerene. Newer materials are getting added to this extensive list regularly.[35–37] In Chapters 5 and 6 of this thesis, elemental 2D pnictogens will be discussed in more detail.

e. Transition metal oxide (TMO)

This is a wide class of 2D materials with strong interlayer ionic bonds which introduces many dangling bonds leading to strong surface polarization. Hence structures of most TMOs are very different from their bulk counterparts along with and the strong surface polarization leads to strong instability for 2D metal oxides which gets compensated by pronounced lattice relaxation, structural reconstruction, and substrate effects. Most studied metal oxide nanosheets are d^0 transition metal oxides (Ti^{4+}, Nb^{5+}, Ta^{5+}, W^{6+} species) and these are mainly insulating or semiconducting. These materials find applications in supercapacitors, rechargeable batteries, photocatalysis, electronics, piezo electronics, superconductivity, dielectrics, etc.[38,39]

f. Metal halides

This is a diverse group of 2D crystals which cannot be represented by a general formula. Most well-studied members of this group include PbI_2, BiI_3, InI, TlBr, CrI_3, etc. which belong to many different space groups. These are generally wide bandgap semiconductors with notable absorption coefficients and are used as photodetectors, flexible photo-harvesting devices, their inherent magnetocrystalline anisotropy makes them useful for different opto-magnetic applications.[40] 2D BiI_3-based flexible visible light photodetectors, as well as large area films, have already been reported as promising applications.[41,42]

g. MXenes

MXenes are an emerging class of 2D materials made of early transition metal carbides and/or nitrides which have found applications in catalysis, sensors, chemical adsorption, energy storage, reinforcement for composites, lubricants, water desalination, etc. These compounds are generally denoted by formulae as M_2X, M_3X_2, M_4X_3, and the newly reported M_5C_4 where M is an early transition metal and X is carbon/nitrogen. These materials are synthesized by selective etching of MAX phases.[43,44] MXene family provides 2D sheets with metallic-like conductivity with fermi-levels tunable by external stimuli, high strength, and

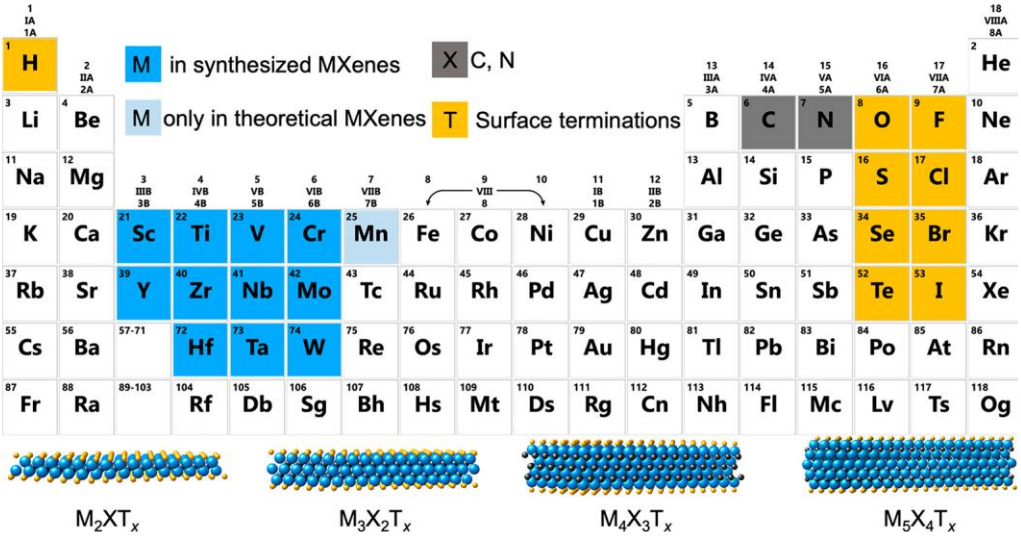

Figure 6: MXene family of 2D materials Reprinted with permission from ref 45, Copyright (2021) American Chemical Society

stiffness, scalable synthesis, high Seebeck coefficients along with biocompatibility.[45]

h. Metal phosphochalcogenides (MPX_3)

Mono and bi-elemental metal phosphochalcogenides constitute a large family of layered materials which are semiconducting and are being used for a variety of applications. In MPX_3, M is a transition metal while X is a chalcogenide S/Se/Te and this class of materials displays many interesting properties such as anisotropy, magnetic and anti-ferromagnetic properties. Moreover, these are wide-bandgap materials and are being considered suitable for optoelectronics, photo, and electrocatalysis, etc.[46] MPX_3 will be discussed in greater detail in Chapter 4.

i. 2D Clays and minerals

In recent years, a new class of 2D materials obtained from delamination of different layered clays and minerals has gained importance. Some commonly studied delaminated minerals include cationic clays like montmorillonite, vermiculite, and anionic clays like hydrotalcite. These are widely available robust materials with many interesting properties.[47,48] 2D clays are known to have outstanding charge storage ability, which results in a large contact area between the electrodes and electrolytes and shorter ion-transport pathways.[49] These are naturally available porous low-cost materials which have already been identified for their high cation exchange capacities and have been used as cathode materials for Li-S batteries.[50]

j. 2D Metals

2D metal nanosheets exhibit unique physical and chemical properties compared to their bulk counterparts owing to the high surface-to-volume ratio. Some important improvements of this group include Au nanosheets have found applications in next-generation transparent and conducting electrodes; Rh nanosheets display excellent catalytic properties; Cd nanosheets display excellent light-trapping effects.[51–53]

k. 2D metal-organic framework (MOF) and covalent organic framework (COF)

These are a new class of 2D materials with a lot of potential that uses the concepts of reticular chemistry for the synthesis of highly porous materials.[54] These 2D

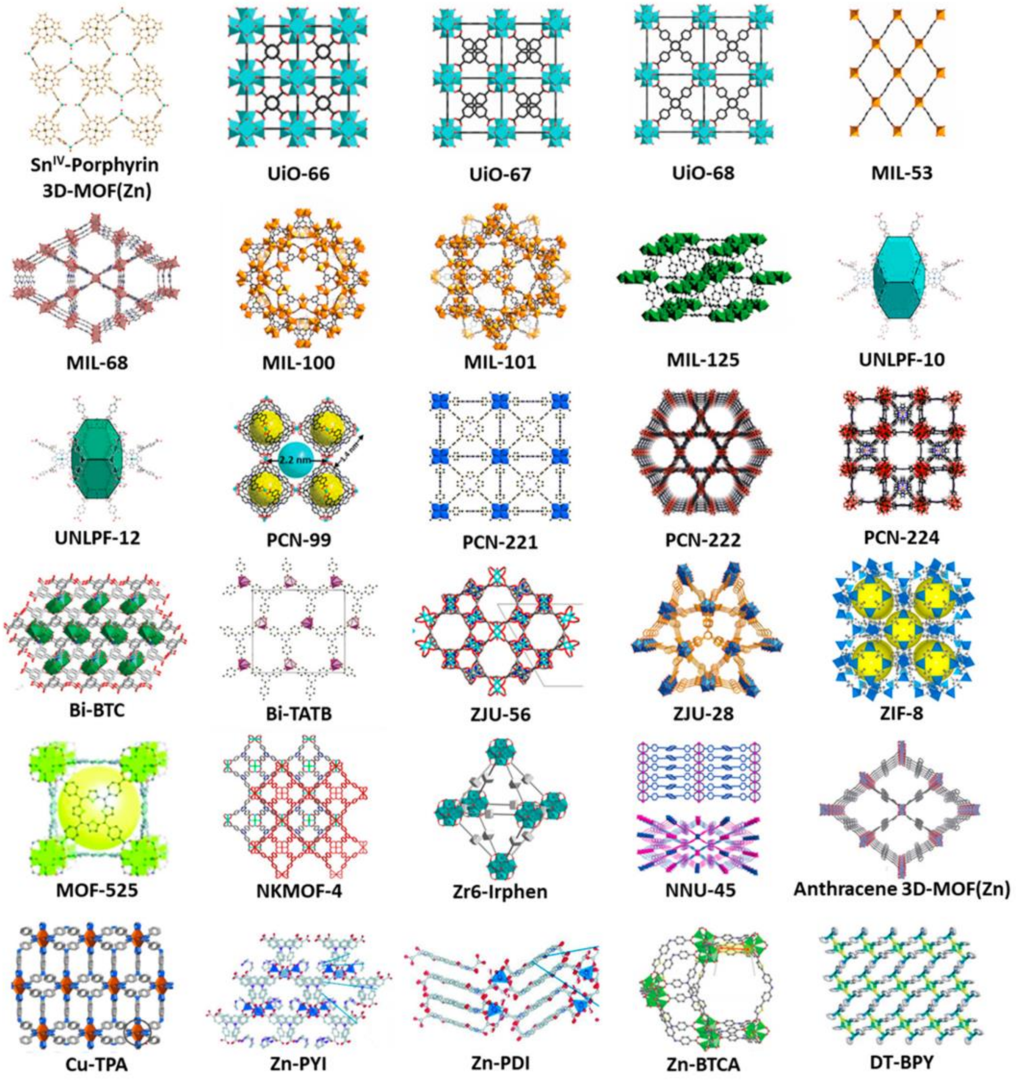

Figure 7: Structural motifs of different classes of MOFs Reprinted with permission from ref 57, Copyright (2020) MDPI

molecular crystals are synthetically designed and subsequently tuned for a multitude of applications. Highly porous by nature and structurally flexible, MOFs/COFs have a high surface area, heightened guest capture, sensing, optoelectronics, water harvesting, and catalytic performance.[55–58] At present there are multiple commercial successes of MOFs as well including the development of MOF based natural gas storage systems, or gas storage systems (ION-X) for the storage and delivery of hazardous gases used in the electronics industry (as arsine, phosphine).[54]

l. 2D perovskites

2D perovskites may be in general considered miniature versions of their 3D counterparts with chemical diversity and interesting properties. This material class may be represented by the general chemical formula $A'_mA_{n-1}B_nX_{3n+1}$, where B is a divalent cation generally Pb^{2+} or Sn^{2+}, A' can be a monovalent ($m = 2$) or divalent ($m = 1$) cation that intercalates between the inorganic layers of $[PbX_6]^{4-}$ octahedra and n defines the number of inorganic layers between layers of A'. When a monovalent A' cation is used, the 2D perovskite is referred to as the Ruddlesden-Popper (RP) phase, while those formed with divalent ($m = 1$) A' cations are referred to as Dion–Jacobson (DJ)- 2D perovskites. In the last few years 2D perovskites have come out to be promising alternatives to their 3D counterparts as solar cell absorbers with their appreciable power conversion efficiencies (18.20%) along with stability towards humidity and light, improved processibility, durability, and high chemical versatility.[59,60]

m. Other carbon-based materials

In recent years, 2D carbon materials other than graphene has also come into prominence. Graphitic carbon nitride ($g-C_3N_4$) is a conjugated polymer that is one of the oldest known artificial polymers in scientific literature. g-C_3N_4 shows exceptional thermal and chemical stability along with appropriate bandgaps for catalysis and optoelectronic applications.[55] With the discovery of graphene, in recent years studies have been directed towards other classes of artificial carbon allotropes like graphynes, diamondynes, etc. Graphynes are a class of layered carbon allotropes with both sp^2 and sp hybridized atoms, with inherent band gaps and electronic properties to be in the range of graphene, which was first theoretically predicted in 1987 and was chemically synthesized only recently.[61] Graphynes will be discussed in more detail in Chapter 3.

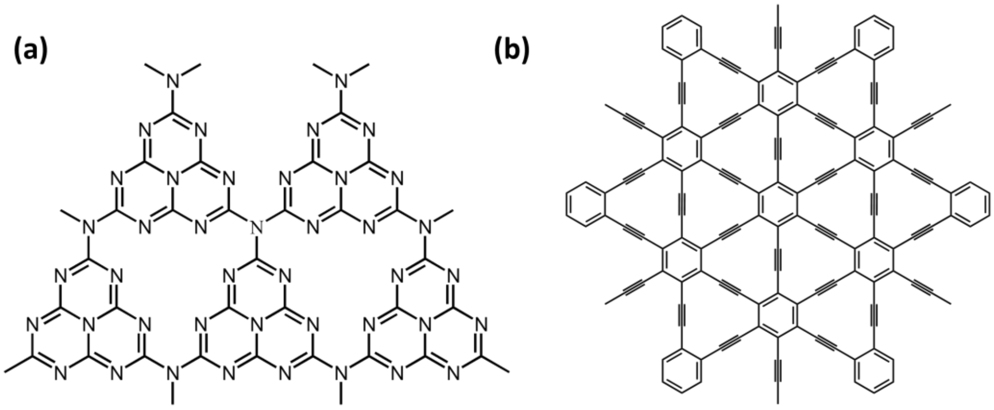

Figure 8: Layered structures of polymeric (a) g-C_3N_4 and (b) γ-graphyne

This list of 2D materials is in no way extensive. Only some of the most studied groups have been included.

1.4 Synthesis of 2D materials

One of the major roadblocks in large-scale applications of 2D materials is the mass production of defect-free nanosheets. Although quite many approaches and synthesis techniques have been developed over the years, each of these has its own merits and demerits. Some commonly used synthesis methods are discussed here:

1.4.1 Top-down approaches – This approach generally involves the controlled synthesis of nanosheets from a 3D bulk. Generally, the bulk material is inherently layered in nature, or some bulk layered counterparts are synthesized from it prior to exfoliation.

a. **Mechanical exfoliation:** This is a top-down method that involves exfoliation of single and few-layered crystals from bulk crystals leading to very crystalline samples ideal for micrometer-scale electronic and optical devices. However, it is a labor-intensive technique with a poor yield and limited to materials with bulk layered allotrope.[35] The discovery of graphene in 2004 involved the synthesis of graphene flakes by this method.[14,62]

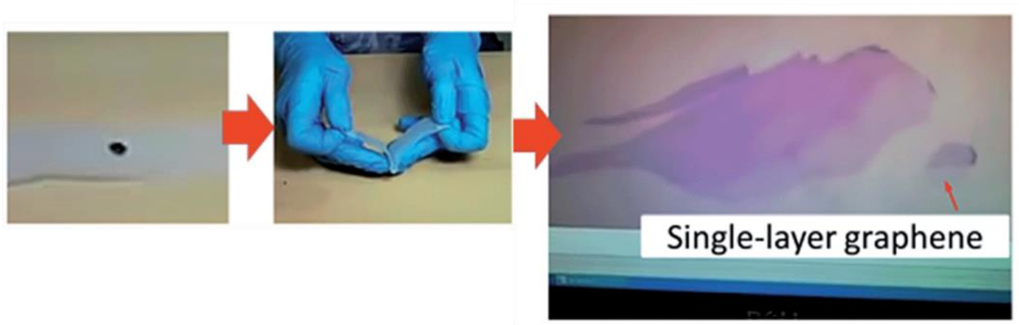

Figure 9: Mechanical exfoliation of graphene. Adapted with permission from Royal Society of Chemistry, ref 62; permission conveyed through Copyright Clearance Center, Inc.

b. **Intercalation:** Layered intercalation compounds were known since the 19th century, and scientists have been trying to make 2D materials from these materials for a long time. This method has been recently used in the exfoliation of large classes of layered materials including graphite, TMDs, TMOs, MXenes.

Intercalation involves the insertion of foreign substances (ions, molecules) into host materials leading to a change in materials properties like carrier concentration, magnetic properties, superconductivity, and phase transitions. Intercalation exfoliation requires that the starting material is layered with weak van der Waals interactions between layers and there is a possibility of side reactions or oxidation.[63]

c. **Liquid exfoliation:** Liquid exfoliation is slowly being considered one of the most used methods for the synthesis of 2D materials. This method involves dispersing the bulk material in a solvent and then treating it with ultrasonication/probe sonication. Ultrasonic waves generate cavitation bubbles in the solvent which coalesce and collapse into high-energy jets producing exfoliated nanosheets. The solvent used for exfoliation plays a crucial role in this synthesis method, and ideal liquid exfoliation conditions are when the surface energy of the solvent is like that

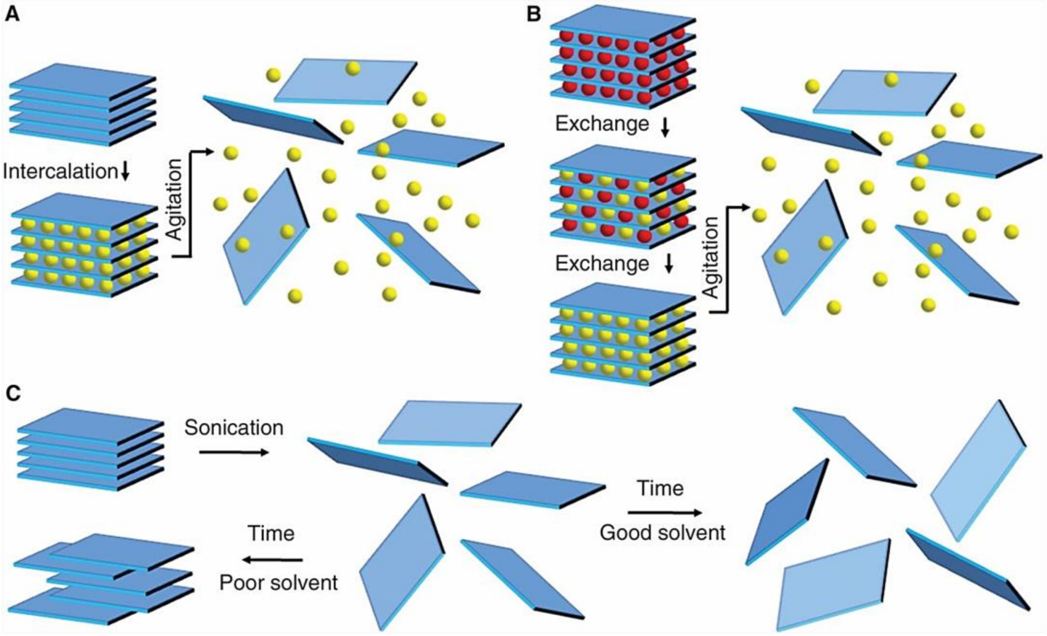

Figure 10: Schematic representation of A. Intercalation based exfoliation, B. Ion-exchange based exfoliation, and C. Liquid exfoliation of materials in solvents. From ref 65, Reprinted with permission from AAAS

of the layered material so that the energy difference between the exfoliated and reaggregated states will be small. Liquid exfoliation is a scalable method for the synthesis of large quantities of 2D materials. For many materials, these dispersions were shown to be stable for months. However, the nanosheets synthesized by this method are not as pristine or defect-free as mechanical exfoliation, and removal of the solvent is difficult.[64,65] In this thesis, in Chapters 3 and 4 we use ultrasonication, and Chapters 5 and 6 we use probe sonication for the synthesis of different 2D materials.

d. **Thermal exfoliation:** Thermal exfoliation of layered materials involves providing a thermal shock to the material. It is a very fast process taking from a few seconds to minutes involves both exfoliation and reduction without the introduction of any foreign species and even avoids problems associated with reaggregation involving removal of intercalants/ solvents from the exfoliated materials. However, even if this method allows the scaled-up synthesis of 2D nanosheets, it also introduces defects in the lattice.[66] Chapter 2 involves thermal exfoliation of graphene oxide at 1050°C. During the synthesis, GO powder was given a thermal shock for a few seconds, which led to the removal of functional groups from the lattice which weakened the van der Waals interactions between the layers and exfoliated graphene was obtained.

e. **Electrochemical exfoliation:** It is also an important method for mass production of nanosheets owing to its mild operational conditions. This process involves the application of a fixed potential that can drive ionic species in solution to intercalate in between layers, weakening the intermolecular forces and leading to exfoliation.

The choice of solvent and electrolyte plays a crucial role in the efficiency of exfoliation and the quality and properties of the exfoliated materials. This method is applicable for only conducting and semiconducting materials that are stable under ambient conditions and can sustain strong anodic and cathodic conditions without significant chemical side reactions.[67]

1.4.2 Bottom-up approaches

Bottom-up approaches - This method involves the build-up of material from the bottom by using atomic or molecular precursors that react and grow in the side and self-assemble into complex structures.

a. **Solvothermal synthesis:** Hydrothermal or solvothermal synthesis is a simple solution-based bottom-up synthesis method involving high temperature and pressure. It is a low-cost, easy operation method for bulk state synthesis.[68]

b. **Physical vapor deposition (PVD) and Chemical vapor deposition (CVD):** These methods provide a scalable and controllable way to grow high-quality and large-area 2D materials with reasonable cost. PVD uses a heated atomic source to deposit a material on a substrate in a controlled manner under ultra-high vacuum conditions using high purity atomic sources. CVD utilizes the decomposition of solid, liquid, and gaseous precursors under UHV in a controlled manner to grow 2D materials. The properties of the materials are highly dependent on the substrate used. The

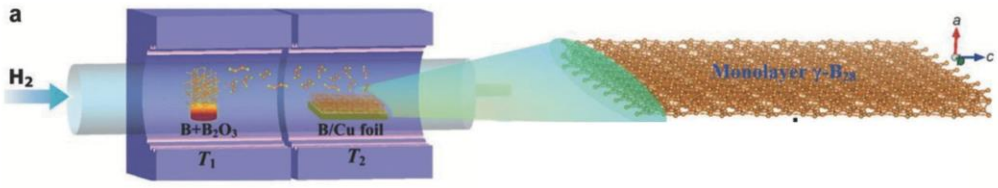

Figure 11: Schematic representation of CVD growth of 2D materials. Adapted with permission from ref 70, Copyright 2018 John Wiley and Sons

number of layers, lateral dimension, morphology, orientation, and introduction of dopants and defects can be controlled by playing with the growth parameters such as temperature, carrier gas flow rate, chamber pressure, relative ratios of source materials, and source-substrate distance.[69,70]

c. **Epitaxial growth:** This is also a CVD-based growth technique involving ultra-high vacuum conditions which lead to clean 2D material surfaces. These 2D films are grown on single-crystalline substrates wherein millions of growth nuclei of similar orientation expand their sizes simultaneously to produce a large continuous film without grain boundaries. Despite ultra-high vacuum conditions and sophisticated instrumentation, epitaxial growth is regarded as one of the most promising techniques for the large-scale production of highly crystalline 2D materials.[71,72]

1.5 Charge transfer studies

One underlying motivation of this thesis is to study different aspects of charge transfer interactions in different classes of 2D materials. Charge transfer is a ubiquitous process which is prevalent in biological, physical, and chemical systems and understanding its underlying mechanism comprises a broad active area of research. In nature, charge transfer is actively used in the transduction of energy e.g., in the photosynthetic reaction center, charge transfer is used to induce charge imbalance across the membrane, which eventually leads to the formation of adenosine triphosphate (ATP) which is known as the energy currency of the cell. From simplest of observations as rusting of iron to bond breaking/formation in organic chemistry, everything comes under the umbrella of charge transfer.[73]

The theoretical framework for charge-transfer was provided by Marcus et al[74] in 1950s and has since been modified to include further considerations. Successful charge transfer between a donor and an acceptor species depends on several factors including band alignment, solvent polarization and reorganization, the distance between the two interacting species and their orbital overlaps, different relaxation processes, kinetics and dynamics, conformational or geometric changes, vibrational and polarization changes, temperature, etc. and hence is a very complicated process. Different techniques have been used to understand different aspects of charge transfer including Raman spectroscopy, UV-visible absorption studies, emission studies, extended X-ray absorption fine structure (EXAFS), transient photo absorption spectroscopy, etc.[73,75]

1.5.1 Charge transfer studies in 2D materials

The silicon-based semiconductor industry is heavily dependent on the doping of semiconductors for modulating charge carrier type and concentrations. The atomically thin 2D class of materials has the potential to overcome many major bottlenecks of Si-based industry e.g., the scaling limit due to the short channel effect. This has in turn encouraged the exploration of different classes of 2D materials. In order to explore 2D materials for different applications, it is of utmost importance to have precise control of their carrier type and concentration. The atomic-level thickness in 2D materials conveys it many unconventional properties. As these materials are thinner than the typical Coulomb interaction lengths, a significant part of the electric field between the charge carriers leaks into the surroundings, which in turn reduces the dielectric screening of these materials and enhanced charge carrier interactions. This poor screening effect helps in easily tuning the properties of these materials compared to bulk.[76–83]

The traditionally explored doping methods as ion implantation and thermal diffusion are not suitable for this atomically thin class of materials, and the most commonly used methods for tailoring the properties of 2D materials include substitutional doping, electrostatic doping, covalent functionalization, and surface charge transfer doping (SCTD)[84]. Although, substitutional doping is a very robust method for tuning a materials property by incorporation of heteroatoms into the lattice, there are chances of significant defect formation with loss of intrinsic properties. Electrostatic doping is an effective doping scheme for 2D materials wherein an external electrostatic field is used to tune the properties, however this method requires sophisticated device fabrication and limits its practical applications. Covalent functionalization is an important method to tune the properties of 2D materials. Due to strong orbital overlap, the products are expected to be stable during various device fabrication stages. This method generally involves rehybridization of atoms in the basal plane of the 2D material leading to formation of defects and/or distortion of the lattice along with disruption of the potential continuum and covalent functionalization with different reactive species like diazonium salts or Grignard reagents leads to formation of insulating layers on the surface. However, the adducts formed by covalent functionalization are generally more robust and thermally stable compared to surface charge transfer doping adducts.[85]

In recent years, surface charge transfer doping (SCTD) is emerging as a facile and effective doping technique for 2D materials wherein interfacial charge transfer between the dopant and the 2D material becomes crucial due to the high surface to volume ratio in 2D materials. At present, different varieties of materials are extensively used for carrying out charge transfer doping in 2D materials including (a) organic molecules (perylene diimides, terathiafulvalene (TTF), tetracyanoquinodimethane (TCNQ)), metals (Li^+, Na^+, K^+), metal oxides (MoO_3, MgO) and gas molecules (NO_2, O_2, SO_2). Surface charge transfer doping (SCTD) allows modulation of fundamental properties of 2D materials like carrier type and concentration, transport properties, bandgap, phase engineering, carrier mobility, emission properties, etc. which helps in optimizing their device performance. There are many successful examples of surface charge transfer studies in 2D material e.g., it has been reported that in WSe_2 FETs, doping of K^+ onto the source and drain contacts improves the conductivity by 5 orders of magnitude and significantly improves the electron mobility[86] while co-doping of WSe_2 FETs by K^+ and NO_2, has been reported to improve the ON/OFF current by 3 orders.[87]

Charge transfer studies in 2D materials is an emerging area of research that is still in the exploration stage. Although different mechanisms have been proposed based on band alignment and interfacial charge transfer, the nature of the interaction between the dopant and the 2D material is still not very clear. Moreover, chemical reaction or orbital hybridization at the interface can lead to many unexpected effects as charge trapping or localization, defect formation, inhibiting the desired charge transfer.[84]

It is crucial to extensively explore the charge transfer behavior of different 2D materials with different types of donor/acceptors to form chemically and thermally stable adducts for practical device applications. Moreover, the effect of such donor/acceptor on other physical properties of the 2D material like magnetic or thermoelectric also needs to be explored.

1.6 Conclusions

Two-dimensional materials are an interesting family of materials that have found applications in different fields starting from electronic and optoelectronic applications in FET devices, logic circuits, memory devices, photodetectors, light emitters, dielectrics, flexible devices, tunneling devices, valley, and spin electronics.[88–91] 2D materials have also come into a lot of prominences as photo or electrocatalysts for hydrogen evolution reaction,[88–90,92,93] CO_2 reduction,[94–97] O_2 reduction,[98,99] N_2 reduction,[100] and chemical and gas sensing applications.[92,93,101–103] 2D magnets are also known to show interesting magnetic properties with tunability compared to bulk like superconductivity, ferromagnets, antiferromagnets, magneto-optical properties, etc.[104,105] Moreover, there is also interest in the use of these materials for biomedical applications.[106] All these interesting properties and applications also brought in the possibility of harnessing the properties of more than one type of 2D material by forming heterostructures, this led to an exciting new research field called van der Waals heterostructures.[107–109] The availability of a wide library of 2D materials with variable electronic/ optical/ magnetic properties and the ability to restack them into heterostructures opens up a new dimension for materials engineering and design. The dangling bond-free surfaces ensure excellent electronic /optical/magnetic properties and the van der Waals interaction ensures flexibility in terms of integrating highly disparate materials without the traditional constraints of lattice mismatch and other incompatibilities. This empowers the design of a new generation of devices with extraordinary performance and unique functionality. In conclusion, 2D materials have brought in a revolution in material science given its short history of 18 years and still has a long way to go.

References

(1) Toumey, C. *Nat. Nanotechnol.*, **2009**, *4*(12), 783–784.

(2) Miró, P.; Audiffred, M.; Heine, T. *Chem.Soc. Rev*., **2014**, *43*(18), 6537–6554.

(3) Novoselov, K. S.; Geim, A. K.; Morozov, S. v; Jiang, D.; Zhang, Y.; Dubonos, S. v; Grigorieva, I. v; Firsov, A. A. *Phys. Rev. Lett.*, **2000**; *404,* 3824

(4) Geim, A. K.; Novoselov, K. S. *Nat. Mater*., **2007**, *6*, 183-191

(5) Meyer, J. C.; Geim, A. K.; Katsnelson, M. I.; Novoselov, K. S.; Booth, T. J.; Roth, S. *Nature*, **2007**, *446* (7131), 60–63.

(6) Katsnelson, M. I. *Mater. Today*, **2007**, *10*, 20–27.

(7) Mermint, N. D. *Phys. Rev. B.*, **1979,** *20*, 4762

(8) Peierls, R., *Annals. Henri Poincare.*, **1935**, 5(3), 177-222

(9) Castro Neto, A. H.; Guinea, F.; Peres, N. M. R.; Novoselov, K. S.; Geim, A. K., *Rev. Mod. Phys.* **2009**, *81* (1), 109–162.

(10) Rao, C. N. R.; Biswas, K.; Subrahmanyam, K. S.; Govindaraj, A. *J. Mater. Chem.*, **2009**, *19* (17), 2457–2469.

(11) Liu, Y.; Weiss, N. O.; Duan, X.; Cheng, H. C.; Huang, Y.; Duan, X., *Nat. Rev. Mater*., **2016**. *1*(9), 16042

(12) Butler, S. Z.; Hollen, S. M.; Cao, L.; Cui, Y.; Gupta, J. A.; Gutiérrez, H. R.; Heinz, T. F.; Hong, S. S.; Huang, J.; Ismach, A. F.; Johnston-Halperin, E.; Kuno, M.; Plashnitsa, V. v.; Robinson, R. D.; Ruoff, R. S.; Salahuddin, S.; Shan, J.; Shi, L.; Spencer, M. G.; Terrones, M.; Windl, W.; Goldberger, J. E. , *ACS Nano*., **2013**, *7*(4), 2898–2926.

(13) Zhang H., *Chem. Rev.*, **2018**, *118* (13), 6089–6090

(14) Novoselov, K. S.; Jiang, D.; Schedin, F.; Booth, T. J.; Khotkevich, V. v; Morozov, S. v; Geim, A. K.; *Proc. Natl. Acad. Sci.* , **2005**. *102* (30), 10451-10453

(15) Golberg, D.; Bando, Y.; Huang, Y.; Terao, T.; Mitome, M.; Tang, C.; Zhi, C; *ACS Nano*., **2010**, *4*(6), 2979–2993.

(16) Ghosh, J.; Mazumdar, S.; Das, M.; Ghatak, S.; Basu, A. K., *Mater. Res. Bull.* **2008**, *43* (4), 1023–1031.

(17) Wang, J.; Ma, F.; Liang, W.; Sun, M., *Mater. Today Phys*., **2017**, *2*, 6–34.

(18) Topsakal, M.; Aktürk, E.; Ciraci, S., *Phys. Rev. B Phys.*, **2009**, *79* (11), 115442.

(19) Shi, Z.; Wang, X.; Li, Q.; Yang, P.; Lu, G.; Jiang, R.; Wang, H.; Zhang, C.; Cong, C.; Liu, Z.; Wu, T.; Wang, H.; Yu, Q.; Xie, X., *Nat. Comm.*, **2020**, *11* (1), 849.

(20) Dean, C. R.; Young, A. F.; Meric, I.; Lee, C.; Wang, L.; Sorgenfrei, S.; Watanabe, K.; Taniguchi, T.; Kim, P.; Shepard, K. L.; Hone, J., *Nat. Nanotechnol.*, **2010**, *5* (10), 722–726.

(21) Chhowalla, M.; Shin, H. S.; Eda, G.; Li, L. J.; Loh, K. P.; Zhang, H., *Nat. Chem.*, **2013**, *5*, 263–275.

(22) Xu, M.; Liang, T.; Shi, M.; Chen, H., *Chem. Rev*., **2013**, *113* (5), 3766–3798.

(23) Chhowalla, M.; Liu, Z.; Zhang, H., *Chem. Soc. Rev.*, **2015**, *44,* 2584–2586.

(24) Wilson, J. A.; Yoffe, A. D., *Adv. Phys.*, **1969**, *18* (73), 193–335.

(25) Chou, S. S.; Sai, N.; Lu, P.; Coker, E. N.; Liu, S.; Artyushkova, K.; Luk, T. S.; Kaehr, B.; Brinker, C. J., *Nat. Comm.*, **2015**, *6*, 8311

(26) Inagaki, M.; Kang, F., *J. Mater. Chem. A,* **2014**, *2* (33), 13193–13206.

(27) Pumera, M.; Sofer, Z, *Chem. Soc. Rev*., **2017**, 4450–4463.

(28) Smith, A. T.; LaChance, A. M.; Zeng, S.; Liu, B.; Sun, L., *Nano Mater. Sci.*, **2019**, *1* (1), 31–47.

(29) Brisebois, P. P.; Siaj, M., *J. Mater. Chem. C*., **2020**, *8*, 1517–1547.

(30) Wang, H.; Maiyalagan, T.; Wang, X., *ACS Catal*., **2012**, *2* (5), 781–794.

(31) Sandoval, S.; Kumar, N.; Oro-Solé, J.; Sundaresan, A.; Rao, C. N. R.; Fuertes, A.; Tobias, G., *Carbon,* **2016**, *96*, 594–602.

(32) Sandoval, S.; Kumar, N.; Sundaresan, A.; Rao, C. N. R.; Fuertes, A.; Tobias, G., *Chem. Eur. J.,* **2014**, *20* (38), 11999–12003.

(33) Kumar, N.; Moses, K.; Pramoda, K.; Shirodkar, S. N.; Mishra, A. K.; Waghmare, U. v.; Sundaresan, A.; Rao, C. N. R., *J. Mater. Chem. A,* **2013**, *1* (19), 5806–5821.

(34) Barua, M.; Sreedhara, M. B.; Pramoda, K.; Rao, C. N. R., *Chem. Phys. Lett.*, **2017**, *683*, 459–466.

(35) Mannix, A. J.; Kiraly, B.; Hersam, M. C.; Guisinger, N. P., *Nat. Rev. Chem*., **2017**. *1*, 0014

(36) Glavin, N. R.; Rao, R.; Varshney, V.; Bianco, E.; Apte, A.; Roy, A.; Ringe, E.; Ajayan, P. M., *Adv.Mater*.,**2020**. *32* (7), 1904302

(37) Vishnoi, P.; Pramoda, K.; Rao, C. N. R., *ChemNanoMat*., **2019**, *5* (9), 1062–1091.

(38) Yang, T.; Song, T. T.; Callsen, M.; Zhou, J.; Chai, J. W.; Feng, Y. P.; Wang, S. J.; Yang, M., *Adv. Mater. Interfaces*, **2019**, *6* (1), 1801160

(39) Osada, M.; Sasaki, T., *Adv. Mater.*, **2012**, *24* (2), 210–228.

(40) Aji Suleiman, A.; Zhou, X.; Zhai, T., *J. Phys. D Appl. Phys*., **2020**. *54*(1), 013002

(41) Wei, Q.; Chen, J.; Ding, P.; Shen, B.; Yin, J.; Xu, F.; Xia, Y.; Liu, Z., *ACS Appl. Mater. Interfaces*, **2018**, *10* (25), 21527–21533.

(42) Wei, Q.; Wang, Y.; Yin, J.; Xia, Y.; Liu, Z., *Adv. Electron. Mater.*, **2019**, *5* (7), 1900159

(43) Anasori, B.; Lukatskaya, M. R.; Gogotsi, Y., *Nat. Rev. Mater*., **2017**. *2*(2), 16098

(44) Zhu, J.; Ha, E.; Zhao, G.; Zhou, Y.; Huang, D.; Yue, G.; Hu, L.; Sun, N.; Wang, Y.; Lee, L. Y. S.; Xu, C.; Wong, K. Y.; Astruc, D.; Zhao, P., *Coord. Chem. Rev*., **2017**, 306–327.

(45) Gogotsi, Y.; Huang, Q., *ACS Nano*, **2021**, *15* (4), 5775–5780.

(46) Brec, R; *Solid State Ion.*, **1986**, *22*, 3-30

(47) Chalasani, R.; Gupta, A.; Vasudevan, S., *Sci. Rep.*, **2013**, *3*, 3498

(48) Gogoi, R. K.; Raidongia, K., *Adv. Mater.*, **2017**, *29* (24), 1701164

(49) Lan, Y.; Liu, Y.; Li, J.; Chen, D.; He, G.; Parkin, I. P., *Adv. Sci*., **2021**, *8*(11), 2004036

(50) Wu, F.; Lv, H.; Chen, S.; Lorger, S.; Srot, V.; Oschatz, M.; van Aken, P. A.; Wu, X.; Maier, J.; Yu, Y., *Adv. Funct. Mater.*, **2019**, *29* (27), 1902820

(51) Chen, Y.; Fan, Z.; Zhang, Z.; Niu, W.; Li, C.; Yang, N.; Chen, B.; Zhang, H., *Chem. Rev*., **2018**, *118* (13), 6409–6455.

(52) Ling, T.; Wang, J. J.; Zhang, H.; Song, S. T.; Zhou, Y. Z.; Zhao, J.; Du, X. W., *Adv. Mater.*, **2015**, *27* (36), 5396–5402.

(53) Zeb Gul Sial, M. A.; Ud Din, M. A.; Wang, X., *Chem. Soc. Rev*., **2018**, *47*, 6175–6200.

(54) Freund, R.; Zaremba, O.; Arnauts, G.; Ameloot, R.; Skorupskii, G.; Dincă, M.; Bavykina, A.; Gascon, J.; Ejsmont, A.; Goscianska, J.; Kalmutzki, M.; Lächelt, U.; Ploetz, E.; Diercks, C. S.; Wuttke, S., *Angew. Chem.*, **2021**, *60* (45), 23975–24001.

(55) Zhao, M.; Huang, Y.; Peng, Y.; Huang, Z.; Ma, Q.; Zhang, H., *Chem. Soc. Rev*., **2018**, *47*, 6267–6295.

(56) Solomos, M. A.; Claire, F. J.; Kempa, T. J., *J. Mater. Chem. A.*, **2019**, *7*, 23537–23562.

(57) Lopez-Magano, A.; Jiménez-Almarza, A.; Aleman, J.; Mas-Ballesté, R., *Catalysts*, **2020**, *10* (7), 720

(58) Xu, W.; Yaghi, O. M. *ACS Cent. Sci.*, **2020**, *6* (8), 1348–1354.

(59) Zhao, X.; Liu, T.; Loo, Y. L., *Adv. Mater*., **2022**. *34* (3), 2105849

(60) Ortiz-Cervantes, C.; Carmona-Monroy, P.; Solis-Ibarra, D., *ChemSusChem*.**, 2019**, *12* (8), 1560–1575.

(61) Baughman, R. H.; Eckhardt, H.; Kertesz, M., *J. Chem. Phys.*, **1987**, *87* (11), 6687–6699.

(62) Yi, M.; Shen, Z., *J. Mater. Chem. A*., **2015**, *3*, 11700–11715.

(63) Cai, X.; Luo, Y.; Liu, B.; Cheng, H. M., *Chem. Soc. Rev*., **2018**, *47*, 6224–6266.

(64) Tsai, H. S.; Liang, J. H., *ChemNanoMat*., **2017**, *3* (9), 604–613.

(65) Nicolosi, V.; Chhowalla, M.; Kanatzidis, M. G.; Strano, M. S.; Coleman, J. N., *Science*., **2013**. *340*, 6139

(66) Zhang, C.; Lv, W.; Xie, X.; Tang, D.; Liu, C.; Yang, Q. H., *Carbon*., **2013**, *62*, 11–24.

(67) Ambrosi, A.; Pumera, M., *Chem Soc Rev*., **2018**, *47* (19), 7213–7224.

(68) Lai, J.; Niu, W.; Luque, R.; Xu, G., *Nano Today*., **2015**, *10* (2), 240–267.

(69) Cai, Z.; Liu, B.; Zou, X.; Cheng, H. M., *Chem. Rev*., **2018**, *118* (12), 6091–6133.

(70) Geng, D.; Yang, H. Y., *Adv. Mater*. **2018.** *30* (45), 1800865

(71) Zhang, Z.; Yang, X.; Liu, K.; Wang, R, *Adv. Sci.* **2022**, *9* (8), 2105201.

(72) Li, G.; Zhang, Y. Y.; Guo, H.; Huang, L.; Lu, H.; Lin, X.; Wang, Y. L.; Du, S.; Gao, H. J., *Chem. Soc. Rev*., **2018**, *47*, 6073–6100.

(73) Barbara, P. F.; Meyer, T. J.; Ratner, M. A., *J. Phys. Chem.* **1996**, *100* (31) 13148–13168

(74) Marcus, R. A., *J. Chem. Phys*,. **1956**, *24* (5), 966–978.

(75) Zahn, D. R. T.; Gavrila, G. N.; Gorgoi, M., *Phys.*, **2006**, *325* (1), 99–112.

(76) Wang, J.; Ding, T.; Gao, K.; Wang, L.; Zhou, P.; Wu, K., *Nat. Commun.*, **2021**, *12* (1), 6333.

(77) Raja, A.; Chaves, A.; Yu, J.; Arefe, G.; Hill, H. M.; Rigosi, A. F.; Berkelbach, T. C.; Nagler, P.; Schüller, C.; Korn, T.; Nuckolls, C.; Hone, J.; Brus, L. E.; Heinz, T. F.; Reichman, D. R.; Chernikov, A., *Nat. Commun.*, **2017**, *8*, 15251.

(78) Ceballos, F.; Cui, Q.; Bellus, M. Z.; Zhao, H., *Nanoscale,* **2016**, *8* (22), 11681–11688.

(79) You, Y.; Zhang, X. X.; Berkelbach, T. C.; Hybertsen, M. S.; Reichman, D. R.; Heinz, T. F., *Nat. Phys.*, **2015**, *11* (6), 477–481.

(80) Hao, K.; Specht, J. F.; Nagler, P.; Xu, L.; Tran, K.; Singh, A.; Dass, C. K.; Schüller, C.; Korn, T.; Richter, M.; Knorr, A.; Li, X.; Moody, G., *Nat. Commun.*, **2017**, *8*, 15552.

(81) Chernikov, A.; Berkelbach, T. C.; Hill, H. M.; Rigosi, A.; Li, Y.; Aslan, O. B.; Reichman, D. R.; Hybertsen, M. S.; Heinz, T. F., *Phys. Rev. Lett.*, **2014**, *113* (7), 076802.

(82) Mak, K. F.; He, K.; Lee, C.; Lee, G. H.; Hone, J.; Heinz, T. F.; Shan, J, *Nat. Mater.*, **2013**, *12* (3), 207–211

(83) He, K.; Kumar, N.; Zhao, L.; Wang, Z.; Mak, K. F.; Zhao, H.; Shan, J., *Phys. Rev. Lett.* **2014**, *113* (2), 026803.

(84) Wang, Y.; Zheng, Y.; Han, C.; Chen, W., *Nano Res*. **2021**, *14*, 1682–1697.

(85) Sreeprasad, T. S.; Berry, V., *Small*. **2013**, *9* (3), 341–350.

(86) Fang, H.; Chuang, S.; Chang, T. C.; Takei, K.; Takahashi, T.; Javey, A., *Nano Lett.*, **2012**, *12* (7), 3788–3792.

(87) Fang, H.; Tosun, M.; Seol, G.; Chang, T. C.; Takei, K.; Guo, J.; Javey, A., *Nano Lett.* **2013**, *13* (5), 1991–1995.

(88) Kang, S.; Lee, D.; Kim, J.; Capasso, A.; Kang, H. S.; Park, J. W.; Lee, C. H.; Lee, G. H., *2D Mater.* **2020**. *7* (2), 022003.

(89) Liu, Y.; Duan, X.; Huang, Y.; Duan, X., *Chem. Soc. Rev*. **2018**, *47*, 6388–6409.

(90) Wang, Z.; Jingjing, Q.; Wang, X.; Zhang, Z.; Chen, Y.; Huang, X.; Huang, W., *Chem. Soc. Rev*. **2018**, *47*, 6128–6174.

(91) Wang, Q. H.; Kalantar-Zadeh, K.; Kis, A.; Coleman, J. N.; Strano, M. S., *Nat. Nanotechnol*. **2012**, *7*, 699–712.

(92) Sun, Y.; Gao, S.; Lei, F.; Xie, Y., *Chem. Soc. Rev*. **2015**, *44*, 623–636.

(93) Luo, B.; Liu, G.; Wang, L., *Nanoscale*. **2016**, *8*, 6904–6920.

(94) Sun, Z.; Ma, T.; Tao, H.; Fan, Q.; Han, B., *Chem*. **2017**, *3* (4), 560–587.

(95) Ayyub, M. M.; Rao, C. N. R., *Mater. Horiz*. **2021**, *8*, 2420–2443.

(96) Liu, J.; Guo, C.; Vasileff, A.; Qiao, S., *Small Methods*. **2017**. *1* (1), 1600006

(97) Yang, S.; Hu, W.; Zhang, X.; He, P.; Pattengale, B.; Liu, C.; Cendejas, M.; Hermans, I.; Zhang, X.; Zhang, J.; Huang, J., *J Am. Chem. Soc.*, **2018**, *140* (44), 14614–14618.

(98) Khan, A. F.; Randviir, E. P.; Brownson, D. A. C.; Ji, X.; Smith, G. C.; Banks, C. E., *Electroanalysis* **2017**, *29* (2), 622–634.

(99) Mao, J.; Liu, P.; Du, C.; Liang, D.; Yan, J.; Song, W., *J. Mater. Chem. A*, **2019**, *7* (15), 8785–8789.

(100) Azofra, L. M.; Sun, C.; Cavallo, L.; MacFarlane, D. R., *Chem. Eur. J.,* **2017**, *23* (34), 8275–8279.

(101) Zhu, Y.; Peng, L.; Fang, Z.; Yan, C.; Zhang, X.; Yu, G., *Adv. Mater*., **2018,** *30* (15), 1706347

(102) Sun, T.; Zhang, G.; Xu, D.; Lian, X.; Li, H.; Chen, W.; Su, C., *Mater. Today Energy*., **2019**, *12*, 215–238.

(103) Tang, L.; Meng, X.; Deng, D.; Bao, X., *Adv. Mater.*, **2019**, *31* (50), 1901996.

(104) Mak, K. F.; Shan, J.; Ralph, D. C., *Nat. Rev. Phys*., **2019**, *1*, 646–661.

(105) Gibertini, M.; Koperski, M.; Morpurgo, A. F.; Novoselov, K. S., *Nat. Nanotechnol*., **2019**, *4*, 408–419.

(106) Kostarelos, K., *Nat. Rev. Mater*., **2016**. *1* (11), 16084.

(107) Liu, Y.; Weiss, N. O.; Duan, X.; Cheng, H. C.; Huang, Y.; Duan, X., *Nat. Rev. Mater*., **2016**, *1*(9), 16042.

(108) Sharma, A.; Harnish, P.; Sylvester, A.; Kotov, V. N.; Neto, A. H. C., *Phys. Rev. B*, **2014**, *89* (23), 235425.

(109) Geim, A. K.; Grigorieva, I. V., *Nature*., **2013**, *499*, 419–425.

(110) Glavin, N. R.; Rao, R.; Varshney, V.; Bianco, E.; Apte, A.; Roy, A.; Ringe, E.; Ajayan, P. M., *Adv. Mater*., **2020,** *32* (7), 1904302

Chapter 2

Quantification of surface functional groups on Graphene, Boron nitride, and Borocarbonitrides and their role as nanofillers in improving the mechanical properties of PVA nanocomposites

SUMMARY

Knowledge of surface functional groups is critical for designing materials for various applications. These surface groups define various properties of a material like chemical reactivity, wettability, adhesion, conduction or insulation, optical transmission, hardness, biocompatibility, and the interaction of the material with its surroundings in general. This is particularly true for synthesized graphene which has multiple oxygen functionalities on its surface and related two-dimensional materials like boron nitride (BN) which contains

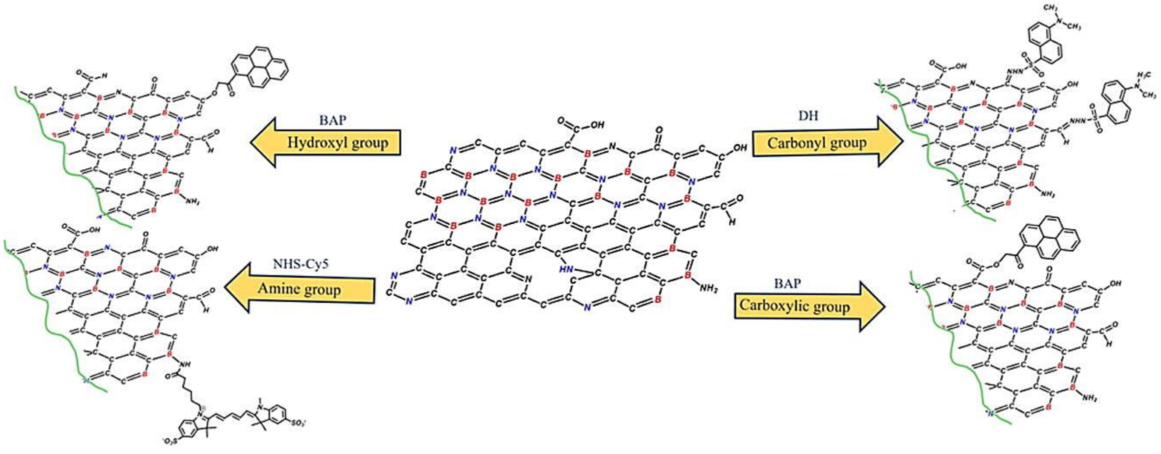

Papers based on this chapter have appeared in *Chem. Phys. Lett.* **2017**, *683*, 459-466; *Carbon* **2018**, *140*, 688-695 amine groups. Borocarbonitrides (BCN) is an interesting class of two-dimensional materials that contain surface functionalities common to both graphene and BN. We have carried out a careful investigation to obtain quantitative estimates of the surface functionalities on graphene, boron nitride, and borocarbonitrides, by employing fluorescence labeling of surface species (FLOSS). This quantitative estimate of different surface functional groups will be useful in understanding molecular-level interactions of these materials with their surroundings.

Polymer nanocomposites are an emerging class of materials with important practical applications. The enhancement in polymer nanocomposites' mechanical and thermal properties depends on the extent of molecular-level interactions and interfacial adhesion between the nanofiller and the matrix material. We have made polymer nanocomposites of polyvinyl alcohol with 0.2 wt% graphene, boron nitride, and borocarbonitrides as nanofillers and observed an improvement by 105% in hardness (*H*) and 69% in elastic modulus (*E*) along with significant improvement in thermal properties. This improvement in mechanical properties can be strongly correlated with the presence of different surface functionalities on the nanofiller.

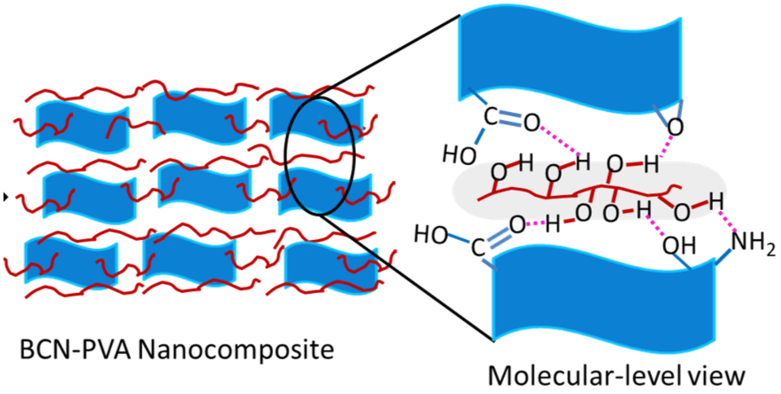

2.1 Introduction

Two-dimensional materials like graphene and boron nitride have multiple functional groups on their surfaces owing to their synthesis techniques or storage conditions. Borocarbonitrides ($B_xC_yN_z$ or BCN) is a class of layered materials wherein both boron and nitrogen are co-doped into the graphene lattice. Boron and nitrogen atoms show sp^2 hybridization like carbon in the lattice along with stronger interlayer coupling although in-plane stability is lower than graphene. [1,2] BCN offers a diverse set of surface functionalities, domain structures, and a high degree of chemical heterogeneity, which make them even more interesting than either graphene or BN. These ternary compounds are robust materials that combine the properties of both graphene and boron nitride along with many unique properties of their own like theoretically predicted tunable bandgap between 5.50 eV to 0.49 eV by controlling the carbon content.[3] BCN has been successfully used for hydrogen evolution reactions, oxygen evolution reactions, as electrode materials in Li-ion batteries, etc.[1,4–6] While graphene contains multiple oxygen functionalities like hydroxide, carbonyls, carboxylic acid, and ether, boron nitride contains hydroxyl and amine functionalities; BCN has domains corresponding to both graphene and BN along with some B-C, N-C, and B-C-N domains containing all the above-mentioned functionalities in the lattice.[7]

2.1.1 Importance of surface functional groups

The surface of a material may be defined as the interface between two states of matter, like solid and fluid. Although typically the bulk properties of a material like electronic, optical, mechanical, thermal, etc., define its use for various applications; it is the surface that determines how a material interacts with the surroundings and if it will behave according to its intended purpose and whether it will be reproducible over multiple cycles. Complete knowledge of a material's surface is important for understanding its chemical reactivity, wettability, adhesion, conduction or insulation, optical transmission, hardness, biocompatibility, and the list goes on.[8] In most studies, surface characterization of materials is generally limited to reporting the surface area and qualitative identification of the functional groups present on the surface, the latter being carried out using X-ray photoelectron spectroscopy (XPS) or Fourier-transform infrared spectroscopy (FT-IR). However, having proper quantitative estimates of surface functional groups might be critical in tuning materials' properties and maintaining the reproducibility in properties of materials when used for various applications.[9] A typical example could be the use of carbon materials in supercapacitors and energy devices. There are a plethora of characterization techniques that could be used for the quantification of surface functional groups, most of these methods like XPS, FT-IR, X-ray photoelectron spectroscopy,[10–12] FT-IR,[13] ultraviolet-visible absorption spectroscopy (UV–Vis),[14] times-of-flight secondary ion mass spectrometry (ToF-SIMS),[15] electron spin resonance (ESR[16]) suffers from low sensitivity.[8] In this work, we concentrate on fluorescence spectroscopy which has the sensitivity to detect in a single-molecule regime.

2.1.2 Fluorescence labeling of surface species

Fluorescence labeling of surface species (FLOSS) is an interesting method for characterizing surface functional groups on materials by chemically attaching different fluorescence probes to them. This technique is reported to have a sensitivity of 10^9 groups/cm^2 [8]and has already been successfully used to quantify surface functionalities in carbon nanotubes,[17,18] carbon nanofibers, [9,19]polymer surfaces,[20,21] self-assembled monolayers[22,] and epoxy groups.[8,23]

2.1.3 Polymer nanocomposites

The concept of material composites is based on the idea of combining valuable properties of different types of materials. The engineering of materials at atomic and molecular levels is bringing in a transformation in the field of material science. Polymer composites having different types of fillers have attracted attention since the 1980s.

In recent years the attention has shifted towards exploring different nanomaterials as filler materials for such composites. A key attribute of nanomaterials is the substantial surface-to-volume ratio (STVR). The subsequent changes in the chemical and physical properties, as compared to the respective bulk properties, are both scientifically interesting and can be exploited for engineering new materials and devices.[24] One such interesting class of materials is polymer matric composites reinforced with nanomaterials of various dimensions. Because of the high STVR of these nanofillers, even a small addition (typically less than 1 vol%) of the nanofillers to the polymer matrix can result in a pronounced enhancement in the latter's mechanical properties while traditional composites will need as much as 60 vol% reinforcement for similar enhancement in mechanical properties.[25–27] Substantial improvements in nanocomposite properties can only be accrued when the fillers are properly dispersed in the polymer matrix such that proper interfacial interaction can take place between the filler and the polymer chains and this is where the functional groups on the surface of the nanocomposite play a crucial role. It has also been successfully demonstrated that the heterogeneous nature of filler like the simultaneous addition of more than one type of nanofiller, especially those with differing dimensionality such as one-dimensional nanotubes to two-dimensional nanosheets can synergistically enhance the mechanical properties.[28,29] We try to understand whether such synergistic benefits can also be observed in heterogeneous borocarbonitride (BCN) nanosheets reinforced poly (vinyl alcohol) (PVA) nanocomposites.

2.1.4 Mechanical properties of a polymer nanocomposite

The mechanical properties of a polymer nanocomposite include multiple parameters like hardness (*H*), elastic modulus (*E*), stiffness (*S*) malleability, ductility, creep, etc. In this work, we have carried out load-displacement studies of the different nanocomposites using Nanoindentation techniques and calculated the corresponding hardness (*H*) and elastic modulus (*E*). The hardness (*H*) of a material is defined as its resistance to plastic deformation while elastic modulus (*E*) refers to the resistance to elastic deformation while stress is applied. Both *E* and *H* can be determined from load-displacement curves.

2.2 Scope of this investigation

In **section 2.4.A**, we have quantitatively characterized the surfaces of graphene, boron nitride, and borocarbonitride surfaces by employing fluorescence spectroscopy.[8] Fluorescence spectroscopy is known to have sensitivity in a single molecule regime. This was done by selectively labeling the surface functional groups on graphene, BN, and BCN with appropriate dye molecules (fluorescent probes) and using emission studies to quantify the number of surface groups.

Given the exceptional mechanical properties of either graphene and BN reinforced polymer nanocomposites,[29] and the possibility of synergy, we expect that BCN polymer nanocomposites might exhibit excellent mechanical and thermal properties, particularly in view of the interesting chemical environments the BCN nanosheets offer. This possibility was investigated in **section 2.4.B** of this study through a detailed characterization of mechanical and thermal properties.

2.3 Experimental section

Materials

All the chemicals used were of high purity and were used without further purification. Natural graphite (Alfa Aesar, 99.9995%), sulphuric acid (SDFCL, 98%), potassium permanganate (Merck), sodium nitrate (SDFCL), hydrogen peroxide 30% (w/w) (Merck), boric acid (Merck), urea (SDFCL), water (Millipore), Polyvinyl alcohol (Kemphasol, 14000 Da)

Synthesis of graphene oxide (GO) and exfoliated graphene (EG)

Graphene oxide was synthesized by the modified Hummer's method. [30,31] In a typical synthesis, 150 mL of concentrated sulphuric acid was slowly added to a 1L beaker, containing 3 g (0.25 moles) each of natural graphite flakes and sodium nitrate, kept in an ice bath. The mixture was stirred for 15 minutes and then 20 g (0.126 moles) of potassium permanganate was added into it, while the beaker is still in an ice bath. The beaker was then transferred to an oil bath maintained at 40 °C and stirred for an hour. To the resulting dark brown suspension, 150 mL of water was added, and the suspension was further stirred at 75 °C for 10 minutes. Finally, 30 mL of H_2O_2 in 300 mL water was added to the reaction mixture. The brown-colored suspension obtained was washed several times with water until the pH of the solution became neutral. The suspension was then lyophilized to obtain flaky brown colored solid graphene oxide (GO). Exfoliated graphene (EG) was obtained by thermal exfoliation of GO at 1050 °C under N_2 atmosphere. During thermal exfoliation, the GO was taken in an alumina boat and subjected to a thermal shock for ~20s which leads to the removal of functional groups from the lattice which in turn weakens the van der Waals interactions between the layered materials and few-layered exfoliated graphene is obtained.

Synthesis of Borocarbonitrides (BCN) and boron nitride (BN)

EG, boric acid, and urea were dispersed in 20 mL water and then stirred at 70 °C to obtain a slurry. This slurry was then transferred into an alumina boat and the reaction mixture was heated to 900 °C under N_2 atmosphere for 5 hours to get borocarbonitrides.[7] By varying the boric acid to carbon ratio, four different compositions of BCN were obtained (**Table 1**). BN was synthesized similarly by using boric acid and urea only.[32]

Table 1: Molar ratios of the precursors used for the synthesis of borocarbonitrides of different compositions

Composition	Boric acid (mg)	Urea (g)	Exfoliated graphene (g)
$(BN)_{20}(C)_{80}$	5.5	0.055	0.050
$(BN)_{50}(C)_{50}$	50	0.50	0.050
$(BN)_{75}(C)_{25}$	150	1.50	0.050
$(BN)_{90}(C)_{10}$	500	5.00	0.050
BN	100	1.00	-

2.3.2 Quantification of surface groups using fluorescent probes

Fluorescence labeling of surface functional groups was carried out for systematically quantifying the number of surface groups on EG, BN, and BCN. The fluorescent probes were chemically attached to specific surface functional groups of these materials as described in the literature. [18] In the case of EG, 5-(Dimethylamino)-1-naphthalenesulfonic hydrazide **(**Dansyl hydrazine, DH) was used for carbonyl group estimation and 1-(bromoacetyl)pyrene (PB) for both carboxylic acid and hydroxyl group detection but under different reaction conditions. For BN, the fluorescent probe used for amine group detection was N-hydroxysuccinimide-Cy5 while for the hydroxyl group again 1-(bromoacetyl)pyrene was used. In BCN where domains of both BN and graphene are present, along with some B-C, N-C, and B-C-N domains, we expect the material to have all the above-mentioned functional groups and the chemical estimation was carried out similarly.

For estimation of surface functional groups, calibration curves of the different dyes were obtained over a known concentration range. The concentrations of the functional groups were determined by measuring the fluorescence intensity of the dye solution before contact with the sample and after the fluorescence labeling reaction with the labeled sample removed from the solution. One of the major problems in fluorescent labeling is the possibility of physical adsorption of the dye molecules on the surface without covalently linking to the surface groups. To validate our results and to prevent wrongful estimation due to physisorption, we have carried out a series of control experiments.

Fluorescence labeling of carbonyl groups using Dansyl hydrazine (DH)[17]

To a 3 mg of the sample under study, a 10 mL 0.68 mM solution of DH in methanol, 1.8 mL of 0.1M hydrochloric acid solution in methanol was added. The resulting solution was stirred in dark at room temperature for 62 hours. After the completion of the reaction, the resulting solutions were centrifuged, and the supernatant was collected in a flask. The remaining sample was washed several times with fresh methanol to remove any physisorbed dye molecules. The washings were collected in the same flask and diluted to known volume to record PL. A control experiment was carried out without the sample under the same conditions. Also, physisorption experiments were carried out without the reagent.

Fluorescence labeling of carboxylic acid groups using 1-(bromoacetyl) pyrene (PB)[17,33]

Chemical tagging of carboxylic acid groups using 1-(bromoacetyl)pyrene has been carried out using standard procedure. To a 2 mg of the sample under study, a 2 mL 1.35 mM solution of 1-(bromoacetyl) pyrene in DMF, 0.54 mg of K_2CO_3, and 0.45 mg of KI were added. The resulting solution was stirred in dark at 50 °C for 12 hours. After the completion of the reaction, the resulting solutions were centrifuged, and the supernatant was collected in a flask. The remaining sample was washed several times with fresh DMF to remove any physisorbed dye molecules. The washings were collected in the same flask and diluted to a known volume to record the PL. A control experiment was carried out without the sample under the same conditions. Also, physisorption experiments were carried out without the reagent.

Fluorescence labeling of hydroxyl groups using 1-(bromoacetyl) pyrene (PB)[33]

To a 2 mg of the sample under study, a 2 mL 0.412 mM solution of 1-(bromoacetyl) pyrene in DMF, 0.2 mL of triethylamine (TEA) was added. The resulting solution was stirred in dark at room temperature for 10 hours. After the completion of the reaction, the resulting solutions were centrifuged, and the supernatant was collected in a flask. The remaining sample was washed several times with fresh DMF to remove any physisorbed dye molecules. The washings were collected in the same flask and diluted to a known volume to record the PL. A control experiment was carried out without the sample under the same conditions. Also, physisorption experiments were carried out without the reagent.

Fluorescence labeling of amine groups using N-Hydroxysuccinimide Cy5 (NHS-Cy5)[34]

Fluorescence labeling of amine groups was carried out as described elsewhere. To a 1 mg sample of the material under study, 3 mL of DMSO, a 5μL of 1.382 mM of NHS-Cy5 dye solution, and 50 μL of triethylamine (TEA) were added. The resulting solution was stirred in dark at room temperature for 6 hours. After the completion of the reaction, the resulting solutions were centrifuged, and the supernatant was collected in a flask. The remaining sample was washed several times with fresh DMSO to remove any physisorbed dye molecules. The washings were collected in the same flask and diluted to a known volume to record the PL. A control experiment was carried out without the sample under the same conditions. Physisorption experiments were carried out without the reagent.

Steps involved in the calculation of surface functional groups

Calibration plots for the different fluorescent probes were obtained by plotting PL intensity vs. dye concentration at a particular wavelength. The PL data for all the samples were plotted against the control. The decrease in fluorescent intensity for the samples, at the wavelength at which the calibration plot was drawn for the probe, was noted. From the calibration plot, we obtain the concentration of reacted fluorescent probes. The concentration obtained was multiplied by the Avogadro number and divided by the amount of sample taken to obtain the number of surface functional groups per gram of the material. By dividing this number by the surface area of the material we get the number of groups per unit surface area of the material.

Synthesis of polymer nanocomposites

A homogeneous dispersion of the nanofillers within the polymer matrix can be achieved by using a common solvent with which both the polymer and BCN can interact simultaneously. Since semi-crystalline PVA is water soluble, and BCN is highly dispersible in water due to the polar surface groups in it, BCN-PVA nanocomposites were synthesized by using water as the solvent.

For preparation of polymer nanocomposites, 499 mg of polyvinyl alcohol (PVA) was dissolved in 40 mL water heated to 80 °C. 1 mg of BCN dispersed in 1 mL water-ethanol, was added to the PVA solution. The resulting solution was further sonicated for about 5 hours, while maintaining a bath temperature of ~ 70 °C such that the total volume of the liquid decreases by 75%. At this stage, the solution was poured into a petri dish, dried at an oven maintained at 55 °C for 72 hours, and then desiccated for at least 72 hours prior to characterization and nanoindentation measurements. For comparison purposes, pure PVA and PVA reinforced with either EG or BN were also prepared by using identical processing steps. In all composites examined in this study, the amount of filler loading was fixed at 0.2 wt%. **Scheme** 1 gives a representation of the steps involved in the preparation of polymer nanocomposites.

Estimation of hardness (*H*) and elastic modulus (*E*)

According to classical indentation theory, the initial part of the load-displacement curve gives information on elastic recovery and this unloading data is crucial for the calculation of elastic modulus (*E*) and Hardness (*H*). In this work, the indentation calculations were carried out according to the Oliver-Pharr method.[35–37]

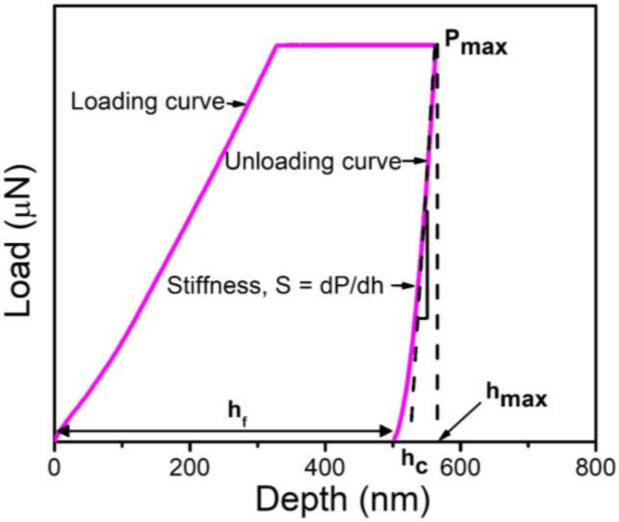

Figure 1: Pictorial representation of a Load-displacement curve

According to this method, unloading curves for load-displacement measurements can be accurately described using power-law relation:

$$P = \alpha\,(h_{max}-h_f)^{m} \qquad (1)$$

where P is the load, $(h_{max} - h_f)$ is the elastic displacement, and α and m are material constants.

The slope of the unloading curve, gives a measure of stiffness (S) of the sample which can be mathematically represented as:

$$S = 2\, E_r A^{1/2} / \pi^{1/2} \qquad (2)$$

where A is the surface contact area at maximum displacement and E_r is reduced elastic modulus given by:

$$E_r = [(1-\upsilon_s^2)/E_s + (1-\upsilon_i^2)/E_i] \qquad (3)$$

where E and υ are elastic modulus and Poisson's ratio of i= indenter and s = specimen material. After rearranging Eq. (2), the reduced elastic modulus can be written as:

$$E_r = 1/2(\pi/A)^{1/2}\, S \qquad (4)$$

for polymers $E_i >> E_s$, so second term of Eq. (3) is negligible, so elastic modulus (E) can be directly calculated from the unloading curve using Eq. (4).

Hardness (H) is defined as the ratio of maximum load by area of indentation:

$$H = P/A \qquad (5)$$

using Eq. (1), hardness can be calculated by the unloading curve.

Physical Characterization

Powder X-ray diffraction patterns were collected using a Bruker D8 Discover diffractometer using Cu-Kα radiation. Raman spectra were collected in the backscattering geometry using a 632 nm HeNe laser with a Jobin Yvon LabRam HR 800 spectrometer. Fourier transform infrared spectra (FT-IR) were recorded in a Bruker FTIR spectrometer in ATR mode. Gravimetric compositions BCN samples were determined by thermogravimetric analyses carried out in an oxygen atmosphere with a Metler Toledo TGA-850 TG analyser at the rate of 3 °C/min. Elemental mapping of B, N, and C was carried out using energy-dispersive X-ray spectroscopy (EDX) and morphology was obtained using scanning electron microscopy Nova NanoSEM 600 FESEM. Chemical compositions and bonding nature of the samples were determined by X-ray photoelectron (XP) spectroscopy in an Omicron nanotechnology spectrometer, using monochromatic Mg-K_{α} as an X-ray source. Atomic force microscope (AFM) images were obtained on SiO_2/Si substrates in tapping mode using the Bruker Innova instrument. Transmission electron microscopy (TEM) images were recorded with an FEI Tecnai G^2 S-Twin operated microscope fitted with a Gatan CCD camera. N_2 sorption profiles were recorded using a Quantachrome Quandasord-*SI* analyzer. Photoluminescence spectra were recorded with a Fluorolog-3 spectrophotometer fitted with Horiba Jobin Yvon Xe lamp light source. The morphologies of nanosheets and polymer matrix were characterized by using a field emission scanning electron microscope (FESEM) Nova NanoSEM 600 (FEI Company). The extent of dispersion of BCN nanosheets in PVA matrix was analysed by cross-sectional FESEM. The cross-sections for this purpose were obtained by fracturing the samples after dipping them in liquid N_2 for ∼600 s. X-ray diffraction (XRD) of the nanocomposites and PVA was performed in a Panalytical diffractometer (Empyrean) using the monochromatic Cu K_{α} radiation (λ=1.54 Å). Thermo-gravimetric analyses (TGA) were carried out in N_2 atmosphere with a Metler Toledo TGA-850 analyzer at the rate of 5 °C/min. Differential scanning calorimetry (DSC) measurements were carried out in TA instrument in N_2 atmosphere with the heating and cooling rate of 3°C/min.

Nanoindentation

The nanoindentation technique was utilized to evaluate the mechanical properties. For this, the Triboindenter system (Hysitron, Inc., Minneapolis, MN, USA), equipped with a cono-spherical tip of radius (R) 1 μm was used. The choice of this particular tip geometry was made, instead of a sharp tip like Vickers or Berkovich that are generally used for nanoindentation, so as to reduce the displacement at any given load.[36] In all cases, the loading and unloading rates were maintained at 0.5and 2mN/s respectively, and the peak load was 500 μN. Faster loading and even speedier unloading rates were utilized to reduce viscoelastic recovery and to avoid the typical 'knee' during unloading. These parameters further help in obtaining a convergent solution for the power-law fit.[38] A hold time of 250 s at the peak load was used to avoid the creep effects that typically result in the overestimation of Young's modulus, E. To avert any inaccuracy in the calculation of depth, h, the area function file had been calibrated using Polycarbonate instead of conventionally used fused quartz. The load, P-displacement curves generated through the following procedure were further fitted using power-law equation given by Oliver and Pharr to obtain the values of E (elastic modulus) and H (hardness).[35,37]

2.4.A Quantification of surface functional groups on Graphene, Boron nitride and Borocarbonitrides using Fluorescence labelling of surface species (FLOSS)

2.4.A Results and discussion

Material characterization

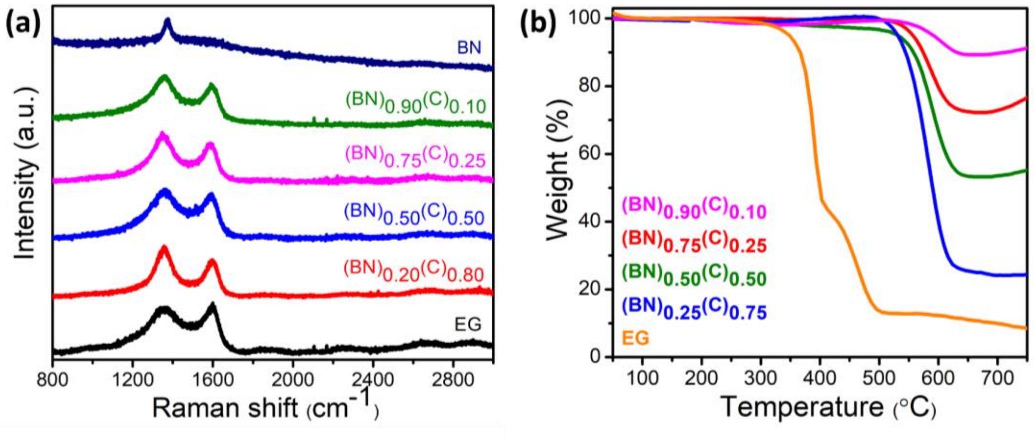

Figure 2: (a) Raman spectra of EG and various compositions of BCN, (b) Thermogravimetric analysis of various compositions of BCN in comparison with EG

All the materials under study exfoliated graphene (EG), boron nitride (BN), and borocarbonitrides (BCN) of four different compositions were synthesized by high-temperature method and have been extensively characterized by spectroscopic and microscopic techniques. The chemical purity of these materials was established by Raman and FT-IR studies. **Figure 2(a)** shows the Raman spectra of EG, BCN of various compositions, and BN. EG shows a broad peak around 1598 cm^{-1} corresponding to sp^2 carbon vibrational modes known as the G band along with a peak at 1355 cm^{-1} due to disorder in the lattice (D mode).[39] Raman spectra of BN show a peak at 1375 cm^{-1} corresponding to its E_{2g} mode.[1] Raman spectra of all BCN shows a peak ~1360 cm^{-1} which will have contributions from both graphite D mode and BN E_{2g} mode and a peak around 1600 cm^{-1} due to graphitic G mode. Gravimetric compositions of the four BCN samples were calculated using Thermogravimetric analysis (TGA). **Figure 2(b)** shows the TGA plots of all the BCN samples along with EG. EG shows a sharp weight loss of about 90%

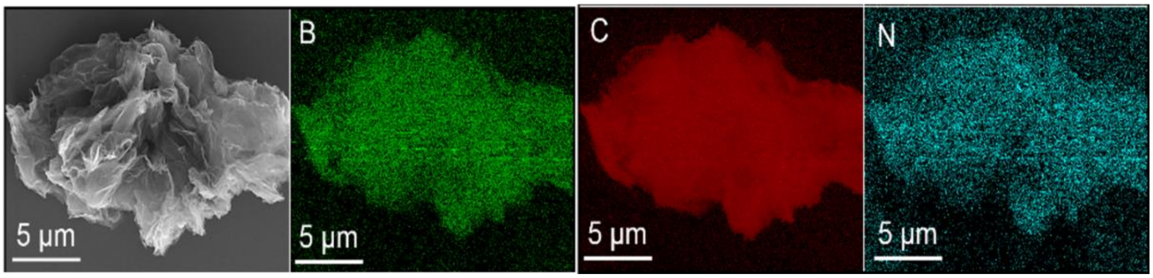

Figure 3: FESEM image of $(BN)_{0.75}(C)_{0.25}$ along with elemental mapping

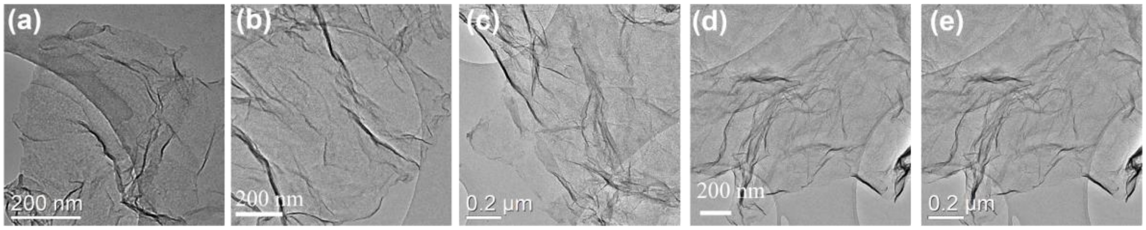

Figure 4: TEM images of (a) EG (b) $(BN)_{0.20}(C)_{0.80}$ (c) $(BN)_{0.50}(C)_{0.50}$ (d) $(BN)_{0.75}(C)_{0.25}$ and (e) $(BN)_{0.90}(C)_{0.10}$

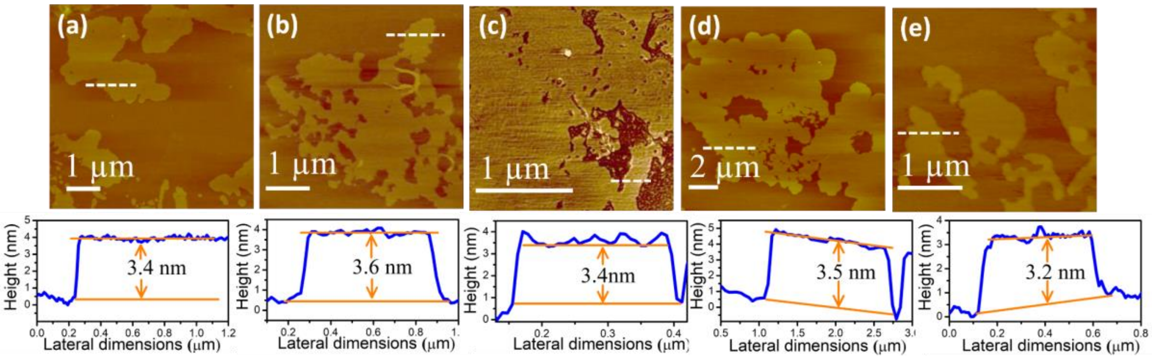

Figure 5: AFM images with corresponding height profile of (a) EG (b) $(BN)_{0.20}(C)_{0.80}$ (c) $(BN)_{0.50}(C)_{0.50}$ (d) $(BN)_{0.75}(C)_{0.25}$ and (e) $(BN)_{0.90}(C)_{0.10}$

in the temperature range of 300-500 °C, followed by further slow decay. Compared to EG, the various BCN compositions show higher thermal stability. The gravimetric compositions were assigned according to the residual weight of the sample at 700°C. Elemental mapping of $(BN)_{0.75}(C)_{0.25}$ composition shows uniform distribution of dopants (**Figure 3**). **Figure 4** shows bright-field TEM images of the nanosheets highlighting the

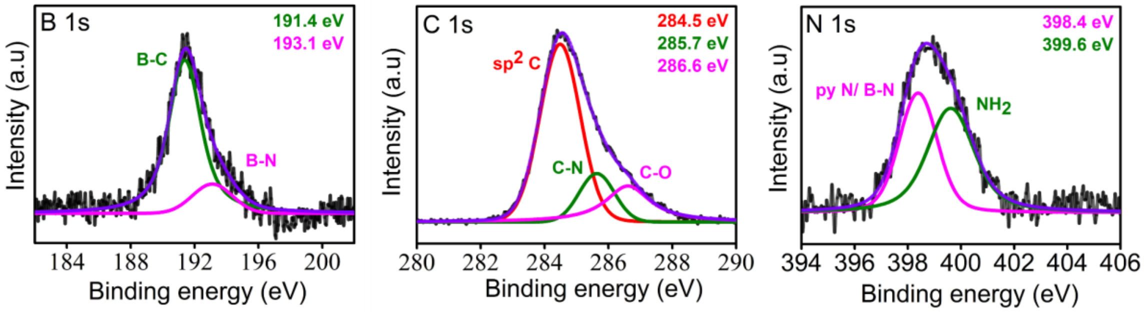

Figure 6: Core-level X-ray photoelectron (XP) spectrum B 1s, C 1s, and N 1s of (BN)$_{0.75}$(C)$_{0.25}$

few-layered nature of the samples with no visible differences in nanosheets morphology with changing compositions. Consistently, AFM images of these nanosheets show that these have an average height of 3.4-3.6 nm which is ~6-8 layers thick with a lateral dimension of ~1µm (**Figure 5**). To have a better understanding of the nature of bonding, XPS measurements were carried out. **Figure 6** shows a representative core level XPS spectra of (BN)$_{0.75}$ (C)$_{0.25}$ composition. B1s core-level spectra can be deconvoluted into two peaks centered at 191.3 eV and 192.3 eV corresponding to B-C and B-N bonds. C 1s spectra can be fitted into three peaks at 284.4, 285.6, and 286.8 eV due to sp^2 carbons, C-N bonds, and C-O bonds respectively. The N 1s spectrum has a major feature at 398.6 eV due to the pyridinic nitrogen and N-B bonds with another feature at 400.3 eV due to amine content. Functional group information on the nanosheets can also be acquired by the FT-IR spectra of the nanosheets (**Figure 7**). The infrared spectrum of BCN shows a characteristic strong band at 1570 cm^{-1} and a weak band around 1728 cm^{-1} due to C=C and carboxylic acid groups respectively. The broadband around 1100-1250 cm^{-1} is due to C-O stretching and O-H bending vibrations and the other broadband around 3200 to 3600 cm^{-1} corresponds to –OH and –NH stretching vibrations. These preliminary spectroscopic results reveal the presence of various functional groups like carbonyl, carboxylic, and

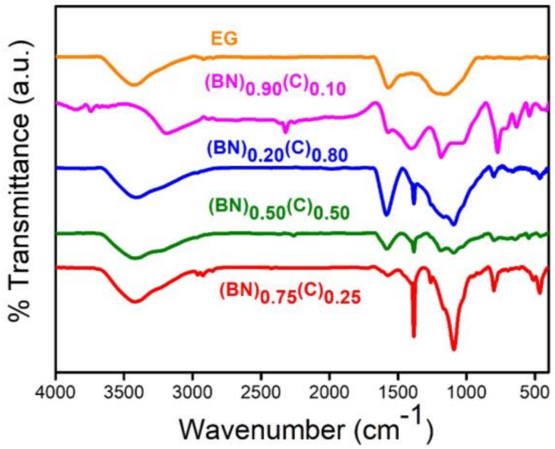

Figure 7: Fourier transform infrared spectrum (FT-IR) of EG and various compositions of BCN

hydroxyl on the surfaces of the nanosheets, and these functional groups are known to affect the various properties of materials along with their reproducibility of these properties when used for different applications. The sensitivity of most commonly used methods like FT-IR, XPS, TPD is low, so we switch to fluorescence spectroscopy which is known to detect up to a single molecule regime. [18]

Quantification of surface functional groups

The surface of EG is estimated to have O-functionalities as, carbonyl, carboxylic acid, hydroxyl, and ether on its surface while BN contains amine functionalities apart from surface hydroxyl groups. BCN which contains both C=C domains as EG and B-N domains as BN along with some B-C, N-C, and B-C-N domains and contains both O-functionalities and amine functionalities on its surface. Quantification of these functional groups is of great significance due to their impact on the properties of materials. [40–42] We have employed fluorescence labeling of surface species (FLOSS) for quantification of the functional groups due to its ability to detect below the detection limit any other available techniques to date.[8,19] FLOSS uses the specificity of chemical reactions to attach labeling molecules to surface functionalities to facilitate detection, identification, and quantification of surface species.[9] **Scheme 1** gives a pictorial description of chemically labeling the surface groups on EG, BN, and BCN by different fluorescent probes.

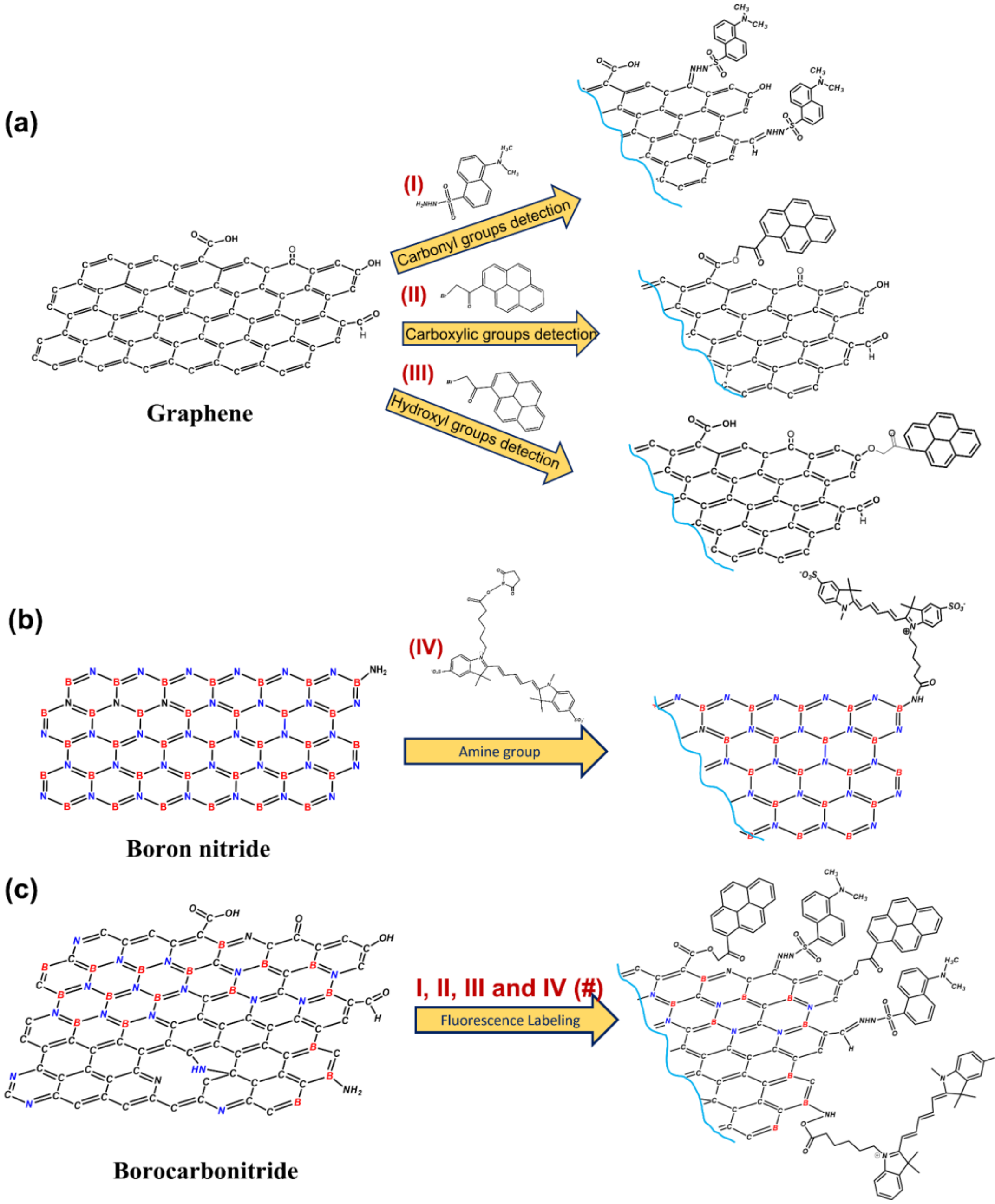

Scheme 1: Schematic representation of surface functional groups on (a) graphene (b) boron nitride and (c) borocarbonitrides, and probing them using (I) dansyl hydrazine (carbonyl groups), (II), and (III) 1-(bromoacetyl)pyrene (for carboxylic and hydroxyl groups) and (IV) NHS-Cy5 (for amine groups) fluorescent probes

The carbonyl groups on EG and BCN were tagged with 5-(Dimethylamino)-1-naphthalenesulfonic hydrazide (DH) molecule.[17] **Figure 8a** shows the emission spectra of DH of various concentrations with excitation at 350 nm with the corresponding calibration curve by monitoring the intensity at 513 nm in the inset. **Figure 8b** illustrates the depletion of the fluorescent intensity of the dye due to the covalent attachment of DH molecules to carbonyl groups on the surface. The numbers of carbonyl groups present on the surface were estimated using a calibration plot. To confirm the quenching of fluorescence intensity due to covalent linking and not due to physisorption, we carried out control experiments without the reagent which showed that there was no observable change in PL intensity (**Figure 8c**).

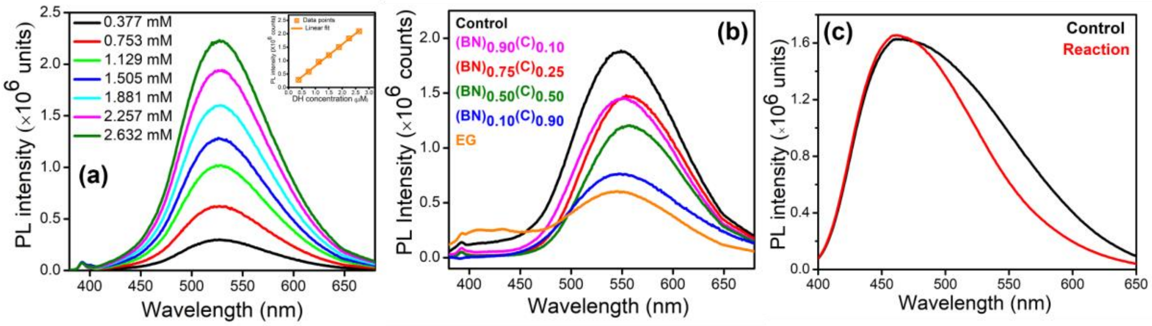

Figure 8: (a) Emission spectra of DH of different concentrations (excitation wavelength 350nm) along with calibration plot at 513 nm (b) Emission spectra of DH reacted with carbonyls of EG and BCN compared with the control experiment (c) Physisorption control experiment for DH with BCN

BCN contains amine functionalities on the surface due to the reaction of urea with graphene during synthesis. The number of these functionalities can vary with the composition due to variation in the number of graphene, BCN and BN domains with composition. BN is also expected to have amine surface groups. To probe the amine functionalities on BN and BCN surfaces, we have used the N-Hydroxysuccinimide Cy5

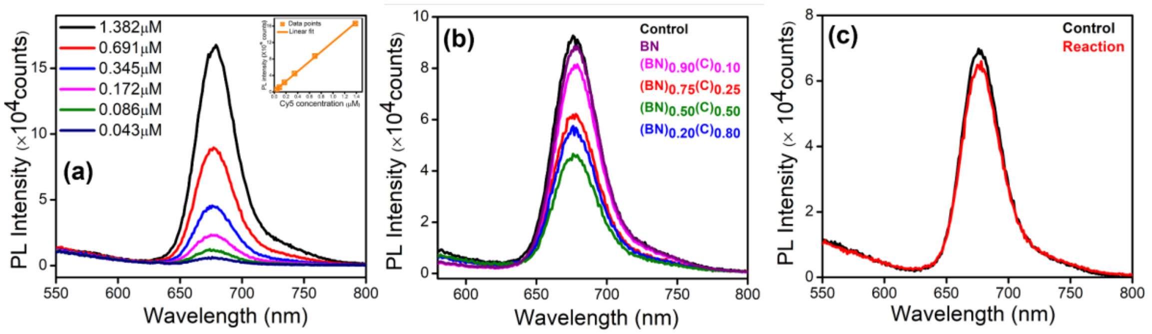

Figure 9: (a) Emission spectra of NHS-Cy5 of different concentrations (excitation wavelength 530nm) along with calibration plot at 680 nm (b) Emission spectra of NHS-Cy5 reacted with amine groups of BN and BCN along with the control experiment (c) Physisorption experiment for NHS-Cy5 with BCN

(NHS-Cy5) as the fluorescent probe which is very specific to amine group.[34] We have measured the fluorescence of various known concentrations of NHS-Cy5 with excitation at 530 nm as shown in **Figure 9a** with the corresponding calibration plot at 680 nm in the inset. The Fluorescence quenching results of NHS-Cy5 reaction with the amine functional groups on BN and various compositions of BCN are shown in **Figure 9b**. We have carried out control reactions without the reagent to rule out the physisorption of dye molecules (**Figure 9c**).

Figure 10a shows the PL emission spectra of 1-(bromomoacetyl) pyrene collected over a known range of concentrations with the calibration curve derived by monitoring the intensity at 410 nm displayed in the inset.[17,33] The PL intensity of carboxylic group reaction shows satisfactory depletion due to the presence of many of these groups on the surface (**Figure 10b**). The hydroxyl group reaction shows a reasonable decrease in intensity compared to the control reaction (**Figure 10c**). Although estimation of carboxylic acid groups and hydroxy groups are carried out using the same dye, the reaction conditions are

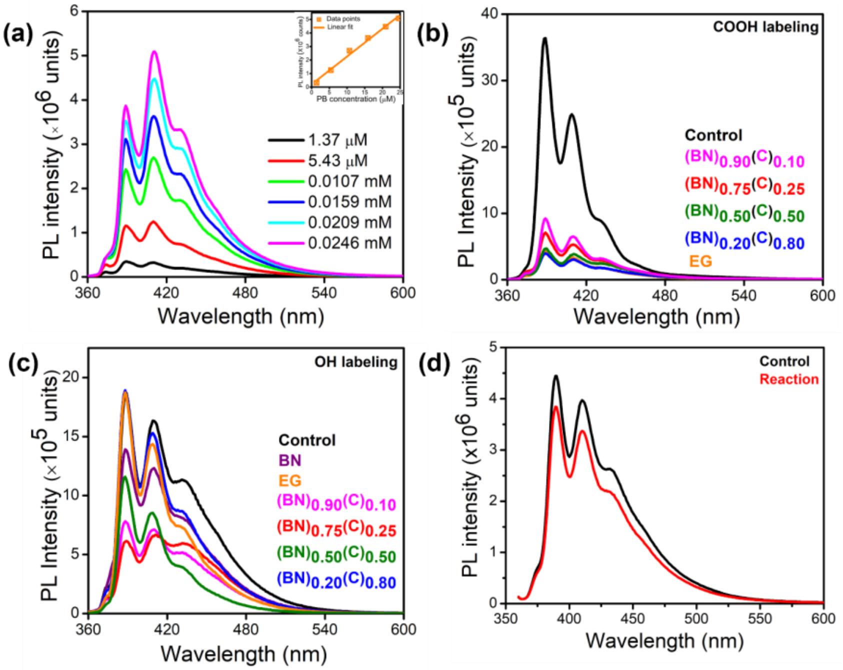

Figure 10: (a) Emission spectra of 1-(bromomoacetyl) pyrene (PB) of different concentrations (excitation wavelength 320 nm) along with calibration plot at 410 nm (b) Emission spectra of PB reacted with carboxylic groups of EG and BCN along with the control experiment (c) Emission spectra of PB reacted with hydroxyl groups of EG, BN, and BCN along with the control experiment, (d) Physisorption experiment for PB with BCN

different keeping in view the different pK_a values for -OH and COOH groups. The estimates of carboxylic and hydroxyl groups based on these results are reasonable, although there could be a slight overestimation due to possible side reactions. Moreover, we have carried out control reactions without the reagents to rule out the physisorption of dye molecules (**Figure 10d).**

Functional group quantification was carried out as explained in **section 2.3.3**. Fluorescence quantification results show that the carbonyl and carboxylic acid groups on

Table 2: FLOSS estimation of various functional groups on graphene, boron nitride and borocarbonitrides

Samples	Surface area (m^2/g)	Carbonyl groups (groups/g) (groups/cm^2)	Carboxylic groups (groups/g) (groups/cm^2)	Hydroxyl groups (groups/g) (groups/cm^2)	Amine groups (groups/g) (groups/cm^2)
EG	948	$2.27X10^{20}$ $(2.39X10^{13})$	$28.32X10^{20}$ $(29.87X10^{13})$	$0.86X10^{20}$ $(0.91X10^{13})$	-
$(BN)_{0.20}(C)_{0.80}$	454	$2.08X10^{20}$ $(4.58X10^{13})$	$28.81X10^{20}$ $(63.46X10^{13})$	$0.03X10^{20}$ $(0.07X10^{13})$	$1.71X10^{20}$ $(3.77X10^{13})$
$(BN)_{0.50}(C)_{0.50}$	437	$1.80X10^{20}$ $(4.12X10^{13})$	$27.36X10^{20}$ $(62.61X10^{13})$	$8.95X10^{20}$ $(20.48X10^{13})$	$2.15X10^{20}$ $(4.92X10^{13})$
$(BN)_{0.75}(C)_{0.25}$	254	$1.33X10^{20}$ $(5.24X10^{13})$	$25.45X10^{20}$ $(100.20X10^{13})$	$11.51X10^{20}$ $(45.31X10^{13})$	$1.36X10^{20}$ $(5.35X10^{13})$
$(BN)_{0.90}(C)_{0.10}$	190	$0.97X10^{20}$ $(5.10\ X10^{13})$	$23.44X10^{20}$ $(123.37X10^{13})$	$10.38X10^{20}$ $(54.63X10^{13})$	$0.44X10^{20}$ $(2.31X10^{13})$
BN	142	-	-	$2.94X10^{20}$ $(20.70X10^{13})$	$0.04X10^{20}$ $(0.03X10^{13})$

the surface of BCN follows a linear trend with increasing carbon content. The number of amine groups on the surfaces also increases with increase in carbon content. But the sample with highest carbon content $(BN)_{0.20}C_{0.80}$ shows deviation from the observed trend and possesses a smaller number of amine groups compared to $(BN)_{0.50}C_{0.50}$. The reason behind this trend could be that the molar proportion of the aminating agent (urea) used to synthesize $(BN)_{0.20}C_{0.80}$ composition is 10 times lesser than that of $(BN)_{0.50}C_{0.50}$. We do not observe any trend on the number of surface hydroxyl groups. The surface group quantification results have been summarised in **Table 2**.

Although techniques like Boehm titrations have been used for functional group detection, these are not specific to surface only.[9,43] Hence FLOSS can be utilized as a simple technique for surface functional group estimation. Although chemical labeling may underestimate the number of functional groups on the surface, upper detection limit will depend on the size of the labeling molecules.

2.4.B Mechanical and thermal properties of Polyvinyl alcohol polymer nanocomposites with Graphene, Boron nitride and Borocarbonitride nanofillers

2.4.B Results and discussion

Characterization of polymer nanocomposite

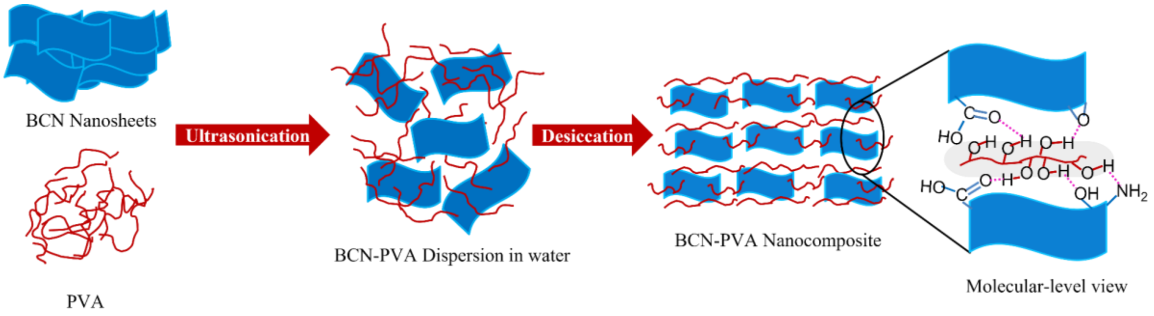

Scheme 2: Pictorial representation of BCN-PVA nanocomposite preparation and the molecular-level view highlighting interactions between BCN functional groups and polymer backbone

Scheme 2 gives a pictorial representation of the BCN-PVA nanocomposites and their possible interaction at the molecular level. The polar functionalities present on the surface of the BCN can establish H-bonding with the hydroxyl groups present on PVA backbone[44–46] which is also illustrated in **Scheme 2**. Cross-sectional FESEM images of BCN-PVA nanocomposites shows BCN nanosheets embedded into PVA matrix (**Figure 11**).

XRD analysis gives crucial information regarding crystallinity, orientation, and size of ordered regions within the polymer matrix. Representative XRD patterns obtained on pristine PVA, EG-PVA, BCN-PVA and BN-PVA nanocomposites are displayed in **Figure 12a**. PVA shows XRD diffraction peaks at 11.5° and 19.5°, which correspond to (110) and (101) planes respectively. The (101) peak of PVA arises due to intermolecular interface between PVA chains in the direction of intermolecular hydrogen bonding.[46] All the BCN-PVA composites do not show any XRD peak corresponding to BCN indicating that BCN is well dispersed in the polymer lattice. Moreover, these composites show a sharp

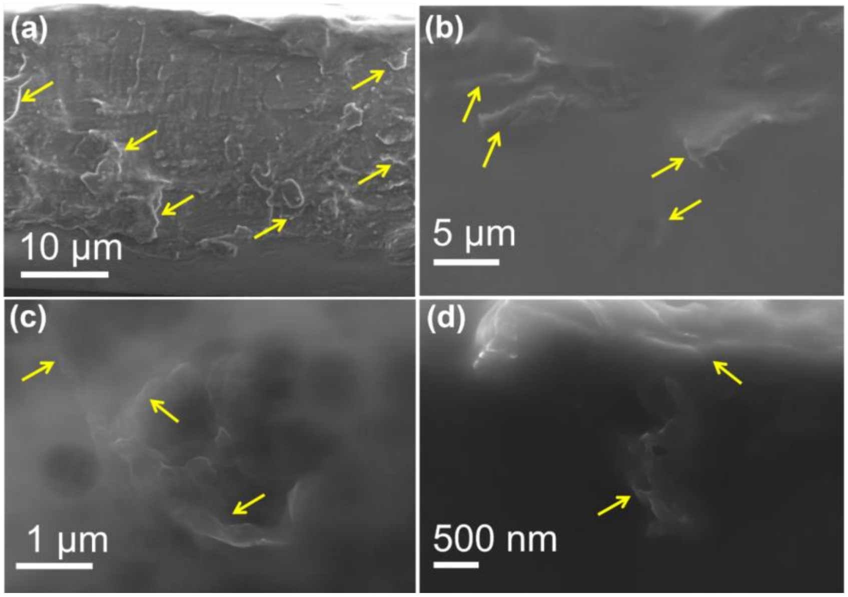

Figure 11: Cross-sectional FESEM images of BCN-PVA nanocomposites

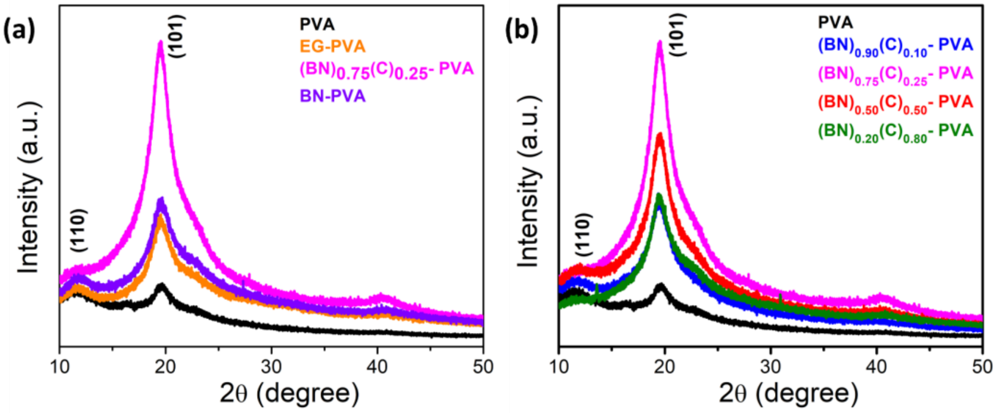

Figure 12: (a) X-ray diffraction patterns of PVA and $(BN)_{0.75}(C)_{0.25}$-PVA composites along with EG-PVA and BN-PVA loading of 0.2 wt% in comparison with for comparison (b) X-ray diffraction patterns of PVA and all BCN-PVA compositions

(101) peak which implies that the nanocomposites are more crystalline than pure PVA. This gives indirect proof of strong H-bonding interaction between PVA and BCN which facilitates crystal growth preferably along (101) plane. The ratios of the intensity of the Bragg peaks associated with (101) to (110) planes of the nanocomposites are much higher

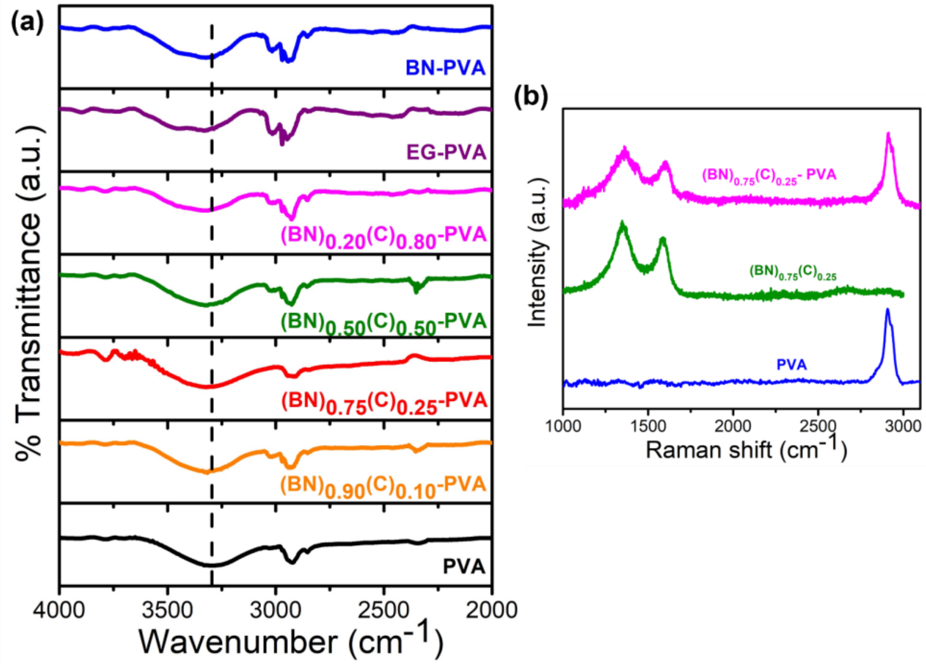

Figure 13: (a) FT-IR spectra of EG-PVA, BN-PVA, BCN-PVA with pure PVA, (b) Raman spectra of Raman spectrum PVA and PVA-BCN composites with the BCN loading of 0.2 wt% in comparison with pristine BCN

than that observed in pristine PVA, which indicates higher degree of crystallinity in the former. $I_{(101)}/I_{(110)}$ is 4.208 in the nanocomposite reinforced with 0.2 wt.% $(BN)_{0.75}(C)_{0.25}$, whereas it is only 1.061 in pristine PVA. Slight shift in the 2θ value of (101) plane also indicate strong interaction of the filler material with PVA. **Figure 12b** shows the XRD patterns of all BCN-PVA nanocomposites along with PVA.

Figure 13a shows the FT-IR spectra BCN-PVA nanocomposites in comparison to EG-PVA, BN-PVA along with pure PVA. The characteristic band at 3282 cm^{-1} in PVA corresponds to the hydroxyl group on the polymer backbone. This band shifts to higher wave number upon the addition of nanofiller to PVA, which indicates stronger intermolecular interactions between BCN and PVA compared to the inherent polymer.

Raman spectra of the nanocomposites (**Figure 13b**) show the characteristic bands at 1350 and 1560 cm^{-1}, which correspond to BCN nanosheets, and at 2900 cm^{-1} that corresponds to PVA's optical phonon mode. No significant difference in the spectra collected at different regions supports the conclusion about the uniformity of nanosheet dispersion in the matrix.

Mechanical properties

Representative load displacement (*P-h)* responses obtained from PVA nanocomposites of BN, $(BN)_{0.90}(C)_{0.10}$, $(BN)_{0.75}(C)_{0.25}$, $(BN)_{0.50}(C)_{0.50}$, $(BN)_{0.20}(C)_{0.80}$, and EG compared to PVA matrix are displayed in **Figure 14a**. **Figure 14b** shows the variations in the average values of Elastic modulus (*E*) and hardness (*H*) with the composition. For the unreinforced PVA, *E* and *H* are 4.2 ± 0.058 GPa and 76 ± 1.2 MPa, respectively which are within the reported range.[47] **Figure 14b** shows that the addition of filler (0.2 wt%) increases *E* to about 7 GPa, which is about 60% enhancement, irrespective of the filler material. The trends in *H* show composition variation. The addition of either EG or BN to PVA enhances *H* to 114 ± 5.1 and 109 ± 3.2 MPa respectively, which are themselves substantial at ~50% and ~43 % enhancement respectively. However, the addition of BCN to PVA, enhances *H* even further, with the $(BN)_{0.75}(C)_{0.25}$-PVA nanocomposite showing the highest *H* of 157 ± 3.4 MPa, i.e., more than double of that of the base PVA.

The substantial enhancement in the mechanical properties of the PVA upon the addition of nanofillers can possibly be due to two factors: (i) an increase in the crystallinity within the polymer matrix and (ii) the reinforcement effect of the nanofillers that arises due to their substantially higher mechanical properties compared to PVA.[48] For the latter, an effective load transfer between the two constituent phases-the polymer matrix and the

---

Mechanical properties measurements were carried out by Dr. Abhishek Chaturvedi and Prof. U. Ramamurthy (IISc)

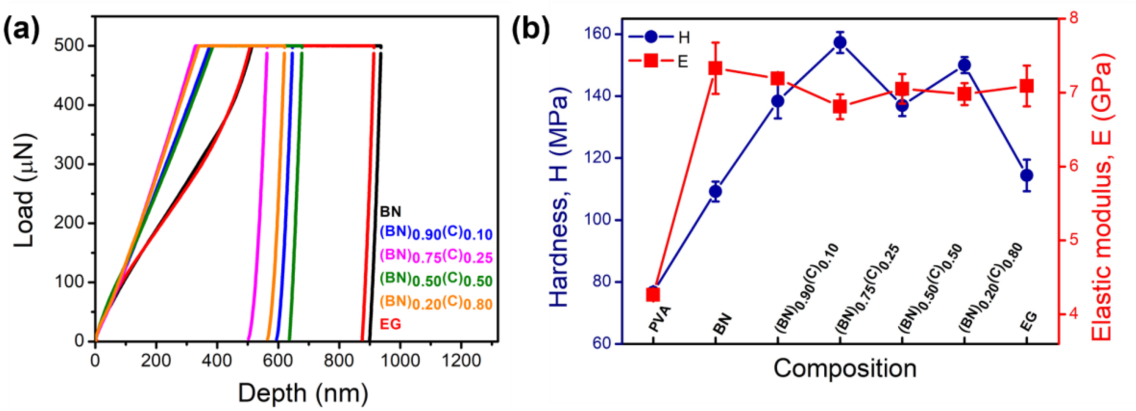

Figure 14: (a) Loading and unloading curves of EG to BN and BCN –PVA nanocomposites (b) variation of Hardness (*H*) and Elastic modulus (*E*) with composition in EG-PVA, BCN-PVA and BN-PVA nanocomposites

nanofiller is essential, which strongly depends on the intermolecular H-bonding between PVA and BCN in the current context. Such a strong interaction restricts the mobility of the polymer chains, which, in turn, can alter the glass transition temperature (T_g) as well.[49–51]

Differential scanning calorimetry (DSC) is a suitable technique for measuring both glass transition temperature (T_g) and degree of crystallinity (χ) in a polymer sample. **Figure 15** shows the DSC scans of PVA along with nanocomposites wherein T_g of PVA (~78 °C) increases to 96 °C upon the addition of $(BN)_{0.75}(C)_{0.25}$. This substantial increase in T_g indicates strong molecular interaction of polymer chains with filler. This was further validated by crystalline melting temperature (T_m). Both the pristine PVA and nanocomposites show T_m in the range of 180 to 200 °C; a slight increase in T_m of PVA on the introduction of filler material suggests that it has a substantial effect on crystalline regions of PVA. The degree of crystallinity χ is measured as the ratio of the amount of heat required to melt 1g of the nanocomposite to that of pure PVA (standard value ΔH_o 138.6 Jg^{-1}). For a semi-crystalline polymer like PVA, a change in the degree of crystallinity can

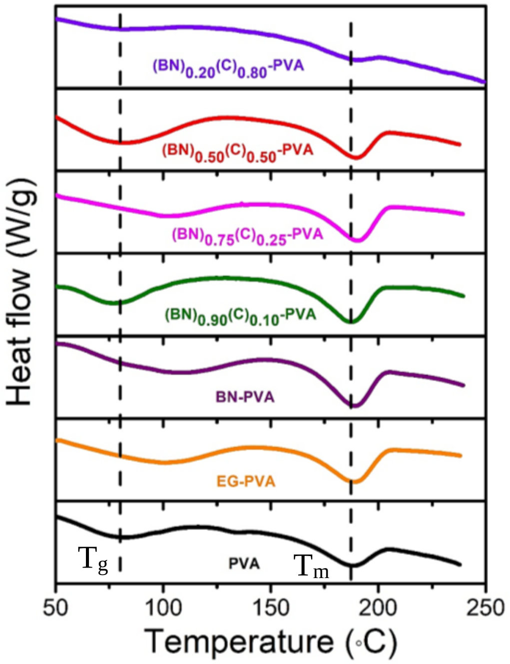

Figure 15: DSC scans of different nanocomposites along with PVA

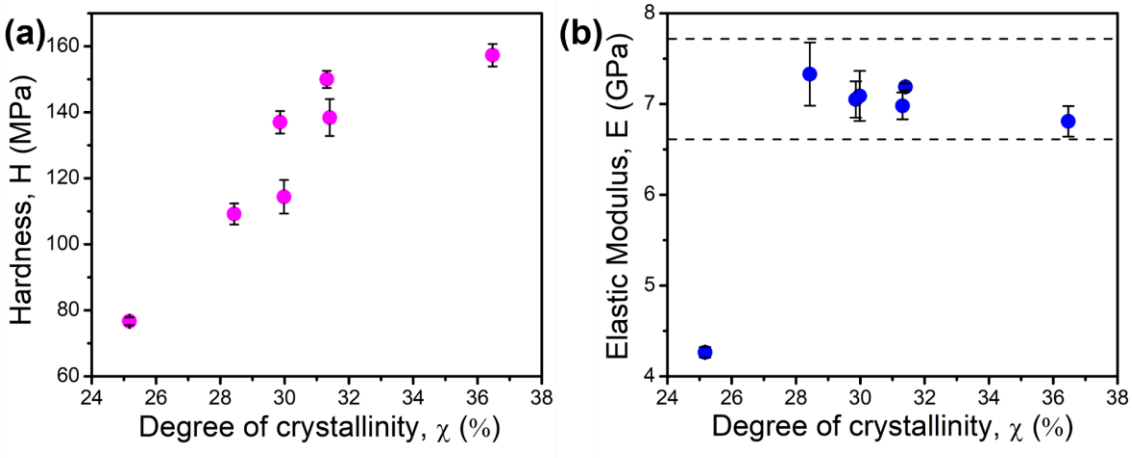

Figure 16: (a) Variation of hardness (*H*) and (b) elastic modulus (*E*) with degree of crystallinity, χ (%)

have a great impact on the mechanical properties of the material. We plotted the variations of *H* and *E* (**Table 3**) with changes in χ (**Figures 16a** and **16b**). It reveals that *H* increases nearly linearly with χ. On the other hand, *E* doesn't show any linear trend with χ. These observations suggest that the enhancement in *E* that was noted in all the nanocomposites is not due to increase in χ. Hence, it must be due to the stress transfer mechanism from the matrix to reinforcement phase which is aided by the strong interactions between those two phases. [47,52,53]

Table 3: Mechanical properties of different polymer nanocomposites

Nanocomposite	Degree of Crystallinity (χ) (%)	Elastic modulus (E) (GPa)	Hardness (H) (MPa)
PVA	25.17	4.265±0.058	76.7±1.2
BN-PVA	28.43	7.33±0.347	109.2±3.2
$(BN)_{0.90}(C)_{0.10}$-PVA	31.4	7.19±0.038	138.4±5.6
$(BN)_{0.75}(C)_{0.25}$-PVA	36.47	6.81±0.168	157.3±3.4
$(BN)_{0.50}(C)_{0.50}$-PVA	29.86	7.05±0.2	137±3.4
$(BN)_{0.20}(C)_{0.80}$-PVA	31.31	6.98±0.148	150±2.6
EG-PVA	29.98	7.09±0.2758	114.4±5.1

Effective stress transfer leads to a substantially higher resistance to elastic deformation offered by the nanocomposites. This, in turn, results in the observed higher *E* of the nanocomposites. Furthermore, the results of XRD scans of the composites indicate that the filler material enhances the polymer chain alignment. The presence of the surface functional groups aids this process through strong intermolecular H-bonding. The alignment of the nanosheets and the presence of multitude of strong intermolecular interactions could be another reason for observed increase in *E*. Effective stress transfer leads to a substantially higher resistance to elastic deformation offered by the nanocomposites, which in turn results in a higher *E* of the nanocomposites.

The enhancements observed in *H*, in contrast to *E*, can be rationalized by recourse to the observed positive correlation between *H* and χ. Since the hardness of any material is

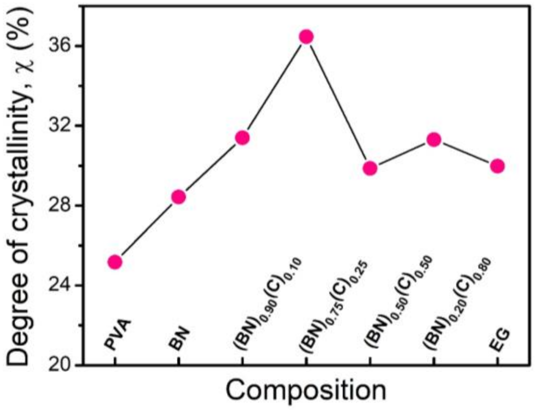

Figure 17: Variation of degree of crystallinity (χ) with composition

a measure of its resistance to plastic deformation, it is pertinent to briefly examine the micromechanisms of plasticity in semicrystalline polymers here. For semicrystalline polymers like PVA, plasticity occurs, broadly, in four stages. They involve elongation of the chains that are in the amorphous regions, reorientation (or alignment) of the crystalline regions in the direction of the tensile stress, separation of crystalline units into chain-unfolded fibrillar structure, and finally tandem stretching of both the crystalline and amorphous regions. Since indentation made with a sharp tip involve large strains, the latter stages of deformation are especially relevant in the current context. Furthermore, the first two stages may not be that significant as such, given the high orientation that the BCN nanosheets induced within the polymers. Since the final stages are controlled by crystalline regions, we can infer that a polymer with a higher χ can offer considerably higher resistance to plastic deformation, which rationalizes the positive correlation found between H and χ in **Figure 16a**. Since the addition BCN to PVA enhances the crystallinity in the latter, the substantially higher H in the nanocomposites can be attributed to the increased χ, which is facilitated by the presence of favourable surface functional groups in BCN and the formation of newer nucleation sites owing to surface roughness of the filler.

One very interesting observation was the variation of χ with composition (**Figure 17**). We observe that the trend is not linear and cannot be attributed to carbon content in the samples, surface area of the sample or the number of surface functional groups. Across all the BCN nanocomposites, the material with $(BN)_{0.75}(C)_{0.25}$ shows better crystallinity and mechanical properties than any other material examined in this study. The outperformance of this composite could be related to its strongest chemical heterogeneity in terms of its surface species and domains (**Table 2**).

Thermal properties

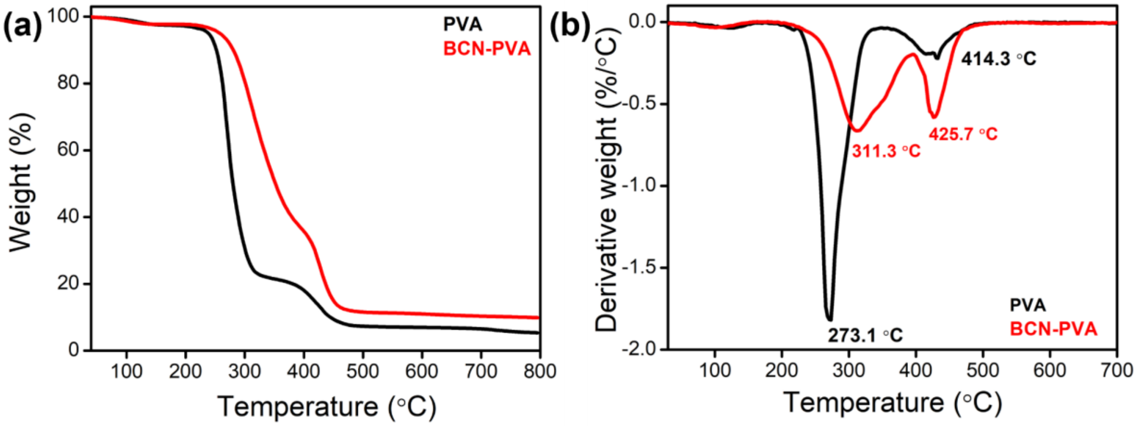

Figure 18: (a) TGA scans obtained on pure PVA and PVA-BCN nanocomposite under N_2 atmosphere and (b) corresponding DTG plot

Figures 18a and **18b** shows TGA scans and corresponding differential thermograms (DTG) plots of pure PVA and $(BN)_{0.75}(C)_{0.25}$-PVA nanocomposite. Both the polymer films undergo a two-step degradation process corresponding to the fragmentation of polymer backbone and then complete decomposition of the polymer at a higher temperature. A substantial shift in the thermogram of the nanocomposite towards higher temperature (**Figure 18b**) gives an indication of higher thermal stability of the nanocomposites which can be attributed to the higher heat capacity of the BCN sheets and better barrier effects which retards the volatilization of the polymer due to improved dispersion and interface.[54–56]

2.5 Conclusions

This work demonstrates successful quantification of surface functional groups on EG, BN and BCN using different dye molecules. The FLOSS results on carbonyl, carboxylic and amine groups are satisfactory, but for hydroxyl groups the results may not be as reliable due to lack of chemo-selectivity. The concentration of carbonyl and carboxylic groups increase with the carbon content in borocarbonitrides. FLOSS is a reliable method for the quantification of surface amine groups as well. We try to use these functional group estimates to understand the interactions of EG, BN and various compositions of BCN with polymer backbones while forming polymer nanocomposites. With BCN as nanofillers, these polymer nanocomposites gave 105% increment in hardness and 69% increment in elastic modulus with only 0.2 wt% of BCN on PVA, which is higher than for EG and BN reinforced polymer nanocomposites. The high surface area, various domains, and surface functionalities on BCN play a crucial role in the interfacial interaction between polymer and nanofiller via H-bonding. The substantial improvement in the mechanical properties upon the addition of nanofiller can be attributed to an increase in crystallinity of the semi-crystalline polymer due to the formation of newer nucleation centers owing to the surface roughness of the filler and effective load transfer between the polymer matrix and the nanofiller, aided by H-bonding. Furthermore, BCN reinforced PVA films have higher thermal stability as compared to pristine PVA. Hence, BCN nanosheets are superior reinforcement materials for enhancing the mechanical and thermal properties of polymers as compared to well-studied graphene and BN. Also, BCN can be produced economically compared to nanotubes and other kinds of nanocarbons.

References

(1) Kumar, N.; Moses, K.; Pramoda, K.; Shirodkar, S. N.; Mishra, A. K.; Waghmare, U. V.; Sundaresan, A.; Rao, C. N. R., *J. Mater. Chem. A*., **2013**, *1* (19), 5806–5821.

(2) Bahadur, R.; Singh, G.; Bando, Y.; Vinu, A., *Carbon*. **2022**, *190*, 142–169.

(3) Wang, S.; Ma, F.; Jiang, H.; Shao, Y.; Wu, Y.; Hao, X., *ACS Appl. Mater. Interfaces*, **2018**, *10* (23), 19588–19597.

(4) Rao, C. N. R.; Chhetri, M., *Adv. Mater*., **2019**. *31*(13), 1803668

(5) Chen, S.; Yang, H.; Chen, Q.; Liu, L.; Hou, X.; Luo, L.; Lin, C.; Li, C.; Chen, Y., *Electrochim. Acta*, **2020**, *346*, 136239.

(6) Hao, Y.; Wang, S.; Shao, Y.; Wu, Y.; Miao, S., *Adv. Energy Mater.*, **2020**, *10* (6), 1902836.

(7) Sreedhara, M. B.; Gopalakrishnan, K.; Bharath, B.; Kumar, R.; Kulkarni, G. U.; Rao, C. N. R., *Chem. Phys. Lett.*, **2016**, *657*, 124–130.

(8) Xing, Y.; Dementev, N.; Borguet, E., *Curr. Opin. Solid State Mater. Sci.*, **2007**, *11* (5–6), 86–91.

(9) Feng, X.; Dementev, N.; Feng, W.; Vidic, R.; Borguet, E., *Carbon*, **2006**, *44* (7), 1203–1209.

(10) Langley, L. A.; Villanueva, D. E.; Fairbrother, D. H, *Chem. Mater.*, **2006**, *18* (1), 169–178.

(11) Kondo, H.; Nishida, Y., *Bull. Chem. Soc. Jpn.*, **2007**, *80* (7), 1405–1412.

(12) Yegen, E.; Lippitz, A.; Treu, D.; Unger, W. E. S., *Surf. Interface Anal.*, **2008**, *40*, 176–179.

(13) Fairbank, R. W. P.; Wirth, M. J.; *J. Chromatogr. A*, **1999**; *830*, 285-291

(14) Moon, J. H.; Shin, J. W.; Kim, S. Y.; Park, J. W. *Langmuir*, **1996**, *12*, 4621-4624

(15) Kim, J.; Shon, H. K.; Jung, D.; Moon, D. W.; Han, S. Y.; Lee, T. G.; *Anal. Chem.*, **2005**, *77* (13), 4137–4141.

(16) Martini, G.; *Colloids Surf.*, **1990**, *45*, 83-133

(17) Chiu, C. F.; Dementev, N.; Borguet, E.; *J. Phys. Chem. A*, **2011**, *115* (34), 9579–9584.

(18) Dementev, N.; Feng, X.; Borguet, E.; *Langmuir*, **2009**, *25* (13), 7573–7577.

(19) Pellenbarg, T.; Dementev, N.; Jean-Gilles, R.; Bessel, C.; Borguet, E.; Dollahon, N.; Giuliano, R.; *Carbon,* **2010**, *48* (15), 4256–4267.

(20) Holländer, A.; *Surf. Interface Anal.,* **2004**; *36*, 1023–1026.

(21) Randall Holmes-Farley, S.; Whitesides, G. M.; *Langmuir*, **1986**, *2*, 266-281

(22) McArthur, E. A.; Ye, T.; Cross, J. P.; Petoud, S.; Borguet, E.; *J. Am. Chem. Soc.*, **2004**, *126* (8), 2260–2261.

(23) Ivanov, V. B.; Behnisch, J; Hollander, A.; Mehdorn, F.; Zimmermann, H.; *Surf. Interface Anal.,* **1996**; *24*, 251-262

(24) Njuguna, J.; Pielichowski, K.; Desai, S.; *Polym. Adv. Technol.,* **2008**, *19*(8), 947–959.

(25) Ramanathan, T.; Abdala, A. A.; Stankovich, S.; Dikin, D. A.; Herrera-Alonso, M.; Piner, R. D.; Adamson, D. H.; Schniepp, H. C.; Chen, X.; Ruoff, R. S.; Nguyen, S. T.; Aksay, I. A.; Prud'Homme, R. K.; Brinson, L. C.; *Nat. Nanotechnol.*, **2008**, *3* (6), 327–331.

(26) Liu, P.; Jin, Z.; Katsukis, G.; Drahushuk, L. W.; Shimizu, S.; Shih, C.-J.; Wetzel, E. D.; Taggart-Scarff, J. K.; Qing, B.; van Vliet, K. J.; Li, R.; Wardle, B. L.; Strano, M. S.; Science, S. O.; *Science*, 2016; *353,* 364-367

(27) Keller, T.; *Prog. Struct. Eng. Mater.*, **2001**, *3* (2), 132–140.

(28) Prasad, K. E.; Das, B.; Maitra, U.; Ramamurty, U.; Rao, C. N. R.; *Proc. Natl. Acad. Sci.,* **2009**; *106*(32), 13186-13189.

(29) Jan, R.; May, P.; Bell, A. P.; Habib, A.; Khan, U.; Coleman, J. N.; *Nanoscale*, **2014**, *6* (9), 4889–4895.

(30) Hummers, W. S.; Offeman, R. E.; *J. Am. Chem. Soc.*, **1958**, *80* (6), 1339.

(31) Subrahmanyam, K. S.; Vivekchand, S. R. C.; Govindaraj, A.; Rao, C. N. R.; *J. Mater. Chem.,* **2008**, *18* (13), 1517–1523.

(32) Nag, A.; Raidongia, K.; Hembram, K. P. S. S.; Datta, R.; Waghmare, U. V.; Rao, C. N. R.; *ACS Nano*, **2010**, *4* (3), 1539–1544.

(33) Jana, A.; Saha, B.; Ikbal, M.; Ghosh, S. K.; Singh, N. D. P.; *Photochem. Photobiol. Sci.,* **2012**, *11* (10), 1558–1566.

(34) Gong, B.; Choi, B. K.; Kim, J. Y.; Shetty, D.; Ko, Y. H.; Selvapalam, N.; Lee, N. K.; Kim, K.; *J. Am. Chem. Soc.*, **2015**, *137* (28), 8908–8911.

(35) Oliver, W. C.; Pharr, G. M.; *J. Mater. Res.*, **1992**, *7* (6), 1564–1583.

(36) Klapperich, C.; Komvopoulos, K.; Pruitt, L., *J. Tribol.*, **2001**, *123* (3), 624–631.

(37) Briscoe, B. J.; Fiori, L.; Pelillo, E. Nano-Indentation of Polymeric Surfaces; *J. Phys. D Appl Phys.*, **1998**; *31*, 2395-2405

(38) Kadambi, S. B.; Pramoda, K.; Ramamurty, U.; Rao, C. N. R.; *ACS Appl. Mater. Interfaces,* **2015**, *7* (31), 17016–17022.

(39) Tuinstra F; Koenig J.L., *J. Chem. Phys.* **1970**, *53* (3), 1126–1130.

(40) Flink, S.; van Veggel, F. C. J. M.; Reinhoudt, D. N., *Adv. Mater.*, **2000**, *12*(18), 1315-1328

(41) Song, S. W.; Hidajat, K.; Kawi, S.; *Langmuir,* **2005**, *21* (21), 9568–9575.

(42) Gallegos-Suarez, E.; Pérez-Cadenas, M.; Guerrero-Ruiz, A.; Rodriguez-Ramos, I.; Arcoya, A.; *Appl. Surf. Sci.,***2013**, *287,* 108–116.

(43) Holländer, A.; *Surf. Interface Anal.*, **2004**; *36*, 1023–1026.

(44) Chen, J.; Gao, Y.; Liu, W.; Shi, X.; Li, L.; Wang, Z.; Zhang, Y.; Guo, X.; Liu, G.; Li, W.; Beake, B. D; *Carbon,* **2015**, *94*, 845–855.

(45) Zhu, Y.; Wang, H.; Zhu, J.; Chang, L.; Ye, L.; *Appl. Surf. Sci.,* **2015**, *349*, 27–34.

(46) Hong, P.-D.; Chen, J.-H.; Wu, H.-L.; *J. Appl. Polym. Sci.,* **1998**; *69*, 2477-2486

(47) Cadek, M.; Coleman, J. N.; Barron, V.; Hedicke, K.; Blau, W. J.; *Appl. Phys. Lett.,* **2002**, *81* (27), 5123–5125.

(48) Schadler, L. S.; Giannaris, S. C.; Ajayan, P. M.; *Appl. Phys. Lett.,* **1998**, *73* (26), 3842–3844.

(49) Das, B.; Eswar Prasad, K.; Ramamurty, U.; Rao, C. N. R.; *Nanotechnology*, **2009**, *20* (12).

(50) Mohsin, M.; Hossin, A.; Haik, Y.; *J. Appl. Polym. Sci.,* **2011**, *122* (5), 3102–3109.

(51) Liang, J.; Huang, Y.; Zhang, L.; Wang, Y.; Ma, Y.; Cuo, T.; Chen, Y.; *Adv. Funct. Mater.,* **2009**, *19* (14), 2297–2302.

(52) Gong, L.; Kinloch, I. A.; Young, R. J.; Riaz, I.; Jalil, R.; Novoselov, K. S.; *Adv. Mater.*, **2010**, *22* (24), 2694–2697.

(53) Coleman, J. N.; Cadek, M.; Blake, R.; Nicolosi, V.; Ryan, K. P.; Belton, C.; Fonseca, A.; Nagy, J. B.; Gun'ko, Y. K.; Blau, W. J.; *Adv. Funct. Mater.*, **2004**, *14* (8), 791–798.

(54) Chen, K.; Song, S.; Liu, F.; Xue, D.; *Chem. Soc. Rev.*, **2015**, *44* (17), 6230–6257.

(55) Morimune, S.; Nishino, T.; Goto, T.; *Polymer,* **2012**, *44* (10), 1056–1063.

(56) Wan, Y. J.; Tang, L. C.; Gong, L. X.; Yan, D.; Li, Y. B.; Wu, L. bin; Jiang, J. X.; Lai, G. Q.; *Carbon*, **2014**, *69*, 467–480.

Chapter-3

A novel method for synthesis of γ-graphyne and their charge transfer properties

SUMMARY

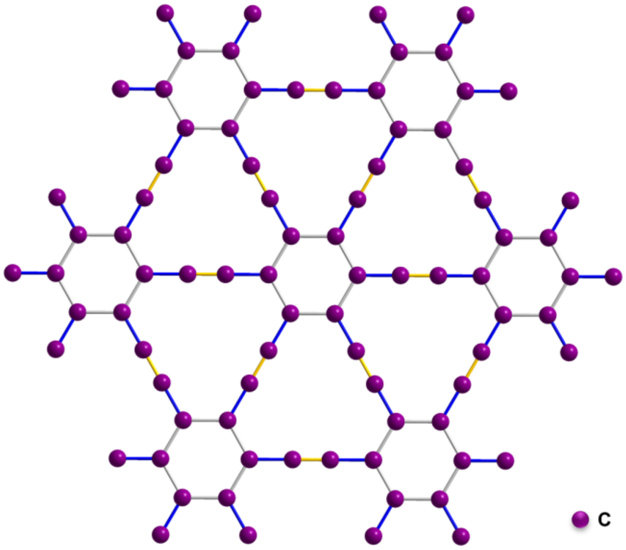

Carbon with its many natural and artificial allotropes of different hybridizations and dimensionalities occupies a very distinctive position in material science. Graphynes are an interesting family of artificial carbon allotropes that are layered in nature and incorporate both sp and sp^2 hybridized carbon in the lattice. Graphynes are predicted to have very high carrier mobilities ~10^5 $cm^2V^{-1}s^{-1}$, with some members of this group having Dirac cones like graphene while some have an inherent bandgap and have been theoretically predicted to be of significance in nanoelectronics, gas separation, water desalination, and energy storage applications. Theoretical reports predict that graphynes might even outdo graphene with respect to its charge transport properties. γ-graphyne, the most stable member of this group is theoretically reported to have carrier

---

*Manuscript under preparation

mobilities in the range of 10^4-10^5 $cm^2V^{-1}s^{-1}$ along with a monolayer bandgap of ~2.23 eV. Synthesis techniques for this class of materials are still at a developing stage. In this work, we report a simple one-pot Sonogashira cross-linking procedure to synthesize γ-graphyne under mild conditions with very high yields. The solid product is found to be chemically pure and has lesser defects than any previous report. Charge transfer studies carried out to understand the electron transfer behavior and defect density of γ-graphyne showed a similar/ slightly better performance with electron acceptors compared to few-layered graphene.

3.1 Introduction

Carbon is a very important member of the periodic table and forms the basis of all life on earth. Its ability to bind to itself or nearly to all other elements offers limitless potential. Carbon's multiple hybridizations (sp, sp^2, and sp^3) along with potential structural diversities offer possibilities for the synthesis of materials for a plethora of applications.[1] Apart from the natural carbon allotropes of graphite (pure sp^2) diamond (pure sp^3), many synthetic allotropes of carbon of various dimensionalities have also been successfully synthesized including fullerenes (0D, sp^2)[2], nanotubes (1D sp^2)[3], graphene (2D, sp^2)[4] and have been found to display outstanding electronic, optical, magnetic, mechanical properties, although carbyne (1D, sp) still remains elusive.[5,6]These interesting discoveries have also encouraged people to explore many other synthetic allotropes of carbon,

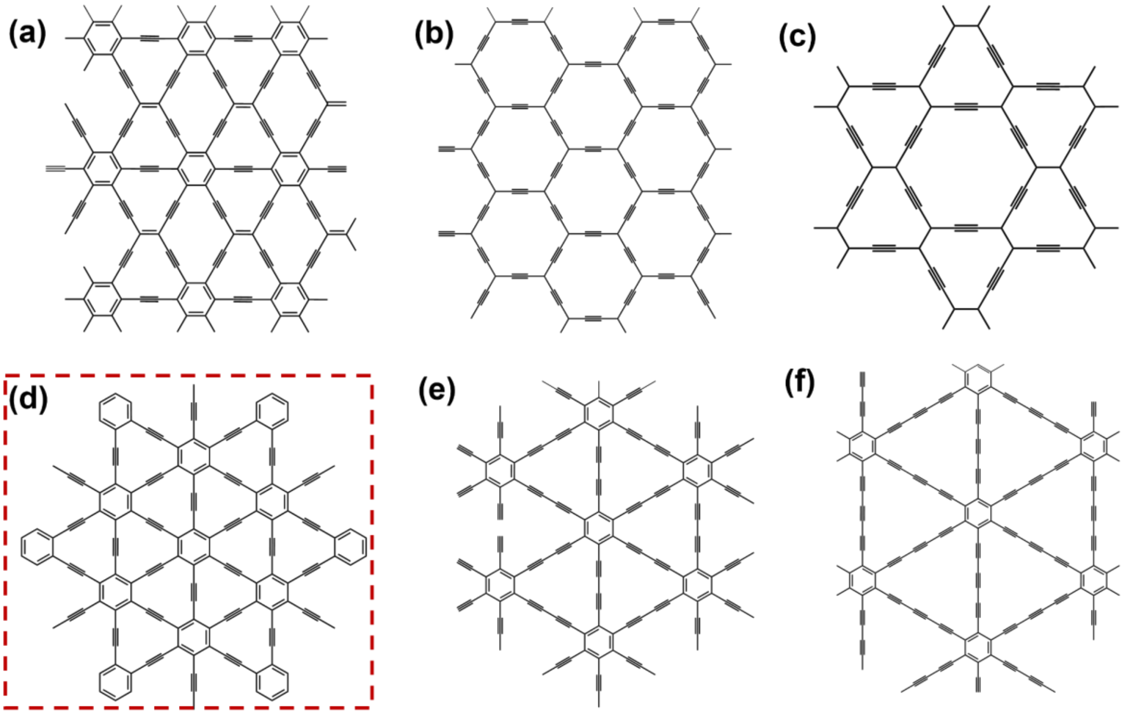

Figure 1: Pictorial representation of some members of graphyne family. (a) 6,6,12-graphyne, (b) α-graphyne, (c) β-graphyne, (d) γ-graphyne, (e) graphdiyne or graphyne-2 and (f) graphyne-3

particularly those with mixed hybridizations like graphynes (sp^2 + sp) and diamondynes (sp^3 + sp). [1,7–20]

Graphynes are a family of synthetic allotropes of carbon wherein both sp^2 and sp carbon atoms coexist in the lattice and can be subdivided into many different structural forms denoted as α, β, γ, graphdiyne, etc. based on the ratio of sp: sp^2 carbon atoms, nature of the sp^2 bond and number of intervening sp carbon atoms in the lattice in between two sp^2 C atoms (**Figure 1**).[21] The existence of graphynes was first conjectured in the 1960s and had attracted a lot of attention since the discovery of fullerenes.[22] Graphynes were first theoretically predicted by Baughman et al[23] in 1987 and since then there have been multiple theoretical reports on them and at present, graphynes form one of the biggest branches of 2D carbons although experimental studies are still in the developing stages.

The most stable member of this group, γ-graphyne (**Figure 1d**) belongs to P6/mmm space group, is kinetically stable against graphitization, and has been predicted to have formation energies comparable to C_{60} and C_{70}.[7] According to theoretical investigations, γ-graphyne is semiconducting due to the Kekule-distortion effect, with a monolayer bandgap of 2.3 eV and high carrier mobility (10^4-10^5 $cm^2V^{-1}s^{-1}$).[7] γ-graphyne is reported to have exceptional flexibility in geometric structure with lower thermal conductance compared to graphene and charge transport properties comparable to graphene and a band structure unique from other existing carbon allotropes.[7,9,11,15,19,21,24] Moreover, owing to their intrinsic porous/hollow structures, γ-graphyne is also being considered a promising material for various energy storage applications.[21]

Since 1987, there have been multiple reports on different approaches to the synthesis of pure graphynes. Initial experimental efforts were mainly based on the synthesis of graphyne oligomers using multiple annulene chemistry routes, alkyne metathesis, and various cross-linking strategies like tandem Sonogashira and Negishi cross-linking, etc.[25–27] These efforts proved the possibility of synthesizing such carbon-rich backbones but had extremely poor yields. One major breakthrough came in 2010 with the successful synthesis of graphdiyne[28] (**Figure 1e**) on Cu foil by Glyser-Hay cross-linking and although the yields were poor, this discovery established the possibility of synthesis of similar artificial carbon allotropes and inspired more rigorous efforts towards developing synthesis strategies for γ-graphyne.[9] Multiple research groups have tried to synthesize γ-graphyne (**Figure 1d**) using interfacial synthesis, but such methods are also limited by their poor yields.[29,30] In recent years, mechanochemical/ultrasonication-based methods for the synthesis of γ-graphyne have come into consideration due to high yields, however, the solid product obtained is very prone to defects in the lattice.[31–33] At present, an effective synthesis strategy is a primary deterrent in all graphyne-related research.

3.1.1 Charge transfer studies

In recent years, low-dimensional materials are gathering immense attention for optoelectronic applications due to their strong light-matter interactions and tunable band structures.[34] For different applications, it is highly desirable to tune the carrier type and carrier concentrations of 2D materials without introducing any defects or scattering sites in the lattice. One key fundamental step underlying these applications is charge transfer from or into the material the theoretical framework of which was suggested by Marcus in the 1950s.[35] Charge transfer process takes place in the nanoscale ranges (~1 nm) and involves the radiation-less transfer of energy between a donor and an acceptor.[36]

One convenient method for tailoring a materials band structure is via charge transfer doping wherein the 2D material is allowed to interact with different donor/acceptor molecules.[37] For layered materials with conjugated π-networks like graphene or graphyne, charge transfer generally takes place via van der Waals interactions, dipole-dipole interaction, or π-π conjugations. These interactions tune the electronic properties of the material without disrupting the inherent lattice. Charge transfer interactions with the dipole of an interfacing donor/ acceptor molecule along with molecular orbital rehybridizations have already been reported for graphene.[38] Band structure tuning by charge transfer studies is more convenient for 2D materials compared to bulk due to the low density of states and weak screening effect.[39] Charge transfer interactions in a material broadly depend on the inherent nature of the material, its chemical purity, and defect density, and hence having a low-defect/pristine sample is of utmost importance. Moreover, theoretical reports claim that graphyne is expected to show an even better charge transport behavior than graphene, hence charge transfer studies in the as-synthesized γ-graphyne might lead to interesting results.[21]

According to theoretical predictions, successful charge transfer of 2D materials with acceptors like 7,7,8,8-Tetracyanoquinodimethane (TCNQ) and donors like Tetrathiafulvalene (TTF) can be predicted by the following equations:[37]

$$\Delta E_{CH} = E_{CBM} – E_{HOMO} \qquad [1]$$

$$\Delta E_{VL} = E_{VBM} - E_{LUMO} \qquad [2]$$

wherein E_{CBM} and E_{VBM} refer to the conduction band minima and valence band maxima of the 2D material and E_{LUMO} and E_{HOMO} refer to the HOMO or LUMO of the donor/acceptor molecule. For successful charge transfer with acceptor $\Delta E_{VL} > 0$, successful charge transfer with donors will occur when $\Delta E_{CH} < 0$.

3.2 Scope of this work

In this work, we have carried out a one-pot Sonogashira cross-linking reaction to synthesize pristine layered γ-graphyne. The reaction procedure used for synthesis is mild and gave us a solid product with high yields. To the best of our knowledge, no other literature report has claimed synthesis of γ-graphyne of such high purity. We have studied the charge transfer interaction of the as-synthesized material with donor/acceptor molecules to understand its charge transport behavior.

3.3 Experimental

Materials

Hexabromobenzene (C_6Br_6) (Merck, 98%), Copper acetylacetonate ($Cu(acac)_2$) (Merck, 99.9%), Palladium (II) acetate ($Pd(OAc)_2$) (Merck, 47% Pd), Triphenylphosphine (PPh_3) (Merck, 99%), Tetrabutylammonium fluoride (TBAF) (Merck, 1M in THF) were used without further purification. Calcium carbide (CaC_2) (Merck, 80%) was ground with mortal-pestle before use. Dimethyl sulfoxide (DMSO) (Sigma-Aldrich, 99%) was dried with 3Å molecular sieves and then degassed with Ar before use. UV studies were carried out using 7,7,8,8-Tetracyanoquinodimethane (TCNQ) (Merck, 98%), Tetrathiafulvalene, (TTF) (Merck, 97%), Acetonitrile (ACN) (Spectrochem, HPLC grade). Acetonitrile was dried using 3 Å molecular sieves and degassed with N_2 before use.

Synthesis

γ-graphyne synthesis was carried out by modifying a previously reported synthesis method for small molecules.[40] Palladium (II) acetate (33.6mg, 0.15 mmol), Copper acetylacetonate (39.6mg, 0.15 mmol), triphenylphosphine (162mg, 0.6mmol) and DMSO (10 mL) were added into an oven-dried schlenk flask, and the solution was purged with Ar for 10 minutes. Then TBAF stock solution (3mL), calcium carbide (according to the desired ratio), and hexabromobenzene (275mg, 0.5 mmol) were successively added to the solution and the reaction was stirred at 65°C for 24 hours. According to the molar ratio between calcium carbide and hexabromobenzene, the samples were labeled as GY (1:1)-GY (14:1). The reaction was allowed to reach room temperature and then quenched with an aqueous ammonium chloride solution (5%), washed with 1M nitric acid solution followed by copious amounts of distilled water, and finally with diethyl ether. The solid products were lyophilized for 48 hours to remove traces of organic solvents from the sample. Exfoliation of these bulk materials was carried out by ultrasonication in isopropyl alcohol for 15 minutes.

Sample preparation for charge transfer studies

TCNQ and TTF stock solutions of 10^{-2} M were prepared in acetonitrile. The solvent and concentrations chosen for charge transfer studies are very crucial as these molecules (TCNQ/TTF) are highly sensitive to reaction conditions. For the selection of an appropriate solvent, the UV cutoff of the solvent was taken into consideration along with its inherent charge transfer behavior with the molecules under study. We have studied these molecules in ethanol, acetonitrile, tetrahydrofuran, N-methyl pyrrolidone, 1,4-Dioxane, 2-Butanol, dichloromethane, chloroform, and acetonitrile turned out to be the most suitable solvent for both the molecules. The concentrations used for the study were also decided according to the charge transfer behavior of the molecule with the solvent. Acetonitrile was the solvent of choice due to its poor charge transfer behavior with TCNQ and TTF. Solutions of concentrations in between $1*10^{-4}$ and $1*10^{-5}$ M were used for the study. Few-layered graphyne (GY) and graphene stock solutions were prepared by dispersing 4.5mg of the solid in 7.5 mL acetonitrile followed by sonication for 30 minutes. The solutions were allowed to settle for 10 minutes prior to use.

For charge transfer studies, 3mL solutions with desired concentrations were prepared. According to the amount of few-layered graphyne/few-layered graphene dispersion into this 3mL solution the concentrations are labeled as c1 (200 µL), c2 (500 µL), c3 (800 µL), c4 (1mL), and c5 (1.5mL). For charge transfer studies with both TCNQ and TTF, the solution was allowed to stir for 6 hours prior to measurement.

Physical Characterization

The solid products were freeze-dried at -105°C for 48 hours in an SP Vitris Benchtop Pro freeze drier. Fourier transform-infrared spectra (FT-IR) were recorded in a Bruker FTIR spectrometer in ATR mode. Raman spectra were recorded on a Horiba LabRAM HR revolution Raman spectrometer equipped with a 405 nm laser with a spectral resolution of 1.0 cm^{-1} for 1800 groves/mm grating, equipped with Labspec software. FESEM images were recorded on Thermofisher FEI Quanta 3D instrument equipped with field emission gun and EDS detector and Thermofisher Apneo 2S with an accelerating voltage range: 200 V – 30 kV and FEG filament with better than 1.2 nm resolution. Bright-field transmission electron microscopy images were recorded on a JEOL 200kV JEM 100

PLUS HRTEM instrument. AFM analyses were carried out in contact mode on a Bruker Innova AFM instrument. Nanoscope analysis software was used to analyze the data. X-ray photoelectron spectroscopy studies were carried out on a Thermo K-alpha+ spectrometer using micro-focused and mono chromated Al K_α radiation (1486.6 eV), 400μm spot size, pass energy of 50 eV and a step size of 0.1 eV and resolution of 0.6 eV. XPS analysis of core-level spectra was done on fityk software using VoigtA function for peak fitting with a linear background. UV studies were carried out in Perkin Elmer LAMDA 750 instruments with Tungsten-halogen, and deuterium light source and high sensitivity R928 Photomultiplier (PMT) detector for UV/Vis and Peltier cooled PBS detector for NIR. Resistivity measurements were carried out in Physical Property Measurement System (PPMS), Quantum design, USA in electrical transport option (ETO).

3.4 Results and Discussion

Material characterization

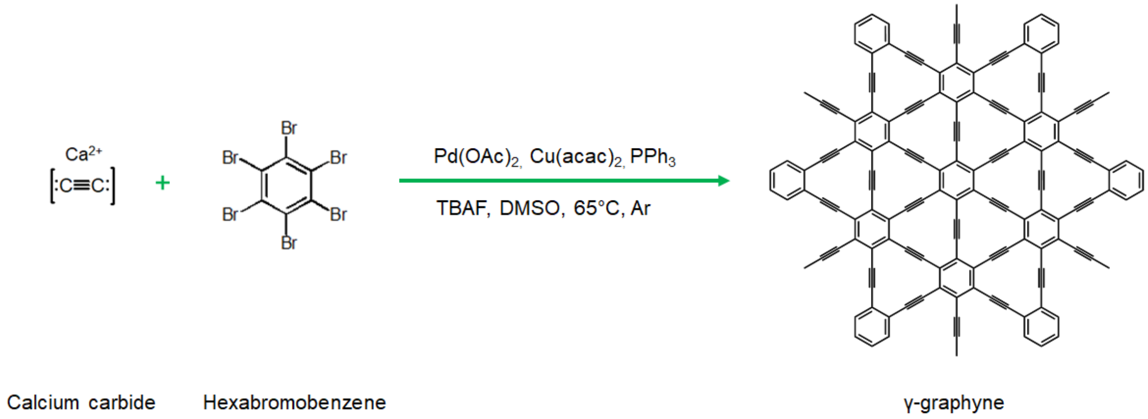

Scheme 1: Pictorial representation of the proposed reaction

Scheme 1 gives a pictorial representation of the reaction under study. We have carried out a simple one-pot Sonogashira cross-linking reaction to synthesize pure γ-

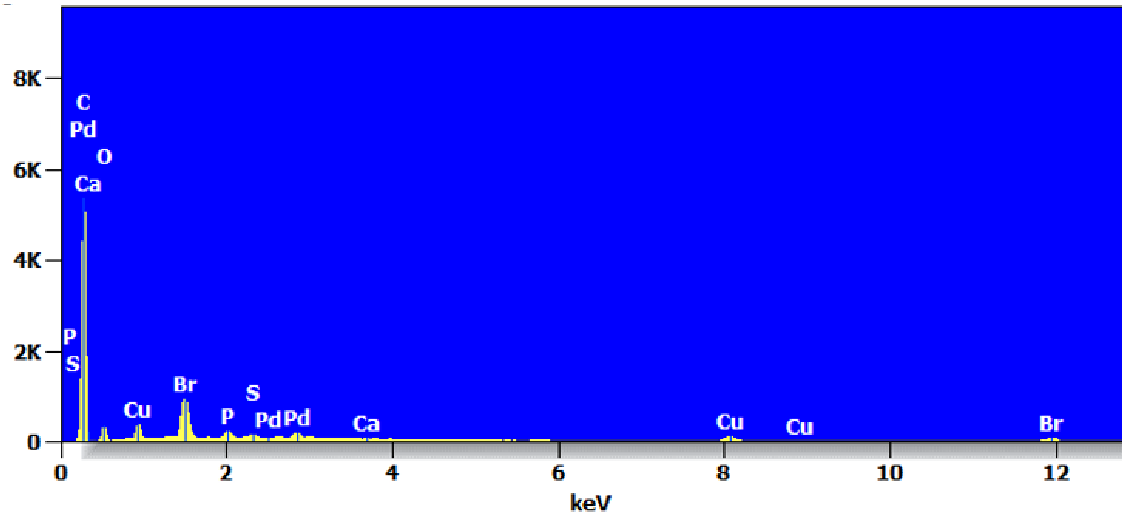

Figure 2: Energy dispersive X-ray spectra of the as-synthesized γ-graphyne

Table 1: Elemental composition of the as-synthesized γ-graphyne

Element	Atomic Percentage
C	82.77
Br	1.67
O	13.53
Pd, P, Ca, Cu, S	<1

graphyne in high yields. According to energy-dispersive spectroscopy (EDS) analysis, the atomic percentage of carbon in the sample is >80% (**Figure 2, Table 1**), which confirms the purity of the sample. **Figure 3** shows the FT-IR spectra of the as-synthesized γ-graphyne along with starting materials. γ-graphyne shows broad aromatic carbon signatures between 1700-1550 cm^{-1} and a broad feature ~2200 cm^{-1}. Inset shows the FT-IR spectra of γ-graphyne in the region 2500-1800 cm^{-1} wherein the broad peak at 2200 cm^{-1} is a characteristic of sp hybridized carbon and the sharp peak at 2300 cm^{-1} is due to atmospheric CO_2 adsorption. The sample also shows residual solvent signatures between

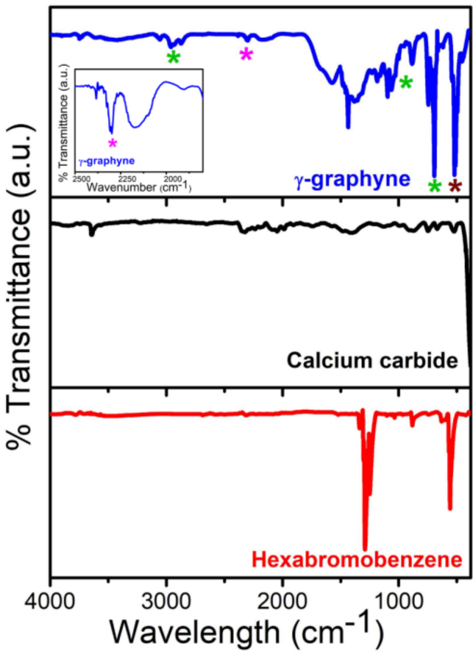

Figure 3: FT-IR spectra of as-synthesized γ-graphyne along with starting materials calcium carbide and hexabromobenzene

* denotes solvent peaks, * denotes CO_2 adsorption, and * denotes possible C-Br vibrational mode

3000-2800 cm^{-1} and 1400-600 cm^{-1} along with a sharp peak at 519 cm^{-1} which could be due to C-Br stretching from side reactions. Calcium carbide shows weak vibrational peaks at 3636 cm^{-1} (O-H stretch) and a broad feature between 1480-1370 cm^{-1} (C≡C stretch). Hexabromobenzene shows two sharp peaks at 1280 cm^{-1} (aromatic sp^2 carbon stretching mode) and 557 cm^{-1} (C-Br stretching mode).

To have a better understanding of the bonding nature of the synthesized compounds we have done Raman measurements. Theoretical calculations predict three Raman active modes for γ-graphyne with two phonons of A_{1g} symmetry (2258, 1221 cm^{-1}) and one phonon with E_g symmetry (1518 cm^{-1}) (**Figure 4c**).[41,42] **Figure 4** shows the Raman spectra of γ-graphyne along with that of starting materials and of pure graphite. γ-graphyne shows

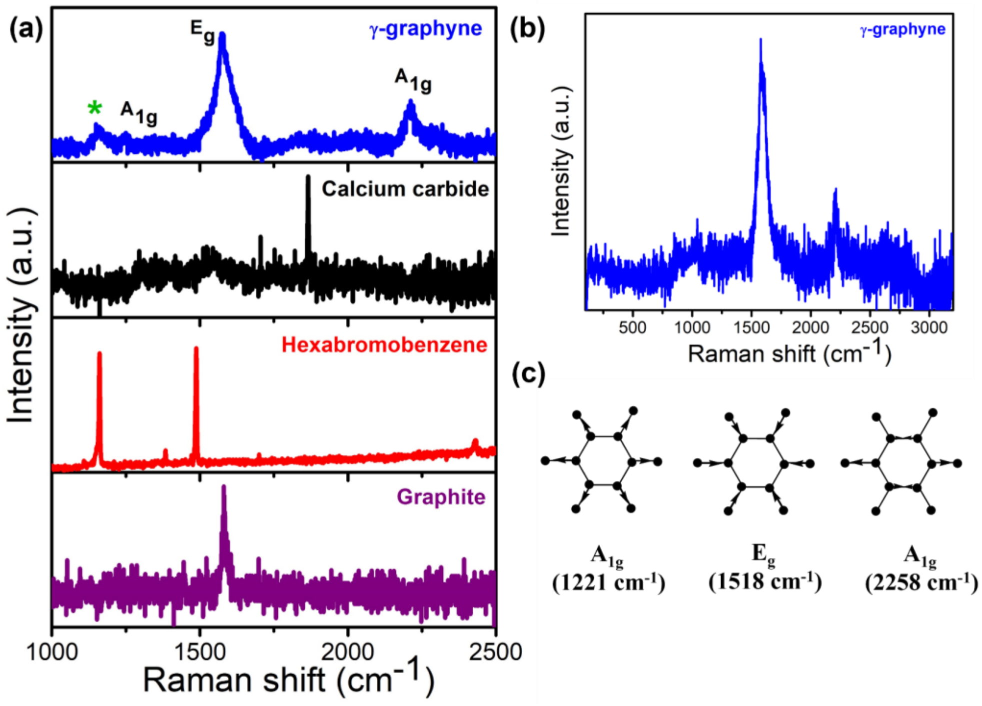

Figure 4: Raman spectra of (a) γ-graphyne along with graphite and starting materials calcium carbide and hexabromobenzene, (b) full-range spectra of γ-graphyne highlighting the absence of any C-Br stretching modes, (c) theoretically predicted Raman active modes of γ-graphyne

* denotes solvent peaks

three peaks at 2209, 1577, and 1250 cm^{-1} which match with the theoretical predictions for γ-graphyne and can be assigned to displacements of sp carbon atoms, G-mode due to sp^2 carbon, and breathing mode of carbon hexagon (**Figure 4c**).[41,42] The Raman spectra of γ-graphyne confirms that the synthesized compound is indeed γ-graphyne. Interestingly, we did not detect any sp^3 C defect signature (~1350 cm^{-1}) in our γ-graphyne sample. The presence of sp^3 C/defect or D band is a common feature for most reported graphyne synthesis methods using mechanochemistry, ultrasonication, or interfacial methods. Hence, Raman spectra of the as-synthesized γ-graphyne confirm its pristine nature compared to all previously available literature reports.[29,31–33] Calcium carbide shows a sharp peak at 1863 cm^{-1} corresponding to sp hybridized C while hexabromobenzene shows two peaks at 1158 and 1486 cm^{-1} corresponding to aromatic ring breathing mode and sp^2 C stretch respectively. Pure graphite shows a sp^2 C signature at 1580 cm^{-1} with no defect band ~1300 cm^{-1}. We did not detect any Raman peak corresponding to C-Br (~ 500 cm^{-1}) bond in the full range spectra of γ-graphyne (**Figure 4b**), thus lowering the possibility of side reactions. The peak at 1150 cm^{-1} is due to the residual solvent in the sample.

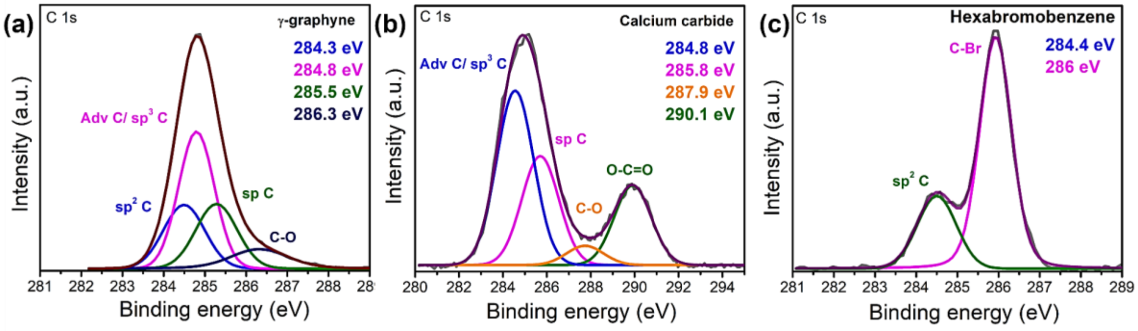

Figure 5: C1s XPS core-level spectra of (a) γ-graphyne showing the presence of sp and sp^2 C in the ratio1:1, (b) calcium carbide, and (c) hexabromobenzene

The C 1s core-level X-ray photoelectron spectra of γ-graphyne can be deconvoluted into four peaks at 284.3, 284.8, 285.5, and 286.3 eV corresponding to sp^2 C, adventitious C/ sp^3 C (from solvent), sp C, and C-O/C-Br species (**Figure 5a**). For this study, a series of reactions were carried out by varying the molar ratios of calcium carbide and hexabromobenzene from 1:1 to 14:1. Amongst the products obtained, for molar ratios 6:1, 8:1, and 10:1, the sp C: sp^2 C ratio ~1 as had been theoretically reported for γ-graphyne.[23] This further validates that the synthesized compound is pristine γ-graphyne. Deconvoluted C1s core-level spectra of calcium carbide show an sp C characteristic peak at 285.8 eV (**Figure 5b**) and hexabromobenzene shows sp^2 C and C-Br signatures at 284.8 and 286 eV (**Figure 5c**).

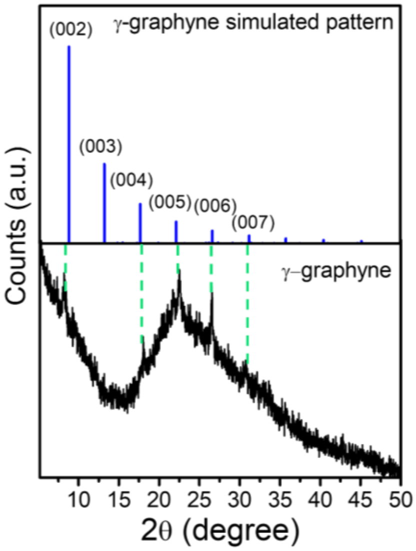

Figure 6: Powder XRD pattern of γ-graphyne matched with the corresponding simulated pattern

In **Figure 6**, the powder X-ray diffraction pattern of γ-graphyne (GY) is matched with the corresponding simulated pattern from the CIF file[7] generated using Diamond software. γ-graphyne shows a broad amorphous carbon-like signature along with some small peaks which match with the simulated pattern further validating the chemical identity of the sample.[7,43]

Morphology of the as synthesized nanosheets was confirmed by FESEM, TEM, and AFM. **Figure 7a** shows the FESEM images of bulk γ-graphyne displaying micron-sized layers stacked together by weak van der Waals interactions. Bulk γ-graphyne was exfoliated by ultrasonication in isopropyl alcohol (**section 3.2**). During sonication, cavitation bubbles are formed which implode together to give high-energy jets which shear apart the bulk layered crystal into few-layered to monolayered nanoflakes.[44] Bright-field TEM images of exfoliated γ-graphyne displays nanosheets of lateral dimensions ~ 1µm with wrinkled morphology establishing the few-layered nature of the sample (**Figures 7b**).

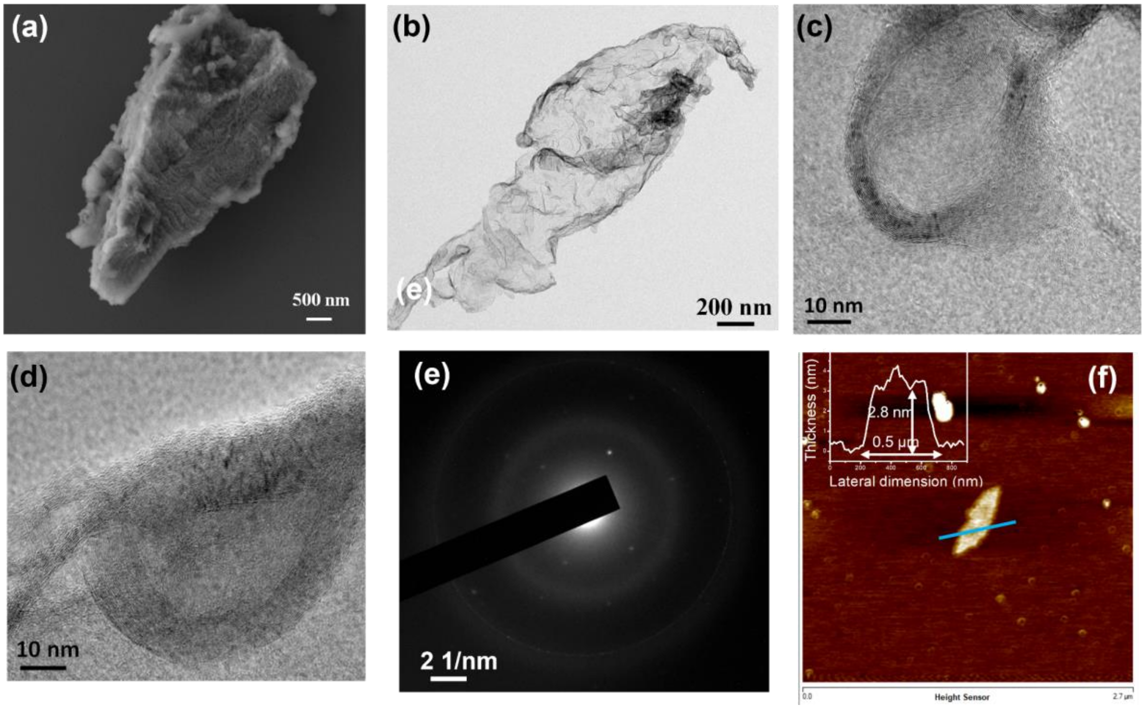

Figure 7: (a) FESEM image of bulk γ-graphyne along (b) bright-field TEM image of exfoliated γ-graphyne, with the corresponding (c-d) HR-TEM images, and (d) electron diffraction pattern, and (f) AFM image of exfoliated γ-graphyne along with corresponding height profile

Figure 7c and 7d show HR-TEM images of γ-graphyne with calculated d spacings of ~3.8 Å which corresponds to (014) refection according to the simulated pattern with 2θ value of 23.4°. SAED patterns of γ-graphyne highlight the crystalline nature of the sample (**Figure 7e**). **Figure 7f** shows a representative AFM image of exfoliated γ-graphyne with a nanosheet of lateral dimension ~500nm and thickness ~3nm. We expect this sample to be < 5 layers thick as AFM is known to overestimate thickness for liquid exfoliated nanosheets due to the presence of residual solvent layer and contribution from capillary forces and adhesion.[45]

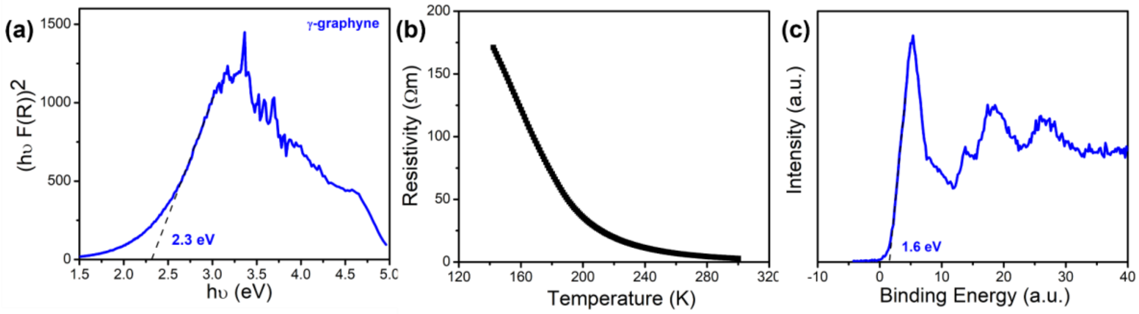

Figure 8: (a) Tauc plot of γ-graphyne, (b) temperature dependent resistivity plot of γ-graphyne, and (c) XPS Valence band spectra of γ-graphyne

While graphene is a very remarkable material displaying excellent electronic, magnetic, mechanical properties, one major limitation is its zero bandgap which limits its applications. One driving force behind the increased interest in graphynes or other carbon allotropes is the promise behind incorporating similar extraordinary properties but with an inherent bandgap. The as-synthesized bulk γ-graphyne shows a bandgap of 2.3 eV while the theoretically reported value for is monolayer 2.23 eV (**Figure 8a**).[20] Temperature-dependent resistivity measurements of bulk γ-graphyne display true semiconducting behavior with a negative temperature coefficient of resistance and a resistivity value of 1.38 Ωm at 300K (**Figure 8b**). For metallic samples, the residual resistivity ratio (RRR) (ρ_{300K}/ρ_{0K}) gives an estimate of the purity and quality of the sample.[46] In the case of γ-graphyne, measurements could only be done till 142K and the corresponding RRR is 0.017 which indicates that the as-synthesized material is pristine in nature. Residual resistivity values have already been reported to be very useful in identifying resonant and non-resonant impurities in semiconductors.[47] **Figure 8c** shows the valence band spectra of γ-graphyne with valence band edge at 1.6 eV which is distinct from the reported valence band spectra of other carbon allotropes as graphite and diamond and of the starting materials and indicates a semiconducting nature for the material.[48]

Gas adsorption studies are important characterizations for understanding the texture of porous materials and hence N_2 adsorption studies were carried out for the γ-graphyne sample at 77 K.[49] **Figure 9a** shows the adsorption isotherm of γ-graphyne displaying Type IVa adsorption isotherm with capillary condensation accompanied by a hysteresis which is a characteristic for mesoporous materials with a multipoint BET surface area of 473 m^2/g. **Figure 9b** shows the corresponding DFT pore-size distribution plots of adsorption *dV(r)* vs pore radius, with the majority pore radius of sizes 8.8 Å and 13.8 Å.

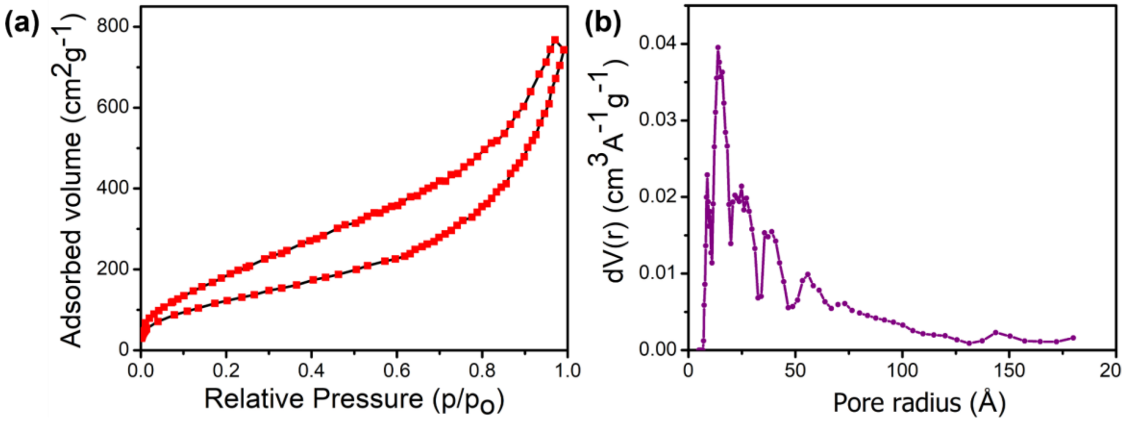

Figure 9: (a) N_2 adsorption isotherm of γ-graphyne and the corresponding (b) pore-size distribution analysis using DFT method

Reaction mechanism

We report the synthesis of pristine layered γ-graphyne using a one-pot Sonogashira cross-linking reaction between hexabromobenzene and calcium carbide at 65°C under an inert atmosphere using Pd(II) catalyst and Cu(II) as cocatalyst.[40] **Scheme 2** gives a detailed representation of the reaction along with the intermediate steps involved. **Scheme 3** shows

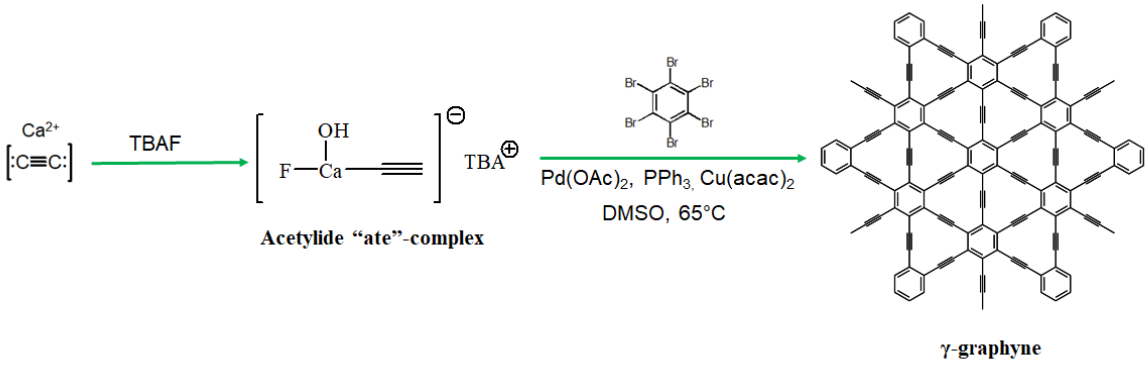

Scheme 2: Pictorial representation of the steps involved in the reaction

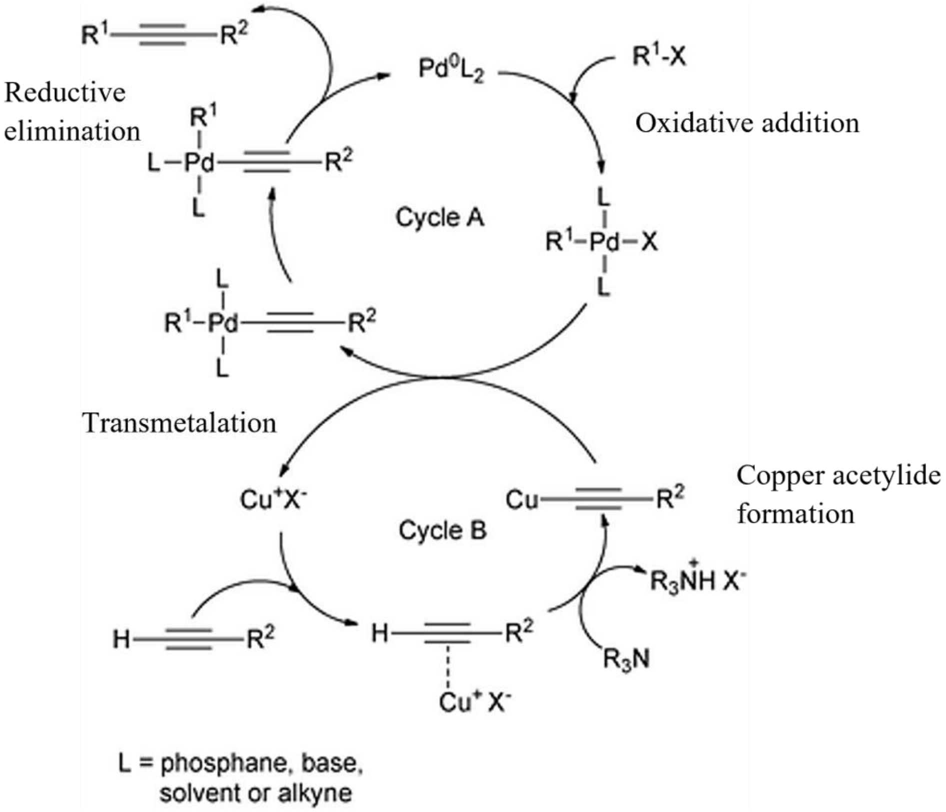

Scheme 3: Typical mechanism of a copper co-catalyzed Sonogashira reaction. Adapted with permission from Royal Society of Chemistry, ref 59; permission conveyed through Copyright Clearance Center, Inc.

a typical Sonogashira cross-linking reaction mechanism. The reaction starts with the reduction of Pd(II) salts to Pd(0) nanoparticles and Cu(II) salts to Cu(0) nanoparticles in the presence of tetrabutylammonium fluoride (TBAF), stabilized by triphenylphosphine ligands (PPh_3). These Pd(0) and Cu(0) nanoparticles are the actual reducing agents for the reaction. Calcium carbide activation is a major challenge for this synthetic procedure and the trace amounts of moisture in the reaction medium helps addition break down the polymeric structure of CaC_2 to give an acetylide "ate"-complex in the presence of tetrabutylammonium fluoride (TBAF). This acetylide "ate" complex reacts with the copper nanoparticles to form the copper acetylide and enters cycle B. Simultaneous the hexabromobenzene undergoes an oxidative addition to Pd(0) nanoparticles with PPh_3 ligands and enters cycle A. This is followed by transmetalation step and finally reductive elimination to give the final product. This synthesis is based on a previously reported method for the synthesis of bis-arylated alkynes[40] and the interesting part regarding this synthetic procedure lies in the choice of the starting materials especially the incorporation of calcium carbide as the cheap, easily available acetylene source and the mild reaction conditions that are used for the generation/stabilization of the intermediate.

One major reason behind poor yields in the previously reported synthesis techniques using various cross-linking strategies or annulene chemistry is in the use of starting materials like cyclo[12]carbon, hexakis(phenylethynyl)benzene or dehydrobenzoannulenes which are generally unstable under ambient conditions and the reaction proceeds via multiple protection/deprotection steps during synthesis which affects the yield.[25,27] Although synthesis procedures with similar starting materials (hexabromobenzene and calcium carbide) have been reported for interfacial/mechanochemical techniques, the products obtained are either of poor yield and/or prone to defects.[31–33] Hence this simple one-pot Sonogashira cross-linking procedure for the synthesis of pure/pristine γ-graphyne in high yields might play a crucial role in the experimental exploration of this material. Moreover, this method also opens up possibilities for the synthesis of other members of the graphyne family by similar methods.

Charge transfer studies

Charge transfer from and into a material is a very crucial step that gives a fundamental understanding of the material for integrating it into various optoelectronic devices.[34] Surface charge transfer doping is a crucial method for tuning the properties of two-dimensional materials owing to their high surface-to-volume ratios. Charge transfer studies give an understanding of the inherent nature of the sample and its defect density. As a proof of concept, we have studied the charge transfer behavior of exfoliated γ-graphyne nanosheets with an electron donor (TTF) and electron acceptor (TCNQ) molecules using UV-visible spectroscopy and compared it with few-layered graphene. 7,7,8,8-Tetracyanoquinodimethane (TCNQ) is a strong electron acceptor molecule that is known to form radical anion $TCNQ^{\cdot-}$ species in the presence of an electron donor. TCNQ exhibits characteristic UV-visible absorption peaks corresponding to its neutral form (~390nm) and as radical anion $TCNQ^{\cdot-}$ (750-850 nm, along with a broad peak ~ 410 nm) (**Figure 10a**).[50–55] **Figure 10b** shows the charge transfer interaction of TCNQ solutions ($5*10^{-5}$ M) with similar concentrations of few-layered graphyne and graphene. The UV-visible spectra clearly demonstrate that few-layered graphyne shows stronger charge-transfer interaction with TCNQ with the peaks corresponding to $TCNQ^{\cdot-}$ being very clearly visible and a relatively lower intensity of neutral TCNQ compared to few-layered graphene. We have calculated the ratio $TCNQ^{\cdot-}$ /TCNQ by comparing the peak intensities I_{742}/I_{393} in **Figure 10a** and also cross-checked it with a background-corrected spectrum, and in both the cases few-layered graphyne had a higher ratio of TCNQ$^{\cdot-}$ than few-layered graphene hence showing a better charge transfer behavior (**Table 2**). Moreover, on increasing the concentration of the graphyne solution, the neutral TCNQ peak almost disappears (**Figure 10c**).

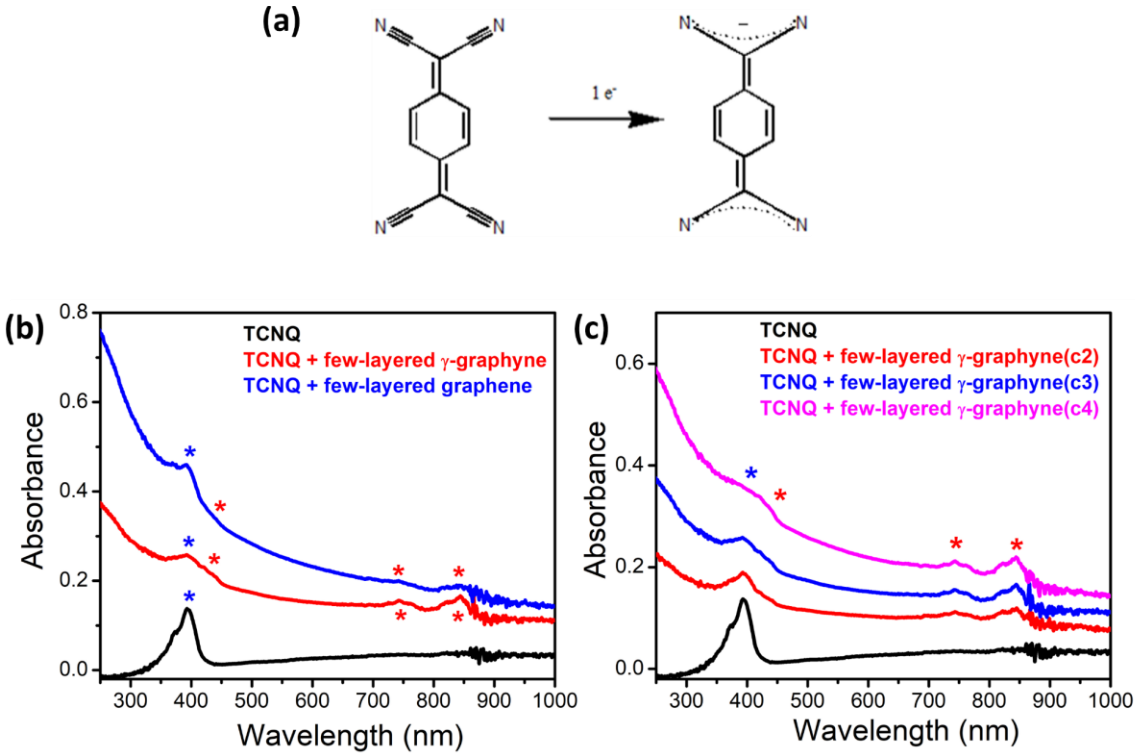

Figure 10: (a) Molecular structure of TCNQ before and after charge transfer, (b) Charge transfer studies of few-layered GY and few-layered graphene with TCNQ solution of concentration 5*10^{-5} M and similar concentrations of GY and graphene (c) Charge transfer studies of exfoliated GY of different concentrations with TCNQ solution of concentration 5*10^{-5} M and with GY concentrations in the order c2 < c3 < c4

* denotes neutral TCNQ peak and * denotes TCNQ$^{\cdot-}$ peak

Table 2: $TCNQ^{-}$ / TCNQ ratios from UV-visible charge transfer studies

Sample name	**I_{742}/I_{393}**	**Background correction and normalization**
TCNQ	0.26	No
TCNQ + few-layered GY	0.60	No
TCNQ + few-layered graphene	0.43	No
TCNQ	0.14	Yes
TCNQ + few-layered GY	0.72	Yes
TCNQ + few-layered graphene	0.33	Yes

We also studied charge transfer of few-layered graphyne with tetrathiafulvalene (TTF), an electron donor. Like TCNQ, tetrathiafulvalene (TTF), displays characteristic UV-visible absorption peaks corresponding to its neutral form (~350nm), and radical cation $TTF^{\cdot +}$ (two broad peaks ~400 and 800nm) (**Figure 11a**).[56] However, we were unable to detect any significant charge transfer signature with both few-layered graphyne and graphene dispersions. Poor charge transfer behavior of graphene with electron donor like TTF is already reported.[57] **Figure 11b** compares the UV-visible charge transfer interaction of few-layered graphene with TTF solutions ($1*10^{-4}$ M) along with the as-synthesized graphyne dispersions of similar concentrations while **Figure 11c** shows the UV-visible absorption spectra of TTF solutions ($1*10^{-4}$ M) with different exfoliated γ-graphyne dispersion concentrations. On increasing the concentration of graphyne/graphene dispersion, the background of the UV spectra increases due to increased scattering from the sample, which is a well-known phenomenon for high-aspect-ratio nanomaterials.[58]

The charge transfer results can be further verified by theoretical reports wherein on comparing the HOMO and LUMO edges of TCNQ and TTF, respectively with the theoretically reported E_{VBM} and E_{CBM} of for γ-graphyne (-4.16 eV and -1.93 eV) we find that $\Delta E_{VL} > 0$ (Eq^n-2) which predicts successful charge transfer from TCNQ acceptor while $\Delta E_{CH} > 0$ (Eq^n-1) predicts poor charge transfer between graphyne and TTF (from **section 3.1.1**).[37]

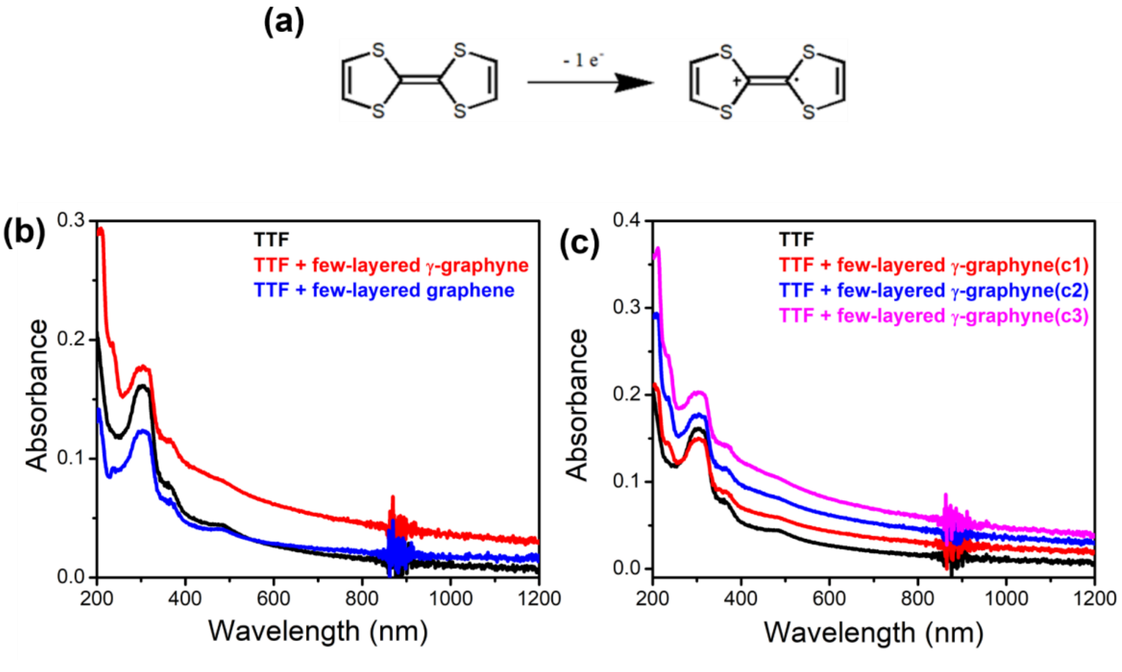

Figure 11: (a) Molecular structure of TTF before and after charge transfer, (b) Charge transfer studies of few-layered GY and few-layered graphene with TTF solution of concentration $1*10^{-4}$ M and similar concentrations of GY and graphene, (c) Charge transfer studies of exfoliated GY of different concentrations with TTF solution of concentration $1*10^{-4}$ M and with GY concentrations in the order c1 < c2 < c3

To conclude, theoretical studies predict graphynes to be very promising 2D artificial carbon allotropes and a simple, yet effective synthesis strategy will play a very crucial role in exploring these materials for various electronic and optoelectronic applications.

3.5 Conclusions

We have successfully synthesized γ-graphyne with high yields using a simple one-pot Sonogashira cross-linking reaction. The chemical purity of the material was confirmed by Raman spectra, XPS, and XRD; and the pristine defect-free nature of the sample was confirmed by Raman studies and temperature-dependent resistivity measurements. Despite having multiple theoretical reports on the excellent properties of γ-graphyne, an effective synthesis strategy is at present the primary deterrent towards the experimental exploration of γ-graphyne. Moreover, this synthesis method will also be useful in designing synthesis strategies for other members of the graphyne family in the future. Preliminary charge transfer studies carried out with acceptor molecule (TCNQ) show impressive charge transfer behavior with γ-graphyne with the relative concentration of $TCNQ^{\cdot-}$ being higher than that of few-layered graphene dispersion.

References

(1) Hirsch, A. *Nat. Mater.*, **2010**, *9* (11), 868–871.

(2) Kroto, H., Heath, J., O'Brien, S., *Nature* ,**1985**, *318* (14), 162–163.

(3) Iijima, S., *Nature*, **1991**, *354*, 56–58.

(4) Novoselov, K. S.; Geim, A. K.; Morozov, S. V; Jiang, D.; Zhang, Y.; Dubonos, S. v; Grigorieva, I. v; Firsov, A. A. *Science*, **2000**, *404*, 666-669

(5) Cataldo, F. *Polym. Int.*, **1997**, *44* (2), 191–200.

(6) Casari, C. S.; Milani, A. *MRS Commun.* **2018**, *8* (2), 207–219.

(7) Ouyang, T.; Cui, C.; Shi, X.; He, C.; Li, J.; Zhang, C.; Tang, C.; Zhong, *J. Phys. Status Solidi - Rapid Res. Lett.* **2020**, *14* (12), 2000437

(8) Huang, L.; Zeng, X.; Cao, D. *J. Mater. Chem. A.,* **2014**, *2* (14), 4899–4902.

(9) Li, Y.; Xu, L.; Liu, H.; Li, Y. *Chem. Soc. Rev.,* **2014**, *43* (8), 2572–2586.

(10) Puigdollers, A. R.; Alonso, G.; Gamallo, P., *Carbon*, **2016**, *96*, 879–887.

(11) Li, Z.; Smeu, M.; Rives, A.; Maraval, V.; Chauvin, R.; Ratner, M. A.; Borguet, E. *Nat. Commun.,* **2015**, *6*, 6321.

(12) He, X. J.; Tan, J.; Bu, H. X.; Zhang, H. Y.; Zhao, M. W. *Chin. Sci. Bull.*, **2012**, *57* (23), 3080–3085.

(13) Narita, N.; Nagai, S.; Suzuki, S.; Nakao, K. *Phys. Rev. B.* **2000**, *62* (16), 11146-11151

(14) Srinivasu, K.; Ghosh, S. K. *J. Phys. Chem. C.*, **2012**, *116* (9), 5951–5956.

(15) Lee, H.; Koo, J.; Huang, B.; Lee, H.; Kim, G.; Nam, J.; Kwon, Y. *J. Phys. Chem. C* **2014**, *118* (5), 2463–2468.

(16) Wang, J. T.; Chen, C.; Li, H. D.; Mizuseki, H.; Kawazoe, Y., *Sci. Rep.* **2016**, *6*, 24665.

(17) Kang, J.; Li, J.; Wu, F.; Li, S. S.; Xia, J. B., *J. Phys. Chem. C*, **2011**, *115* (42), 20466–20470.

(18) Kim, B. G.; Choi, H. J. Graphyne: Hexagonal Network of Carbon with Versatile Dirac Cones. *Phys. Rev. B.,* **2012**, *86* (11), 115435.

(19) Qiu, H.; Xue, M.; Shen, C.; Zhang, Z.; Guo, W., *Adv. Mater.,* **2019**, *31* (42), 1970296.

(20) Srinivasu, K.; Ghosh, S. K., *J. Phys. Chem. C.,* **2012**, *116* (9), 5951–5956.

(21) Ivanovskii, A. L. *Prog. Solid State Ch.*, **2013**, *41* (1-2), 1–19.

(22) Zhang, R. S; Jiang, J. W. *Front.Phys.*, **2019**, *14* (1), 13401.

(23) Baughman, R. H.; Eckhardt, H.; Kertesz, M., *J. Chem. Phys.*, **1987**, *87* (11), 6687–6699.

(24) Malko, D.; Neiss, C.; Viñes, F.; Görling, A. *Phys. Rev. Lett.*, **2012**, *108* (8), 086804

(25) Haley, M. M. *Pure Appl. Chem.*, **2008**, *80*, 519–532.

(26) Kehoe, J. M.; Kiley, J. H.; English, J. J.; Johnson, C. A.; Petersen, R. C.; Haley, M. M., *Org. Lett.*, **2000**, *2* (7), 969–972.

(27) Sonoda, M.; Inaba, A.; Itahashi, K.; Tobe, Y., *Org. Lett.*, **2001**, *3* (15), 2419–2421.

(28) Li, G.; Li, Y.; Liu, H.; Guo, Y.; Li, Y.; Zhu, D., *Chem. Commun.*, **2010**, *46* (19), 3256–3258.

(29) Song, Y.; Li, X.; Yang, Z.; Wang, J.; Liu, C.; Xie, C.; Wang, H.; Huang, C., *Chem. Commun.*, **2019**, *55* (46), 6571–6574.

(30) Matsuoka, R.; Sakamoto, R.; Hoshiko, K.; Sasaki, S.; Masunaga, H.; Nagashio, K.; Nishihara, H., *J Am Chem Soc* **2017**, *139* (8), 3145–3152.

(31) Li, Q.; Li, Y.; Chen, Y.; Wu, L.; Yang, C.; Cui, X., *Carbon*, **2018**, *136*, 248–254.

(32) Yang, C.; Li, Y.; Chen, Y.; Li, Q.; Wu, L.; Cui, X., *Small*, **2019**, *15* (8), 1804710.

(33) Ding, W.; Sun, M.; Zhang, Z.; Lin, X.; Gao, B., *Ultrason. Sonochem.*, **2020**, *61*, 104850.

(34) Wang, J.; Ding, T.; Gao, K.; Wang, L.; Zhou, P.; Wu, K., *Nat. Commun.*, **2021**, *12* (1), 6333.

(35) Marcus, R. A., *J. Chem. Phys.*, **1956**, *24* (5), 966–978.

(36) Bradac, C.; Xu, Z. Q.; Aharonovich, I., *Nano Lett*., **2021**, *21* (3), 1193–1204.

(37) Hou, R.; Xia, Y.; Yang, S. A, *ACS Omega*, **2020**, *5* (41), 26748–26754.

(38) Sreeprasad, T. S.; Berry, V., *Small*., **2013**, *9* (3), 341–350.

(39) Chen, X.; Zhou, Z.; Deng, B.; Wu, Z.; Xia, F.; Cao, Y.; Zhang, L.; Huang, W.; Wang, N.; Wang, L., *Nano Today*, **2019**, *27*, 99–119.

(40) Hosseini, A.; Pilevar, A.; Hogan, E.; Mogwitz, B.; Schulze, A. S.; Schreiner, P. R., *Org. Biomol. Chem.*, **2017**, *15* (32), 6800–6807.

(41) Zhang, S.; Wang, J.; Li, Z.; Zhao, R.; Tong, L.; Liu, Z.; Zhang, J.; Liu, Z.; *J. Phys. Chem. C*, **2016**, *120* (19), 10605–10613.

(42) Popov, V. N.; Lambin, P. *Phys. Rev. B*, **2013**, *88* (7), 075427.

(43) Lee, S. M.; Lee, S. H.; Roh, J. S., *Crystals,* **2021**, *11* (2), 1–11.

(44) Nicolosi, V.; Chhowalla, M.; Kanatzidis, M. G.; Strano, M. S.; Coleman, J. N., *Science,* **2013**, *340*, 6139

(45) Englert, J. M.; Dotzer, C.; Yang, G.; Schmid, M.; Papp, C.; Gottfried, J. M.; Steinrück, H. P.; Spiecker, E.; Hauke, F.; Hirsch, A., *Nat. Chem.,* **2011**, *3* (4), 279–286.

(46) Schindler, A. I.; la Roy, B. C., *J. Appl. Phys.*, **1966**, *37* (9), 3610–3612.

(47) Wiendlocha, B.; Misra, S.; Dauscher, A.; Lenoir, B.; Candolfi, C., *Mater. Horiz.*, **2021**, *8* (6), 1735–1743.

(48) Mcfeely, F. R.; Kowalczyk, S. P.; Ley, L.; Caveh, R. G.; Pollak, R. A.; Shirley, D. A., *Phys. Rev. B*, **1974**, *12* (9), 5268

(49) Thommes, M.; Kaneko, K.; Neimark, A. v.; Olivier, J. P.; Rodriguez-Reinoso, F.; Rouquerol, J.; Sing, K. S. W., *Pure Appl. Chem.,* **2015**, *87* (9–10), 1051–1069.

(50) Abellán, G.; Lloret, V.; Mundloch, U.; Marcia, M.; Neiss, C.; Görling, A.; Varela, M.; Hauke, F.; Hirsch, A., *Angew. Chem.,* **2016**, *128* (47), 14777–14782.

(51) Ma, L.; Hu, P.; Kloc, C.; Sun, H.; Michel-Beyerle, M. E.; Gurzadyan, G. G., *Chem. Phys. Lett.,* **2014**, *609*, 11–14.

(52) Jonkman, H. T.; Kommandeur, J., *Chem. Phys. Lett.* **1972**, *15* (4), 496-499.

(53) Suchanski, M. R.; van Duyne, R. P., *J. Am. Chem. Soc.* **1976**, *98* (1), 250–252

(54) Milián, B.; Pou-Amérigo, R.; Viruela, R.; Ortí, E. A, *J. Mol. Struct.,* **2004**; *709*, 97–102

(55) Roberts, G. M.; Lecointre, J.; Horke, D. A.; Verlet, J. R. R., *Phys. Chem. Chem. Phys.,* **2010**, *12* (23), 6226–6232.

(56) Schröder, H. v.; Schalley, C. A., *Beilstein J. Org. Chem.* **2018**, *14*, 2163–2185. h

(57) Manna, A. K.; Pati, S. K. *Chem. Asian J.,* **2009**, *4* (6), 855–860.

(58) Harvey, A.; Backes, C.; Boland, J. B.; He, X.; Griffin, A.; Szydlowska, B.; Gabbett, C.; Donegan, J. F.; Coleman, J. N., *Nat. Commun.,* **2018**, *9* (1), 4553

(59) Chinchilla R., Najera, C., *Chem. Soc. Rev*., **2011**, *40*, 5084–5121

Chapter-4

Photochemical HER activity of layered metal phosphochalcogenides

SUMMARY

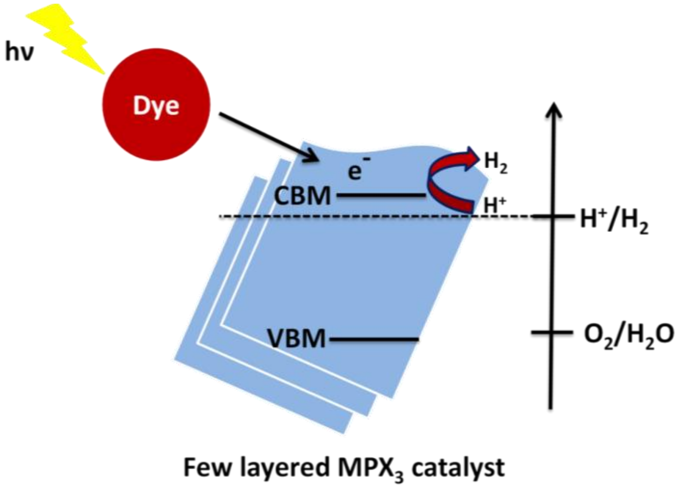

Metal phosphochalcogenides (MPX_3) are an interesting and relatively less explored class of two-dimensional materials with ~200 known members. These materials have already attracted attention for their interesting magnetic and ferroelectric properties along with applications in hydrogen storage and lithium batteries. These materials occupy a very coveted position in the atlas of 2D materials due to their bandgaps in the range of 1.5-3.5 eV which makes them suitable for optoelectronic and catalytic applications. Recent theoretical reports predict that the band edges of these materials are suitable for hydrogen evolution reaction (HER) and there are some reports on electrocatalytic hydrogen evolution reaction (HER) of these materials while photocatalytic HER studies are still limited. In this work, we have synthesized eight monometallic ($NiPS_3$, $FePS_3$, $MnPS_3$, $CdPS_3$ $ZnPS_3$, $NiPSe_3$, $FePSe_3$, and $MnPSe_3$) and two bimetallic

Paper based on this work has appeared in *J. Mater. Chem. A*, **2019**,*7*, 22500-22506

phosphochalcogenide compounds ($Ag_{0.5}In_{0.5}PS_3$ and $Ag_{0.5}In_{0.5}PSe_3$) by high temperature synthesis method and studied their photocatalytic HER activity. Among the ternary MPS_3, the Nickel compound exhibits the highest HER activity (2.6 mmol $h^{-1}g^{-1}$), while $MnPS_3$, $ZnPS_3$ and $CdPS_3$ exhibit low activity, due to their large band gaps and presence of long P-P and M-S bonds. Amongst phosphoselenides, $FePSe_3$ shows higher HER activity of 1.7 mmol $h^{-1}g^{-1}$ than the Mn and Cd compounds. The quaternary phosphochalcogenide, $Ag_{0.5}In_{0.5}PS_3$, shows high photochemical HER activity of 1.9 mmol $h^{-1}g^{-1}$.

4.1 Introduction

Metal phosphochalcogenides (MPX_3) are an interesting class of materials in the 2D family with bandgaps in the range of 1.5-3.5 eV which makes them suitable for various electronic, optoelectronic, and catalytic applications.[1] These layered bulk materials were discovered in the late 1800s and were significantly explored around 1970-2000s for H_2 storage and Li-ion battery applications. However, bulk MPX_3 have been exfoliated into the corresponding 2D counterparts only recently and this opens up new horizons for investigating their properties.[2] This is a vastly unexplored class of 2D materials with ~200 known members but explored for only limited applications to date.[3–22] Monometallic phosphochalcogenides can be represented by the general formula $M^{II}PX_3$ wherein M^{II} is a divalent cation (V, Mn, Fe, Co, Ni, Zn, Cd, Sn or Hg) and X is a chalcogen S or Se. Structurally monometallic MPX_3 consists of a cubic/hexagonal arrangement of S/Se wherein metal cations occupy 2/3rd of the octahedral voids and P-P bonds occupy 1/3rd of the octahedral voids.[1,2] Bimetallic phosphochalcogenides can be represented by the general formula $M^{I}_{0.5}M^{III}_{0.5}PX_3$ wherein M^{I} represents a monovalent cation (Ag or Cu) and M^{III} is a trivalent cation (Cr, V, In, Ga, Bi) and X is a chalcogen. Structurally bimetallic phosphochalcogenides can be represented as a trigonal arrangement of S or Se wherein M^{I}, M^{III}, and P-P occupy octahedral voids in the ratio of 1:1:1. Most of the bulk compounds are layered in nature with strong in-plane interactions and weak out-of-plane van der Waals interactions. The calculated cleavage energies for these materials are lower than graphite and hence can be easily exfoliated to the corresponding nanosheets.[22] Theoretical studies predict that band-edges and band gaps of these materials are suitable for hydrogen evolution reaction (HER) and there are multiple reports on electrochemical HER using

MPX_3 catalyst showing good HER activity over a wide pH range, however very few on photocatalytic HER.[13–17,20] **Figure 1** shows a pictorial representation of the crystal structures of monometallic and bimetallic phosphochalcogenides.

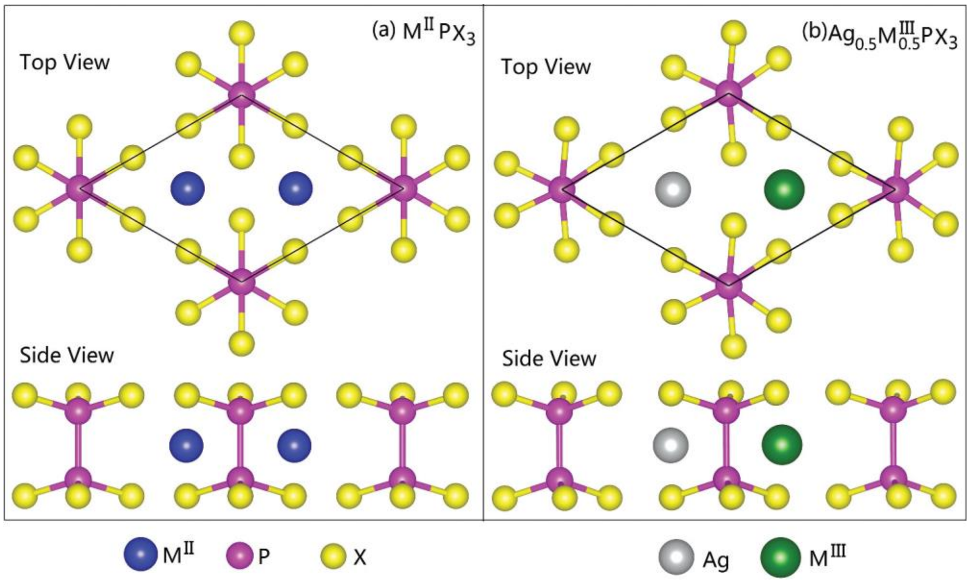

Figure 1: Crystal structures of (a) $M^{II}PX_3$ and (b) $Ag_{0.5}M^{III}_{0.5}PX_3$. Reprinted from ref 1, with the permission of AIP Publishing

In this work we have synthesized five monometallic phosphosulfides ($NiPS_3$, $FePS_3$, $MnPS_3$, $CdPS_3$ $ZnPS_3$) which belong to monoclinic *C2/m* space group; three monometallic phosphoselenides ($NiPSe_3$, $FePSe_3$ and $MnPSe_3$) which belong to hexagonal $R\bar{3}$ space group and two bimetallic phosphochalcogenides ($Ag_{0.5}In_{0.5}PS_3$ and $Ag_{0.5}In_{0.5}PSe_3$) belonging to trigonal $P\bar{3}1c$ space group.

4.1.1 Photocatalytic hydrogen evolution reaction

Photocatalysis refers to the use of photonic energy for carrying out chemical transformations. The interest in photocatalytic HER is rooted at the possibility of using solar radiation for generation of pure hydrogen.[23,24] Water splitting is an uphill reaction

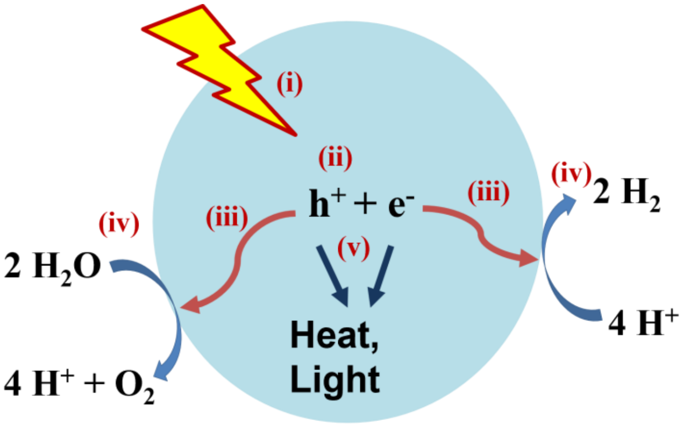

Scheme 1: Steps involved in photocatalytic water splitting: (i) Light absorption, (ii) generation of electron-hole pair, (iii) charge transfer to catalyst surface, (iv) redox reactions and concurrent adsorption, desorption, and mass diffusion of chemical species, and (v) charge recombination

with Gibbs free energy value of 237 $kJmol^{-1}$. The energy required to drive this reaction forward is provided by light or ideally sunlight. Ideally photocatalytic HER involves multiple steps with different time scales and spatial resolutions which need to be optimized for improving the efficiency of the reaction. A schematic for the photocatalytic HER reaction process with the steps involved is shown (**Scheme 1**). The reaction starts with the absorption of light by the semiconductor photocatalyst which leads to the generation of electron and hole pairs. These photoexcited charge carriers are transferred to surface active sites and subsequently consumed by surface redox reactions. Mass diffusion of reactants and products proceeds concurrently. Moreover, charge carrier recombination also takes place simultaneously. Therefore, separation of charge carriers and surface redox reactions must proceed within the lifetimes of photoexcited carriers, preventing recombination for a successful water-splitting reaction. One primary requirement for a photocatalyst is that its band edges must span the water oxidation and reduction potentials.

4.1.2 Dye sensitized photocatalytic hydrogen evolution reaction

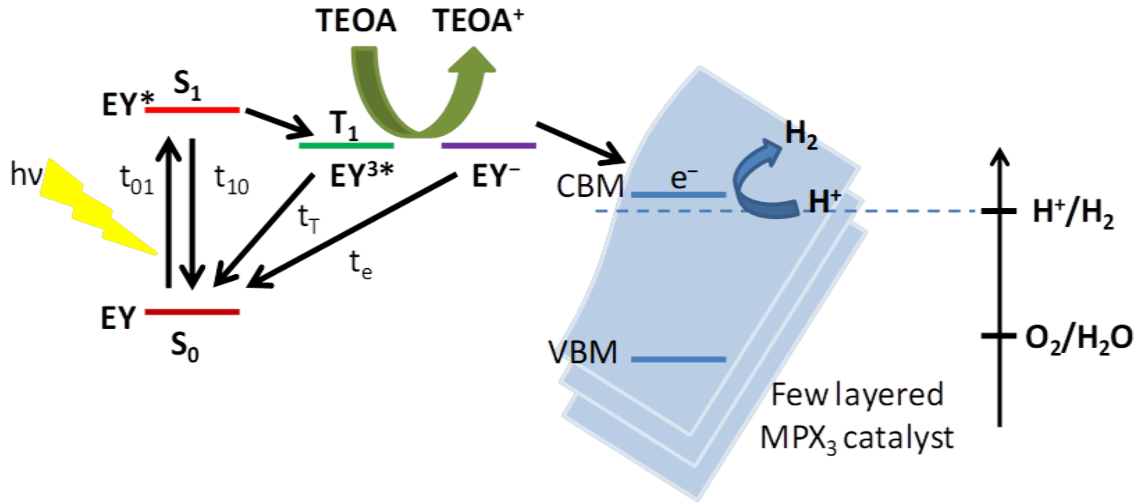

Scheme 2: Pictorial representation of dye sensitized photocatalytic HER mechanism of MPX_3 nanosheets

Dye-sensitized HER is an interesting method for carrying out photocatalytic HER studies for materials with poorer absorption coefficient, which uses dye molecules as photosensitizers and additional sacrificial reagents to aid in the catalytic process. **Scheme 2** gives a pictorial representation of dye-sensitized HER reaction using MPX_3 catalyst. The dye used for the study is Eosin Y (EY) and the sacrificial reagent is triethanolamine (TEOA). The reaction proceeds by photoexcitation of EY followed by subsequent intersystem crossing to yield a triplet excited state (EY^{3}*). The acceptance of an electron via reductive quenching from a sacrificial electron donor yields radical EY^- species. This highly reductive EY^- species can react in two ways (i) with a proton to form H_o and return the electron to an oxidized TEOA or (ii) transfer the electron to the conduction band of another catalyst. Control experiments carried out in this study show that the contribution of step (i) if any is very poor. Hence, the reaction predominantly follows step (ii) wherein EY^- transfers its electron to the conduction band of MPX_3 wherein water reduction reaction can take place.[25–27] In this study dye-sensitized HER reaction was carried out for all the ten synthesized MPX_3 compounds

4.2 Scope of this investigation

In this work, we have synthesized eight monometallic ($NiPS_3$, $FePS_3$, $MnPS_3$, $CdPS_3$ $ZnPS_3$, $NiPSe_3$, $FePSe_3$ and $MnPSe_3$) and two bimetallic phosphochalcogenide compounds ($Ag_{0.5}In_{0.5}PS_3$ and $Ag_{0.5}In_{0.5}PSe_3$) by high temperature synthesis technique and studied their photocatalytic hydrogen evolution activities. We were able to correlate the trends observed in the hydrogen evolution activities with the corresponding crystal field stabilization energies (CFSE), P-P bond lengths and M-S bond lengths of these compounds.

4.3 Experimental section

Material synthesis

Bulk monometallic $MnPS_3$, $FePS_3$, $NiPS_3$, $ZnPS_3$, $CdPS_3$, $MnPSe_3$, $FePSe_3$, $CdPSe_3$ were synthesized by high-temperature reactions by sealing stoichiometric amounts of the corresponding elemental powders under high vacuum and heating it at 650°C for 7 days.[19] Bulk bimetallic $Ag_{0.5}In_{0.5}PS_3$ and $Ag_{0.5}In_{0.5}PSe_3$ were prepared by chemical vapor transport (CVT) without the use of any other transport agent. In a typical synthesis, stoichiometric amounts of the corresponding elemental powders were sealed under high vacuum and heated at 700°C for 14 days.[28,29] Pure crystals were collected from the other end of the tube. For the synthesis of few-layered MPX_3, the bulk compounds were added to Millipore water in a beaker and sonicated for 1 hour in the case of monometallic MPX_3 and for 2 hours for the bimetallic MPX_3 compounds using a bath sonicator (**Scheme 3**). The unexfoliated material was allowed to settle for 10 min after sonication. Subsequently, the dispersion was centrifuged at 3000 rpm (4721 *g*) for 10 min and the supernatant was decanted and used for further characterization.

Photochemical studies

In a typical HER reaction of monometallic MPX_3, 5ml of exfoliated MPX_3 was dispersed in a 15% (v/v) solution of triethanolamine (TEOA) in water (50 mL). In the case of bimetallic MPX_3, 2 mL of the exfoliated MPX_3 was dispersed in a 15% (v/v) solution of triethanolamine in water (50 mL). Eosin Y was used as a photosensitizer and TEOA acts as a sacrificial agent in both cases. The mixture was thoroughly purged with N_2. The vessel was illuminated under Xenon lamp (450 W) with a steady stirring of the mixture. A 3 mL amount of evolved gas was collected from the headspace of the glass vessel and analyzed using a thermal conductivity detector equipped gas chromatograph (PerkinElmer ARNL 580C). Prior to the measurements, the GC was calibrated with reference gas (hydrogen concentrations of 10 and 100 ppm). For cycling studies, the reaction was stopped at 5 hours. The vessel was then purged with inert gas, photosensitizer was added, and irradiation was continued.

Physical Characterization

XRD patterns of MPX_3 compounds were recorded on a Rich-Siefert XRD-300-TT diffractometer with Cu-Kα radiation. Raman spectra were collected in the backscattering geometry using a 514 nm Ar laser with a JobinYvon LabRam HR 800 spectrometer. Raman spectra for all the samples are recorded by dropcasting catalyst on to a glass slide. Morphological analysis has been performed using Nova Nano SEM 600, FEI and ZEISS Gemini SEM500 while TEM imaging has been carried using JEOL TEM 3010 instruments fitted with a Gatan CCD camera operating at an accelerating voltage of 300 kV and in a FEI Tecnai G2 T20 operated microscope fitted with a Gatan CCD camera operating at an accelerating voltage of 200 kV. Atomic force microscope (AFM) images were obtained on Si substrates in tapping mode using Bruker Innova instrument. UV-visible absorption spectra were recorded on a Perkin–Elmer Lambda 650 UV/Vis Spectrometer fitted with an integrating sphere to cancel the contribution from scattering.

4.4 Results and discussion

Material characterization

In this work, eight monometallic phosphochalcogenides ($NiPS_3$, $FePS_3$, $MnPS_3$, $CdPS_3$ $ZnPS_3$, $NiPSe_3$, $FePSe_3$ and $MnPSe_3$) and two bimetallic phosphochalcogenides ($Ag_{0.5}In_{0.5}PS_3$ and $Ag_{0.5}In_{0.5}PSe_3$) were studied. Layered nature of these materials was further confirmed by FESEM images (**Figure 2**) which shows stacks of platelets of various

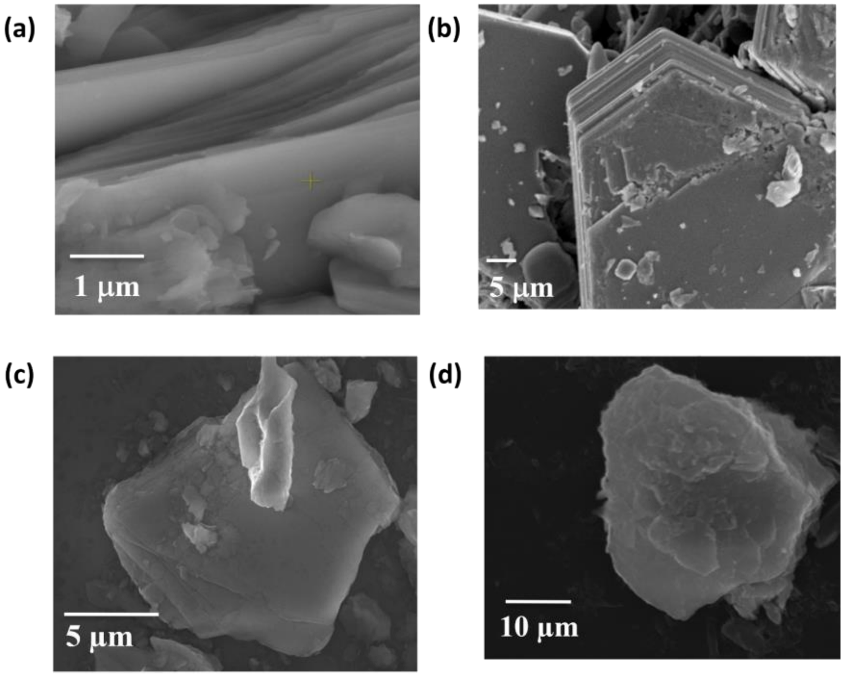

Figure 2: FESEM images of (a) $NiPS_3$, (b) $FePSe_3$ (c) $Ag_{0.5}In_{0.5}PS_3$ and (d) $Ag_{0.5}In_{0.5}PSe_3$

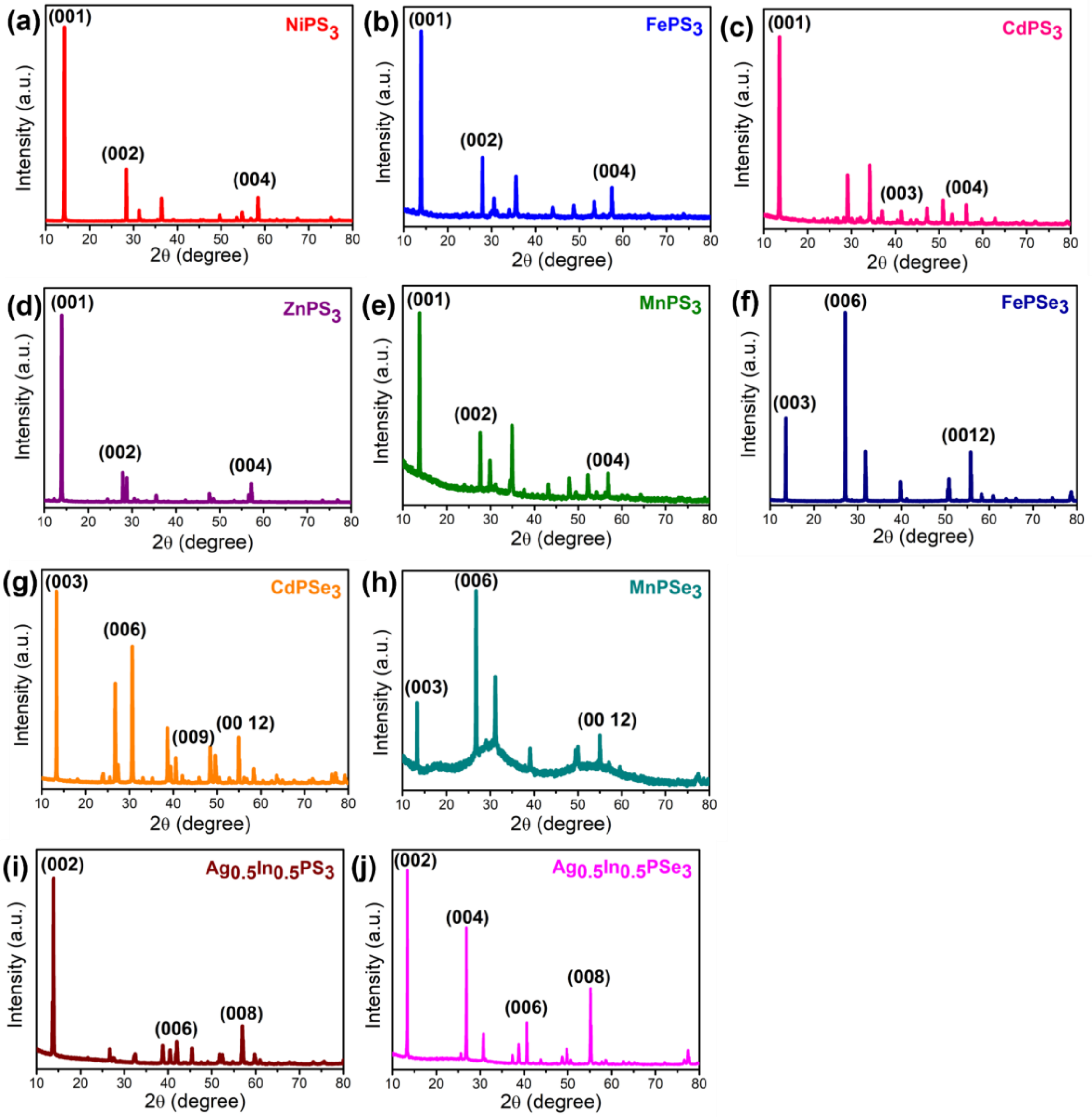

Figure 3: Powder XRD patterns of all synthesized MPX_3 compounds

thickness arranged on top of each other. The as-synthesized materials (MPX_3) were thoroughly characterized to confirm chemical purity. **Figure 3** shows the powder X-ray diffraction patterns of these bulk compounds which show preferential orientation along *(00l)* which is due to preferential stacking orientation in layered materials which makes some planes more exposed to X-rays compared to others.[19] **Figure 4** shows the Energy-dispersive X-ray spectra of these materials confirming elemental composition.

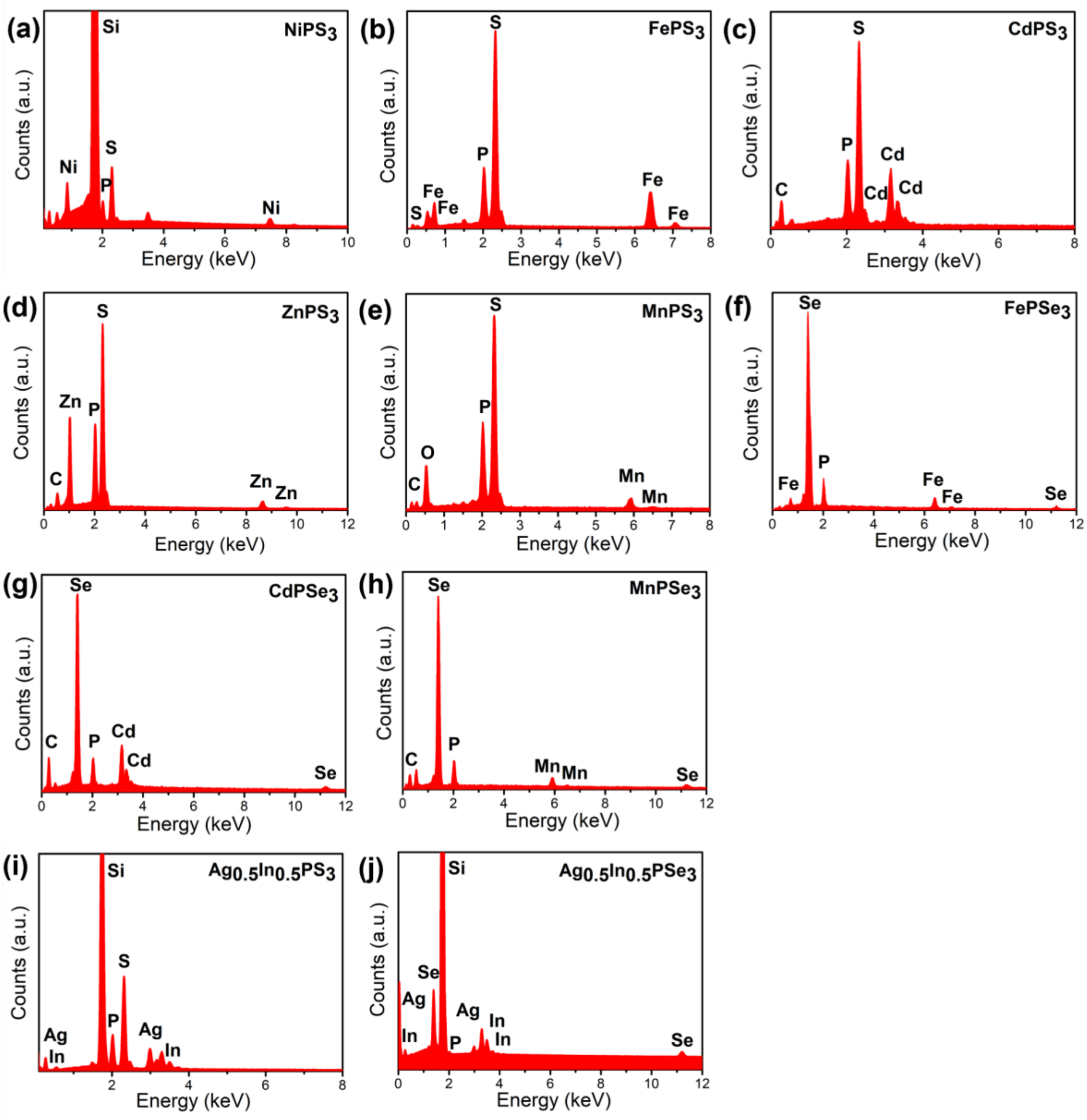

Figure 4: EDS showing elemental composition of all synthesized MPX_3 compounds

To have a better understanding of the bonding nature of these materials, X-ray Photoelectron Spectroscopy (XPS) analysis was carried out. **Figure 5** shows the representative XPS spectra of $NiPS_3$, $FePSe_3$, and $Ag_{0.5}In_{0.5}PS_3$. Ni 2p core-level XPS spectra of $NiPS_3$ (**Figure 5a**) show two peaks at binding energies of 855.1 and 872.7 eV corresponding to the $2p_{3/2}$ and $2p_{1/2}$ levels of Ni^{2+} in $NiPS_3$.[30,31] These binding energies are

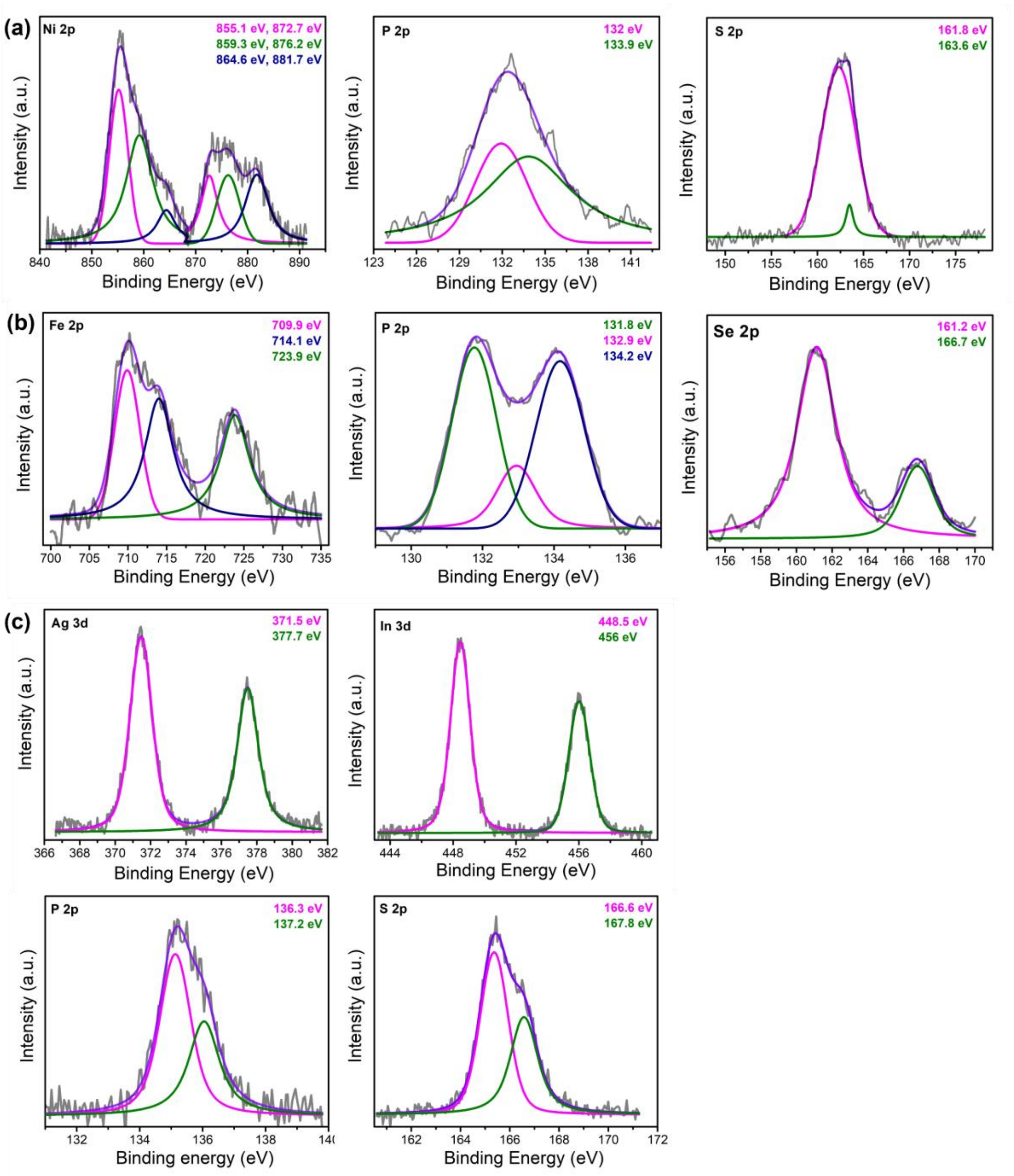

Figure 5: XPS core-level spectra of (a) $NiPS_3$, (b) $FePSe_3$, and (c) $Ag_{0.5}In_{0.5}PS_3$

distinct from Ni (852 eV), Ni_2P (853.1 eV), NiS (852.8 eV) and NiS_2 (853.6 eV).[32,33] The peaks at binding energies of 859.3, 864.6, 876.2, and 881.7 eV is assigned to satellite 2p peaks of Ni. S 2p core-level spectra shows $2p_{3/2}$ and $2p_{1/2}$ peaks at binding energies at 161.8 and 163.6 eV, respectively, and the P core-level shows $2p_{3/2}$ and $2p_{1/2}$ level peaks at binding energies of 132 and 133.9 eV respectively.[30,31] **Figure 5b** shows the core-level XPS spectra of $FePSe_3$ with Fe 2p peaks at around 709.9 and 723.9 eV corresponding to $2p_{3/2}$ and $2p_{1/2}$ of Fe^{2+} accompanied by a satellite peak at 714.1 eV. Fe peaks in iron phosphides are at ~707 eV which rules out the possibility of the formation of iron phosphides. The peaks at 131.8 and 132.9 eV correspond to the $2p_{3/2}$ and $2p_{1/2}$ peaks for P respectively while the peak at 134.2 eV suggests the presence of P_4O_{10} states due to surface oxidation. Phosphorus peaks in iron phosphides should be at lower binding energies of 129.5 eV (Fe_2P), 129.4 eV (Fe_3P), and 129.8eV (FeP_2) which further confirms the absence of any phosphides in the system. The peaks for Se $3p_{3/2}$ and Se $3p_{1/2}$ levels are observed at ~161.2 and ~166.7 eV respectively.[34,35] XPS core-level spectra of Ag in $Ag_{0.5}In_{0.5}PS_3$ (**Figure 5c**) shows peaks at 371.5 and 377.7 eV corresponding to the $3d_{5/2}$ and $3d_{3/2}$ levels. Peaks with binding energy 448.5 and 456 eV correspond to the $3d_{5/2}$ and $3d_{3/2}$ levels of In. $3d_{5/2}$ levels for Ag and In in the corresponding sulfides and phosphides lie at lower binding energy as Ag (368.1 eV), Ag_2S (368.2 eV), In (443.15 eV) and InP (443.9eV), thus confirming the bonding nature of these materials. Sulfur $2p_{3/2}$ and $2p_{1/2}$ levels show peaks at binding energies of 166.6 and 167.8 eV, respectively, and the phosphorus $2p_{3/2}$ and $2p_{1/2}$ levels show peaks at binding energies of 136.3 and 137.2 eV, respectively.[36,37]

These as-synthesized MPX_3 compounds were exfoliated (by bath sonication) to give the corresponding few-layered counterparts. **Scheme 3** gives a pictorial representation of it. During ultrasonication, cavitation bubbles are formed in the solvent, which then implodes into higher energy jets and carries out delamination of these layered materials.[38,39] **Figure 6** shows the bright-field TEM images of these nanosheets confirming few-layered nature. **Figure 7** shows the AFM images and corresponding height profiles for $NiPS_3$,

$FePSe_3$, $Ag_{0.5}In_{0.5}PS_3$ and $Ag_{0.5}In_{0.5}PSe_3$ exfoliated in water with < 8 layers thickness. **Figure 8** gives the Tauc plots of the as synthesized MPX_3 compounds displaying band-

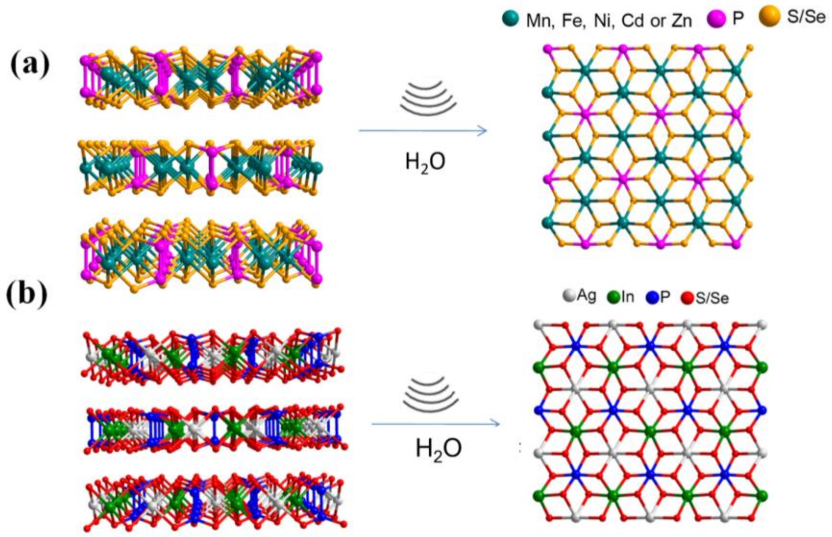

Scheme 3: Bulk structure and corresponding single layer of (a) monometallic and (b) bimetallic layered MPX_3 compounds

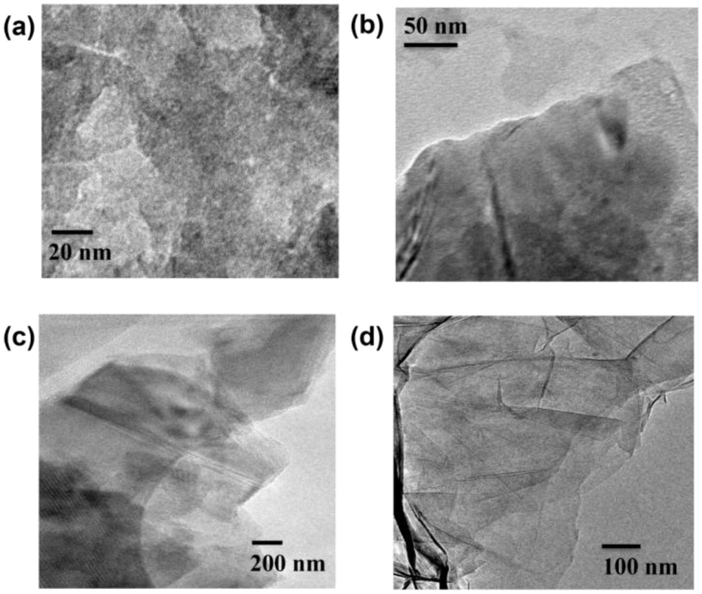

Figure 6: Bright field TEM images of exfoliated of (a) $NiPS_3$, (b) $FePSe_3$ (c) $Ag_{0.5}In_{0.5}PS_3$ and (d) $Ag_{0.5}In_{0.5}PSe_3$

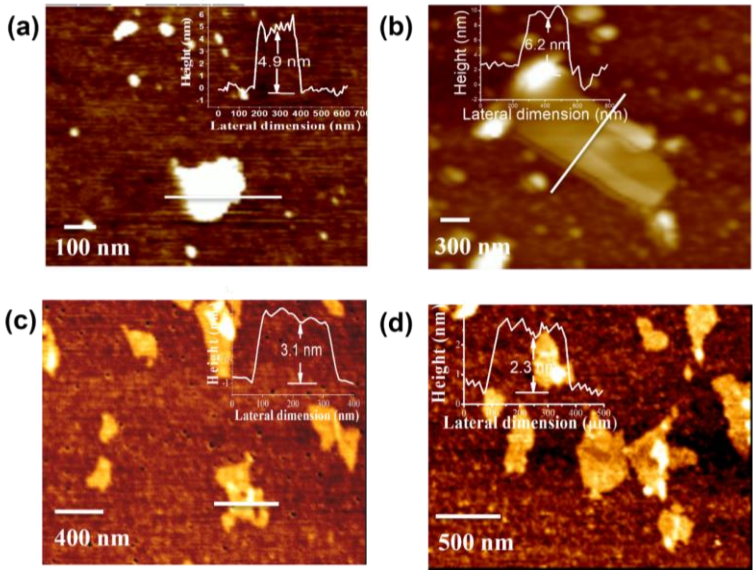

Figure 7: AFM images and corresponding height profiles of exfoliated of (a) $NiPS_3$, (b) $FePSe_3$ (c) $Ag_{0.5}In_{0.5}PS_3$ and (d) $Ag_{0.5}In_{0.5}PSe_3$

gaps in the range of 1.3-3.3eV with the gaps in selenides being smaller than the corresponding sulfides due to the difference in electronegativity between the two elements.

Photocatalytic HER studies

Theoretically, it has been predicted that the band edges and band gaps of these MPX_3 materials are suitable for HER, hence photocatalytic water-splitting experiments were carried out with these exfoliated MPX_3 compounds.[1,2] In a typical HER reaction, exfoliated MPX_3 compounds in water were sensitized with Eosin Y dye and triethanolamine (TEOA) was used as the sacrificial agent. A steady rate of hydrogen evolution was observed with all the MPX_3 compounds in the presence of the dye, which becomes negligible in the absence of the dye (**Figure 9**). Control experiments were carried out to rule out the possibility of hydrogen evolution from the dye or sacrificial agent (**Figure 10d**). HER trend in monometallic phosphosulfides was found to be $NiPS_3 > FePS_3$

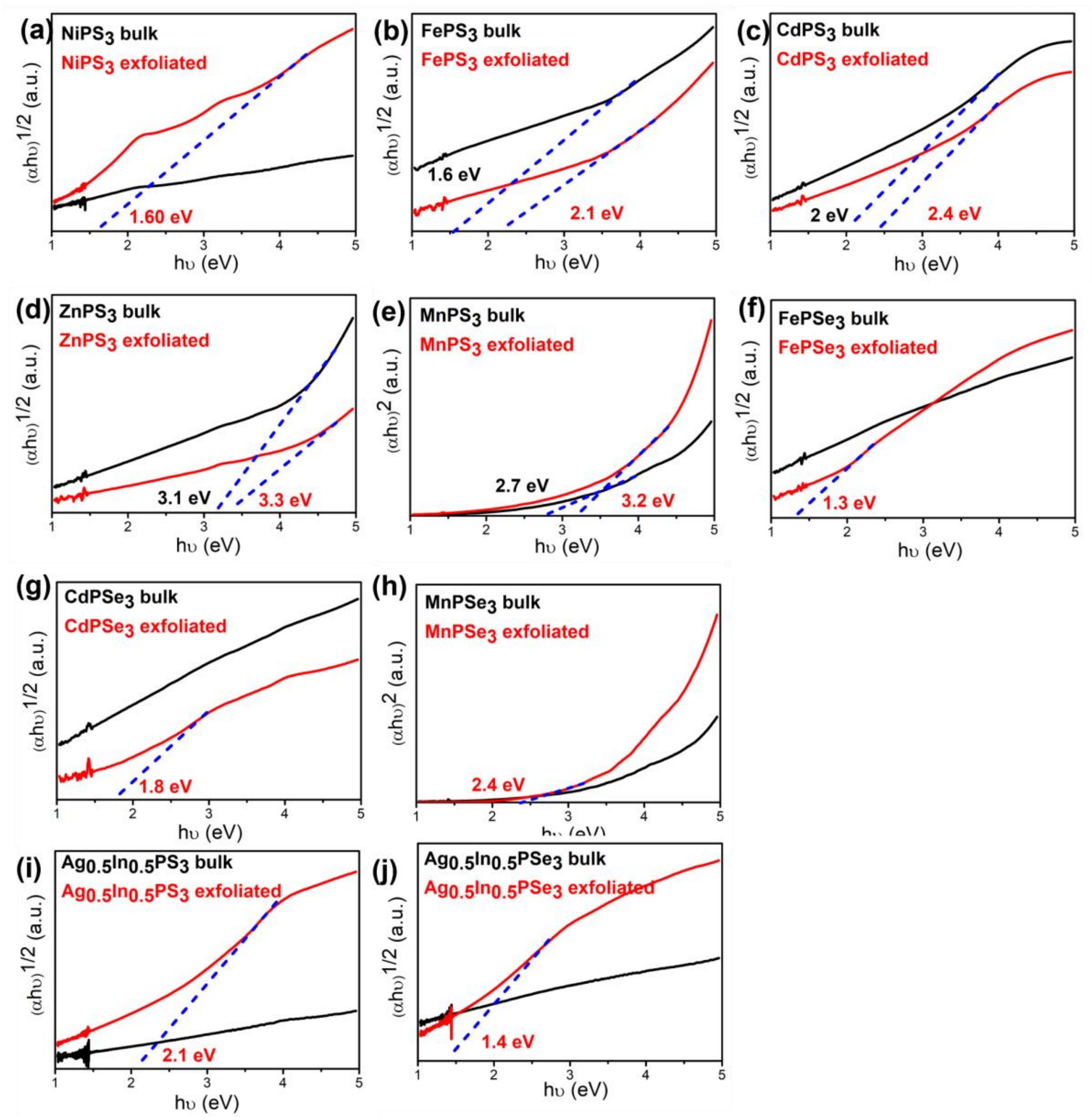

Figure 8: Tauc plots of bulk and exfoliated (a) $NiPS_3$, (b) $FePS_3$, (c) $CdPS_3$, (d) $ZnPS_3$, (e) $MnPS_3$, (f) $FePSe_3$, (g) $CdPSe_3$, (h) $MnPSe_3$, (i) $Ag_{0.5}In_{0.5}PS_3$ and (j) $Ag_{0.5}In_{0.5}PSe_3$

> $CdPS_3$ ~ $MnPS_3$ ~ $ZnPS_3$. $NiPS_3$ shows the highest rate of hydrogen evolution of 2.6 mmol h^{-1} g^{-1}. Among the monometallic selenides, $FePSe_3$ shows the highest HER activity at 1.7 mmol h^{-1} g^{-1}. In the case of the bimetallic compounds, both $Ag_{0.5}In_{0.5}PS_3$ and $Ag_{0.5}In_{0.5}PSe_3$ showed good HER activity, with the sulfide being slightly better at 1.9 mmol

h^{-1} g^{-1}. Cycling studies show appreciable stability for up to 10 hours (**Figure 10**). Saturation of hydrogen evolution was observed in all cases which could be due to dye degradation.[40,41]

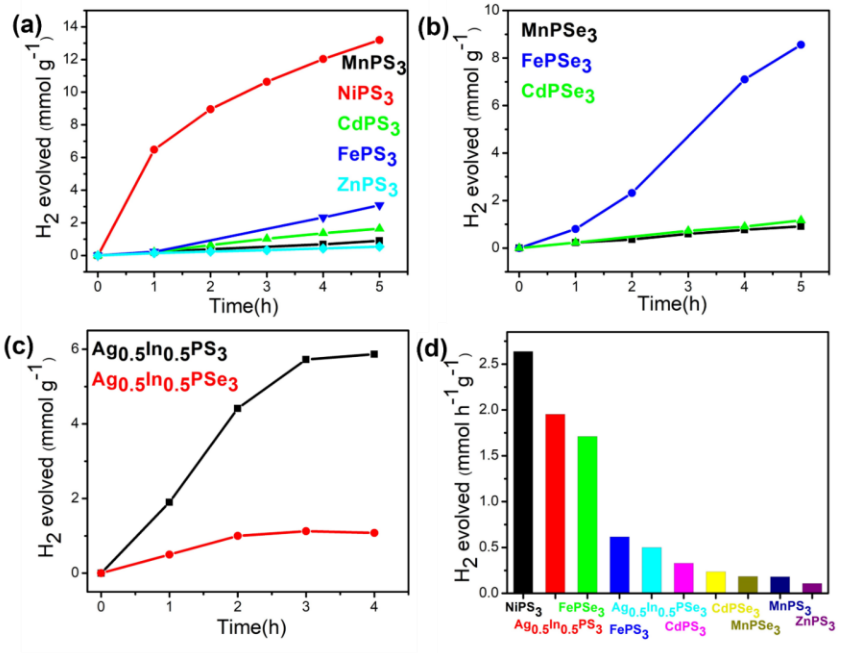

Figure 9: Hydrogen evolution activities of (a) monometallic MPS_3, (b) monometallic $MPSe_3$ and (c) bimetallic $Ag_{0.5}In_{0.5}PX_3$, (d) Comparison of hydrogen evolved

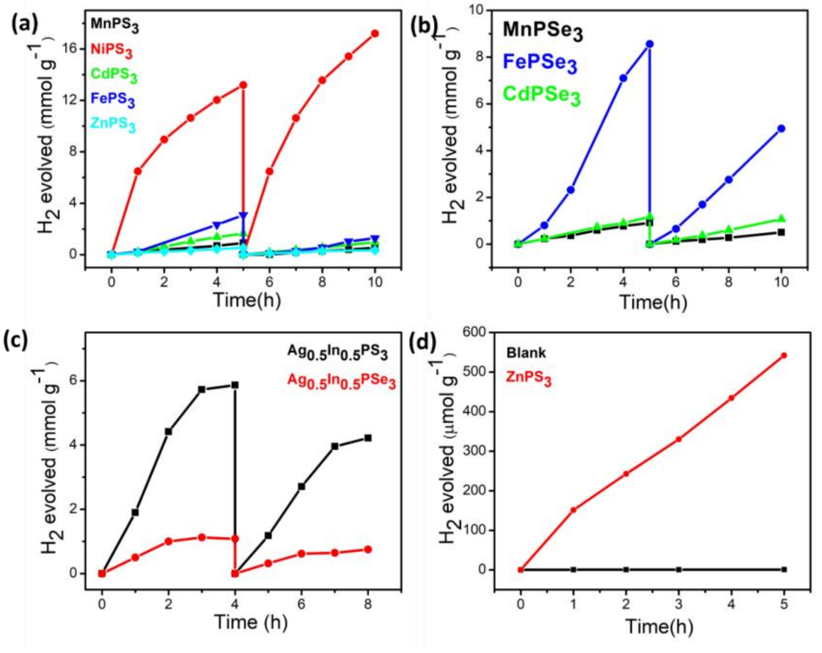

Figure 10: (a-c) HER cycling studies for MPX_3 compounds, (d) HER blank reaction

Raman studies confirm that the nanosheets maintain their structural integrity after water splitting experiments, any minor changes observed in the relative intensity of Raman peaks after HER might be due to residual physisorbed dye on the catalyst surface (**Figure 11**). **Table 1** summarizes the HER activities of all the materials.

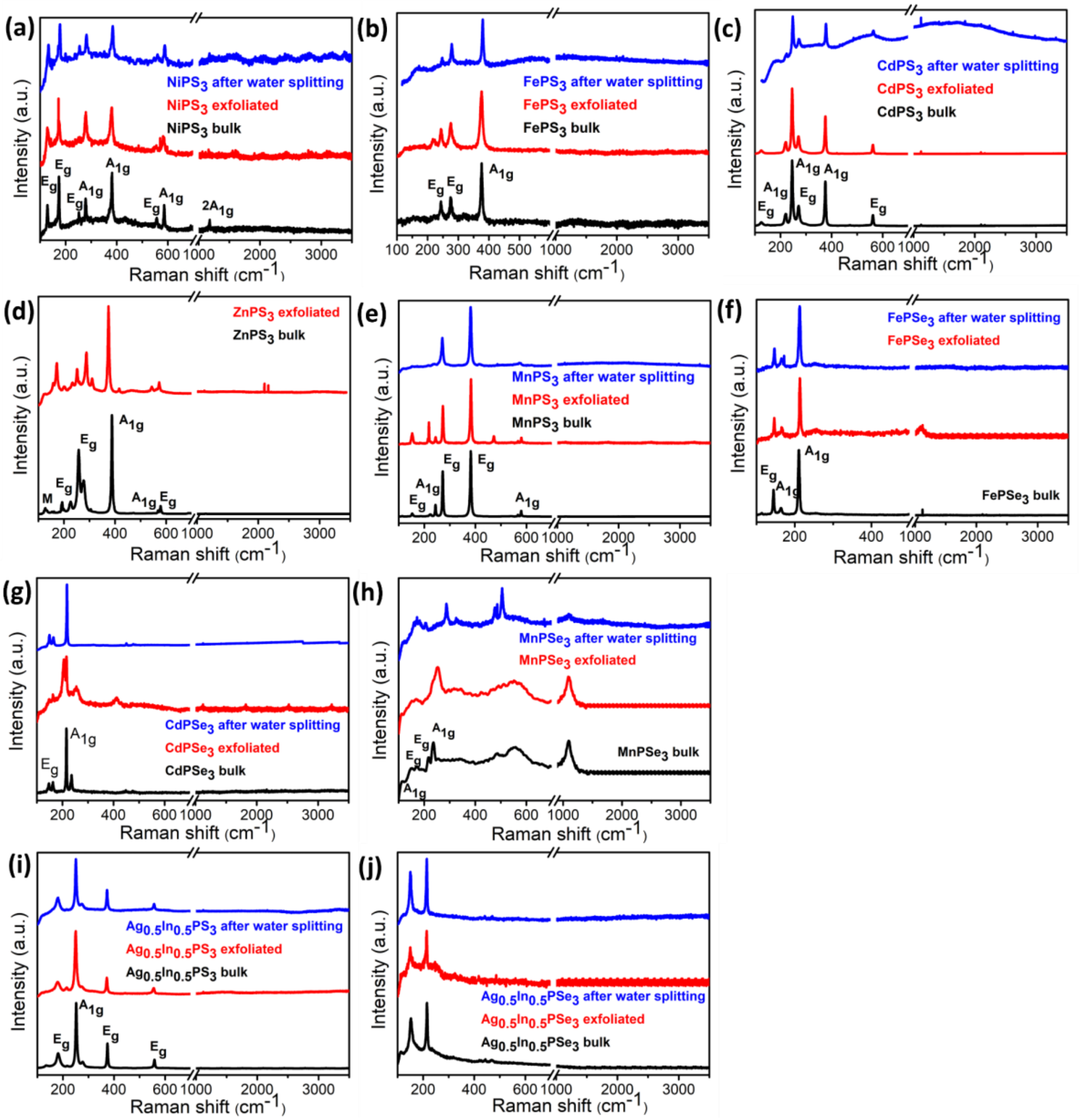

Figure 11: Raman spectra of all synthesized metal phosphosulfides and selenide compounds in bulk form, exfoliated form and after water splitting

Table 1: Summary of photocatalytic activity of all synthesized MPX_3 compounds

Compounds	Bandgap	H_2 yields (mmol $h^{-1}g^{-1}$)
$MnPS_3$	3.2	0.2
$FePS_3$	2.1	0.6
$NiPS_3$	1.6	2.6
$ZnPS_3$	3.3	0.1
$CdPS_3$	2.4	0.3
$MnPSe_3$	2.4	0.2
$FePSe_3$	1.3	1.7
$CdPSe_3$	1.8	0.2
$Ag_{0.5}In_{0.5}PS_3$	2.1	1.9
$Ag_{0.5}In_{0.5}PSe_3$	1.4	0.5

Scheme 2 gives a plausible mechanism of H_2 evolution using the metal phosphochalcogenides catalysts, with the dye molecules involved in the absorption of light and then transfer of an electron to the catalyst surface. Conduction band of MPX_3 accepts this electron from the negatively charged dye molecule. Total density of states (DOS) calculations reported for $NiPS_3$, $FePS_3$, $MnPS_3$ mention that the conduction band minima mainly have contribution from metal 3d orbitals.[11,42,43] Considering the metal centers in $NiPS_3$, $FePS_3$, $MnPS_3$, on addition of an integral or less of electron density to these 3d orbitals, the crystal field stabilization energy (CFSE) values follow the order $NiPS_3$ > $FePS_3$ > $MnPS_3$. This explains how easily these materials can accept electrons from the dye molecules during photocatalytic HER. The electronegativity values of the respective metal centers also follow a similar trend. As for $ZnPS_3$ and $CdPS_3$, both have d^{10} configuration and hence conduction band minimal has contributions from higher s and p

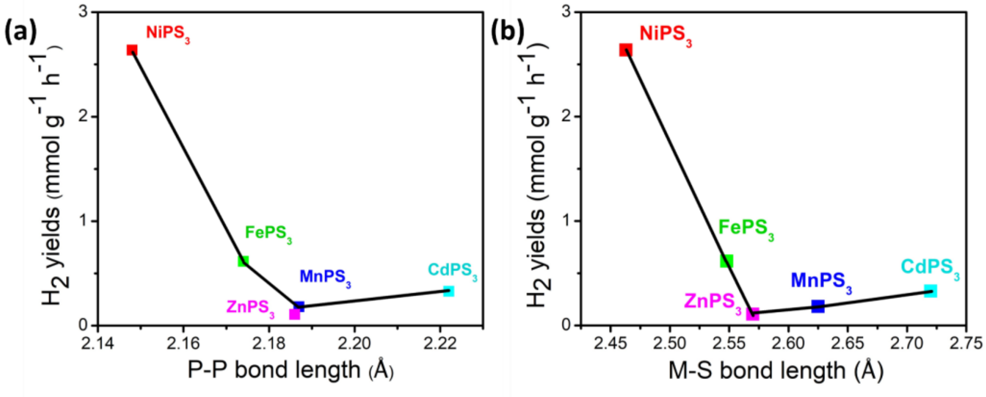

Figure 12: Variation of photocatalytic HER activity with (a) P-P bond length and (b) M-S bond length

orbitals and $\sigma^*_{P\text{-}P}$ and $\sigma^*_{P\text{-}S}$.[44,45] The free energy of hydrogen adsorption (ΔG_H) on the catalyst surface is a good descriptor of the catalytic activity of a material. For the monometallic sulfides, comparing the ΔG_H values for basal planes and edge states of the materials show that the edge states are more favorable toward hydrogen adsorption. The possible adsorption sites present for these materials are the M (Ni, Fe, Mn, Zn, and Cd), P, and S sites. According to theoretical calculations, H adsorption in MPX_3 preferentially takes place at the P site.[15,46,47] The variation of HER activity of the monometallic phosphosulfides with P-P bond length is plotted in **Figure 12a** which shows a decrease in HER activity with increasing P-P bond length.[44] The increase in P-P bond length leads to a decrease in the electron density at each P center, which is the site for H adsorption, and hence affects the trend in the HER activity. The low HER activity of $ZnPS_3$ and $CdPS_3$ might be because its CBM has contributions mainly from $\sigma^*_{P\text{-}P}$ and $\sigma^*_{P\text{-}S}$ orbitals and the addition of electron density to these orbitals increases the P-P bond length. **Figure 12b** shows the variation of HER activity with M-S bond length. We see that on increasing the ionic character of the M-S bond, the HER activity decreases. Of all the listed MPS_3

compounds, Ni-S and Fe-S bonds are more covalent while Zn-S, Mn-S and Cd-S bonds are more ionic.

HER studies were also carried out for the as synthesized metal phosphoselenides. The HER activity of these compounds follows the trend $FePSe_3 > CdPSe_3 \sim MnPSe_3$. With the substitution of S with Se, no general trend was visible. In case of metal phosphoselenides, the ΔG_H values of both Se and P sites are close to zero and hence both can efficiently adsorb H.[48] Pumera et al[49] studied the electrochemical properties of various metal phosphorus triselenides and found $FePSe_3$ to be active catalyst for electrochemical HER and due to its low charge transfer resistance value (R_{ct}).[49] $NiPSe_3$ and $ZnPSe_3$ could not be synthesized in pure phase by the present experimental conditions. Theoretical

Table 2: Comparison of photocatalytic HER activities of different metal phosphochalcogenides catalysts

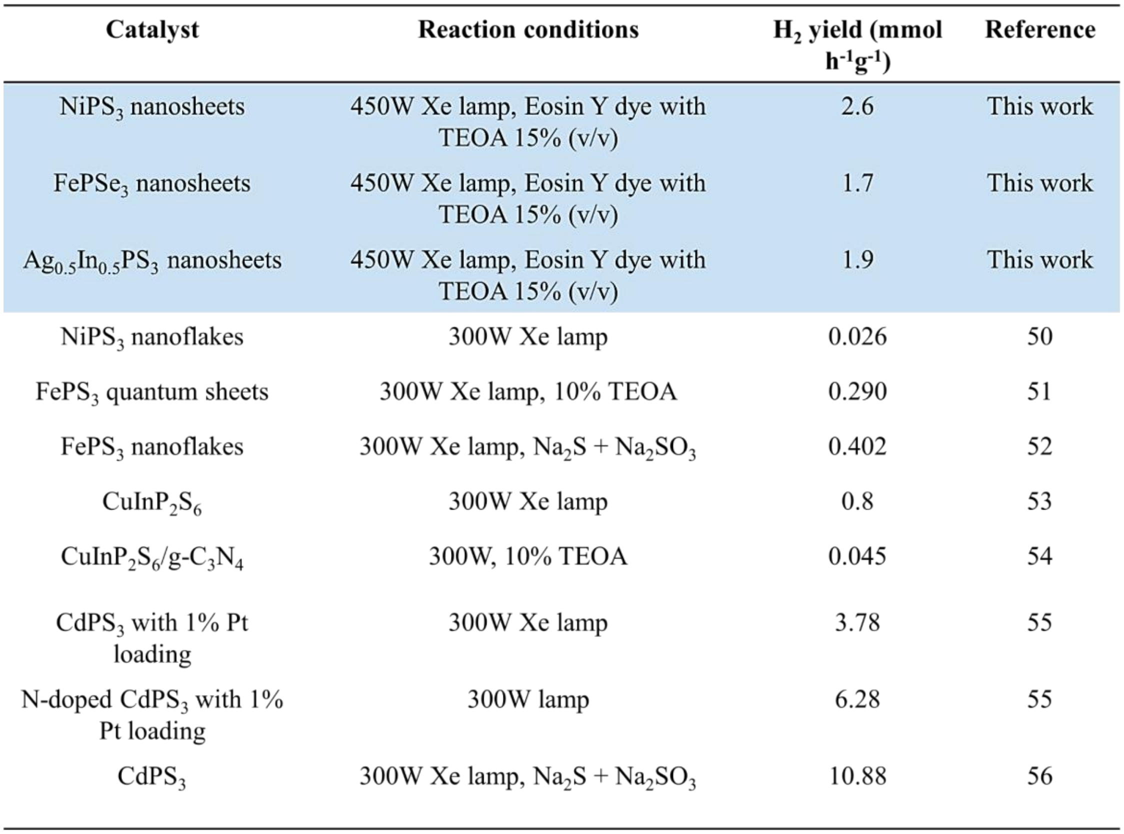

Catalyst	Reaction conditions	H_2 yield (mmol $h^{-1}g^{-1}$)	Reference
$NiPS_3$ nanosheets	450W Xe lamp, Eosin Y dye with TEOA 15% (v/v)	2.6	This work
$FePSe_3$ nanosheets	450W Xe lamp, Eosin Y dye with TEOA 15% (v/v)	1.7	This work
$Ag_{0.5}In_{0.5}PS_3$ nanosheets	450W Xe lamp, Eosin Y dye with TEOA 15% (v/v)	1.9	This work
$NiPS_3$ nanoflakes	300W Xe lamp	0.026	50
$FePS_3$ quantum sheets	300W Xe lamp, 10% TEOA	0.290	51
$FePS_3$ nanoflakes	300W Xe lamp, $Na_2S + Na_2SO_3$	0.402	52
$CuInP_2S_6$	300W Xe lamp	0.8	53
$CuInP_2S_6$/g-C_3N_4	300W, 10% TEOA	0.045	54
$CdPS_3$ with 1% Pt loading	300W Xe lamp	3.78	55
N-doped $CdPS_3$ with 1% Pt loading	300W lamp	6.28	55
$CdPS_3$	300W Xe lamp, $Na_2S + Na_2SO_3$	10.88	56

calculations predict that bimetallic phosphochalcogenides like $Ag_{0.5}In_{0.5}PS_3$ have suitable band alignment for water splitting reactions but the same has not been explored experimentally previously.[1,2] We found that both the bimetallic phosphochalcogenides are active for hydrogen production with appreciable yields of 1.9 mmol $h^{-1}g^{-1}$ for $Ag_{0.5}In_{0.5}PS_3$ and 0.5 mmol $h^{-1}g^{-1}$ for $Ag_{0.5}In_{0.5}PSe_3$. This study opens up possibilities for the exploration of bimetallic phosphosulfides and selenides for their catalytic activity. This study was one of the first reports on photocatalytic HER in metal phosphochalcogenides and since then there have been multiple reports in the literature.[50–57] **Table 2** compares the photocatalytic HER activities from this study with available literature reports and see that our H_2 yields are at par.

4.5 Conclusions

In conclusion, we have successfully synthesized ternary and quaternary metal phosphochalcogenides by high-temperature reactions and studied their photocatalytic HER activities. Among the studied ternary compounds, $NiPS_3$ exhibits the highest catalytic activity of 2.6 mmol $h^{-1}g^{-1}$ while low activity is observed in the case of monometallic phosphosulfides of Mn, Zn, or Cd. We were able to correlate this photocatalytic behavior with CFSE values, P-P, and M-S bond lengths of these materials. Among the studied quaternary compounds $Ag_{0.5}In_{0.5}PS_3$ exhibits a higher HER activity of 1.9 mmol $h^{-1}g^{-1}$.

References

(1) Liu, J.; Li, X. B.; Wang, D.; Lau, W. M.; Peng, P.; Liu, L. M.; *J. Chem. Phys.*, **2014**, *140* (5), 054707.

(2) Susner, M. A.; Chyasnavichyus, M.; McGuire, M. A.; Ganesh, P.; Maksymovych, P. *Adv. Mater.*, **2017**, *29* (38), 1602852.

(3) Taylor, B.; Steger, J.; Wold, A.; Kostinerlb, E., *Inorg. Chem.*, **1974**, *13* (11), 2719-2721

(4) Foot, P. J. S.; Nevettb, B. A., *J. Chem. Soc., Chem Commun.*, **1987**, 380-381

(5) Liu, F.; You, L.; Seyler, K. L.; Li, X.; Yu, P.; Lin, J.; Wang, X.; Zhou, J.; Wang, H.; He, H.; Pantelides, S. T.; Zhou, W.; Sharma, P.; Xu, X.; Ajayan, P. M.; Wang, J.; Liu, Z., *Nat. Commun.*, **2016**, *7*, 12357

(6) Boucher, F.; Evain, M.; Brec, R., *J. Alloys. Compd*., **1994**, *215*, 63-70.

(7) Tsurubayashi, M.; Kodama, K.; Kano, M.; Ishigaki, K.; Uwatoko, Y.; Watanabe, T.; Takase, K.; Takano, Y., *AIP Adv.*, **2018**, *8* (10), 101307.

(8) Joy, P. A.; Vasudevan, S., *J. Chem. Phys.*, **1993**, *99* (6), 4411–4422.

(9) Cheng, Z.; Shifa, T. A.; Wang, F.; Gao, Y.; He, P.; Zhang, K.; Jiang, C.; Liu, Q.; He, J., *Adv. Mater.*, **2018**, *30* (26), 1707433

(10) Vladlen Zhukov, Florent Bloucher, Pere Alemany, Michel Evain, Santiago Alvarez; *Inorg. Chem.*, **1995**, *34* (5), 1159–1163

(11) Mercier, H.; Mathey, Y.; Canadell, E., *Inorg. Chem.*,**1987**, *26* (6), 963–965.

(12) Gusmão, R.; Sofer, Z.; Sedmidubský, D.; Huber, Š.; Pumera, M., *ACS Catal.*, **2017**, *7* (12), 8159–8170.

(13) Mukherjee, D.; Austeria, P. M.; Sampath, S., *ACS Energy Lett.*, **2016**, *1* (2), 367–372.

(14) Wang, F.; Shifa, T. A.; He, P.; Cheng, Z.; Chu, J.; Liu, Y.; Wang, Z.; Wang, F.; Wen, Y.; Liang, L.; He, J., *Nano Energy*, **2017**, *40*, 673–680.

(15) Jenjeti, R. N.; Austeria, M. P.; Sampath, S., *ChemElectroChem*, **2016**, *3* (9), 1392–1399.

(16) Zhang, J.; Cui, R.; Li, X.; Liu, X.; Huang, W., *J. Mater. Chem. A*, **2017**, *5* (45), 23536–23542.

(17) Zhang, X.; Zhao, X.; Wu, D.; Jing, Y.; Zhou, Z., *Adv. Sci.*, **2016**, *3* (10), 1600062

(18) Konkena, B.; Masa, J.; Botz, A. J. R.; Sinev, I.; Xia, W.; Koßmann, J.; Drautz, R.; Muhler, M.; Schuhmann, W., *ACS Catal.*, **2017**, *7* (1), 229–237.

(19) Mayorga-Martinez, C. C.; Sofer, Z.; Sedmidubský, D.; Huber, Š.; Eng, A. Y. S.; Pumera, M., *ACS Appl. Mater. Interfaces,* **2017**, *9* (14), 12563–12573.

(20) Yu, J.; Li, W. J.; Zhang, H.; Zhou, F.; Li, R.; Xu, C. Y.; Zhou, L.; Zhong, H.; Wang, J., *Nano Energy*, **2019**, *57*, 222–229.

(21) Jenjeti, R. N.; Kumar, R.; Austeria, M. P.; Sampath, S., *Sci. Rep.*, **2018**, *8* (1), 8586

(22) Du, K. Z.; Wang, X. Z.; Liu, Y.; Hu, P.; Utama, M. I. B.; Gan, C. K.; Xiong, Q.; Kloc, C., *ACS Nan,o* **2016**, *10* (2), 1738–1743.

(23) Hisatomi, T.; Kubota, J.; Domen, K., *Chem. Soc. Rev*., **2014**, *43* (22), 7520–7535.

(24) Takanabe, K., *ACS Catal*., **2017**, *7* (11), 8006–8022.

(25) Min, S.; Lu, G., *J Phys. Chem. C,* **2011**, *115* (28), 13938–13945.

(26) Chou, S. S.; Sai, N.; Lu, P.; Coker, E. N.; Liu, S.; Artyushkova, K.; Luk, T. S.; Kaehr, B.; Brinker, C. J., *Nat. Commun*., **2015**, *6*, 8311

(27) Maitra, U.; Gupta, U.; De, M.; Datta, R.; Govindaraj, A.; Rao, C. N. R., *Angew. Chem.*, **2013**, *52* (49), 13057–13061.

(28) Pfitzner, A.; Seidlmayer, S.,*Z. Anorg. Allg. Chem*., **2009**, *635* (4–5), 704–707.

(29) Ouilt, Z.; Leblanc, A.; Colombet, P., *J. Solid State Chem.*, **1987**; *66*, 86-94

(30) Piacentini, M. ’; Khumalo, F. S.; Olson, C. G.; Anderegg, J. W.; Lynch, D. W., *Chem. Phys.*, **1982**; *65*, 289-304

(31) Currb, G. M.; Grasso, V.; Neri, F.; Silipigni, L., *Il Nuovo Cimento D,* **1995**; *17*. 37–52

(32) Shalvoy, R. B.; Reucroft, P. J., *J Vac Sci Technol*, **1979**, *16* (2), 567–569.

(33) van der Heide, H.; Hemmel, R.; van Bruggen, C. F.; Haas, C., *J. Solid State Chem*., **1980**; *33*, 17-25

(34) Mukherjee, D.; Muthu Austeria, P.; Sampath, S., *ACS Appl. Energy Mater.*, **2018**, *1* (1), 220–231.

(35) Yu, J.; Li, W. J.; Zhang, H.; Zhou, F.; Li, R.; Xu, C. Y.; Zhou, L.; Zhong, H.; Wang, J., *Nano Energy*, **2019**, *57*, 222–229.

(36) Babuka, T.; Glukhov, K.; Vysochanskii, Y.; Makowska-Janusik, M., *RSC Adv.*, **2018**, *8* (13), 6965–6977.

(37) Wang, X.; Du, K.; Liu, W.; Hu, P.; Lu, X.; Xu, W.; Kloc, C.; Xiong, Q., *Appl. Phys. Lett.*, **2016**, *109* (12), 123103

(38) Cao, W.; Wang, J.; Ma, M., *J. Phys. Chem. Lett.,* **2019**, *10* (5), 981–986.

(39) Backes, C.; Higgins, T. M.; Kelly, A.; Boland, C.; Harvey, A.; Hanlon, D.; Coleman, J. N., *Chem. Mater*., **2017**, *29* (1), 243–255.

(40) Gonce, M. K.; Aslan, E.; Ozel, F.; Hatay Patir, I., *ChemSusChem*, **2016**, *9* (6), 600–605.

(41) Jia, T.; Li, M. M. J.; Ye, L.; Wiseman, S.; Liu, G.; Qu, J.; Nakagawa, K.; Tsang, S. C. E., *Chem. Commun.*, **2015**, *51* (70), 13496–13499.

(42) Hashemi, A.; Komsa, H. P.; Puska, M.; Krasheninnikov, A. V., *J. Phys. Chem. C*, **2017**, *121* (48), 27207–27217.

(43) Scagliotti, M.; Jouanne, M.; Balkanski, M.; Ouvrard, G.; Benedek, G.; *Phys. Rev. B*., **1987**; *35*, 7097

(44) Brec, R.; Ouvrard, G.; Rouxel, J.; *Mat. Res. Bull*., **1985**; *20*, 1257-1263

(45) Whangbo, M.-H.; Brec, R.; Ouvrard, G.; Rouxel, J.; *Inorg. Chem.*, **1985**; *24*, 2459-2461

(46) Zhang, J.; Cui, R.; Li, X.; Liu, X.; Huang, W.; *J. Mater. Chem. A*, **2017**, *5* (45), 23536–23542.

(47) Song, B.; Li, K.; Yin, Y.; Wu, T.; Dang, L.; Cabán-Acevedo, M.; Han, J.; Gao, T.; Wang, X.; Zhang, Z.; Schmidt, J. R.; Xu, P.; Jin, S.; *ACS Catal.*, **2017**, *7* (12), 8549–8557.

(48) Anantharaj, S.; Ede, S. R.; Sakthikumar, K.; Karthick, K.; Mishra, S.; Kundu, S.; *ACS Catal.*, **2016**, *6* (12), 8069–8097.

(49) Gusmão, R.; Sofer, Z.; Sedmidubský, D.; Huber, Š.; Pumera, M.; *ACS Catal.*, **2017**, *7* (12), 8159–8170.

(50) Wang, F.; Shifa, T. A.; He, P.; Cheng, Z.; Chu, J.; Liu, Y.; Wang, Z.; Wang, F.; Wen, Y.; Liang, L.; He, J.; *Nano Energy*, **2017**, *40*, 673–680.

(51) Cheng, Z.; Shifa, T. A.; Wang, F.; Gao, Y.; He, P.; Zhang, K.; Jiang, C.; Liu, Q.; He, J.; *Adv. Mater.*, **2018**, *30* (26), 1707433

(52) Cheng, Z.; Sendeku, M. G.; Liu, Q., *Nanotechnol.*, **2020**, *31* (13), 205707

(53) Yu, P.; Wang, F.; Meng, J.; Shifa, T. A.; Sendeku, M. G.; Fang, J.; Li, S.; Cheng, Z.; Lou, X.; He, J.; *CrystEngComm.*, **2021**, *23* (3), 591–598.

(54) Lin, B.; Chaturvedi, A.; Di, J.; You, L.; Lai, C.; Duan, R.; Zhou, J.; Xu, B.; Chen, Z.; Song, P.; Peng, J.; Ma, B.; Liu, H.; Meng, P.; Yang, G.; Zhang, H.; Liu, Z.; Liu, F.; *Nano Energy*, **2020**, *76*, 104792

(55) Li, H.; Wells, N.; Chong, B.; Xu, B.; Wei, J.; Yang, B.; Yang, G.; *Chem. Eng. Sci.*, **2021**, *229*, 116069.

(56) Zhang, Y.; Zhao, Y.; Bao, C.; Xiao, Y.; Xiang, Y.; Song, M.; Huang, W.; Ma, L.; Hou, H.; Chen, X.; *J. Alloys Compd.,* **2022**, *909*, 164731.

(57) Shifa, T. A.; Wang, F.; Cheng, Z.; He, P.; Liu, Y.; Jiang, C.; Wang, Z.; He, J.; *Adv. Func. Mater.* **2018**, *28* (18), 1800548

Chapter 5

Charge-transfer studies in phosphorene and phosphorene quantum dots

SUMMARY

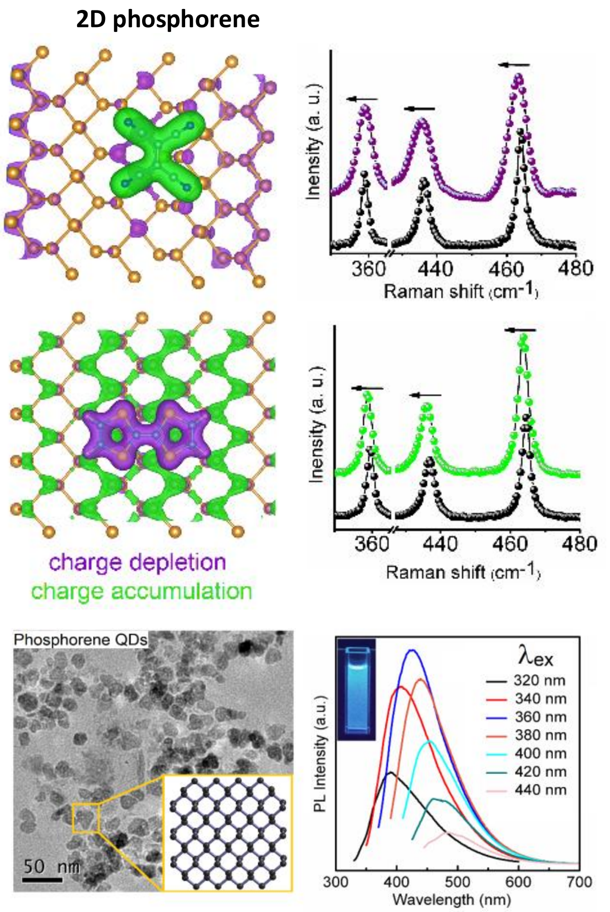

In recent years, elemental two-dimensional materials are being considered promising candidates for nanoelectronics and optoelectronics. The most explored member of the group, phosphorene has in recent years been considered the most plausible alternative to graphene due to its inherent direct bandgap, and high carrier mobilities. Phosphorene also shows many other interesting features like anisotropic electric conductance and optical responses, tunable band structure, etc. The chemical reactivity of phosphorene is due to the presence of lone pair on each atom and the same has been utilized for tuning the properties and passivating the surface of phosphorene. We try to understand the charge transfer behavior of 2D

Papers related to this work have appeared in *Chem. Phys. Chem.* **2017**, *18*(21), 2985-2989, and *Chem. Phys. Lett*. **2018**, *699*, 223-228 phosphorene with different donor and acceptor molecules using Raman spectroscopy and we establish that both hole and electron can be doped into phosphorene by molecular charge transfer. Optoelectronic applications of phosphorene are still limited by its narrow bandgap. In recent years people have started exploring phosphorene quantum dots for their interesting optoelectronic properties. We were able to prepare blue-fluorescent phosphorene quantum dots of average diameters ~5 nm, 3 nm, and 1 nm by liquid exfoliation in different powers. These quantum dots showed excitation-dependent emission characteristics. We have also studied the charge transfer behavior of these quantum dots with donor and acceptor molecules.

5.1 Introduction

Research on monoelemental monolayers can be traced back to the 1930s to the pioneering work of Langmuir who studied the effect of the formation of alkali metal atoms on metal films and laid down the foundations of surface science as an area of research.[1,2] The field of elemental two-dimensional materials is undergoing a reawakening since the discovery of graphene in 2004. This renewed interest in post-graphene elemental 2D materials is in search of atomically thin materials with a unique and exciting blend of properties. This is an ever-expanding list of materials and as of now, 15 elemental main group 2D materials have been synthesized or theoretically predicted.[1] One major inspiration for the exploration of new 2D materials is the absence of any bandgap in graphene.[3] Among the main group elemental 2D materials, group 13 monolayers like borophene, aluminene, gallenene are metallic in nature; group 14 monolayers like silicene, germanene are semi-metallic, while group 15 monolayers like phosphorene, arsenene, antimonene, and bismuthene are semiconducting with bandgaps in the range of 0-2.6 eV and among group 16 monolayers tellurene is predicted to have a bandgap of ~1.5 eV.[4–6]

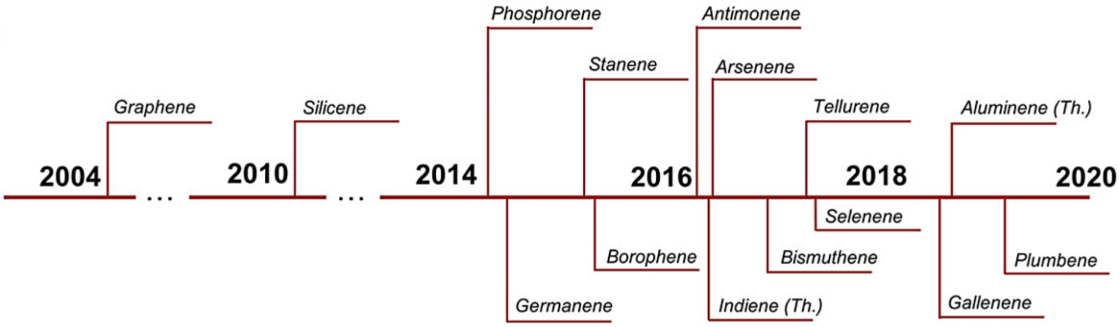

Figure 1: Timeline for experimental realization of different elemental 2D materials. Reprinted with permission from ref 1, Copyright (2020) John Wiley and Sons

5.1.1 2D pnictogens

Pnictogens are an interesting class of elemental 2D materials with broad bandgaps and high carrier mobilities (several thousand $cm^2V^{-1}s^{-1}$), making them promising candidates for various electronic, optoelectronic, spintronic, and thermoelectric applications.[4–6] In its bulk layered state, Black phosphorous (the most stable allotrope of P) has a bandgap of 0.3eV while bulk As, Sb, and Bi are semi-metallic. 2D pnictogens show typical effects induced by quantum confinement along with a rich variety of second-order effects. Each atom in the lattice has three σ sp^3 hybridized bonds with three nearest neighbors and a lone pair of electrons, leading to significant puckering and pseudo Jahn-Teller distortion.[4] The layers are held together by weaker van der Waals-like interactions. The members of this group can structurally manifest in five typical honeycomb structures (α, β, γ, δ, ε) and four non-honeycomb structures (ζ, η, θ, ι).[6] **Figure 2** gives the pictorial

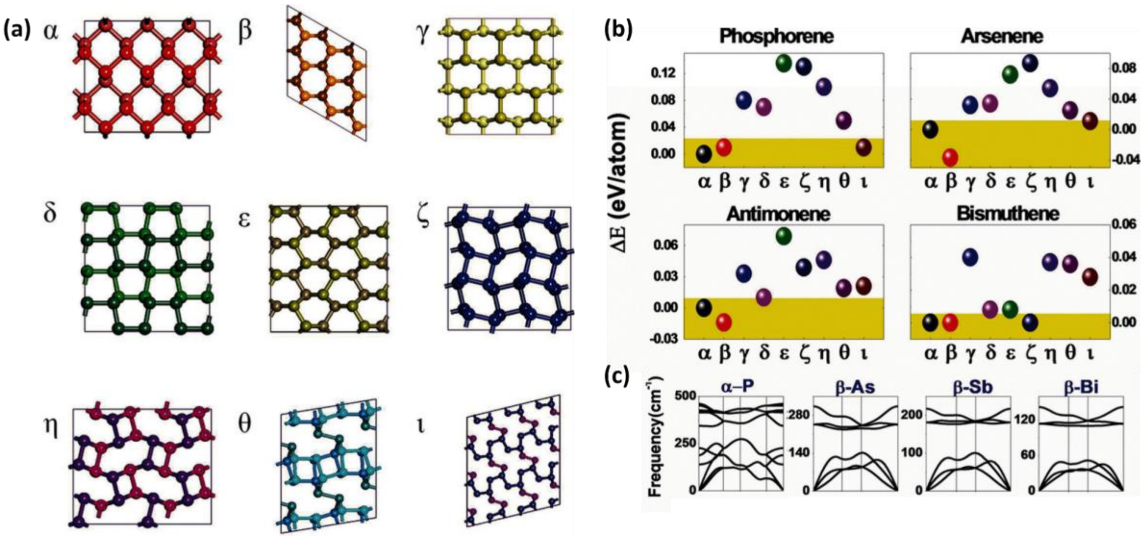

Figure 2: a) Top view of the group 15 relaxed monolayer allotropes, (b) Calculated average binding energies of all group 15 monolayer allotropes with (c) the corresponding phonon band dispersions of the most stable allotropes. Reprinted with permission from ref 6, Copyright 2016 John Wiley and Sons

representation of all the allotropes of layered pnictogens along with their binding energy plots and phonon band dispersions for the most stable allotropes. For phosphorene, the α-form is most stable while for both arsenene and antimonene the β-form is most stable, for bismuthene all three forms seem equally stable (α, β, ζ) wherein β-Bi is the naturally available most stable allotrope. The phonon dispersions show that these materials are semiconducting in the monolayer regime. In this work, we have studied both 2D phosphorene and phosphorene quantum dots

5.1.2 Phosphorene

Monolayer phosphorene was the first 2D elemental material after graphene to be discovered and was instrumental in reviving the interest in the field of elemental 2D materials.[7–11] Phosphorene occupies a very important position in the atlas of 2D materials due to its direct bandgap in the range of 0.3-1.5 eV, which lies between graphene (0 eV) and transition metal dichalcogenides (~1-2 eV). Moreover, phosphorene has higher carrier mobility than transition metal dichalcogenides and is theoretically predicted to be an important candidate for high-speed flexible electronics.[9] α-phosphorene has a puckered orthorhombic structure and belongs to the *Cmca* space group. However, one bottleneck in the use of phosphorene for various device applications is its inherent instability under ambient conditions. Phosphorene is highly oxophilic and undergoes dissociative chemisorption with oxygen. At present, multiple approaches are being used to stabilize phosphorene for device incorporation including synthesis of a protective AlO_x or HfO_x layer on phosphorene by atomic layer deposition (ALD),[12] encapsulation in polymer nanocomposites,[13,14] insulating carbon layers by covalent functionalization[15] or non-covalent functionalization with donor-acceptor molecules.[16,17]

5.1.3 Phosphorene quantum dots (PQDs)

Although phosphorene has an inherent bandgap (0.3-1.45 eV), the material still shows no absorption/emission in the visible region, limiting its optoelectronic applications. Quantum dots are an interesting class of nanomaterials with dimension-dependent electronic and optical properties owing to quantum confinement and edge effects and have been successfully used in photovoltaic devices, optoelectronic devices, memory devices, and biological analysis.[18–22] Phosphorene quantum dots (PQD) have the potential to include many of the interesting properties of 2D phosphorene along with an emission in the visible region and maybe some other interesting properties.[23,24] The inherent instability of phosphorene under ambient conditions poses limitations in the synthesis and stabilization of PQDs. There are few literature reports on the synthesis of phosphorene quantum dots using liquid exfoliation, pulsed laser ablation or solvothermal methods wherein these materials have been used in flexible memory devices or as NIR photothermal agents along with a report on their blue-violet emission however there are even fewer reports on optical properties of these materials.[23–28]

5.1.4 Charge transfer studies

Charge transfer processes between interacting donors and acceptors are the bedrock for many fundamental studies, and various applications ranging from biosensing to energy storage.[29] In recent years, low-dimensional quantum confined materials have attracted attention for various optoelectronic devices due to their strong light-matter interactions and size-tunable band edge, and optical properties. Charge transfer interactions into and from low-dimensional materials are key steps underlying this process.[30] The reactivity of phosphorene is due to the presence of lone pair on each atom, hence charge transfer complexes are crucial for improving the inherent stability of 2D phosphorene and phosphorene quantum dots under ambient conditions.

5.2 Scope of this investigation

Section 5.4.A discusses charge-transfer studies with different donor/acceptor molecules in 2D phosphorene. We have synthesized few-layered phosphorene nanosheets by liquid exfoliation and studied their charge-transfer interaction properties with different donor and acceptor molecules using Raman spectroscopy. Thses results were further verified by theoretical calculations. This study showed that there is no gross electron-hole asymmetry in phosphorene.

In **section 5.4.B** we have synthesized phosphorene quantum dots (PQD) of three different sizes (diameters ~ 5nm, 3nm, and 1nm) by liquid exfoliation in toluene. PQD dispersions showed an excitation-dependent emission feature, a characteristic of quantum dots. We have calculated the quantum yields of these materials and studied their charge-transfer behavior with different donor-acceptor molecules. Charge-transfer complexes can be effectively utilized to tune the electronic properties of phosphorene nanosheets and quantum dots and improve their ambient stability.

5.3 Experimental section

Materials

Black phosphorous crystals (Smart elements, UK), N-Methyl-2-pyrrolidone (NMP) (Spectrochem, 99%), and Toluene (Spectrochem, 99%) were purchased from commercial sources and used as received.

Synthesis of phosphorene

Phosphorene was synthesized by liquid exfoliation of black phosphorous (BP) crystals in NMP.[31] Anhydrous NMP was purged with N_2 gas for 2 hours to remove dissolved oxygen. BP crystals were stored in an MBraun N_2 glove box with O_2 and H_2O levels of < 1.0 ppm. The BP crystals were ground into thin flakes. 20 mg of BP crystals were taken in a 50 mL centrifuge tube fitted with the probe sonicator tip to its cap. 20 mL of deoxygenated NMP was added to this vessel. The above steps were carried out in N_2 atmosphere as BP crystals are very sensitive to O_2. This sample was then probe sonicated at 20% amplitude and 20 kHz, 4 sec on / 4 sec off pulses for 4 hours. The set-up was connected to a chiller maintained at 5 °C. After sonication, the BP dispersion was centrifuged at 2000 rpm (3148 *g*) for 20 minutes. The supernatants were collected and further centrifuged at 5000 rpm (7870 *g*) for 1 hour. The light-yellow supernatants were stored under a nitrogen environment in a Schlenk flask.

Preparation of phosphorene samples for Raman charge transfer studies

Samples for Raman studies were prepared by sonication of phosphorene and donor/acceptor compounds. Typically, an aliquot amount of the solution of the respective donor/acceptor compound was mixed with 50 μL of as-prepared phosphorene dispersion and bath sonicated for 2 hours. After sonication, the mixture was drop-casted on a glass slide and dried at 150 ^{O}C in an oven or under vacuum.

Synthesis of phosphorene quantum dots

Phosphorene quantum dots (PQDs) were prepared in dry and degassed toluene by probe sonication. 20 mg of BP crystals were taken in a 50 mL centrifuge tube fitted with the probe sonicator tip to its cap. Anhydrous toluene purged with N_2 gas was added into this centrifuge tube under N_2 atmosphere. The vessel was immersed in a water bath and connected to a probe sonicator which was operated at 150 Watt and 4 sec on/ 4 sec off pulses for 8 hours. The grey dispersion obtained was centrifuged at 10000 rpm (15740 *g*) for two cycles of 1 hour each to remove non-exfoliated BP particles. The supernatants were collected and stored under nitrogen in a Schlenk flask. Similarly, PQDs were also prepared by applying sonication power of 187.5 and 225 Watt.

Charge transfer studies of 2D phosphorene nanosheets with donor-acceptor molecules

Computational details

Density Functional Theory-based calculations for phosphorene were performed using Vienna Ab initio Simulation Package (VASP). To describe the exchange and correlation of electrons Perdew-Burke-Ernzerhof (PBE) functional within the generalized gradient approximation (GGA) has been considered.[32] Projected augmented-wave (PAW) potential has been used in all the calculations.[33,34] A plane-wave basis set with a sufficient energy cutoff of 500 eV has been used to represent valence electrons. To avoid spurious interactions in the non-periodic direction, we created a vacuum of 30 Angstrom along the non-periodic direction and our supercell consideration keeps the molecules 10 Å away from each other. The systems are optimized until the forces acting on per atom are less than 0.02 eV/Å. We have considered the sampling of the Brillouin zone using a Monkhorst Pack grid of 5 X 5 X 1, and for the electronic property calculations, we have considered a 21 X 21 X 1 grid. For the Raman mode of molecules, Gaussian 09 software package was used.[35]

Steady-state and time-resolved fluorescence measurements for phosphorene quantum dots

Quantum yield measurements

For quantum yield measurements, wavelength integrated fluorescence intensities of various samples of PQD and quinine sulfate were plotted against their absorbances, giving rise to a linear plot. The slope values of these plots were substituted in the below equation to calculate fluorescence quantum yield. Quantum yields were determined relative to quinine sulfate by using the following formula[36]:

$$\phi_{PQD} = \phi_{\text{quinine sulphate}} \left(\frac{\text{slope}_{PQD}}{\text{slope}_{\text{quinine sulphate}}} \right) \left(\frac{\eta^2_{\text{toluene}}}{\eta^2_{0.1\text{ M }H_2SO_4}} \right)$$

where ϕ_{PQD} = fluorescence quantum yield (ϕ for quinine sulphate standard in 0.1 M H_2SO_4 = 54%), η = refractive index (toluene = 1.4869 and 0.1 M H_2SO_4 = 1.33), slope $_{\text{quinine sulphate}}$ = 6.25×10^8 , slope $_{PQD}$ = 9.07×10^7, 7.04×10^7 and 7.36×10^7 for PQDs prepared at 150, 187.5 and 225 W respectively. Four different samples of each PQD (in dry toluene) and quinine sulfate (in 0.1 M H_2SO_4) were prepared. To ensure the linearity of the integrated fluorescence intensities with optical densities, the absorbance at 360 nm was adjusted below 0.1 for all the samples by dilution.

Quenching studies using Stern-Volmer plots

Stern-Volmer equation helps in gaining information regarding fluorescence lifetime and the quenching of fluorescence of a material in the presence of a quencher molecule.[37] In simplest form a plot of $\frac{\Phi°}{\Phi}$ or $\frac{F°}{F}$ vs concentration of quencher [Q] gives a linear relationship according to the equation:

$$\frac{F°}{F}\left(\text{or } \frac{\Phi°}{\Phi}\right) = 1 + K_{sv}[Q] \qquad [1]$$

wherein Φ° and F° are quantum yields or emission intensity in the absence of quencher and Φ and F are the same quantities in the presence of different concentrations of quencher. The factor "K_{SV}" is called the Stern-Volmer constant and is obtained from the slope of the Stern-Volmer plot according to Eq^n 1. K_{SV} helps in calculating the quencher rate coefficient which in turn helps in understanding the kinetics of the deactivation process.

Computation details

First-principles-based Density Functional Theory calculations for PQDs have been performed in SIESTA (Spanish Initiative for Electronic Simulation with Thousands of Atoms) Package,[38] and Gaussian 16 software. To study the absorption spectra of black phosphorene PQDs of varying sizes, Siesta package was used with a plane wave basis set having energy cutoff of 400 Ry to describe all the systems, along with PAW (Projected Augmented Wave) potentials. Interelectronic correlations and exchange were treated with PBE (Perdew-Burke-Ernzerhorf) functionals as implemented in the GGA (Generalized Gradient Approach) method. The Brillouin zone was sampled with a 5 x 5 x 1 Monkhorst Pack grid. All systems were optimized until the total force was reduced to 0.02 eV/atom. A vacuum of 30 Angstroms was maintained in the non-periodic direction to prevent deluding interlayer interactions and the supercell length was chosen to be 15 Angstroms to avoid coulombic interactions in the periodic direction. Charge-transfer interactions with donor and acceptor molecules, namely TTF (tetrathiafulvalene) as the electron-donating moiety and TCNE (tetracyanoethylene) and TCNQ (tetracyanoquinodimethane) as electron-accepting groups with phosphorene PQD were studied using Mulliken Population Analysis.

Physical characterization

Liquid exfoliation was carried out using a probe sonicator (Sonics Vibra cell™ VCX 750Ultrasonic processor). Raman spectroscopic studies were conducted by using a LabRAM HR high-resolution Raman spectrometer (Horiba-Jobin Yvon) using an Ar laser (λ = 514.5 nm). Transmission Electron Microscope (TEM) images were collected using a JEOL-3010 and FEI Titan3^{TM} with an accelerating voltage of 80 kV. Atomic Force Microscope (AFM) images were collected with a Bruker Innova Microscope. Absorption and photoluminescence (PL) spectra were recorded with a Perkin–Elmer UV/VIS/NIR lambda-750 and a Horiba–Jobin–Yvon (*i*HR 320) spectrometers respectively.

5.4.A Charge transfer studies in phosphorene

5.4.A Results and discussions

Material Characterization

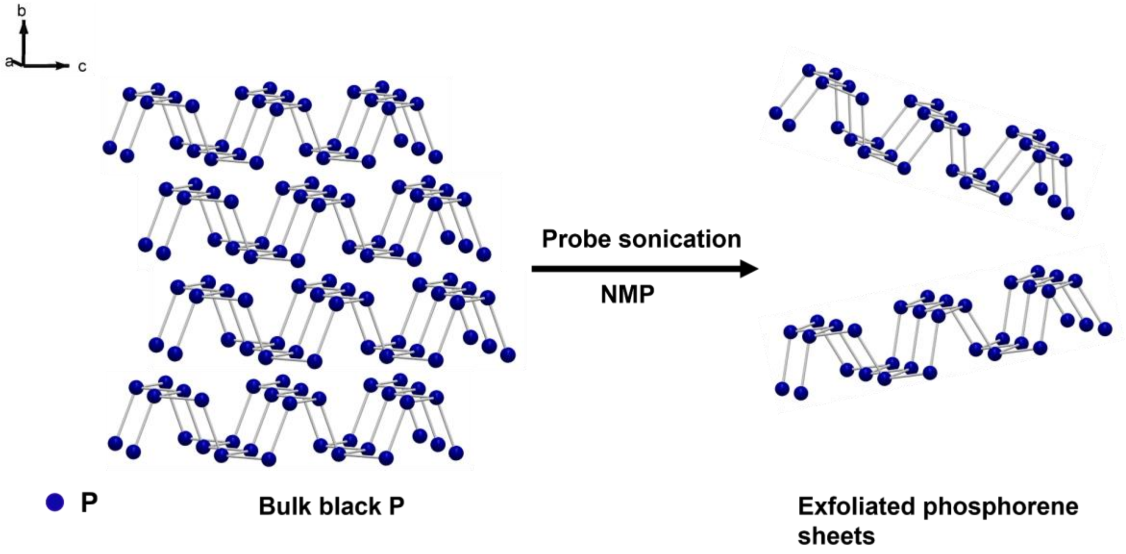

Scheme 1: Pictorial representation of exfoliation of phosphorene from bulk black phosphorous

2D Phosphorene was synthesized from bulk black phosphorous by liquid exfoliation in N-Methylpyrrolidone. During liquid exfoliation, cavitation bubbles are formed which implode together to give high-energy jets which shear the different layers apart to give few-layered to monolayers phosphorene which are then separated using graded centrifugation.[39] The stabilization of the nanosheets in a few-layered state depends on the surface energy of the material and solvent. **Scheme 1** gives a pictorial representation of the exfoliation of black phosphorous.

Figure 3a shows the FESEM image of bulk black phosphorous which highlights its layered nature. The chemical purity of the material before and after exfoliation was confirmed by Raman studies wherein both exfoliated and bulk materials show three Raman modes (A_g^1, B_{2g}, A_g^2) as has been theoretically predicted (**Figure 3b**).[40] A_g^1 involves out-

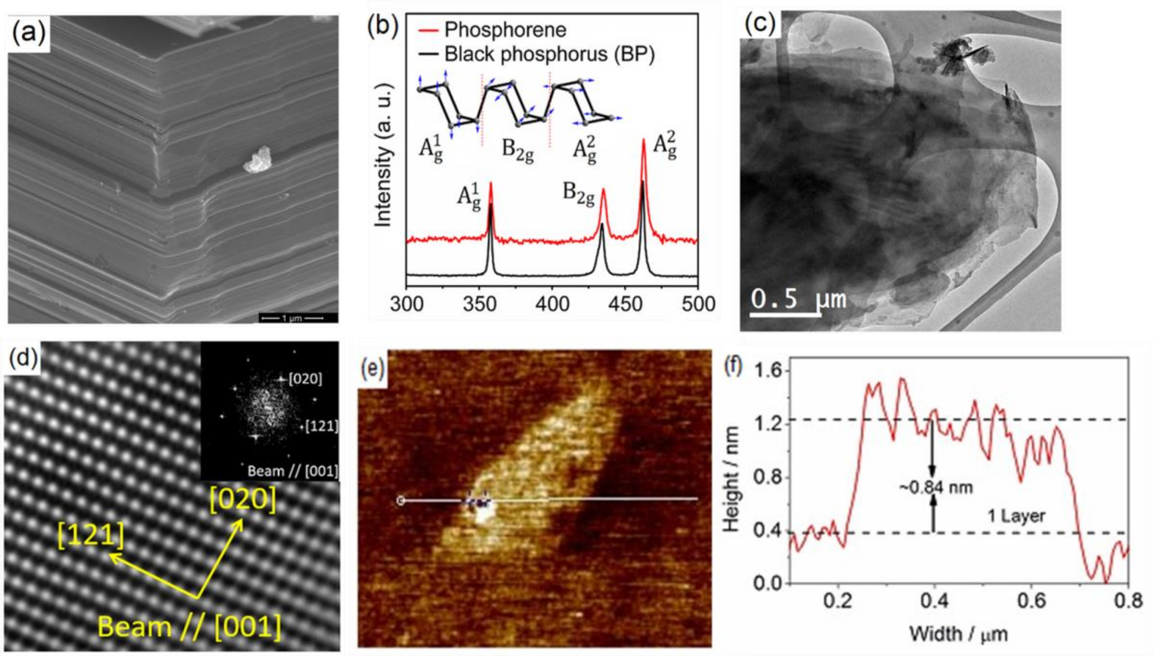

Figure 3: (a) FESEM of black phosphorous (b) Raman spectra of phosphorene (c-d) TEM images of phosphorene (e-f) AFM image of phosphorene along with the corresponding height profile

of-plane displacement of atoms while B_{2g} and A_g^2 modes involve in-plane displacements along the zigzag and arm chain direction respectively.[40,41] Moreover, A_g^1/A_g^2 peak intensity ratios is generally used to indicate the extent of oxidation of phosphorene sheets, with sheets for which $A_g^1/A_g^2 > 0.6$ are considered to have very low oxide content.[42] **Figure 3c** shows the bright-field Transmission electron microscopy image of phosphorene along with a high-resolution TEM image in **Figure 3d** with the corresponding FFT in the inset. **Figure 3e** gives a representative atomic force microscopy (AFM) image of as-synthesized phosphorene nanosheets with lateral dimensions ~ 500 nm and thickness of ~0.84 nm. The thickness measured by AFM will be slightly overestimated due to the residual solvent layer on the nanosheet along with contributions from capillary forces and adhesion.[43]

Charge-transfer studies with different donor/acceptor molecules

Charge transfer is a crucial step involved in the integration of low-dimensional materials for various device applications due to their strong light-matter interaction and tunable band structure.[30] We study the interaction of phosphorene with different donor and acceptor molecules using Raman spectroscopy. **Figure 4** gives the structures of all the donor (D) and acceptor (A) molecules under study.

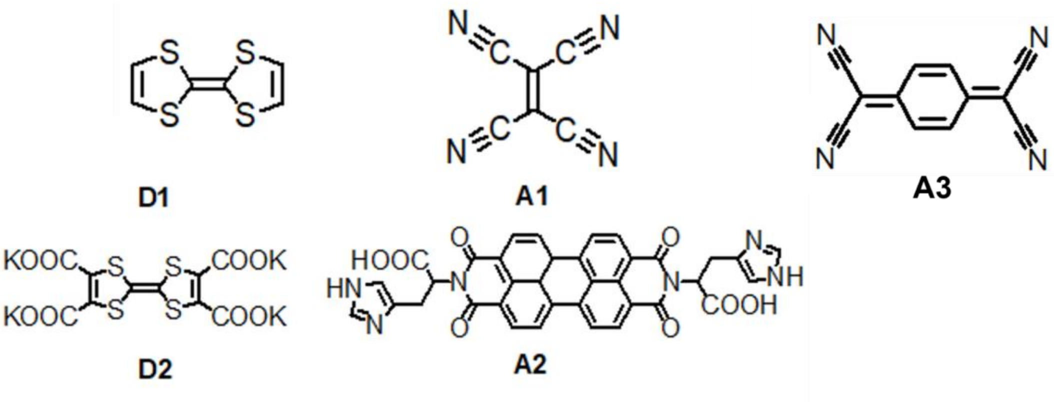

Figure 4: Different donor and acceptor molecules used for this study D1 (Tetrathiafulvalene or TTF), D2 (Tetrathiafulvalene tetracarboxylate), A1 (Tetracyanoethylene), A2 (perylenediimide histidine derivative) and A3 (7,7,8,8-Tetracyanoquinodimethane or TCNQ)

We started our study by trying to understand the charge transfer behavior of phosphorene with TCNE (A1) and TTF (D1), which are typical acceptor and donor molecules and for which theoretical studies are already available.[44] On the interaction of phosphorene with different concentrations of tetracyanoethylene (TCNE) (A1) and tetrathiafulvalene (TTF) (D1) we observe a softening and broadening of the Raman modes but with negligible shifts (**Figure 5a** and **5b**). Similar softening and broadening of Raman modes on interaction with different donor/acceptor molecules have already been reported for graphene and attributed to electron-phonon coupling.[45,46] The broadening of Raman

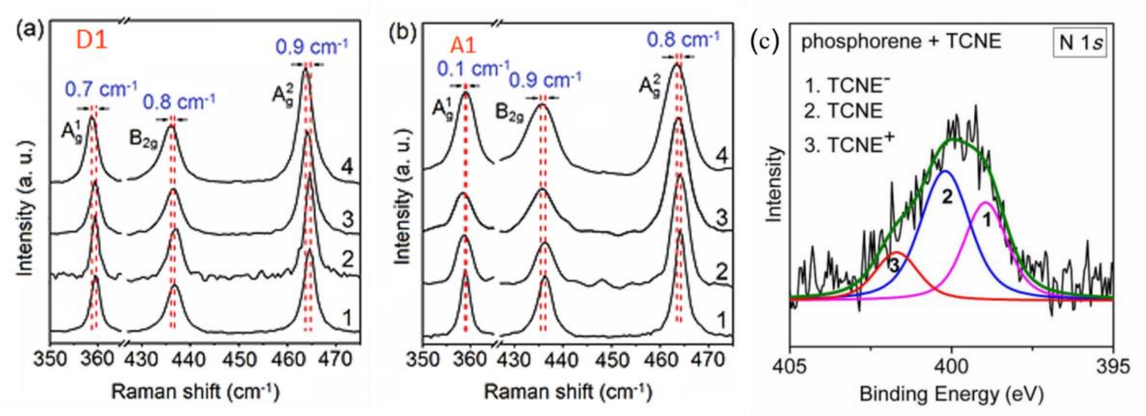

Figure 5: Raman bands of phosphorene on interaction with varying concentrations of (a) D1 (**1**; 0.0, **2**; 0.4, **3**; 0.8 and **4**; 1.6 mM) and (b) A1 (**1**; 0.0, **2**; 0.4, **3**; 0.8 and **4**; 1.2 mM) and (c) N1s core-level XPS spectra of TCNE-phosphorene

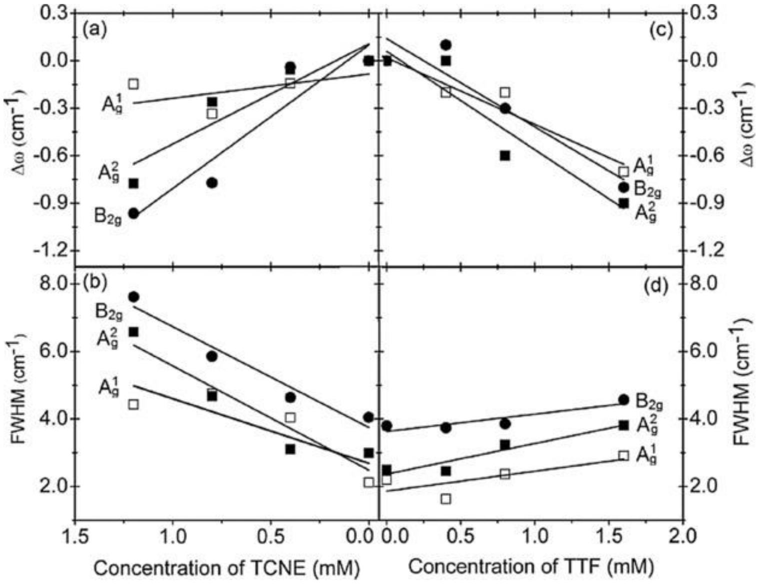

Figure 6: Shifts of the phonon frequencies (Δω) and the full width at half maxima (FWHM) of A_g^1, B_{2g}, A_g^2 bands of phosphorene as the function of concentration of (a-b) TCNE (A1) and (c-d) TTF (D1). Increase in concentration of TCNE and TTF corresponds to increase in hole and electron doping respectively

peaks is more pronounced in the case of A1 compared to D1 which probably indicates that the interaction of A1 with phosphorene is stronger. Moreover, the $\mathrm{A_g^1}$ mode becomes more prominent in the case of A1 indicating a higher A_g^1/A_g^2 and hence more effective surface passivation which indirectly indicates a stronger charge transfer complex with A1. **Figure 6** gives an estimate of the shifts in phonon frequencies (Δω) and the full-width at half-maxima (FWHM) of A_g^1, B_{2g} and A_g^2 peaks of phosphorene as a function of concentration of A1 and D1. Further proof of effective charge transfer interaction was provided by the N1s core-level spectra of phosphorene-A1 which can be deconvoluted into three peaks at 398.9, 400.2 and 401.7 corresponding to $TCNE^{\cdot -}$, neutral TCNE, and oxidized TCNE or solvent (**Figure 5c**). These results were further corroborated by first-principles calculations which predict that A1 and D1 molecules lie flat on phosphorene at distances of 3.32 and 3.15 Å respectively. Charge-transfer in the case of A1 was calculated to be 0.346e while in the case of D1 it was 0.187e. Thus, A1 as an acceptor interacts more strongly with phosphorene through charge transfer. Moreover, the C=C bond distance decreases from 1.43 Å to 1.40 Å in A1 and increases from 1.35 Å to 1.37 Å for D1. **Figure 7** shows the calculated charge difference maps for the corresponding study.

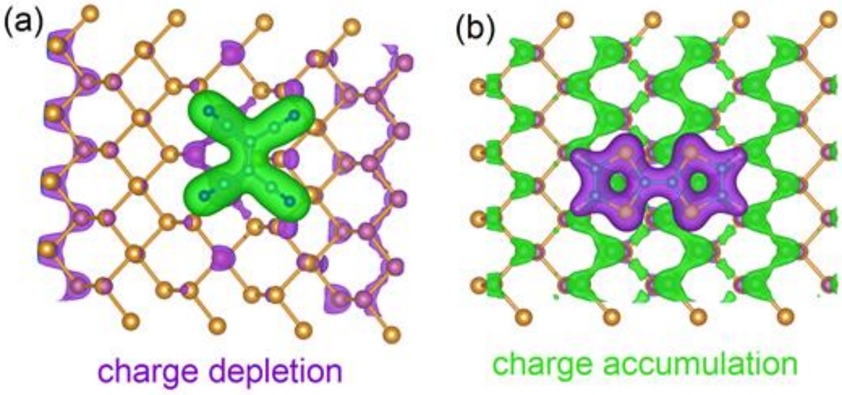

Figure 7: Charge density maps of phosphorene with (a) A1 (TCNE) and (b) D1 (TTF)

We tried to understand the charge transfer behavior of phosphorene with aromatic donor and acceptor molecules D2 and A2. Interaction of phosphorene with varying

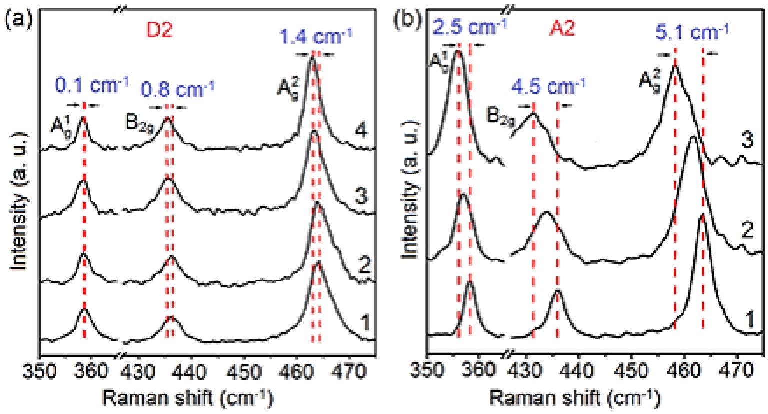

Figure 8: Raman bands of phosphorene on interaction with varying concentrations of (a) electron donor D2 (**1**; 0.0, **2**; 0.5, **3**; 0.8 and **4**; 1.0 mM) and (b) electron acceptor A2 (**1**; 0.0, **2**; 0.5 and **3**; 1.0 μM)

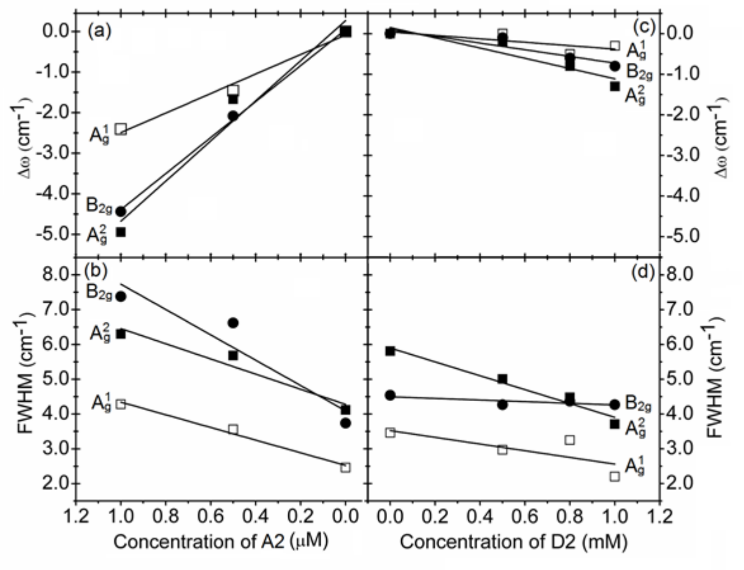

Figure 9: Shifts of the phonon frequencies (Δω) and the full width at half maxima (FWHM) of A_g^1, B_{2g}, A_g^2 bands of phosphorene as the function of concentration of (a-b) TCNE (A1) and (c-d) TTF (D1). Increase in concentration of TCNE and TTF corresponds to increase in hole and electron doping respectively

concentrations of D2 and A2 shows prominent shifts along with softening and broadening in the Raman modes of phosphorene (**Figure 8**). The broadening and the shifts (Δω) in the Raman spectra for A2 are quite more pronounced than D2 probably indicating that A2

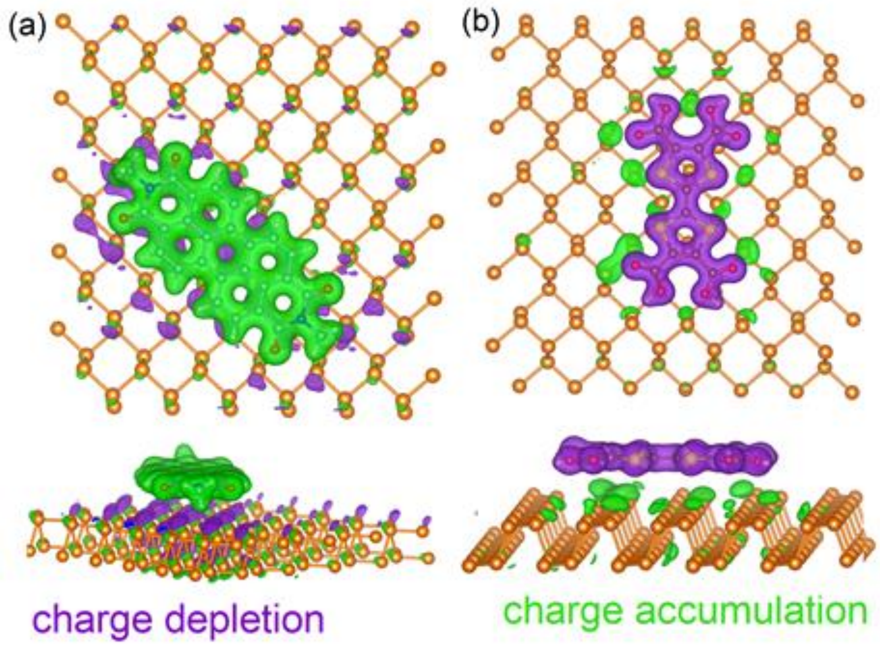

Figure 10: Charge density maps of phosphorene with (a) A2 and (b) D2, calculated by first-principles calculations

shows stronger charge-transfer interaction with phosphorene compared to D2 (**Figure 9**). Moreover, in both cases, the in-plane vibrational modes show greater broadening/shifts than out-of-plane vibrations indicating that the charge transfer or adduct formation affects the in-plane modes more. The prominent shifts observed in the Raman peaks of phosphorene with A2 are due to strain-induced in the lattice due to charge transfer and steric repulsions. Moreover, the relatively higher A_g^1 /A_g^2 on interaction with A2 compared to the D2 as is evident from **Figure 8** further indicates better surface passivation with A2 compared to D2 and hence greater charge transfer. First-principles calculations confirm that A2 shows a greater charge-transfer (0.17e) compared to the donor D2 (0.04e). The distance between A2 and phosphorene was calculated to be 3.33 Å and that between D2 and phosphorene is 3.32 Å. Charge difference maps reveal the nature of charge transfer interaction between phosphorene and the donors as well acceptor molecules (**Figure 10**).

Figure 11 shows the projected density of states pDOS for D2 and A2 on phosphorene. While D2 shows a donor level just below Fermi energy, for A2 a molecular acceptor level arises, and this confirms the occurrence of charge transfer. Acceptors take electrons from the filled $3p_z$ orbitals of phosphorene which are delocalized in nature, whereas donor molecules give electrons to the vacant 3d bands of phosphorene. Hence for donors, the electrons are donated to the localized orbitals, and because of this, the donor molecule-phosphorene interaction becomes unfavorable compared to that of the acceptors.

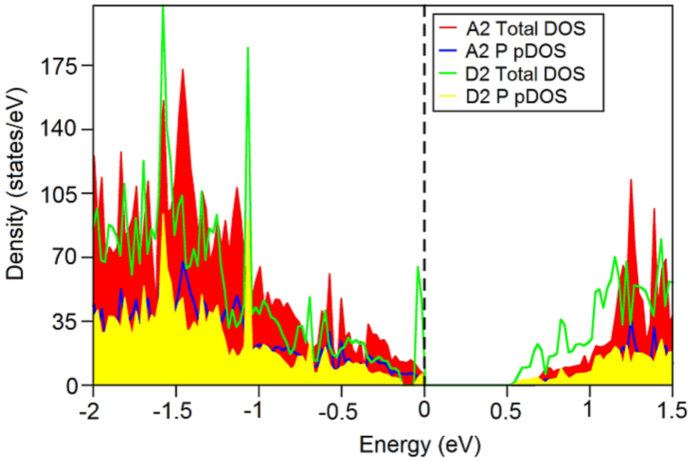

Figure 11: Projected density of states (pDOS) plot for A2 and D2 on phosphorene

Charge-transfer interaction with both donor and acceptor molecules leads to redshifts in the Raman spectra along with softening and broadening in the Raman modes which could be due to the strain induced in the lattice due to steric repulsions along with charge transfer.[47] Moreover, the extent of charge transfer calculated by first-principles calculations for D1 (0.187e) and A1(0.346e) by first-principles calculations is higher than for D2 (0.04e) and A2 (0.17e), while Raman peak shifts are much higher for D2 and A2 this could be due to increased steric repulsions from the bulkier aromatic donor and acceptor molecules along with additional relaxation pathways possible in the system.

Theoretical studies predict that charge-transfer interactions with different donor-acceptor molecules introduce localized midgap states into the band structure which opens up additional relaxation pathways to facilitate the electron transfer upon photoexcitation.[16] Similar phonon-assisted intraband relaxation dynamics have already been reported for carbon nanotubes and this could also be the reason behind the greater extent of redshifts in the Raman spectra of aromatic compounds.[48]

5.4.B Charge transfer studies in phosphorene quantum dots

5.4.B Phosphorene quantum dots

Material characterization

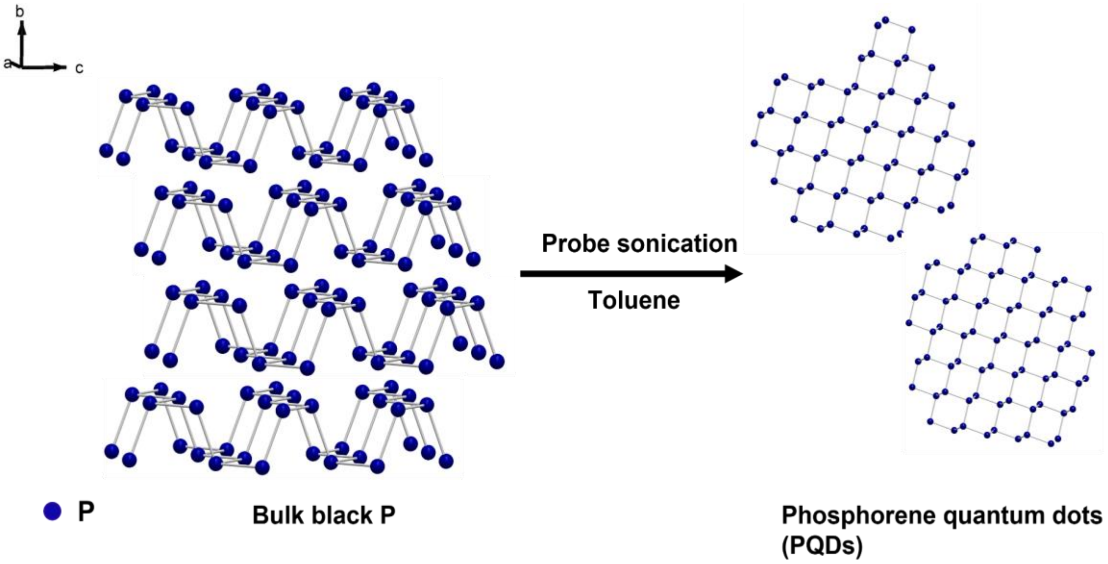

Scheme 2: Pictorial representation of synthesis of phosphorene quantum dots by liquid exfoliation

Phosphorene quantum dots (PQDs) were synthesized from black phosphorous by probe sonication in hydrophobic solvent toluene by varying power between 150-225 W. The choice of solvents is based on previous studies wherein exfoliation in diethyl ether led to the formation of multiple surface functionalities which in turn could attribute to saturation passivation of emission.[24] **Scheme 2** gives a pictorial representation of the synthesis of phosphorene quantum dots by probe sonication. The particle size and crystallinity of the PQDs were established by bright-field transmission electron microscopy images with the insets showing lattice fringes in the HR-TEM images (**Figures 12a** and **12b**). The lattice spacing of 2.16 and 2.62 Å correspond to (020) and (004) crystallographic planes of black phosphorous respectively. **Figures 12c** and **12d** show the AFM images of PQDs prepared at 187.5 and 225 W power highlighting that an increase in power of ultrasonic waves decreases particle size. The average diameter of the particles prepared at 150, 187.5, and 225 W power is ~5, 3, and 1 nm respectively.

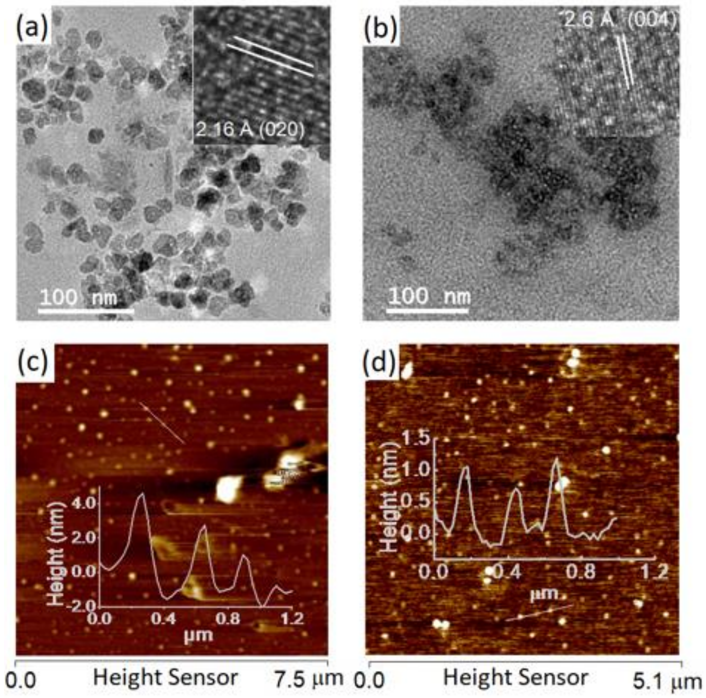

Figure 12: (a-b) TEM images (c-d) AFM images along with respective height profiles for PQDs synthesized at (a, c) 187.5 W and (b, d) 225 W

Optical properties

Figures 13a and **13b** show the photographs of PQD dispersion of different sizes under visible and ultra-violet radiation (365 nm), revealing intense blue emission. The color intensity slightly increases with sonication power from 150 to 225 W. The color intensity under visible and UV radiation remains unchanged after vacuum evaporation of the solvent. The UV-visible absorption spectra of the as-synthesized PQDs show a sharp peak in the UV region with a long tail into the visible region (**Figure 13c**). These features in the UV-visible absorption spectra have already been predicted theoretically in PQDs due to quantum confinement.[25]

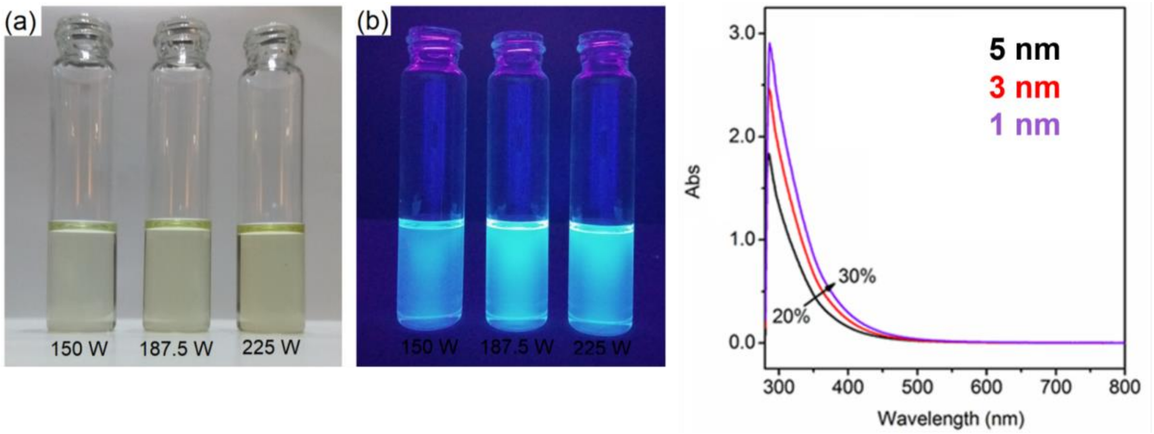

Figure 13: (a-b) Photographs of the PQD dispersion under visible and UV radiation (365 nm), (c) Absorption spectra of PQDs of different sizes

Figure 14a-c shows the excitation-dependent photoluminescence spectra of PQDs measured in the excitation wavelength range 320-420 nm with the corresponding emission band shifting linearly. This excitation-dependent emission feature could be due to the polydispersity of the sample as has been previously reported for graphene and MoS_2 quantum dots.[49–51] The emission intensity increases progressively till an excitation wavelength of 360 nm beyond which it starts to decrease. Interestingly, at any fixed excitation wavelength, emission spectra are redshifted with decreasing particle size and a similar anomalous size dependence has already been theoretically reported in phosphorene quantum dots due to possible structure distortion induced by excited-state relaxation (**Figure 14d**).[25]

The photoluminescence quantum yield (Φ) of a material/molecule is a measure of the number of photons emitted to the number of photons absorbed and is crucial for understanding molecular behavior and interactions (**section 5.3.3**).[36] Quantum yield is a very important factor in determining the utility of material for various optoelectronic applications. The photoluminescence quantum yields of PQDs (relative to 0.1M H_2SO_4

quinine sulfate solution) are found to be 9.73, 7.60, and 7.98% for PQDs of average sizes ~5, 3, and 1 nm respectively. These values are comparable to the literature values.[24] The quantum yields remain unchanged even after a month.

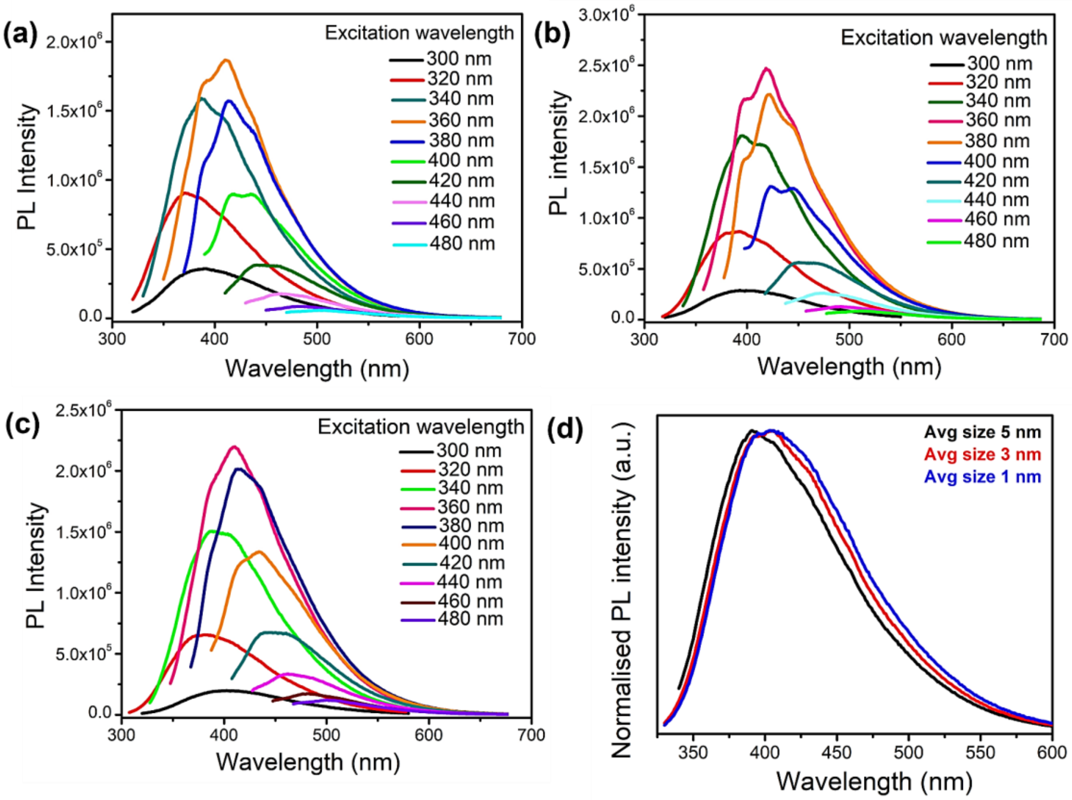

Figure 14: Excitation dependent emission spectra of PQDs synthesized under powers (a) 150W, (b) 187.5 W and (c) 225 W and (d) Red shifts in the emission spectra with varying particle size of PQDs

Charge transfer studies

The charge transfer behavior of PQDs was understood by investigating their fluorescence quenching on interaction with different donor and acceptor molecules. The donor and acceptor molecules used for this study are D1 (TTF), A1 (TCNE), and A3 (TCNQ) (**Figure 4**). **Figures 15a-c** show the emission spectra of PQDs with increasing concentrations of donor and acceptors and **Figure 15d** gives the Stern-Volmer plots of

TTF, TCNE, and TCNQ (**section 5.3.3**). From the slopes of these linear curves, the Stern-Volmer constant (K_{SV}) was found to be $6.6*10^3$, $1.0*10^4$, and $7*10^4$ M^{-1} for TTF (D1), TCNE (A1), and TCNQ (A3) respectively. This suggests that acceptors interact more strongly with PQDs than the donor. In addition, TCNE and TCNQ cause a redshift while TTF causes a blue shift in the emission spectra. A similar behavior was also observed in the Raman studies with 2D phosphorene.

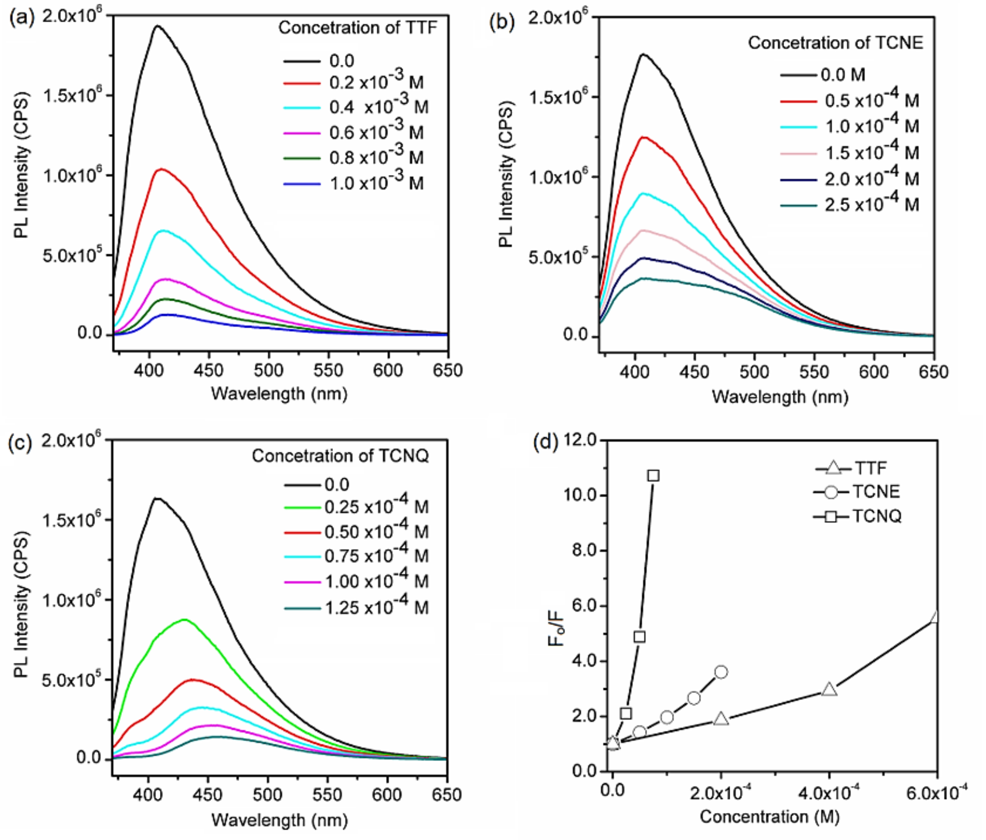

Figure 15: (a-c) Quenching of emission intensity of PQDs with TTF, TCNE and TCNQ respectively (d) Stern-Volmer plots of TTF, TCNE and TCNQ

First-principles calculations suggest that PQDs show an absorption maximum in the 300-650 nm region of the electromagnetic spectra. A redshift is observed in the absorption maxima on increasing the size (40 to 60 atoms) of PQDs. The size-dependence

---

First-principles calculations carried out by Ms. Madhulika Mazumdar and Prof. S K. Pati

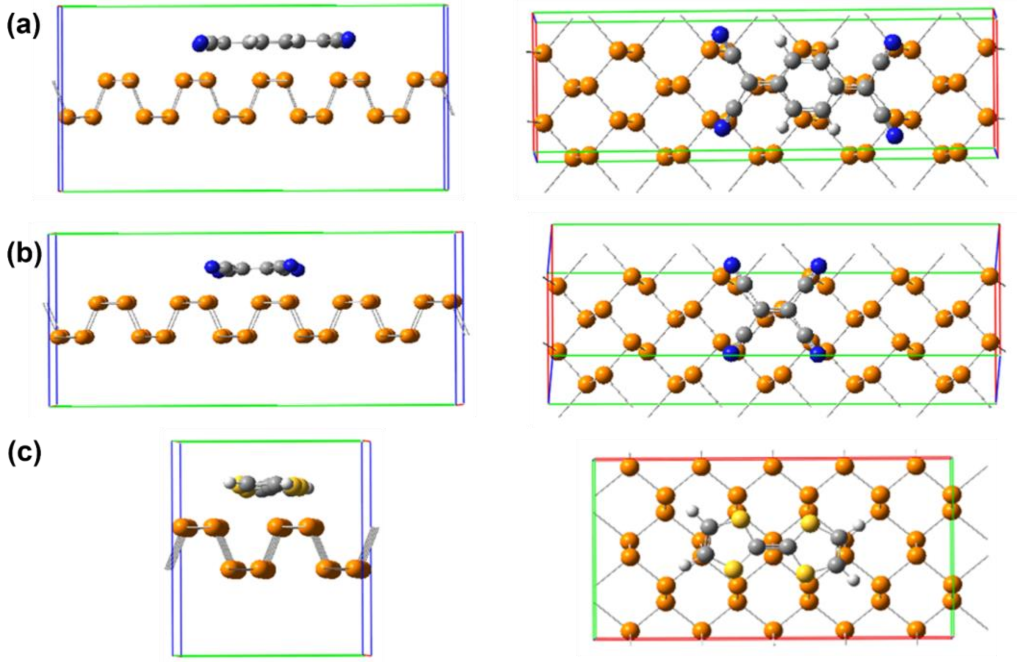

Figure 16: Optimized structures of PQDs with (a) TCNQ (A3), (b) TCNE (A1) and (c) TTF (D1)

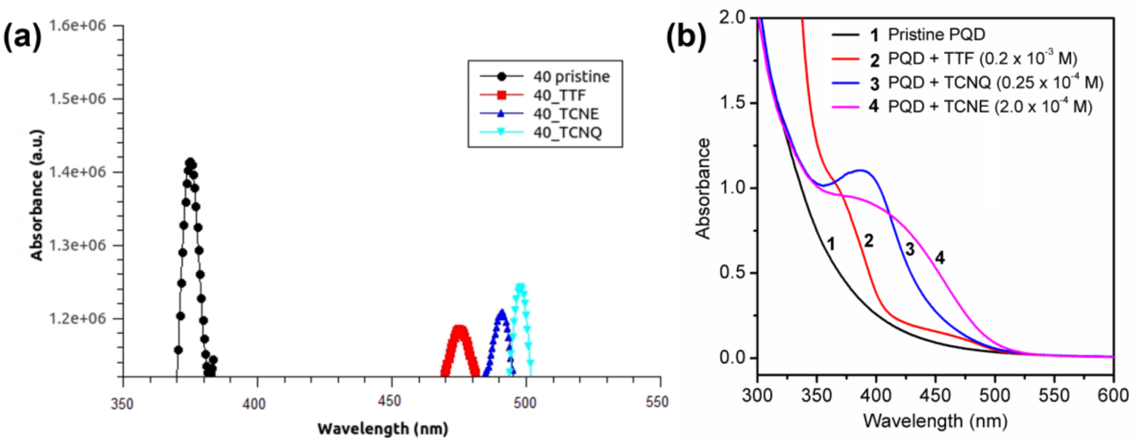

Figure 17: (a) Calculated UV–visible absorption spectra of PQD (40 atoms) with TTF, TCNE and TCNQ, (b) UV–visible absorption spectra of PQD prepare at 187.5W power with TTF, TCNE and TCNQ

of the absorption spectra can be attributed to quantum confinement leading to discretely spaced energy levels. This trend doesn't follow a smooth function as the surface and edge structure of PQDs do not scale with the size and the intensities of absorption peaks depend crucially on the surface to the bulk ratio of the atoms and saturates beyond a point (60 atoms). Mulliken population analysis is an effective tool for studying partial atomic charges and giving qualitative insights into the net charge of the system. A differential population analysis of the orbitals proves that PQDs accept electrons from TTF into the empty 3d bands of phosphorous atoms and donate electrons to TCNE/TCNQ from the 3p orbitals of phosphorous. The optimized structures suggest that these donor/acceptor molecules lie flat on the phosphorene surface (**Figure 16**). **Figure 17a** shows the calculated absorption spectra of PQDs with TTF, TCNE, and TCNQ, and the shifts are consistent with the experimental absorption spectra (**Figure 17b**).

5.5 Conclusions

This work demonstrates the possibility of tuning the properties of phosphorene by charge transfer interactions with different donor and acceptor molecules. We were able to establish that both holes and electrons can be doped into phosphorene by molecular charge transfer. Although electron acceptor or hole doping causes a greater effect on the spectral characteristics and magnitude of association, there is no gross electron-hole asymmetry from our Raman analysis. Moreover, we could also detect signatures of surface passivation upon charge transfer interactions with different molecules. The present study also demonstrates that stable phosphorene quantum dots with average sizes varying between 1.0 to 5.0 nm can be conveniently prepared by sonication of black phosphorus. The particles size of PQDs can be changed by changing sonication input power. The PQDs exhibit quantum yield in the range of 7.60-9.73%. Electron donors (TTF) as well as acceptors (TCNE and TCNQ) quench the photoluminescence, however quenching is more marked with acceptors. Experimentally and theoretically, we observed charge transfer signatures for both electron donors and acceptors from the absorption spectra.

References

(1) Glavin, N. R.; Rao, R.; Varshney, V.; Bianco, E.; Apte, A.; Roy, A.; Ringe, E.; Ajayan, P. M. *Adv. Mater.*, **2020**, *32* (7), 2070052

(2) K. B. Blodgett and I. Langmuir, *J. Am. Chem. Soc.* **1937**, *59* (11), 2400–24141934.

(3) Geim, A. K.; Novoselov, K. S., *Nat. Mater.*, **2007**, *6*, 183–191.

(4) Zhang, S.; Guo, S.; Chen, Z.; Wang, Y.; Gao, H.; Gómez-Herrero, J.; Ares, P.; Zamora, F.; Zhu, Z.; Zeng, H., *Chem. Soc. Rev*. **2018**, *47* (3), 982–1021.

(5) Jellett, C.; Plutnar, J.; Pumera, M., *ACS Nano*. **2020**, *14* (7), 7722–7733.

(6) Zhang, S.; Xie, M.; Li, F.; Yan, Z.; Li, Y.; Kan, E.; Liu, W.; Chen, Z.; Zeng, H., *Angew. Chem.*, **2016**, *128* (5), 1698–1701.

(7) Carvalho, A.; Wang, M.; Zhu, X.; Rodin, A. S.; Su, H.; Castro Neto, A. H., *Nat. Rev. Mater*. **2016,** *1* (11), 16061

(8) Castellanos-Gomez, A.; Vicarelli, L.; Prada, E.; Island, J. O.; Narasimha-Acharya, K. L.; Blanter, S. I.; Groenendijk, D. J.; Buscema, M.; Steele, G. A.; Alvarez, J. v.; Zandbergen, H. W.; Palacios, J. J.; van der Zant, H. S. J, *2D Mater.* **2014**, *1* (2), 025001.

(9) Ling, X.; Wang, H.; Huang, S.; Xia, F.; Dresselhaus, M. S., *Proc. Natl. Acad. Sci.*, **2015**, *112* (15) 4523–4530.

(10) Brent, J. R.; Savjani, N.; Lewis, E. A.; Haigh, S. J.; Lewis, D. J.; O’Brien, P., *Chem. Commun.* **2014**, *50* (87), 13338–13341.

(11) Liu, H.; Neal, A. T.; Zhu, Z.; Luo, Z.; Xu, X.; Tománek, D.; Ye, P. D., *ACS Nano* **2014**, *8* (4), 4033–4041.

(12) Kim, D. K.; Chae, J.; Hong, S. B.; Park, H.; Jeong, K. S.; Park, H. W.; Kwon, S. R.; Chung, K. B.; Cho, M. H., *Nanoscale* **2018**, *10* (48), 22896–22907.

(13) Kumar, A., *ACS Appl. Nano Mater.*, **2019**, *2* (4), 2397–2404.

(14) Telesio, F.; Passaglia, E.; Cicogna, F.; Costantino, F.; Serrano-Ruiz, M.; Peruzzini, M.; Heun, S., *Nanotechnol.*, **2018**, *30* (6), 2036-2048

(15) Ryder, C. R.; Wood, J. D.; Wells, S. A.; Yang, Y.; Jariwala, D.; Marks, T. J.; Schatz, G. C.; Hersam, M. C., *Nat. Chem.* **2016**, *8* (6), 597–602.

(16) Zhang, R.; Li, B.; Yang, J. A, *J. Phys. Chem. C,* **2015**, *119* (5), 2871–2878.

(17) Abellán, G.; Lloret, V.; Mundloch, U.; Marcia, M.; Neiss, C.; Görling, A.; Varela, M.; Hauke, F.; Hirsch, A., *Angew. Chem.* **2016**, *128* (47), 14777–14782.

(18) Baker, S. N.; Baker, G. A., *Angew. Chem.*, **2010**, *122* (38), 6876–6896.

(19) Ritter, K. A.; Lyding, J. W., *Nat. Mater.* **2009**, *8* (3), 235–242.

(20) Konstantatos, G.; Badioli, M.; Gaudreau, L.; Osmond, J.; Bernechea, M.; de Arquer, F. P. G.; Gatti, F.; Koppens, F. H. L., *Nat. Nanotechnol.*, **2012**, *7* (6), 363–368.

(21) Li, Y.; Hu, Y.; Zhao, Y.; Shi, G.; Deng, L.; Hou, Y.; Qu, L., *Adv. Mater.*, **2011**, *23* (6), 776–780.

(22) Liu, Q.; Guo, B.; Rao, Z.; Zhang, B.; Gong, J. R., *Nano Lett.,***2013**, *13* (6), 2436–2441.

(23) Zhang, X.; Xie, H.; Liu, Z.; Tan, C.; Luo, Z.; Li, H.; Lin, J.; Sun, L.; Chen, W.; Xu, Z.; Xie, L.; Huang, W.; Zhang, H., *Angew. Chem.*, **2015**, *54* (12), 3653–3657.

(24) Ge, S.; Zhang, L.; Wang, P.; Fang, Y., *Sci.Rep.*, **2016**, *6*, 27307.

(25) Niu, X.; Li, Y.; Shu, H.; Wang, J., *J. Phys. Chem. Lett.*, **2016**, *7* (3), 370–375.

(26) Gu, W.; Pei, X.; Cheng, Y.; Zhang, C.; Zhang, J.; Yan, Y.; Ding, C.; Xian, Y., *ACS Sens.*, **2017**, *2* (4), 576–582.

(27) Sun, Z.; Xie, H.; Tang, S.; Yu, X.-F.; Guo, Z.; Shao, J.; Zhang, H.; Huang, H.; Wang, H.; Chu, P. K., *Angew. Chem.* **2015**, *127* (39), 11688–11692.

(28) Han, S. T.; Hu, L.; Wang, X.; Zhou, Y.; Zeng, Y. J.; Ruan, S.; Pan, C.; Peng, Z., *Adv. Sci.*, **2017**, *4* (8), 1600435.

(29) Bradac, C.; Xu, Z. Q.; Aharonovich, I., *Nano Lett*. **2021**, *21* (3) 1193–1204.

(30) Wang, J.; Ding, T.; Gao, K.; Wang, L.; Zhou, P.; Wu, K., *Nat. Commun.*, **2021**, *12* (1), 6333.

(31) Brent, J. R.; Savjani, N.; Lewis, E. A.; Haigh, S. J.; Lewis, D. J.; O'Brien, P., *Chem. Commun.*, **2014**, *50* (87), 13338–13341.

(32) Perdew, J. P.; Burke, K.; Ernzerhof, M. *Phys. Rev. Lett.* **1996**, *77* (18), 3865-3868

(33) Kresse, G.; Joubert, D. *Phys. Rev. B.* **1999**, *59* (3), 1758-1775

(34) Blochl, P. E., *Phys. Rev. B.* **1994**, *50* (24), 953-979

(35) Lopes, S.; Fausto, R.; Khriachtchev, L., *J. Chem. Phys.* **2016**, *144* (8), 084308.

(36) Hellar, C.A.; Henry, R. A.; McLaughlin, B. A.; Bliss, D.E.., *J. Chem. Eng. Data* **1974**, *19* (3), 214–219.

(37) Gehlen, M. H., *J. Photochem. Photobiol. C: Photochem. Rev*., **2020**, *42*, 100338.

(38) Soler, J.M.; Artacho, E.; Gale, J.D.; Garcia, A.; Junquera, J.; Ordejon, P.; Sanchez-Portal, D., *J. Condens. Matter Phys*., **2002**, *14* (11), 2745.

(39) Nicolosi, V.; Chhowalla, M.; Kanatzidis, M. G.; Strano, M. S.; Coleman, J. N., *Science*. **2013**, *340*, 6139

(40) Sugai, S.; Shirotani, I., *Solid State Communications* **1985**, *53* (9), 753–755.

(41) Chakraborty, B.; Gupta, S. N.; Singh, A.; Kuiri, M.; Kumar, C.; Muthu, D. V. S.; Das, A.; Waghmare, U. v.; Sood, A. K., *2D Mater.*, **2016**, *3* (1), 015008.

(42) Favron, A.; Gaufrès, E.; Fossard, F.; Phaneuf-Laheureux, A. L.; Tang, N. Y. W.; Lévesque, P. L.; Loiseau, A.; Leonelli, R.; Francoeur, S.; Martel, R., *Nat. Mater.* **2015**, *14* (8), 826–832.

(43) Szirmai, P.; Márkus, B. G.; Chacón-Torres, J. C.; Eckerlein, P.; Edelthalhammer, K.; Englert, J. M.; Mundloch, U.; Hirsch, A.; Hauke, F.; Náfrádi, B.; Forró, L.; Kramberger, C.; Pichler, T.; Simon, F., *Sci. Rep.* **2019**, *9* (1), 19480

(44) Jing, Y.; Tang, Q.; He, P.; Zhou, Z.; Shen, P., *Nanotechnol.*, **2015**, *26* (9), 095201.

(45) Late, D. J.; Ghosh, A.; Chakraborty, B.; Sood, A. K.; Waghmare, U. v.; Rao, C. N. R., *J. Expt. Nanosci.*, **2011**, *6* (6), 641–651.

(46) Chakraborty, B.; Gupta, S. N.; Singh, A.; Kuiri, M.; Kumar, C.; Muthu, D. V. S.; Das, A.; Waghmare, U. v.; Sood, A. K., *2D Mater.*, **2016**, *3* (1), 015008.

(47) Fei, R.; Yang, L., *Appl. Phys. Lett.*, **2014**, *105* (8), 083120.

(48) Chu, I. H.; Kilin, D. S.; Cheng, H. P., *J. Phys. Chem. C.*, **2013**, *117* (35), 17909–17918.

(49) Dey, S.; Chithaiah, P.; Belawadi, S.; Biswas, K.; Rao, C. N. R., *J. Mater. Res.*, **2014**, *29* (3), 383–391.

(50) Dong, H.; Tang, S.; Hao, Y.; Yu, H.; Dai, W.; Zhao, G.; Cao, Y.; Lu, H.; Zhang, X.; Ju, H., *ACS Appl. Mater. Interface.*, **2016**, *8* (5), 3107–3114.

(51) Dey, S.; Govindaraj, A.; Biswas, K.; Rao, C. N. R., *Chem. Phys. Lett.* **2014**, *595–596*, 203–208.

Chapter 6

Covalent functionalization and Lewis acid-base adduct formation in Bismuthene nanosheets

SUMMARY

Elemental 2D pnictogens (group 15) are an interesting class of materials with tunable band structures and high carrier mobilities. Heavier pnictogens (Sb and Bi) are more stable under ambient conditions compared to the lighter members (P, As) and are emerging as interesting candidates for various electronic and optoelectronic applications. Bismuthene, the heaviest member of the 2D pnictogen family, has interesting electronic, spintronic, and photonic properties owing to its unique band structure, large spin-orbit coupling, and ambient stability. The carrier mobility of bismuthene is of the order of several thousand $cm^2V^{-1}s^{-1}$. Theoretically, bismuthene shows a semi-metal to semiconductor transition with an indirect

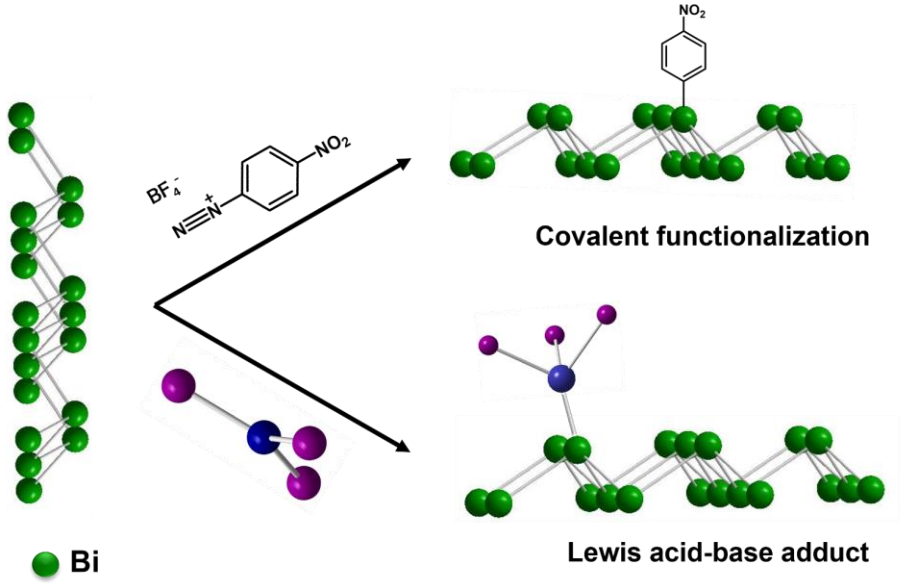

bandgap of ~0.74 eV and absorption maxima at ~1.72 eV. We were able to observe emission in liquid exfoliated few-layered bismuthene sheets by photoluminescence and FESEM cathodoluminescence spectroscopy. Chemical functionalization includes many interesting techniques to tune the electronic and optoelectronic properties of a material. The reactivity of 2D pnictogens is due to the presence of lone pair on each atom which can be effectively utilized to tune material properties via different functionalization strategies. We demonstrate a redshift in the bismuthene emission upon covalent functionalization with p-Nitrobenzenediazonium tetrafluroborate. Spontaneous covalent functionalization of bismuthene nanosheets with diazonium salt leads to the formation of quaternary Bi species with the preferential attachment of organic moieties via Bi-C linkage along with simultaneous rehybridization of bismuthene band structure. We have also functionalized these bismuthene sheets with group 12 and 13 Lewis acids ($ZnCl_2$, $CdCl_2$, BCl_3, $GaCl_3$, $AlCl_3$, and $InCl_3$). Interaction of these Lewis acids with the lone pairs on Bi leads to the formation of Lewis acid-base adduct with corresponding changes in bonding environment along with lattice distortion and rehybridization of the band structure. Interestingly, Lewis acid-base adduct formation leads to a blue shift in the bismuthene emission. This work demonstrates the easy tunability of bismuthene emission by different functionalization strategies leading to the rehybridization of the band structure and opens a route for tuning the properties of bismuthene for integration in electronic and optoelectronic devices.

6.1 Introduction

Group 15 monoelemental pnictogens occupy a special position among 2D materials owing to their tunable bandgaps in the range of 0-2.5eV.[1–4] Applications of phosphorene, the most studied pnictogen are still limited due to its instability under ambient conditions.[5] Heavier members of this group (Sb and Bi) are quite stable and have recently attracted researchers due to their optical properties.[1] Bismuth, the heaviest member of this group, has come into focus recently due to its interesting band structure, large spin-orbit coupling, excellent non-linear optical response, and long-term stability.[6–9]

Bulk bismuth crystallizes in a rhombohedral layered structure ($R\bar{3}m$, β-phase) which is similar to the honeycomb lattice of graphene, however heavier pnictogens are not true van der Waals materials as the interaction between two buckled layers is stronger making their exfoliation difficult. Bismuth the heaviest member of group 15, has the lowest difference between in-plane and out-of-plane lattice constants, making bismuthene the most difficult to exfoliate using top-down approaches among pnictogens.[1] Bismuthene undergoes a transition from semi-metal to an indirect semiconductor of bandgap ~ 1eV in the monolayer regime.[6,10] However bismuthene behaves as a direct bandgap semiconductor under tensile strain and if the inter-layer distance is increased beyond 5.94 Å, bilayer bismuthene is reported to exhibit an indirect bandgap of 0.3eV.[11] Moreover, theoretical reports indicate that in spite of having a bandgap of <1eV, bismuthene absorption maximum occurs at 1.74 eV which opens up the possibility of higher energy optical transitions in the visible region.[12] Although theoretically, bandgap opens up in bismuth in monolayer regime only; experimental reports indicate multiple emissions in the visible range from bulk Bi, Bi thin films, and nanosheets which could be due to Bi^{3+} color centers, defect/trapped states, and band edge emission, respectively.[11,13]

6.1.2 Chemical functionalization

Chemical functionalization is an interesting method for tuning the properties of nanomaterials. It is an important step in the fabrication of material for various device applications. At present, despite the great potential and interests garnered by elemental 2D materials, there is still no robust universal method that can be used to tailor their properties which could be due to difficulty in the synthesis of materials with good yields, the inherent instability of some members, difficulty in characterizing modified materials, poor reactivity of some of the materials, etc.[14] Therefore, it is highly imperative to look for newer techniques for the stabilization and functionalization of these elemental 2D materials so that those could be utilized to the highest potential. According to the literature, chemical functionalization can be carried out by various methods including defect engineering, intercalation, donor-acceptor adducts, Lewis acid-base adducts, covalent modification, etc.[14–16] Each of these methods has its own merits and demerits, and the choice of the technique used for functionalization will depend on the inherent nature of the elemental 2D material and the kind of chemical modification desired with the ultimate aim of preserving the inherent lattice of the material.

Covalent functionalization is an interesting method to tune the inherent properties of pnictogens. Compared to other functionalization approaches, covalently functionalized products are generally more robust. One such well-studied approach is the functionalization of nanosheets by different diazonium salts.[17–21] The same has already been reported to passivate phosphorene, hence stabilizing it under ambient conditions along with tuning its properties.[22]

Pnictogens have lone pairs which are highly reactive, and these lone pairs make Bi act as a soft Lewis base that can interact with different Lewis acids to form Lewis acid-base adducts. Such adducts involve weaker overlap between the orbitals without any significant disruption of the inherent lattice structure which helps tune certain aspects of the material while preserving its intrinsic properties.[23]

6.2 Scope of this investigation

In **section 6.4.A**, we have synthesized few-layered bismuthene by liquid exfoliation and used diazonium salt p-Nitrobenzenediazonium tetrafluroborate to carry out a covalent functionalization of bismuthene. We try to understand the inherent mechanism of the reaction. We have used FESEM-cathodoluminescence spectroscopy to study the effects of functionalization on the band structure of bismuthene.

In **section 6.4.B,** we have studied the Lewis acid-base type adducts of bismuthene with different Groups 12 and 13 metal halides ($ZnCl_2$, $CdCl_2$, BCl_3, $GaCl_3$, $AlCl_3$, and $InCl_3$). We could correlate the strength of the adduct formed with the Lewis acidity/basicity and hard/soft nature of the materials. Moreover, the changes in the band structure with the formation of these adducts were studied by FESEM-cathodoluminescence spectroscopy.

6.3 Experimental section

Materials

Bismuth crystals (Smart Elements, 99.99995%), N-Methyl-2-pyrrolidone (NMP) (Spectrochem, 99%), acetonitrile (ACN) (Spectrochem, dry solvent, 99.5%), tetrahydrofuran (THF) (Spectrochem, dry solvent, 99.5%), toluene (Spectrochem, dry solvent, 99.5%), methanol (Spectrochem, dry solvent, 99.5%), p-nitrobenzene diazonium tetrafluoroborate (p-NBD) (Merck, 97%), Si substrate (University wafer, <100>, thickness 525±25 µm, $\rho = 0.1\text{-}100\ \Omega$ cm). Before synthesis, NMP and acetonitrile solvents were degassed by purging inert gas (Ar) for 30 minutes with continuous stirring.

Synthesis of bismuthene

Bismuth crystals stored in an MBraun N_2 glove box with O_2 and H_2O levels of < 1.0 ppm, were ground in a mortar pestle to obtain a fine powder. Bi powder (400 mg) was transferred to a round bottom centrifuge tube and filled with degassed N-methyl-2-pyrrolidone (17.5 mL). The tube was closed with a cap fitted with the sonicator probe and packed under an inert atmosphere. Probe sonication was carried out for 5 hours with a pulse sequence of 4 s on and 4 s off at 25% amplitude. The resulting dispersion of exfoliated Bi was centrifuged at 2500 rpm (3935 *g*) to separate the unexfoliated Bi. Further centrifugation at higher speeds was done to separate different grades of Bi sheets. Bi nanosheets (Bi-NS) obtained as solid by centrifugation at 14500 rpm (22819 *g*) were separated and washed multiple times with acetonitrile to remove residual NMP. Few-layered Bi (Bi-FL) was obtained as supernatant on centrifugation at 15500 rpm (24393 *g*) for 1 hour.

Reaction of bismuthene with p-nitrobenzene diazonium tetrafluoroborate

Bi-NS was dispersed in acetonitrile and sonicated for 15 minutes to get a uniform dispersion in a round bottom flask. p-Nitrobenzene diazonium tetrafluoroborate (p-NBD) (100 mg) was added to the above dispersion and sonicated for another 5 minutes to completely dissolve the salt. This reaction mixture was kept stirring continuously for 48 hours under ambient light conditions. After 48 hours, the reaction mixture was washed multiple times with acetonitrile to remove any unreacted diazonium salt. The obtained black solid was named Bi-NS-NO_2.

Few-layered Bi (Bi-FL) dispersion in NMP was drop coated on Si substrate and vacuum dried for further characterizations. Si substrate with Bi-FL sample was dipped in a solution of p-NBD (100 mg) in acetonitrile (5 mL) and left undisturbed for 48 hours under ambient conditions in light. After 48 hours, the substrate was removed and washed multiple times with acetonitrile to remove unreacted p-NBD from the surface. The obtained sample was named Bi-FL-NO_2.

Lewis acid-base adduct formation with bismuthene

For Lewis acid-base adduct formation, solvents for the reaction were selected based on the solubility of Lewis acids. Tetrahydrofuran (THF) was used for BCl_3, $GaCl_3$, $InCl_3$, and $ZnCl_2$; toluene was used for $AlCl_3$; methanol was used for $CdCl_2$. Prior to the reaction, Bi nanosheets (Sb-NS) were washed multiple times with the solvent appropriate for the Lewis acid. Bi-NS dispersion in the dry solvent under an inert atmosphere was kept in a Schlenk flask and an equimolar amount of Lewis acid was added to this dispersion. The solutions were kept stirring under an inert atmosphere and monitored regularly. BCl_3 and $GaCl_3$ reacted vigorously and formed a colorless solution instantaneously. $AlCl_3$ reacted relatively mildly but formed a colorless solution after 1 hour. Reactions with $InCl_3$ and $CdCl_2$ were considerably slower and didn’t corrode the material. After optimization, reaction with $AlCl_3$ was done for 15 min, $CdCl_2$ for 10 days, and $InCl_3$ for 14 days. The solid products obtained were washed multiple times with solvents and utilized for further characterizations.

Bi-FL was obtained as supernatant on centrifugation at 15500 rpm for 1 hour. The dispersion in NMP was drop coated on Si substrate and vacuum dried. Bi-FL substrate was dipped in a solution of Lewis acid (same concentration as in Bi-NS) in the desired solvent under an inert atmosphere. After the reaction, the substrate was washed multiple times with solvent to remove any unreacted Lewis acid.

Cleaning Si substrate: Si substrates were first dipped in acetone and heated to 50°C for 10 mins. After this, the substrates were rinsed with methanol and dried under an N_2 gun. The dried substrates were dipped in Piranha solution for 10 mins and washed rigorously with water afterward. In the final step, the substrates were dipped in 2% HF solution for 10 minutes, washed rigorously with water, and then dried under an N_2 gun.

Physical Characterization

Liquid-phase exfoliation was carried out with a Sonics Vibracell probe sonicator (750 W) equipped with a titanium alloy (Ti-6Al-4V) based tapered probe (tip diameter = 6 mm). The probe sonicator assembly was maintained at 5°C by circulating cold water to avoid overheating the probe. Raman spectra of the samples were collected on a Renishaw inVia microscope fitted with a 784 nm laser. Samples for Raman measurements were prepared by drop coating the dispersion on a glass slide and dried under vacuum. Bright-field transmission electron microscopy images were recorded on a JEOL 300kV HRTEM instrument. AFM analyses were carried out in contact mode on a Bruker Innova AFM instrument. Bi nanosheets separated at different centrifugation speeds were drop coated on Si substrate and dried under vacuum. Nanoscope analysis software was used to analyze the data. X-ray photoelectron spectroscopy studies were carried out on a Thermo K-alpha+ spectrometer using micro-focused and mono chromated Al K_α radiation (1486.6 eV), 400μm spot size, pass energy of 50 eV, and a step size of 0.1 eV and resolution of 0.6 eV. Samples for XPS were prepared by drop coating a thick layer of samples on Si substrate and dried under vacuum. XPS analysis of core-level spectra was done on fityk software using VoigtA function for peak fitting with a linear background. FESEM images were recorded on Thermofisher FEI Quanta 3D instrument equipped with a field emission gun and EDS detector. Photoluminescence measurements were performed on Edinburgh Instruments FLS 1000 spectrometer equipped with a Xe arc lamp (450 W) and a visible photomultiplier tube detector (PMT-900) (sensitivity > 35000:1). Cathodoluminescence images and spectra were recorded with a Gatan MonoCL4 accessory with a standard photomultiplier tube (PMT) detector (185-850 nm) attached with a FESEM instrument. Samples for FESEM-EDX-CL analysis were prepared by drop coating dispersion of Sb-FL on Si substrate. FT-IR measurements were done with a Perkin Elmer frontier IR instrument equipped with a DTGS detector. Samples were prepared by grinding the sample dispersions with heated KBr and pressed into pellets. Spectra were recorded in transmittance mode with 64 scans and a spectral resolution of 4 cm^{-1}. Heated FT-IR samples were prepared by drop-coating Bi-NS-NO_2 dispersions on Si substrate and heating it at 200 and 500°C under vacuum.

6.4.A Covalent functionalization of Bismuthene

6.4.A Results and discussion

Material characterization

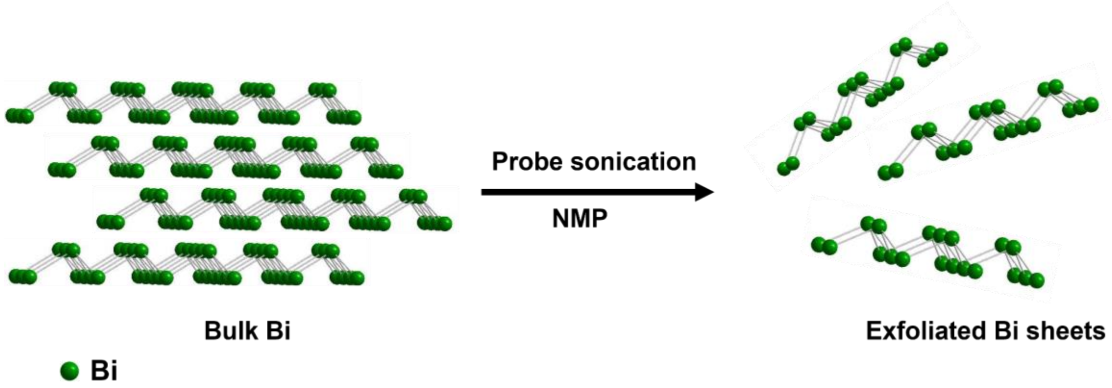

Scheme 1: Pictorial representation of exfoliation of bismuthene by probe sonication

Liquid exfoliation of bismuthene was carried out by probe sonication of bulk Bi in N-methyl pyrrolidone followed by centrifugation to separate out two grades of exfoliated Bi: bismuthene nanosheets (Bi-NS) and few-layered bismuthene (Bi-FL). **Scheme 1** gives a pictorial representation of the exfoliation of bismuthene nanosheets. Bright-field transmission electron microscopy images of Bi-FL show layered morphology (**Figure 1a**). Atomic force microscopy (AFM) analysis was carried out to understand the surface morphology and dimensions of the as-synthesized samples (**Figure 2**). AFM particle size distribution analysis for Bi-NS shows that most of the sheets have lateral dimensions ~400nm and thickness of ~8nm, while in Bi-FL lateral dimensions of ~500nm and thickness <5nm. Thickness calculated from AFM is known to be overestimated for liquid exfoliated samples due to the presence of residual solvent layer and contributions from capillary forces and adhesion,[24] therefore we expect Bi-NS to be ~ 8 layers and Bi-FL to be ~ 3 layers. The chemical purity of the samples was confirmed by Raman spectroscopy. Theoretically, bulk Bi is known to have three Raman active modes, a pair of degenerate E_g

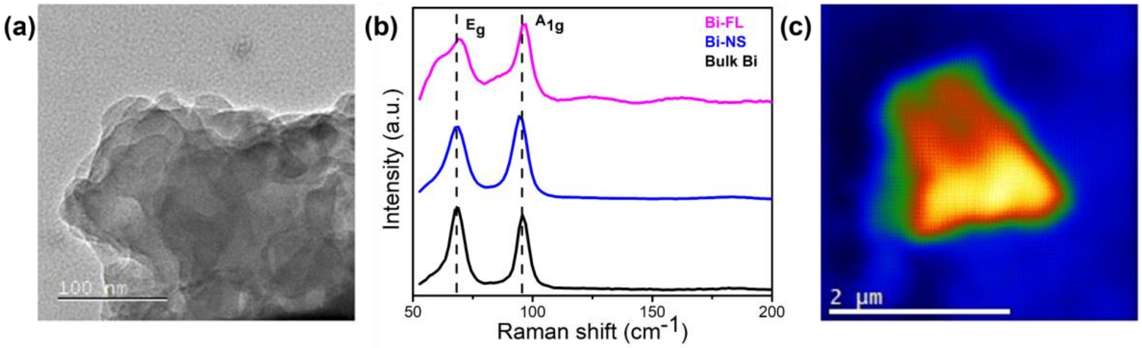

Figure 1: (a) Transmission electron microscopy image of bismuthene (Sb-FL), (b) Raman spectra of bulk Bi along with Bi-NS and Bi-FL, and (c) Cathodoluminescence mapping of Bi-FL

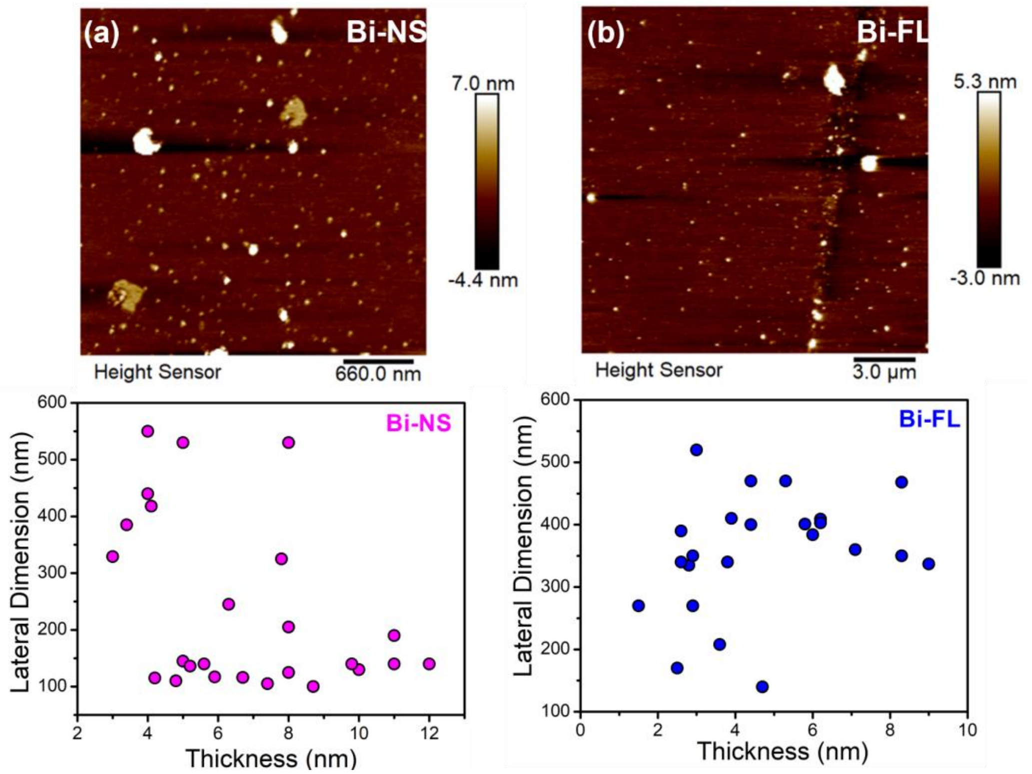

Figure 2: Atomic Force microscopy images and the corresponding particle size distributions in (a) Bi-NS and (b) Bi-FL

modes (~ 70 cm^{-1}) corresponding to in-plane transversal and longitudinal vibrations in opposite directions, and an A_{1g} mode (97 cm^{-1}) corresponding to opposite in-phase out-of-plane vibrations.[25] Experimentally bulk bismuth shows two phonon modes E_g (68.9 cm^{-1})

and A_{1g} (95.7 cm^{-1}). **Figure 1b** shows the Raman spectra of bulk Bi in comparison with Bi-NS and Bi-FL. Compared to bulk Bi, we did not observe any prominent shift in Bi-NS whereas in Bi-FL both the E_g and A_{1g} peaks are blue-shifted to 70.3 and 97 cm^{-1} respectively due to contraction of the lattice on exfoliation.[26] Oxides were not detected in Raman spectra, establishing the chemical purity of the exfoliated samples. Bulk Bi is semi-metallic and undergoes a transition to a semiconductor on exfoliation.[10] To understand the optical properties of exfoliated Bi, FESEM-cathodoluminescence studies were carried out wherein a single sheet was identified and mapped. Bi-NS did not show any emission due to its semi-metallic nature owing to its thickness, interestingly Bi-FL was found to be emissive due to the opening of bandgap owing to quantum confinement and turbostratic stacking (**Figure 1c**).

Covalent functionalization

Scheme 2: Pictorial representation of covalent functionalization of bismuthene using diazonium salt

Bi-NS was functionalized with p-Nitrobenzenediazonium tetrafluoroborate (p-NBD) under ambient conditions. **Scheme 2** gives a pictorial representation of the reaction under study. The first indication of functionalization of Bi-NS was provided by FT-IR spectroscopy and **Figure 3a** encloses the FT-IR spectra of Bi-NS-NO_2 along with p-NBD.

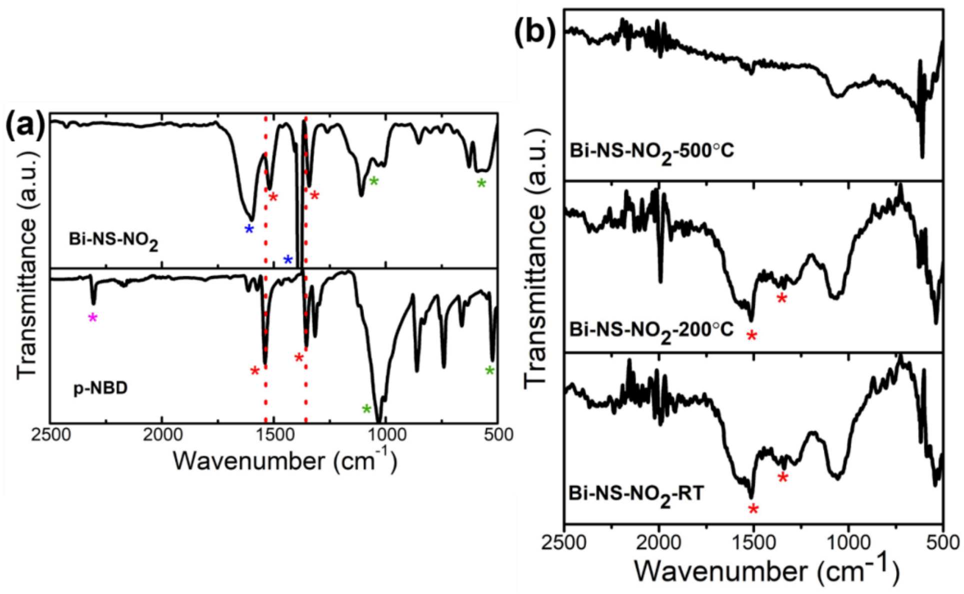

Figure 3: (a) FT-IR spectra of p-nitrobenzene diazonium tetrafluoroborate (p-NBD) and functionalized bismuthene nanosheets (Bi-NS-NO_2), (b) FT-IR spectra of Bi-NS-NO_2 heated at different temperatures

Peaks corresponding to symmetric and asymmetric stretching modes of -NO_2 are highlighted by (*), stretching mode of N_2^+ species (*), peaks corresponding to BF_4^- (*), KBr impurity (*)

FT-IR spectra of p-NBD show the N_2^+ signature peak at 2302 cm^{-1} along with sharp peaks at 1540 and 1356 cm^{-1} assigned to asymmetric and symmetric -NO_2 stretching modes; the peak at 1314 cm^{-1} is assigned to C-N stretching mode and the peaks near 1118-1030 cm^{-1} are assigned to asymmetric and symmetric stretching modes of BF_4^- counter-ion and the peak at 522 cm^{-1} correspond to bending deformation of BF_4^- counter-ion. In the FT-IR spectra of Bi-NS-NO_2, the N_2^+ peak is missing signifying the absence of unreacted diazo species in the sample. Peaks corresponding to -NO_2 stretching modes are red-shifted to 1518 and 1341 cm^{-1} (compared to p-NBD) indicating a change in the bonding environment. Interestingly, stretching modes corresponding to BF_4^- species were observed around 1150-

1007 cm^{-1} along with a bending mode at 590 cm^{-1} which are blue-shifted compared to p-NBD. The presence of BF_4^- could be insightful towards understanding the reaction mechanism. To have a better understanding of the bonding nature of the functionalized samples, Bi-NS-NO_2 was heated to 200 and 500°C, and the corresponding FT-IR spectra were analyzed (**Figure 3b**). On heating the samples at 200°C, we expect the physisorbed nitrobenzene/diazonium species if present will be removed. Since the -NO_2 stretching nodes are still intact after heating at 200°C we can conclude that the bond formed is covalent in nature. This was further confirmed by heating the samples at 500°C wherein the -NO_2 signatures disappear.

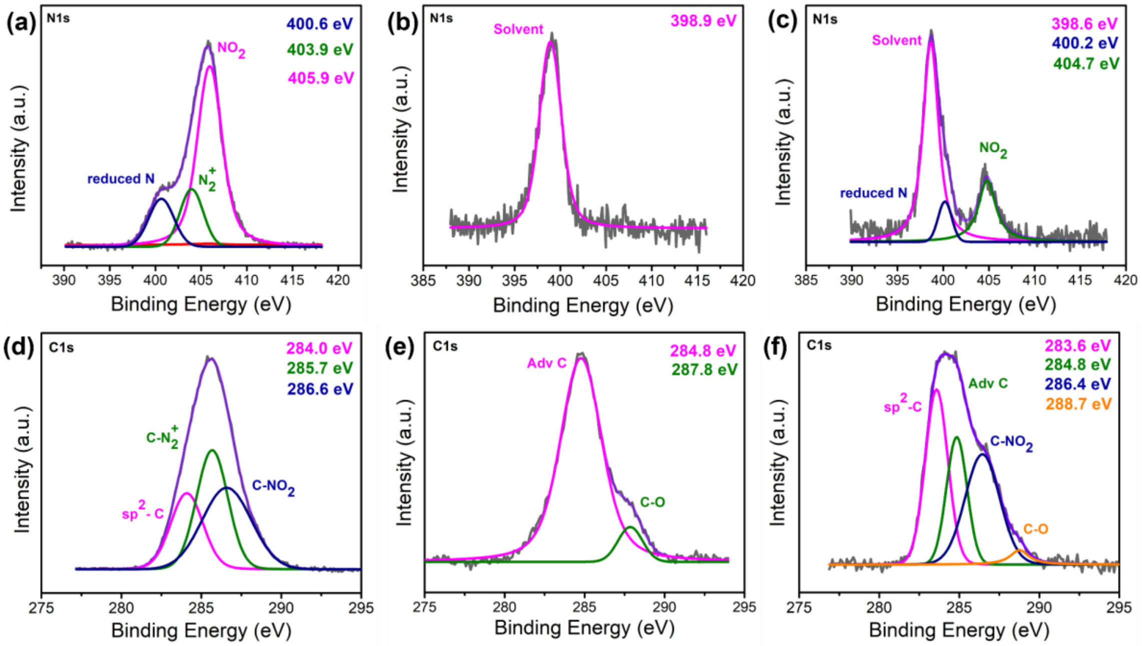

Figure 4: N1s core-level XPS spectra of (a) p-NBD, (b) Bi-NS and (c) Bi-NS-NO_2 and C1s core level spectra of (d) p-NBD, (e) Bi-NS and (f) Bi-NS-NO_2

X-ray photoelectron spectroscopy (XPS) studies were carried out to get more insights into the bonding environment (**Figure 4**). N1s core-level spectra of p-NBD (**Figure 4a**) show peaks at 405.9, 403.9, and 400.6 eV corresponding to -NO_2, -N_2^+, and reduced nitrogen species, respectively. The presence of reduced nitrogen species could be due to the reduction of the diazo/NO_2 group under storage conditions or on exposure to X-rays. The single N1s core-level peak of Bi-NS (**Figure 4b**) is due to solvent residues. N1s core-level spectra of Bi-NS-NO_2 (**Figure 4c**) show peaks at 404.7, 400.2, and 398.6 eV corresponding to -NO_2, reduced nitrogen species/azo linkage, and solvent residue, respectively. C1s core-level spectra of p-NBD (**Figure 4d**) can be deconvoluted into three peaks at 286.6, 285.7, and 284 eV corresponding to C-NO_2, C- N_2^+ and aromatic sp^2 C, respectively. For Bi-NS, C1s core-level peaks occur at 287.8 and 284.8 eV corresponding to C-O and adventitious carbon, respectively (**Figure 4e**). C1s spectra of Bi-NS-NO_2 show peaks at 288.7, 286.4, 284.8, and 283.6 eV corresponding to C-O, C-NO_2, adventitious C, and aromatic sp^2 C, respectively (**Figure 4f**). The presence of -NO_2 species and aromatic sp^2 carbon suggest that nitrobenzene-like species are covalently bonded to Bi in Bi-NS-NO_2. Quantitative analysis of XPS peaks reveals the extent of functionalization to be ~12%.

Mechanism of reaction

A good understanding of the mechanism of a reaction is crucial for tuning the extent of functionalization with varying organic moieties. To this effect, in-depth FT-IR and XPS analyses were carried out. FT-IR spectra of p-NBD show a sharp peak at 2307 cm^{-1} corresponding to N_2^+ species (**Figure 5**). p-NBD solvated in acetonitrile shows peaks at 2307 and 2279 cm^{-1} which are assigned to N_2^+ species and solvated N_2^+ species. FT-IR spectra of supernatant of the reaction mixture after 48 hours of reaction still show a peak at 2280 cm^{-1} indicating that the diazonium salt is stable in acetonitrile even after 48 hours. Moreover, the presence of a peak corresponding to BF_4^- in solvated p-NBD and supernatant

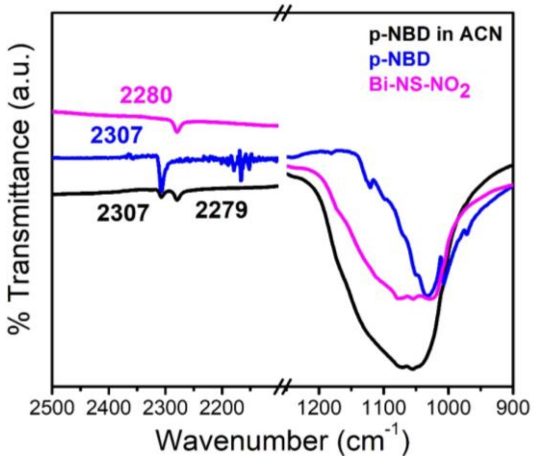

Figure 5: FT-IR spectra of diazonium salt (p-NBD), diazonium salt (p-NBD) in acetonitrile (ACN), and supernatant after reaction from Bi-NS-NO_2 (after 48 hours)

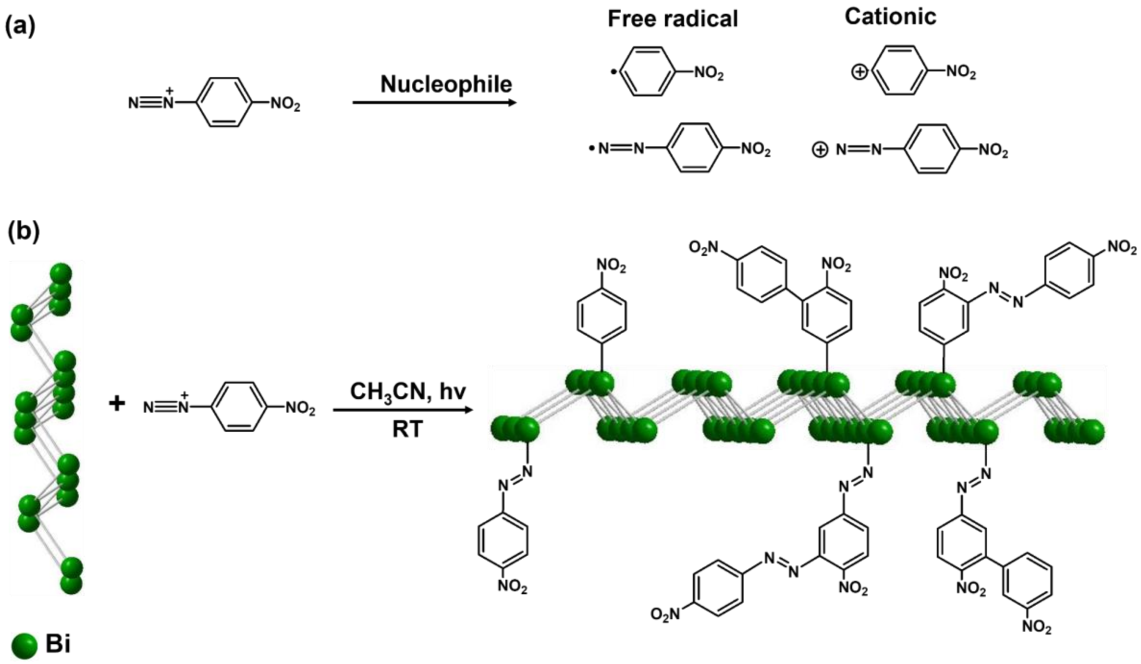

Scheme 3: Schematic illustration of (a) possible reaction intermediates of p-NBD and (b) corresponding products on covalent functionalization of bismuthene with p-Nitrobenzenediazonium tetrafluroborate

provides further proof regarding the stability of p-NBD in acetonitrile. **Scheme 3a** shows all the possible reaction intermediates for p-NBD in the presence of a nucleophile and

Scheme 3b shows the possible products. Initially, the diazonium salt can attach to Bi via Bi-C or Bi-N=N- or Bi-O-C- linkages. The presence of NO_2 peaks in the FT-IR spectra of the sample indicates preferential attachment via Bi-C or Bi-O-C since azo linkages are generally unstable above 100°C.[27] Moreover, N1s core level XPS spectra of Bi-NS-NO_2 (**Figure 4c**) did not show any distinguishable peak for azo linkage because of overlap with residual solvent peak. F1s core-level XPS spectra of Bi-NS-NO_2 show a binding energy shift of 3.6 eV compared to p-NBD (**Figure 6**) which indicates the presence of a positively charged species in the system which is counter-balanced by BF_4^- ion.

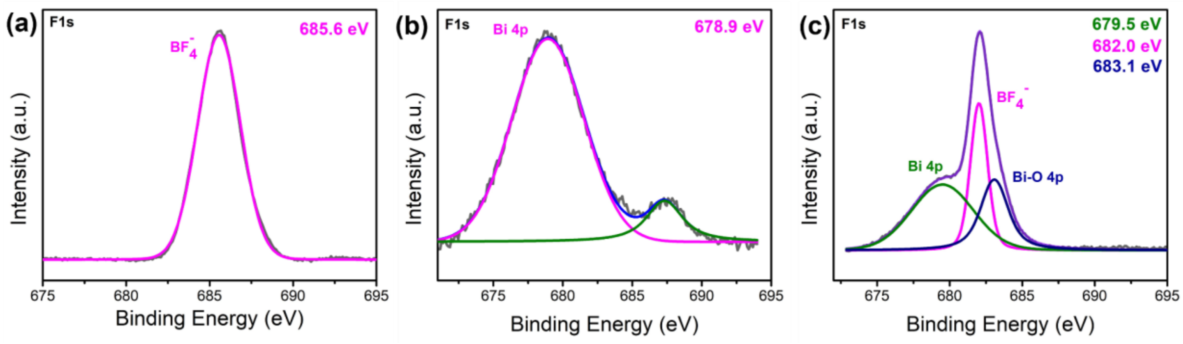

Figure 6: F1s core-level spectra of (a) p-NBD, (b) Bi-NS, and (c) Bi-NS-NO_2

Based on the stability of reactive intermediates and the nature of the nucleophile, the reaction with diazonium salts can proceed via a free-radical or cationic mechanism. For materials like Cu/Ag/Au/graphene, reaction with diazonium salts proceeds via the transfer of a single electron from the material to the diazonium salt and is reported to predominantly follow a free radical mechanism.[17,18,22,28–30] For bismuthene, we propose that the reaction will proceed via the transfer of its lone pair of electrons (VBM) to the diazonium salt with the formation of quaternary Bi^+ species and therefore will predominantly follow a cationic mechanism. There are a few reports on functionalization reactions involving two-electron transfer and the formation of quaternary species for other pnictogens.[31–33] Since Bi-O-C linkages will lead to the formation of neutral species, we expect the contribution of Bi-O-C linkage will be less i.e., the reaction will predominantly proceed via Bi-C linkage.[31]

Effects of functionalization

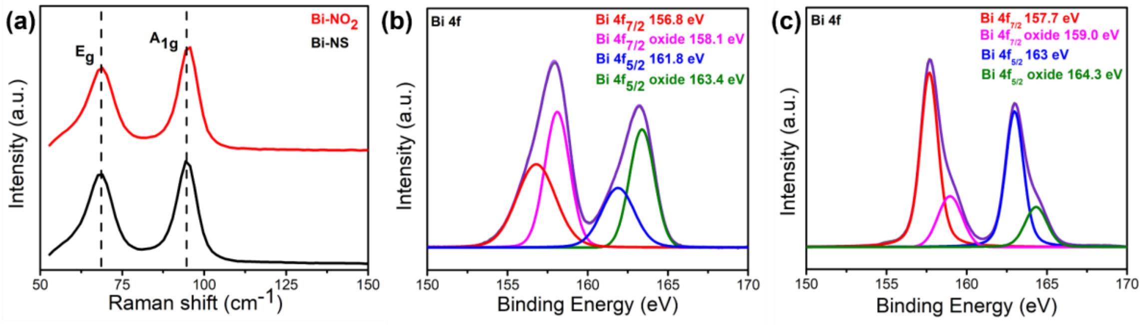

Figure 7: (a) Raman spectra of Bi-NS and Bi-NS-NO_2. Bi 4f core-level spectra of (b) Bi-NS and (c) Bi-NS-NO_2

To understand the effects of functionalization, Raman spectrum of Bi-NS-NO_2 was analyzed (**Figure 7a**). We observe a slight blue shift in A_{1g} mode from 94.3 to 95.7 cm^{-1} which indicates a change in the out-of-plane lattice constant due to the formation of Bi^+ species.[26] XPS core-level spectra of Bi-NS show peaks at 156.8 and 161.8 eV corresponding to $4f_{7/2}$ and $4f_{5/2}$, respectively (**Figure 7b**). For Bi-NS-NO_2, Bi 4f peaks are blue-shifted to 157.7 and 163 eV which confirms charge transfer from Bi to the diazonium salt and further substantiates the formation of Bi^+ species (**Figure 7c**). Moreover, Bi-NS shows Bi-oxide species which might arise due to storage and measurement conditions. Interestingly, Bi-oxide species are considerably reduced for Bi-NS-NO_2 indicating surface passivation of Bi by nitrobenzene type species.

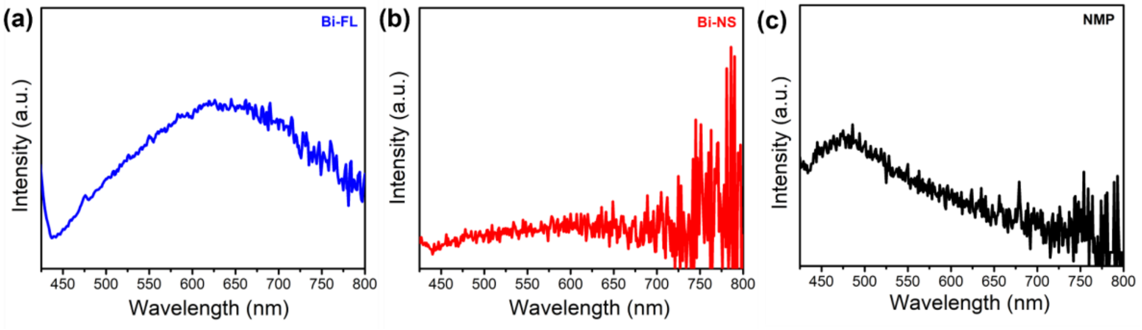

Figure 8: Photoluminescence emission spectra of (a) Bi-FL , (b) Bi-NS and (c) probe sonicated NMP

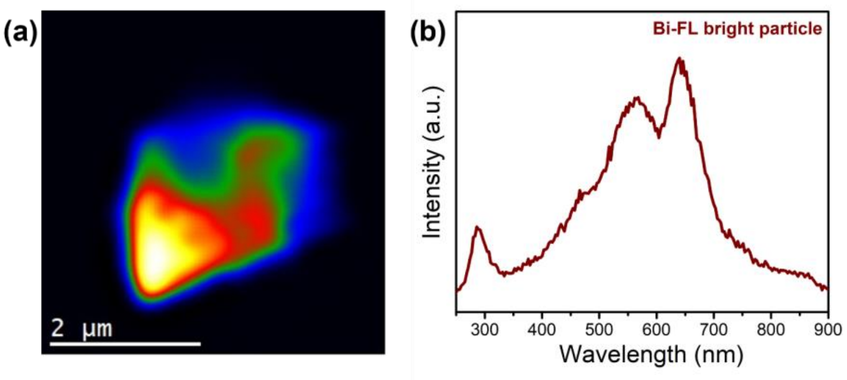

Figure 9: FESEM cathodoluminescence mapping of Bi-FL bright particle and the corresponding emission spectra used as the basis of deconvolution

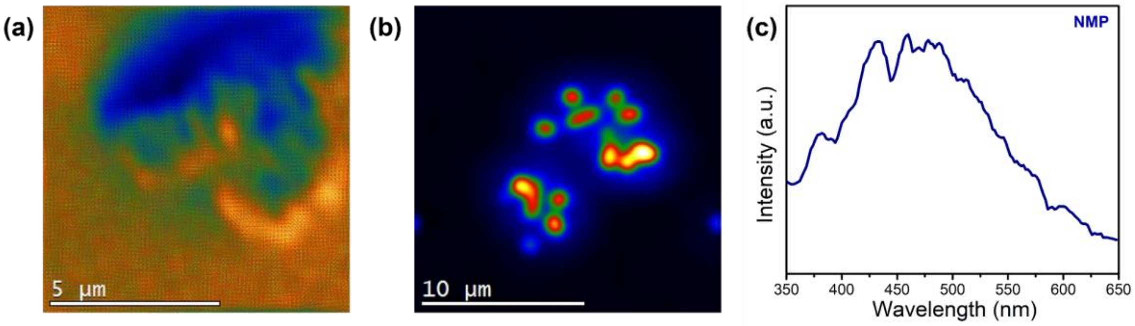

Figure 10: FESEM cathodoluminescence mapping of (a) NMP background, (b) NMP polymers and (c) CL spectra of NMP polymer

Rhombohedral bulk Bi is semi-metallic and exhibits a transition to an indirect band-gap semiconductor when thinned down to a monolayer.[10] Theoretical calculations show that bismuthene has an absorption edge at 0.74 eV with absorption maxima at 1.72 eV which shows the possibility of higher energy optical transitions in the visible range.[12] The semiconducting nature of bismuthene can be studied by photoluminescence spectroscopy. Understandingly, we did not detect any emission from Bi-NS since it comprises of thicker sheets. Interestingly, Bi-FL exhibits a broad PL emission centered around 640 nm which could be due to the possibility of multiple transitions and cumulative emission from nanosheets of various dimensions, and hence drawing out any conclusions will be inaccurate (**Figure 8**). Emissions in nanomaterials are very sensitive to their dimensions and hence for this study, a single nanosheet was tracked before and after functionalization. CL emission was not observed in Bi-NS due to its multilayered semi-metallic nature. Deconvolution of CL spectra was based on control experiments carried out on multiple Bi-FL sheets wherein some sheets seemed to have very bright emissions between 300-900 nm region with some prominent signatures since the number of such very bright sheets were only a few, such sheets were used as the basis of deconvolution (**Figure 9**). Moreover, the solvent used for exfoliation, NMP is known to be emissive in nature, and control experiments show that although in most regions the NMP signature was very blurred (**Figure 10a**), in some regions NMP undergoes polymerization to give some bright spots with an emission maximum ~ 475 nm (**Figure 10b** and **10c**). Hence, the emissions for Bi-FL under 500nm were not considered.

We have carried out FESEM cathodoluminescence (CL) studies wherein we have tracked a single nanosheet and studied its emission spectra before and after functionalization with p-NBD. (**Figure 11**). CL spectra of Bi-FL show peaks at 532 (~ 2.33 eV), 590 (~ 2.10 eV), and 660 nm (~1.88 eV) labeled as A, B, and C respectively, along with a broad feature below 500 nm and a small peak above 700 nm. Emission A

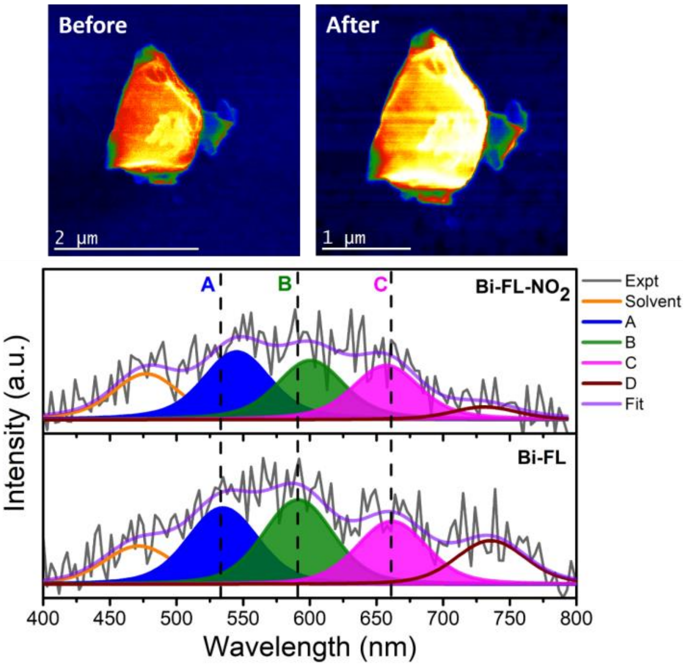

Figure 11: FESEM cathodoluminescence mapping of Bi-FL before and after reaction and the corresponding spectra

corresponds to the absorption maxima as has already been theoretically reported.[12] The presence of emissions B and C could be due to other possible emissions, defect states, and/or Bi^{3+} species which could arise during synthesis. Since we could not detect any emission from Bi-NS we can assume that the contribution of Bi^{3+} will be negligible. After functionalization, we observe a redshift in peaks A and B to 546 nm (~2.27 eV) and 601 nm (~2.01 eV) however peak C remains constant. A decrease in bandgap on the addition of a more electronegative species has already been reported for other pnictogens[34] and could arise in Bi due to the electronegativity difference between Bi and C in nitrobenzene moiety, we expect a similar closing of the bandgap. Peak C doesn't show any appreciable shift in functionalization which could be due to the nature of the defect site. The peak area ratios (C/B) increase from 74% to 91% upon functionalization which indicates the formation of more/new defect states.

This work successfully demonstrates the possibility of tuning the optical properties of bismuthene nanosheets by covalent functionalization with aryl species.

6.4.B Lewis acid-base adducts of Bismuthene

6.4.B Results and discussion

Lewis acid-base adducts

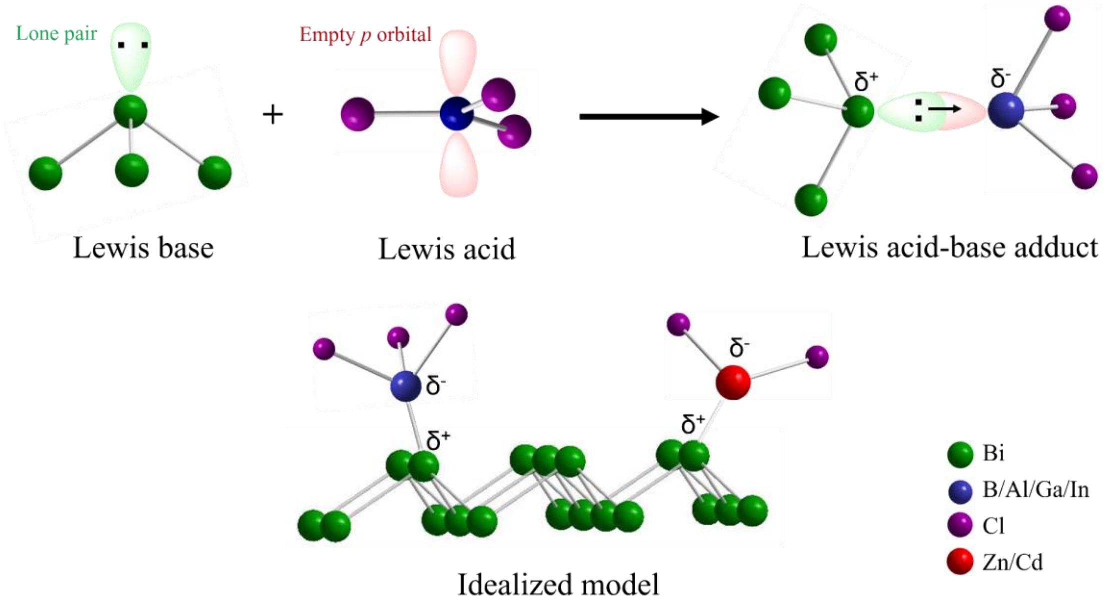

Scheme 4: Pictorial representation of the formation of Lewis acid-base adducts in bismuthene

Pnictogens, owing to the presence of lone pairs, are interesting candidates for Lewis acid-base adduct formation wherein the pnictogen atom (Bi) acts as a Lewis base (**Scheme 4**).[1] Strength of an acid/base depends on two factors: Lewis acidity/basicity and hard-soft nature with Bi being the softest and the weakest base among group 15 pnictogens. The strength/stability of a Lewis acid-base adduct depends on the inherent Lewis acidity/basicity of the two involved species along with their hard-soft nature with the strongest adducts formed between species with similar nature. We have functionalized Bi-NS and Bi-FL with group-13 metal halides with Lewis acidity order $BCl_3 > AlCl_3 \geq GaCl_3 > InCl_3$.[35–37] Amongst these, BCl_3 reacted instantaneously with a crackling sound and did not yield a solid product implying complete oxidation/corrosion of Bi lattice. Reaction with

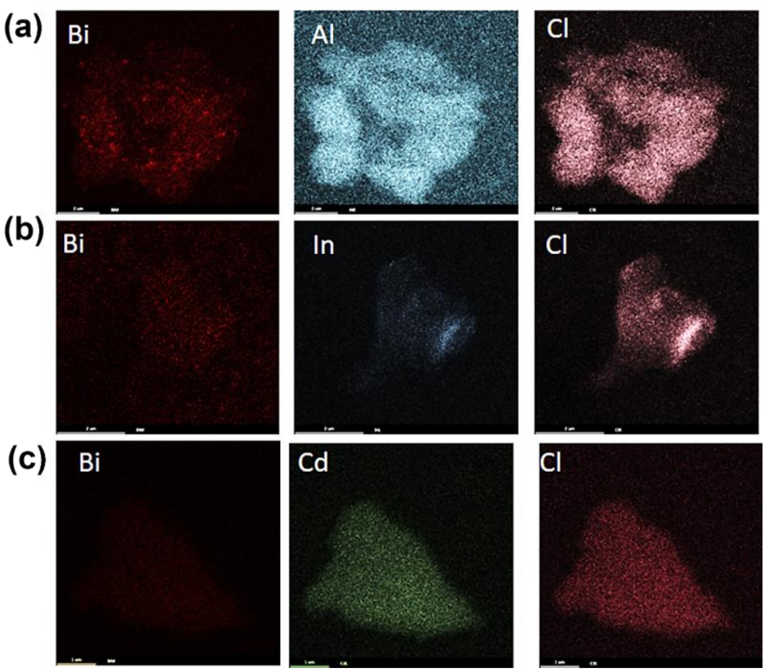

Figure 12: EDS mapping of (a) Bi-$AlCl_3$, (b) Bi-$InCl_3$, and (c) Bi-$CdCl_2$

$AlCl_3$ and $InCl_3$ yielded a solid product, wherein the reaction with $AlCl_3$ was faster than $InCl_3$ while $GaCl_3$ gave a colorless solution. This observation was not in line with the Lewis acidity order of group 13 halides which predict $GaCl_3$ to be of similar Lewis acidity to $AlCl_3$. This anomalous behavior is due to the increased softness of $GaCl_3$ which results in a corrosive reaction with Bi. $InCl_3$ being the softest and weakest Lewis acid of the group, forms the most stable adduct with Bi. We tried verifying this theory by reacting Bi-NS and Bi-FL with group 12 metal halides: $ZnCl_2$ and $CdCl_2$. Like $GaCl_3$, $ZnCl_2$ did not yield a solid product while $CdCl_2$ formed a stable adduct since its Lewis acidity and softness are similar to $InCl_3$. Energy dispersive spectroscopy mapping of functionalized materials shows uniform distribution of all the elements giving an initial indication of functionalization (**Figure 12**). Core-level XPS spectra area analysis shows the presence of Al:Cl, In:Cl, and Cd:Cl in the expected stoichiometry (**Figure 13**).

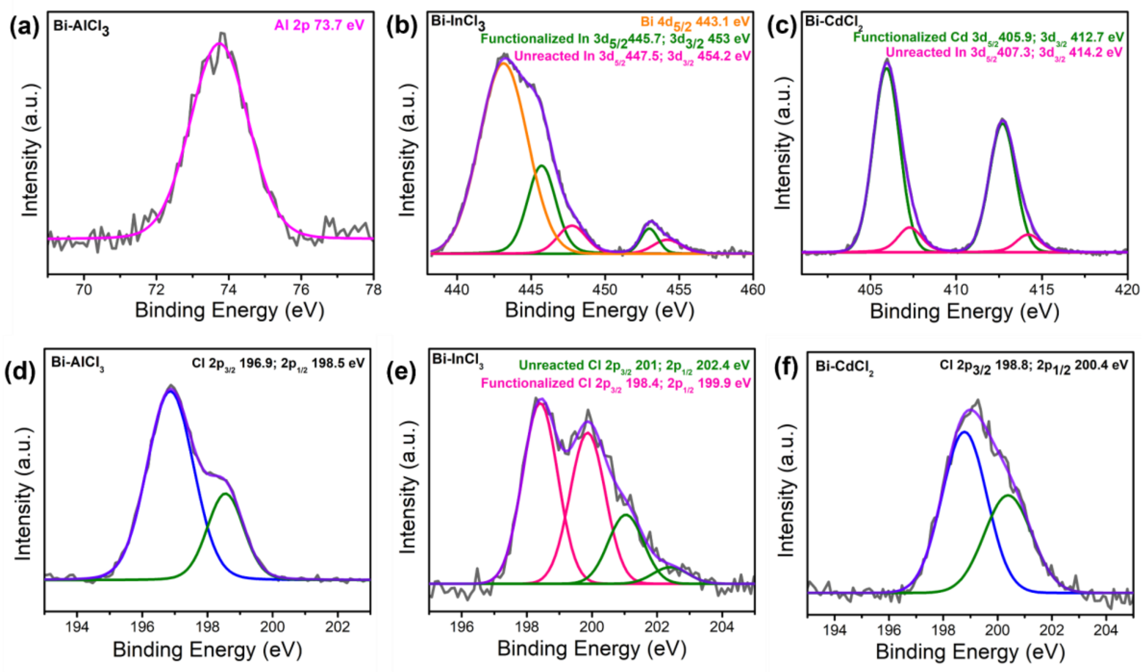

Figure 13: XPS core level spectra of (a) Al 2p Bi-$AlCl_3$, (b) In 3d Bi-$InCl_3$ and (c) Cd 3d Bi-$CdCl_2$, and Cl 2p core level spectra of (d) Bi-$AlCl_3$, (e) Bi-$InCl_3$, (f) Bi-$CdCl_2$

Charge transfer due to functionalization was probed by Raman spectroscopy (**Figure 14**). The E_g and A_{1g} modes of Bi-NS are redshifted from 70 and 95.7 cm^{-1} to 67.6 and 93 cm^{-1} in Bi-$CdCl_2$; and 67.6 and 91.7 cm^{-1} in Bi-$InCl_3$ while it remains almost constant for Bi-$AlCl_3$. Redshift in vibrational modes arises due to the strain introduced in the lattice owing to charge transfer and steric repulsions on functionalization which affects the out-of-plane lattice constant more strongly compared to the in-plane lattice constant.[38] Similar redshifts in Raman peaks on functionalization with Lewis acid have been previously reported for InSe-$TiCl_4$ wherein the strain introduced on interaction with $TiCl_4$ forces Se out of its lattice.[39] A similar redshift of Raman peaks due to strain is also reported for graphene, phosphorene, and other materials.[38] The extent of redshift on interaction/adduct formation depends upon the Lewis acidity/basicity and nature of the materials. From our study, we observe the highest redshift for $InCl_3$ signifying stronger charge transfer and steric repulsion in $InCl_3$ followed by $CdCl_2$ and negligible shifts in $AlCl_3$. Raman modes corresponding to Lewis acids were not observed in any functionalized sample.

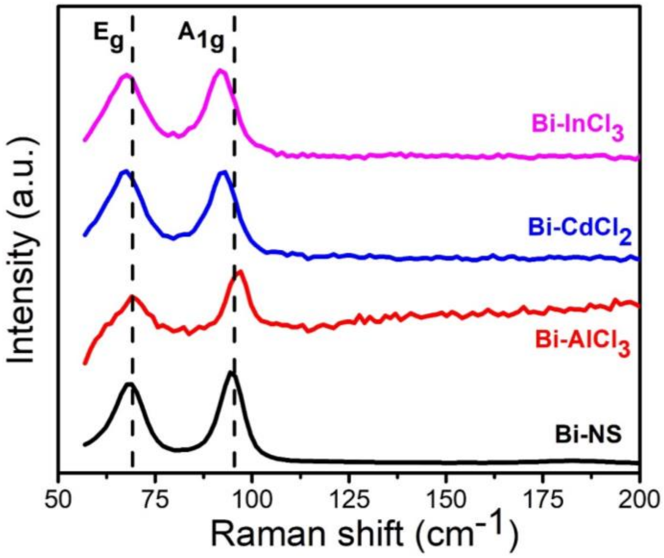

Figure 14: Raman spectra of functionalized bismuthene samples

To gain further insights into the bonding nature of the adducts, core-level XPS spectra were deconvoluted and analyzed (**Figure 15**). Bi core level XPS consists of Bi $4f_{7/2}$ and $4f_{5/2}$. Bi $4f_{7/2}$ core level spectra of Bi-NS show two peaks at 156.8 and 158.1 eV corresponding to Bi(0) and surface Bi-oxide species. On functionalization, Bi $4f_{7/2}$ peaks can be deconvoluted into two peaks corresponding to functionalized Bi and functionalized surface Bi-oxide species. Functionalized Bi $4f_{7/2}$ peak is blue-shifted by 0.9, 2.7 and 2.6 eV for $AlCl_3$, $InCl_3$ and $CdCl_2$, respectively. Based on the core level shifts, both $InCl_3$ and $CdCl_2$ interact to give more stable adducts. Core level spectra of Al 2p, Cd 3d, and In 3d are correspondingly red-shifted by 1, 1.8, and 1.4 eV indicating the transfer of electrons from Bi to Lewis acid. Blueshift in Bi-metal $4f_{7/2}$ peak and redshift in Lewis metal core level peak proves the successful functionalization and adduct formation with Bi. Moreover, there is a decrease in relative oxide content after functionalization indicating surface passivation.

Effects of functionalization

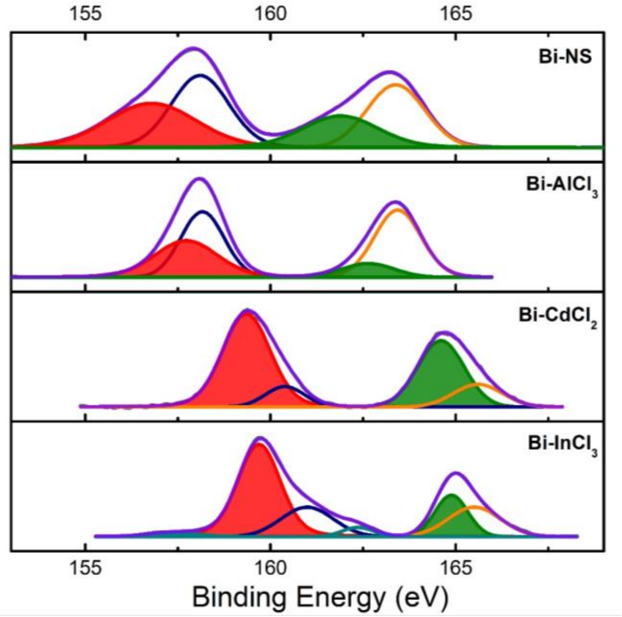

Figure 15: Bi 4f XPS core-level spectra of functionalized bismuthene samples

To understand the effects of functionalization on the band structure, FESEM cathodoluminescence (CL) studies were carried out. Emissions in nanomaterials are very sensitive to their dimensions and hence for this study, a single nanosheet was tracked before and after functionalization. Deconvolution of CL spectra and emission contributions from solvent (NMP) have already been discussed in **section 6.4.A**.

The broad emission feature in Bi-FL (**Figure 16**) can be deconvoluted into three emissions (A, B, and C) corresponding to absorption maxima (A) and defect emissions or emissions related to other possible optical transitions (B and C) along with weaker defect

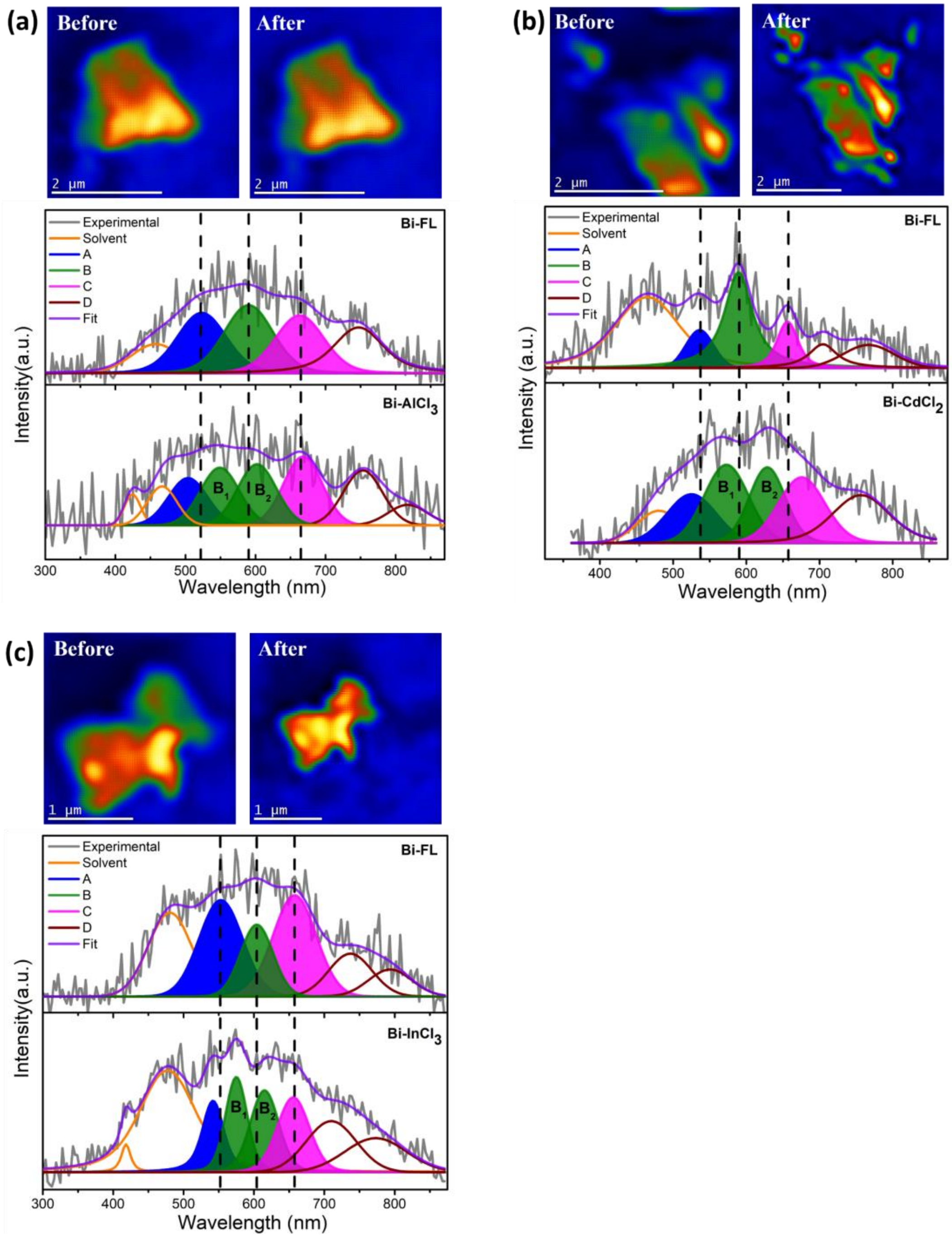

Figure 16: FESEM cathodoluminescence mapping and the corresponding spectra for (a) Bi-$AlCl_3$, (b) Bi-$CdCl_2$ and (c) Bi-$InCl_3$

emission above 700 nm and a broad band below 500 nm corresponding to solvent emission. The absence of any emissions in Bi-NS rules out the contribution from Bi^{3+} species.

Absorption maxima (emission A) in Bi-FL sheets considered for functionalization with $AlCl_3$, $InCl_3$ and $CdCl_2$ occurs at 2.37, 2.24 and 2.31 eV, respectively. Interestingly, these emissions are blue-shifted to 2.46, 2.29, and 2.36 eV, respectively. Blue shifts were also observed in the other emission/defect bands due to the introduction of new defect states in the lattice and are more pronounced for peak B which is split into two emissions after functionalization. The extent of shifts in band edge cannot be directly correlated with the extent of shifts in XPS or Raman as the changes in band structure are dominated by the incorporation of Lewis acid metal bands in the band structure bismuthene.[38] Splitting/ addition of a new defect state in Bi-FL might be due to strong adduct formation and corroborates with the XPS and Raman results. The shifts in XPS core level, Raman modes, and emission spectra indicates charge transfer from Bi to Lewis acids, lattice distortion due to strain-induced by attachment of Lewis acids, and rehybridization of band structure on successful functionalization of few-layered Sb/Bi (**Table 1**).

Table 1: Summary of experimental results of functionalization of bismuthene with Lewis acids

Shifts on functionalization with	**XPS**	**Raman**	**CL**
	Bi $4f_{7/2}$ (eV)	(E_g, A_{1g}) (cm^{-1})	Emission A (eV)
$AlCl_3$	0.9	0,0	-0.09
$InCl_3$	2.7	-1.3, -4	-0.05
$CdCl_2$	2.6	-1.3, -2.7	-0.05

This work successfully demonstrates the possibility of tuning the optical properties of bismuthene nanosheets by Lewis acid-base adduct formation.

6.5 Conclusions

We have synthesized bismuthene nanosheets by liquid exfoliation and studied their emission properties. Theoretically, bismuthene shows semi-metal to semiconductor transition in monolayer regime with a bandgap of 0.74 eV and absorption maxima at 1.72 eV. The presence of emission in few-layered bismuthene could be due to band opening on account of quantum confinement and turbostratic stacking. Few-layered bismuthene nanosheets displayed emissions corresponding to the absorption maxima at ~ 2.3 eV along with other possible transitions/defect-related emissions. We could successfully redshift this peak by 0.06 eV on functionalization with p-Nitrobenzenediazonium tetrafluoroborate. Covalent functionalization with diazonium salt proceeds with the transfer of lone pair from Bi to diazonium salt forming a quaternary Bi^+ species with the attachment of organic moieties predominantly via Bi-C linkages. We have also studied Lewis acid-base adduct formation of bismuthene with group 12 and 13 Lewis acids which leads to lattice distortion, charge transfer, and rehybridization of the band structure. We observed a blue shift in the emission of bismuthene after functionalization with different Lewis acids. The strength/stability of the adduct and the corresponding change in property depends on the Lewis acidity and basicity of the interacting materials and their hard-soft nature along with changes in band structure due to rehybridization by Lewis acid metal bands. Based on these two parameters, different Lewis acids can be used to achieve desirable tunability and surface passivation. The present study demonstrates the efficacy of covalent and Lewis acid-base adduct formation in tuning material properties and will be instrumental for the incorporation of pnictogens for electronic and optoelectronic applications.

References

(1) Zhang, S.; Xie, M.; Li, F.; Yan, Z.; Li, Y.; Kan, E.; Liu, W.; Chen, Z.; Zeng, H. *Angew. Chem.,* **2016**, *128* (5), 1698–1701.

(2) Liu, X.; Zhang, S.; Guo, S.; Cai, B.; Yang, S. A.; Shan, F.; Pumera, M.; Zeng, H. *Chem. Soc. Rev*., **2020**, *1* (1) 263–285.

(3) Zhang, S.; Guo, S.; Chen, Z.; Wang, Y.; Gao, H.; Gómez-Herrero, J.; Ares, P.; Zamora, F.; Zhu, Z.; Zeng, H. *Chem. Soc. Rev*., **2018**, *47* (3), 982–1021.

(4) Zhang, S.; Yan, Z.; Li, Y.; Chen, Z.; Zeng, H. *Angew. Chem.,* **2015**, *127* (10), 3155–3158.

(5) Liu, H.; Neal, A. T.; Zhu, Z.; Luo, Z.; Xu, X.; Tománek, D.; Ye, P. D., *ACS Nano*, **2014**, *8* (4), 4033–4041.

(6) Aktürk, E.; Aktürk, O. Ü.; Ciraci, S., *Phys. Rev. B,* **2016**, *94* (1), 014115.

(7) Kadioglu, Y.; Kilic, S. B.; Demirci, S.; Aktürk, O. Ü.; Aktürk, E.; Ciraci, S., *Phys. Rev. B,* **2017**, *96* (24), 245424

(8) Aguilera, I.; Friedrich, C.; Blügel, S., *Phys. Rev. B,* **2015**, *91* (12), 125129

(9) Wang, Y.; Huang, W.; Zhao, J.; Huang, H.; Wang, C.; Zhang, F.; Liu, J.; Li, J.; Zhang, M.; Zhang, H., *J. Mater. Chem. C,* **2019**, *7* (4), 871–878.

(10) Liu, M. Y.; Huang, Y.; Chen, Q. Y.; Li, Z. Y.; Cao, C.; He, Y., *RSC Adv.,* **2017**, *7* (63), 39546–39555.

(11) Gui, R.; Jin, H.; Sun, Y.; Jiang, X.; Sun, Z., *J. Mater. Chem. A*, **2019**,*7*, 25712-25771

(12) Kecik, D.; Özçelik, V. O.; Durgun, E.; Ciraci, S., *Phys. Chem. Chem. Phys.,* **2019**, *21* (15), 7907–7917.

(13) Hussain, N.; Liang, T.; Zhang, Q.; Anwar, T.; Huang, Y.; Lang, J.; Huang, K.; Wu, H., *Small,* **2017**, *13* (36), 1701349.

(14) Jellett, C.; Plutnar, J.; Pumera, M., *ACS Nano*, **2020**, *14* (7), 7722–7733.

(15) Glavin, N. R.; Rao, R.; Varshney, V.; Bianco, E.; Apte, A.; Roy, A.; Ringe, E.; Ajayan, P. M., *Adv. Mater*., **2020**, *32* (7), 1904302

(16) Mannix, A. J.; Kiraly, B.; Hersam, M. C.; Guisinger, N. P., *Nat. Rev. Chem*., **2017**, *1*, 0014

(17) Betelu, S.; Tijunelyte, I.; Boubekeur-Lecaque, L.; Ignatiadis, I.; Ibrahim, J.; Gaboreau, S.; Berho, C.; Toury, T.; Guenin, E.; Lidgi-Guigui, N.; Félidj, N.; Rinnert, E.; Chapelle, M. L., *J. Phys. Chem. C,* **2016**, *120* (32), 18158–18166.

(18) Mesnage, A.; Lefèvre, X.; Jégou, P.; Deniau, G.; Palacin, S., *Langmuir,* **2012**, *28* (32), 11767–11778.

(19) Mohamed, A. A.; Salmi, Z.; Dahoumane, S. A.; Mekki, A.; Carbonnier, B.; Chehimi, M. M., *Adv. Colloid Interface Sci*., **2015**, *225*, 16–36.

(20) Dyke, C. A.; Tour, J. M., *Nano Lett.,* **2003**, *3* (9), 1215–1218.

(21) Stewart, M. P.; Maya, F.; Kosynkin, D. v.; Dirk, S. M.; Stapleton, J. J.; McGuiness, C. L.; Allara, D. L.; Tour, J. M., *J Am. Chem. Soc.,* **2004**, *126* (1), 370–378.

(22) Ryder, C. R.; Wood, J. D.; Wells, S. A.; Yang, Y.; Jariwala, D.; Marks, T. J.; Schatz, G. C.; Hersam, M. C., *Nat. Chem.,* **2016**, *8* (6), 597–602.

(23) Ghodrati, H.; Antonatos, N.; Sofer, Z., *Small*, **2019**, *15*(43), 1903495.

(24) Szirmai, P.; Márkus, B. G.; Chacón-Torres, J. C.; Eckerlein, P.; Edelthalhammer, K.; Englert, J. M.; Mundloch, U.; Hirsch, A.; Hauke, F.; Náfrádi, B.; Forró, L.; Kramberger, C.; Pichler, T.; Simon, F., *Sci. Rep.,* **2019**, *9* (1), 19480.

(25) Trentelman, K. A., *J Raman Spectrosc.,* **2009**, *40* (5), 585–589.

(26) Gibaja, C.; Rodriguez-San-Miguel, D.; Ares, P.; Gómez-Herrero, J.; Varela, M.; Gillen, R.; Maultzsch, J.; Hauke, F.; Hirsch, A.; Abellán, G.; Zamora, F., *Angew. Chem.,* **2016**, *55* (46), 14345–14349.

(27) Saint-Cricq, P.; Deshayes, S.; Zink, J. I.; Kasko, A. M., *Nanoscale,* **2015**, *7* (31), 13168–13172.

(28) Englert, J. M.; Dotzer, C.; Yang, G.; Schmid, M.; Papp, C.; Gottfried, J. M.; Steinrück, H. P.; Spiecker, E.; Hauke, F.; Hirsch, A., *Chem.,* **2011**, *3* (4), 279–286.

(29) Paulus, G. L. C.; Wang, Q. H.; Strano, M. S., *Acc. Chem. Res.,* **2013**, *46* (1), 160–170.

(30) Hurley, B. L.; McCreery, R. L., *J. Electrochem. Soc.,* **2004**, *151* (5), B252.

(31) van Druenen, M.; Davitt, F.; Collins, T.; Glynn, C.; O'Dwyer, C.; Holmes, J. D.; Collins, G., *Chem. Mater.,* **2018**, *30* (14), 4667–4674.

(32) Abellán, G.; Ares, P.; Wild, S.; Nuin, E.; Neiss, C.; Miguel, D. R.-S.; Segovia, P.; Gibaja, C.; Michel, E. G.; Görling, A.; Hauke, F.; Gómez-Herrero, J.; Hirsch, A.; Zamora, F., *Angew. Chem.,* **2017**, *129* (46), 14581–14586.

(33) Wild, S.; Fickert, M.; Mitrovic, A.; Lloret, V.; Neiss, C.; Vidal-Moya, J. A.; Rivero-Crespo, M. Á.; Leyva-Pérez, A.; Werbach, K.; Peterlik, H.; Grabau, M.; Wittkämper, H.; Papp, C.; Steinrück, H. P.; Pichler, T.; Görling, A.; Hauke, F.; Abellán, G.; Hirsch, A., *Angew. Chem.,* **2019**, *58* (17), 5763–5768.

(34) Zhang, S.; Zhou, W.; Ma, Y.; Ji, J.; Cai, B.; Yang, S. A.; Zhu, Z.; Chen, Z.; Zeng, H., *Nano Lett.*, **2017**, *17* (6), 3434–3440.

(35) Satchell, D. P. N.; Satchell, R. S., *Chem. Rev.*, **1969**, *69* (3), 251–278

(36) Satchell, D. P. N.; Satchell, R. S., *Chem. Soc. Rev.,* **1971**, *25* (1), 171–199.

(37) Å Kobayashi, S.; Busujima, T.; Nagayama, S., *Chemistry*, **2000**, *6* (19), 3491-3494.

(38) Ienco, A.; Manca, G.; Peruzzini, M.; Mealli, C., *Dalton. Trans.,* **2018**, *47* (48), 17243–17256.

(39) Lei, S.; Wang, X.; Li, B.; Kang, J.; He, Y.; George, A.; Ge, L.; Gong, Y.; Dong, P.; Jin, Z.; Brunetto, G.; Chen, W.; Lin, Z. T.; Baines, R.; Galv'o, D. S.; Lou, J.; Barrera, E.; Banerjee, K.; Vajtai, R.; Ajayan, P., *Nat. Nanotechnol.*, **2016**, *11* (5), 465–471.

Appendix

Covalent functionalization of semiconducting metal chalcogenide nanoparticles

SUMMARY

Covalent functionalization of semiconducting nanoparticles was carried out to tune the properties of the material. This work also shows the possibility of studying Förster resonance energy transfer (FRET) in similar systems by covalently attaching the donor-acceptor species.

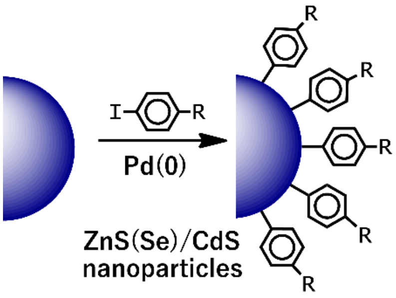

Results and discussion

Covalent functionalization is an interesting strategy to tune the inherent properties of materials for various applications.[1–5] We have covalently functionalized

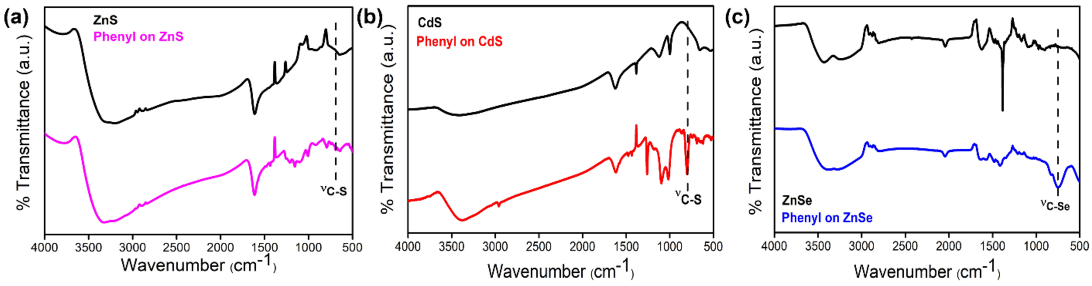

Figure 1: FT-IR spectra of iodobenzene functionalized (a) ZnS, (b) CdS, and (c) ZnSe

Paper based on this work has appeared in *ChemNanoMat*, **2018**, *4*, 41

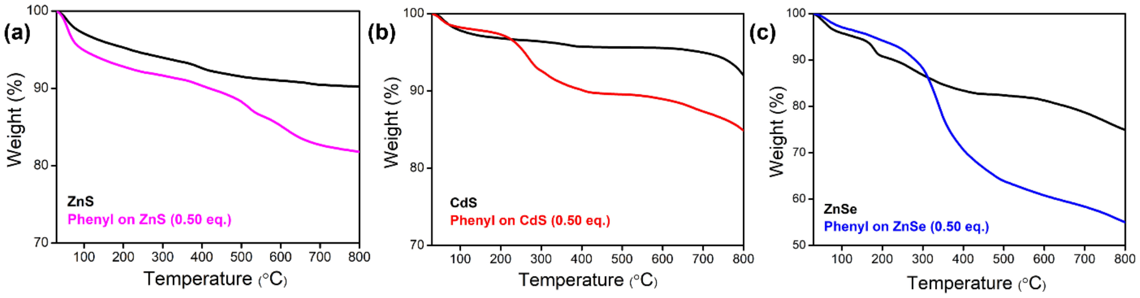

Figure 2: TGA plots of iodobenzene functionalized (a) ZnS, (b) CdS, and (c) ZnSe

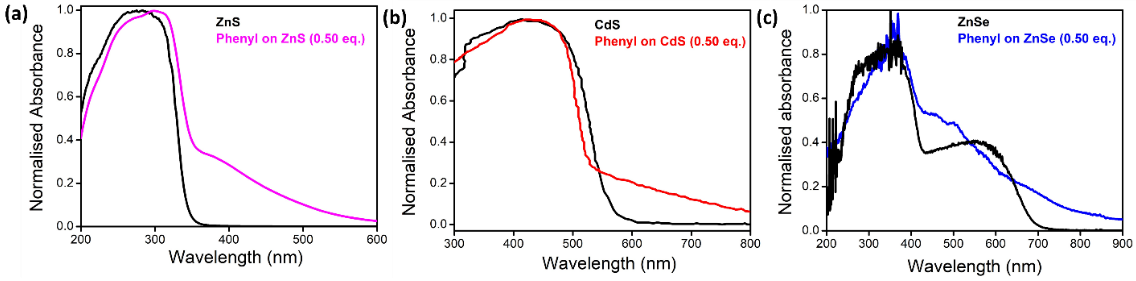

Figure 3: UV-visible absorption spectra of (a) ZnS, (b) CdS and (c) ZnSe nanoparticles along with the corresponding functionalized spectra showing a broad charge transfer band at higher wavelengths

ZnS, CdS, and ZnSe nanoparticles with iodobenzene. The synthesis procedures used have already been reported previously for similar materials.[2,6,7] Successful functionalization was confirmed by the presence of C-S/C-Se bond vibrations in the FT-IR spectra of the functionalized products (**Figure 1**). The extent of functionalization can be determined by the corresponding TGA plots of the functionalized products (**Figure 2**). We expect the covalent functionalization of these nanoparticles to proceed via the transfer of electrons from the valence band of these nanoparticles dominated by 2p/3p orbitals of S/Se to the 2p orbitals of benzene with the release of iodide ion in the presence of Pd(0) catalyst and the same has been validated by First-principles calculations. The UV-visible absorption spectra of the functionalized products show the presence of a charge transfer band at a higher wavelength which could be due to band structure modification upon functionalization along with the introduction of new levels corresponding to the benzene ring (**Figure 3**).[1] The new charge transfer bands in ZnS, CdS, and ZnSe are observed at ~380, 600, and 700 nm respectively. Relative positions of the charge transfer bands can be understood by comparing the valence band edges of the three types of materials.

Literature reports suggest that one primary criterion for a donor-acceptor molecule pair to show Förster resonance energy transfer (FRET) is that the emission spectra of the donor and the absorption spectra of the acceptor species must overlap for effective non-radiative energy transfer to take place. Naphthalene and coumarin or naphthalene and pyrene are such FRET active donor-acceptor pairs. We have conducted photoluminescence titration experiments using a donor (2-(bromoacetyl)naphthalene) - acceptor (3-(bromoacetyl)coumarin) mixture with increasing concentrations of ZnS (**Figure 4**). The photoluminescence spectrum of 2-(bromoacetyl)naphthalene on excitation at 280 nm shows an emission band around 340 nm, while the donor-acceptor mixture shows a broad coumarin-based

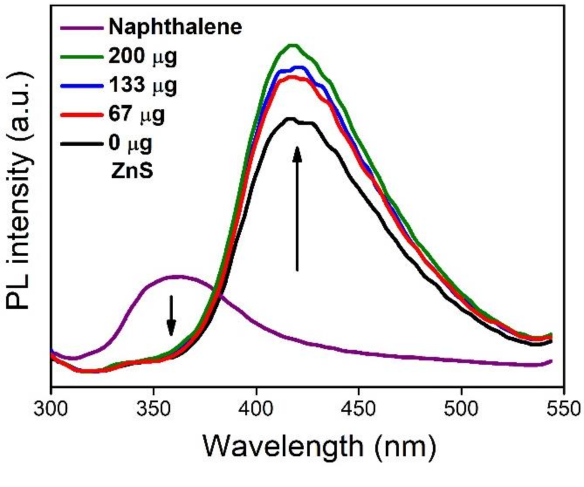

Figure 4: Fluorescence emission spectra of the mixture of 2-(bromoacetyl)naphthalene and 3-(bromoacetyl)coumarin (16.5 μM each) in the presence of increasing concentration of ZnS in DMF. The excitation wavelength is 280 nm. Downward arrow indicates decrease in intensity of naphthalene- based emission band.

emission band around 420 nm. Upon addition of ZnS into the reaction mixture, the intensity of naphthalene emission decreases further while the intensity of coumarin emission increases hence indicating successful Förster resonance energy transfer (FRET) between the donor-acceptor pair as this gives control on the relative arrangement of the donor-acceptor dipoles which in-turn affect the FRET efficiency.

This work demonstrates the successful functionalization of semiconducting nanoparticles using iodobenzene with the functionalized nanoparticles showing a charge transfer band at a higher wavelength. This report also shows the possibility of attaching multichromatic donor-acceptor dyads (as naphthalene-coumarin) on the surface of semiconducting metal chalcogenide nanoparticles to study Förster resonance energy transfer (FRET) in similar systems.

References

(1) Voiry, D.; Goswami, A.; Kappera, R.; Silva, C. D. C. C. E.; Kaplan, D.; Fujita, T.; Chen, M.; Asefa, T.; Chhowalla, M., *Nat. Chem.,* **2015**, *7* (1), 45–49.

(2) Vishnoi, P.; Sampath, A.; Waghmare, U. v.; Rao, C. N. R., *Chem.Eur. J.,* **2017**, *23* (4), 886–895.

(3) Maitra, U.; Jain, A.; George, S. J.; Rao, C. N. R., *Nanoscale,* **2011**, *3* (8), 3192–3197.

(4) Pelaz, B.; del Pino, P.; Maffre, P.; Hartmann, R.; Gallego, M.; Rivera-Fernández, S.; de La Fuente, J. M.; Nienhaus, G. U.; Parak, W. J., *ACS Nano,* **2015**, *9* (7), 6996–7008.

(5) Presolski, S.; Pumera, M., *Mater. Today*., **2016**, *19* (3), 140–145.

(6) Li, H. L.; Zhu, Y. C.; Chen, S. G.; Palchik, O.; Xiong, J. P.; Koltypin, Y.; Gofer, Y.; Gedanken, A., *J. Solid State Chem.,* **2003**, *172* (1), 102–110.

(7) Zhu, J.; Koltypin, Y.; Gedanken, A., *Chem. Mater.,* **2000**, *12* (1), 73–78.